

**The Phonon Entropy of Transition Metals and Alloys:  
Effects of Impurities and of a Martensitic Phase Transition**

Thesis by  
Olivier Delaire

In Partial Fulfillment of the Requirements  
for the Degree of  
Doctor of Philosophy



California Institute of Technology  
Pasadena, California

2006

(Defended May 12th, 2006)



## Acknowledgements

First and foremost, I would like to thank my advisor, Brent Fultz, for his guidance and support throughout my graduate student experience at Caltech. I count myself as very fortunate for having him as a research mentor and collaborator during these years.

I wish to acknowledge the help and support of our collaborators at Los Alamos and Argonne National Laboratories: Rob McQueeney, Ray Osborn and Frans Trouw, as well as Markus Hehlen and Eugene Goremychkin. They made our inelastic neutron scattering experiments possible through their advice and unrelenting support and were always willing to share their deep knowledge and understanding of neutron scattering.

I am also indebted to all the members of the Caltech community who have helped me in my research endeavours over the years: Bill Johnson, for his illuminating thermodynamics lectures, being receptive to my interrogations, and letting me use the equipment in his group extensively; Tahir Çağın, who responded to my computational inquiries with interest and guided me through my first steps with density functional theory simulations; and Haibin Su, for interesting discussions about first-principles calculations and solid-state physics in general.

I wish to thank all the members and collaborators of the Fultz group. I am particularly indebted to previous graduate students in Brent Fultz's research group, Mike Manley and Peter Bogdanoff, whose steps I have followed into: you tremendously impressed me and inspired me. I extend special thanks to my long-time officemates, Tabitha Swan-Wood, Jiao Lin, Jason Graetz, and Max Kresch. All of you have been wonderful; you made work so much more enjoyable, both at Caltech and our trips. Thanks also to Alex Papandrew, Ryan Monson, Joanna Dodd, Matt Lucas and Rebecca Stevens for helping out, sharing ideas and for interesting conversations. I thank Tim Kelley for his expert help on neutron scattering data reduction. I wish to thank also Mike McKerns and John McCorquodale for their expert support with computing and Jonny Lin for his work on, and help with, development of parallel software for Born-von Kármán inversions. Special thanks are due to Jorge Muñoz, who devoted considerable effort and achieved impressive results during his MURF project in our group. I also wish my best to younger students in Brent's group, who all show great promise of overachieving, Mike Winterrose, Chen Li, and Justin Purewal.

Thanks to Rachid Yazami, for accepting to serve on my candidacy exam with short notice, and for sharing his experience as a researcher in several countries. Thanks also to Channing Ahn, for his kind help with experimental matters. Special thanks to Itzhak Halevy for an interesting collaboration, for introducing me to high-pressure investigations and the basics of Hebrew. Thanks also to Carol Garland and Mike Wondrus for their technical help and to all the staff members in Materials Science for their support.

I wish to take this opportunity to also thank Arthur Motta, my M.S. advisor at PennState, for allowing me to come to the USA during my third year at the Ecole Centrale de Lyon, for guiding me through my first steps in research, and for his friendship. Merci.

My special thoughts go to the friends who have made these years at Caltech much more enjoyable. In particular, I extend my gratitude to my long-time roommates and friends Nicolas Ponchaut, Matthieu Liger, Pierre Moreels, Frank Ducheneaux, and Chin-Wen Chou: thanks for bearing with me and keeping me sane. Chaleureux remerciements to all the current and former French students and visitors in the Materials Science department, who have made Caltech a home away from home: Yvan Reynier, Anne Dailly, Aurélie and JY, Mélanie and Houria. Come back to visit, I know you miss SoCal!

All my deepest thoughts go to Celia: for all the love and support you have given me during these past years. Your determination and optimism have been a constant source of inspiration to me. You made this possible.

Finally, all my gratitude goes to my parents, my sisters Stéphanie and Emilie, and my family, for their unconditional love and constant support across the distance and throughout the years.

Financial support for the work presented in this thesis was provided by the US Department of Energy.

# The Phonon Entropy of Transition Metals and Alloys: Effects of Impurities and of a Martensitic Phase Transition

by

Olivier Delaire

In Partial Fulfillment of the  
Requirements for the Degree of  
Doctor of Philosophy

## Abstract

For a fixed configuration of ions on a given crystalline lattice, low energy excitations around the static average configuration can be thermally activated and will contribute to the entropy of the system. As such, nuclear vibrations, spin-waves, or electronic excitations have their own entropic contribution. The entropy associated with these degrees of freedom is usually neglected in calculations of alloy thermodynamics, however. A simple reason is that the systematics of so-called excess entropy terms are not understood very well, and these terms are difficult to compute. This thesis investigates the entropic effects of lattice vibrations, or phonons, in transition metal alloys, both from experimental and computational points of view.

From inelastic neutron scattering measurements, it is found that a few percent of transition metal solutes strongly affect the phonon density of states (DOS) of pure vanadium. In particular, alloying with 6% Pt solutes produces a strong stiffening of the phonon DOS, inducing a large and negative vibrational entropy of mixing, which overcomes the positive gain in configurational entropy. This result is the first reported observation of a negative total entropy of mixing in a binary alloy. Chemical trends in the phonon DOS and vibrational entropy of dilute vanadium alloys were investigated, for impurity elements across the  $3d$ ,  $4d$  and  $5d$ -series. A previously unknown correlation is established between the vibrational entropy of alloying and the difference in electronegativity of the solute and the host atoms. First-principles charge transfer calculations were conducted and confirmed the occurrence of systematic charge transfers correlating with the electronegativity, which can affect the

interatomic force-constants and the phonons.

Phonons in vanadium exhibit an anomalous behavior, showing a stiffening with increasing temperature at constant volume. The effect of impurities on the anomalous temperature-dependence is investigated. It is found that the solutes that affect the phonon density of states most strongly at room temperature also suppress the anomalous temperature behavior. This observation is compared to trends in the phonons and elastic constants of BCC transition metals. Electron-phonon and phonon-phonon couplings are examined as potential sources of this effect, through a careful accounting of contributions to the heat capacity, derived from neutron scattering experiments, calorimetry measurements, and electronic structure calculations.

Finally, the changes in the phonon DOS and the vibrational entropy across the low-temperature martensitic phase transformation in  $\text{Fe}_{71}\text{Ni}_{29}$  are investigated. The respective contributions of the phonons and magnetism to the entropy of the direct and reverse transformation are evaluated from neutron scattering experiments and scanning calorimetry measurements. A significant magnetic entropy is found in the reverse transformation, which is not present in the direct transformation. This result stresses the necessity to account for the respective contributions of all microscopic degrees of freedom in evaluating entropy changes in solid-solid phase transitions.

# Contents

<b>1</b>	<b>Introduction</b>	<b>1</b>
1.1	Alloy Thermodynamics . . . . .	1
1.2	Vibrational Entropy . . . . .	2
1.3	Expected Trends . . . . .	3
1.4	Overview . . . . .	4
<b>2</b>	<b>Theoretical Background</b>	<b>6</b>
2.1	Hamiltonians and Densities . . . . .	6
2.1.1	Condensed-Matter Hamiltonian . . . . .	6
2.1.2	Born-Oppenheimer Approximation . . . . .	7
2.1.3	Density Functional Theory . . . . .	8
2.1.4	Kohn-Sham Equations . . . . .	9
2.2	Lattice Dynamics . . . . .	11
2.2.1	Born-von Kármán Model . . . . .	12
2.2.2	Electron-Phonon Interaction . . . . .	19
2.3	First-Principles Phonon Calculations . . . . .	19
2.3.1	Frozen Phonons . . . . .	19
2.3.2	Hellmann-Feynman Forces . . . . .	20
2.3.3	Linear Response . . . . .	22
2.3.4	Molecular Dynamics . . . . .	24
2.4	Thermal Properties . . . . .	25
2.4.1	Harmonic Oscillators . . . . .	25
2.4.2	Anharmonicity . . . . .	27

2.4.3	Electronic Entropy . . . . .	33
<b>3</b>	<b>Inelastic Neutron Scattering</b>	<b>34</b>
3.1	Introduction . . . . .	34
3.2	Scattering Cross-Section . . . . .	36
3.2.1	General Case . . . . .	36
3.2.2	Phonon Scattering . . . . .	37
3.3	Scattering Function . . . . .	41
3.4	Time-of-Flight Neutron Spectrometer . . . . .	42
3.4.1	Principle . . . . .	42
3.4.2	Sampling Region . . . . .	44
3.5	Data Analysis . . . . .	44
3.5.1	Background . . . . .	46
3.5.2	Multiphonon Scattering . . . . .	48
3.5.3	Instrument Resolution . . . . .	49
3.5.4	Neutron-Weighting . . . . .	50
<b>4</b>	<b>Effects of Alloying on Phonons in Vanadium</b>	<b>52</b>
4.1	Introduction . . . . .	52
4.2	Experimental Details . . . . .	53
4.2.1	Sample Preparation and Characterization . . . . .	53
4.2.2	Elastic Moduli . . . . .	56
4.2.3	Inelastic Neutron Scattering . . . . .	60
4.3	Data Analysis . . . . .	61
4.3.1	Density of States . . . . .	61
4.3.2	Neutron-Weighting . . . . .	62
4.4	Phonon DOS . . . . .	63
4.4.1	Pure Vanadium . . . . .	63
4.4.2	Trend Across the $3d$ -Series . . . . .	63
4.4.3	Trend Down the Ti Column . . . . .	64
4.4.4	Trend Down the V Column . . . . .	64

4.4.5	Trend Down the Ni Column . . . . .	66
4.4.6	Concentration Dependence in V-Co . . . . .	67
4.5	Born–von Kármán Inversions . . . . .	69
4.5.1	Lattice Dynamics Model and Fitting Procedure . . . . .	71
4.5.2	Minimization Results . . . . .	72
4.6	Vibrational Entropy . . . . .	82
4.6.1	Trend with Alloying Element . . . . .	82
4.6.2	Effect of Neutron-Weighting . . . . .	85
4.6.3	Vibrational Entropy of Mixing . . . . .	85
4.6.4	Concentration Dependence in V-Co . . . . .	86
4.6.5	Connection with Elastic Constants . . . . .	86
4.7	Chemical Trends . . . . .	87
4.7.1	Effect of Metallic Radius . . . . .	89
4.7.2	Effect of Electronegativity . . . . .	90
4.7.3	Comparison with Trends for BCC Transition Metals . . . . .	91
4.8	Summary . . . . .	94
<b>5</b>	<b>First-Principles Simulations of V-X Alloys</b>	<b>95</b>
5.1	Introduction . . . . .	95
5.2	Simulation Parameters . . . . .	95
5.2.1	Wien2k . . . . .	95
5.2.2	VASP . . . . .	96
5.3	Geometry Relaxation . . . . .	97
5.3.1	Procedure . . . . .	97
5.3.2	Results . . . . .	98
5.4	Electronic Structure . . . . .	103
5.5	Electronic Topological Transition . . . . .	110
5.6	Superconductivity and Electron-Phonon Coupling . . . . .	112
5.7	Electronic Entropy . . . . .	116
5.8	Charge Transfer . . . . .	118
5.9	Deformation Potential . . . . .	123

5.10	Summary . . . . .	125
<b>6</b>	<b>Phonons in Vanadium Alloys at High Temperatures</b>	<b>127</b>
6.1	Introduction . . . . .	127
6.2	High-Temperature Phonon DOS . . . . .	128
6.2.1	Pure Vanadium . . . . .	128
6.2.2	Vanadium Alloys . . . . .	130
6.3	High-Temperature Entropy . . . . .	134
6.3.1	Pure Vanadium . . . . .	134
6.3.2	Vanadium Alloys . . . . .	135
6.3.3	Vibrational Entropy of Alloying . . . . .	137
6.4	High-Temperature Properties of BCC Transition Metals . . . . .	139
6.4.1	Phonon DOS . . . . .	139
6.4.2	Elastic Constants . . . . .	141
6.5	Effects of Electron-Phonon Interaction . . . . .	144
6.5.1	Theoretical Predictions . . . . .	144
6.5.2	Heat Capacity Measurements . . . . .	146
6.6	Summary . . . . .	150
<b>7</b>	<b>Vibrational Entropy of the <math>\gamma - \alpha</math> Transformation in <math>\text{Fe}_{71}\text{Ni}_{29}</math></b>	<b>152</b>
7.1	Introduction . . . . .	152
7.2	Experimental Details . . . . .	153
7.2.1	Sample Preparation . . . . .	153
7.2.2	X-ray Diffractometry . . . . .	154
7.2.3	Calorimetry . . . . .	157
7.2.4	Neutron Scattering . . . . .	157
7.3	Analysis of the Phonon Density of States . . . . .	160
7.3.1	Data Reduction . . . . .	160
7.3.2	Neutron-Weight Correction . . . . .	160
7.4	Results and Discussion . . . . .	162
7.4.1	Phonons . . . . .	162

7.4.2	Entropy . . . . .	170
7.5	Analysis of Time-of-Flight Coherent Phonon Scattering . . . . .	175
7.5.1	General Considerations . . . . .	178
7.5.2	Calculation of $S(Q, E)$ for FCC and BCC Fe-Ni . . . . .	180
7.6	Conclusion . . . . .	183
<b>8</b>	<b>Conclusions</b>	<b>185</b>
8.1	Summary . . . . .	185
8.2	Future Work . . . . .	186
<b>A</b>	<b>The Electron-Phonon Interaction</b>	<b>188</b>
A.1	Coupling Operators . . . . .	188
A.2	Perturbative Treatment . . . . .	190
A.2.1	Matrix Elements . . . . .	190
A.2.2	Coupling Functions . . . . .	193
<b>B</b>	<b>Implementations of DFT</b>	<b>195</b>
B.1	Approximations for Exchange and Correlation . . . . .	195
B.2	Solving the Kohn-Sham Equations . . . . .	196
B.2.1	Pseudopotentials and Plane Waves . . . . .	197
B.2.2	Augmented Plane Waves . . . . .	198
<b>C</b>	<b>VASP and Wien2k Input Files</b>	<b>200</b>
C.1	VASP files . . . . .	200
C.1.1	INCAR file . . . . .	200
C.1.2	POSCAR file . . . . .	201
C.1.3	KPOINTS file . . . . .	202
C.1.4	POTCAR file . . . . .	202
C.2	Wien2k files . . . . .	202
C.2.1	case.struct file . . . . .	203
C.2.2	case.inst file . . . . .	204
C.2.3	case.in1 file . . . . .	205

C.2.4	case.in2 file . . . . .	206
C.2.5	case.inm file . . . . .	207
<b>D</b>	<b>Calculation of BCC Elastic Moduli from Interatomic Force-Constants</b>	<b>208</b>
D.1	General Considerations . . . . .	208
D.2	BCC Lattice . . . . .	210
D.3	Calculation up to 1NN shell . . . . .	212
D.3.1	$c_{11}$ elastic constant . . . . .	212
D.3.2	$c_{12}$ elastic constant . . . . .	213
D.3.3	$c_{44}$ elastic constant . . . . .	214
D.4	Calculation up to 2NN shell . . . . .	215
D.5	Sum up to 3NN shell . . . . .	216
<b>E</b>	<b>Mannheim Impurity Model and Application to V-X Alloys</b>	<b>218</b>

## List of Figures

2.1	First-principles phonon DOS calculations for Al, Cr and Fe. . . . .	23
3.1	Neutron scattering geometry. . . . .	36
3.2	Scattering process for creation of one phonon. . . . .	38
3.3	Direct-geometry time-of-flight neutron spectrometer. . . . .	43
3.4	Scattering kinematics for LRMECS instrument with $E_i = 55$ meV. . . . .	45
3.5	Sampling volume in reciprocal space for vanadium single crystal. . . . .	45
3.6	Scattering intensity $S(E)$ for $\text{Fe}_{71}\text{Ni}_{29}$ sample. . . . .	46
3.7	Scattering intensity $S(\Phi, E)$ from V sample and empty holder. . . . .	47
3.8	Multiphonon scattering correction for V-6.25%Pd sample at 295 K. . . . .	49
3.9	Energy Resolution for LRMECS and Pharos spectrometers. . . . .	50
4.1	Experimental lattice parameters. . . . .	57
4.2	Metallic radius of transition metals with BCC coordination. . . . .	57
4.3	Change in bulk and shear moduli in V-6.25%X upon alloying. . . . .	59
4.4	Pure vanadium phonon DOS. . . . .	63
4.5	Neutron-weighted Phonon DOS for impurities across the 3d-series. . . . .	65
4.6	Neutron-weighted Phonon DOS for impurities down the Ti column. . . . .	66
4.7	Neutron-weighted Phonon DOS for impurities down the V column. . . . .	67
4.8	Neutron-weighted Phonon DOS for impurities down the Ni column. . . . .	68
4.9	Neutron-weighted Phonon DOS for V and V-6.25%Pt. . . . .	68
4.10	Phonon DOS for V-Co alloys of different composition. . . . .	70
4.11	Supercell model used in lattice dynamics inversions. . . . .	71

4.12	Longitudinal and transverse force-constants from optimized lattice dynamics model. . . . .	75
4.13	Comparison of bulk and shear moduli from ultrasonics and inversion. . . . .	76
4.14	Relative change in bulk modulus and shear modulus. . . . .	77
4.15	Partial phonon DOS for the solute atom and its V neighbors. . . . .	79
4.16	Neutron-weight function derived from partial phonon DOS. . . . .	80
4.17	Experimental phonon DOS and phonon DOS from Born–von Kármán inversion. . . . .	81
4.18	Neutron-weighted vibrational entropy of alloying. . . . .	84
4.19	Average phonon energy. . . . .	84
4.20	Vibrational entropy of alloying for V-Co alloys with different Co concentrations. . . . .	86
4.21	Correlation of elastic moduli with average phonon energy. . . . .	88
4.22	Neutron-weighted vibrational entropy of alloying versus relative change in metallic radius. . . . .	89
4.23	Vibrational entropy of alloying versus Pauling’s electronegativity. . . . .	91
5.1	Energy-volume curve for $V_{15}X_1$ supercell calculated with Wien2k. . . . .	98
5.2	Comparison of volume relaxation curves from Wien2k and VASP. . . . .	100
5.3	Relative change in lattice parameter. . . . .	101
5.4	Impurity-host 1NN bond-length. . . . .	103
5.5	Impurity-host bond-length for 1NN, 2NN and 3NN bonds. . . . .	104
5.6	Electronic density of states for pure vanadium and the relaxed $V_{15}X_1$ $2 \times 2 \times 2$ supercells for $3d$ impurities. . . . .	106
5.7	Electronic density of states for pure vanadium and the relaxed $V_{15}X_1$ $2 \times 2 \times 2$ supercells for column VIII impurities. . . . .	107
5.8	Local $d$ -electron density of states on impurity, for $3d$ impurities. . . . .	108
5.9	Local $d$ -electron density of states on impurity, for column VIII impurities. . . . .	109
5.10	Topological transition in Fermi surface of V-Cr alloys. . . . .	111
5.11	Brillouin zone for BCC lattice. . . . .	112
5.12	Electronic density at the Fermi level calculated with Wien2k. . . . .	114
5.13	Change in electronic density at the Fermi level upon alloying. . . . .	114
5.14	Estimated superconducting critical temperature for V-6.25%X. . . . .	116

5.15	Electron-phonon coupling strength for V-6.25%X. . . . .	117
5.16	Electronic entropy of alloying at 295 K for $V_{15}X_1$ relaxed supercells. . . . .	118
5.17	Charge transfer onto each atom for impurities across the 3 <i>d</i> -series. . . . .	120
5.18	Charge transfer on impurity versus impurity-host difference in electronegativity. . . . .	121
5.19	Experimental vibrational entropy of alloying plotted against Bader charge transfer and electronegativity difference. . . . .	122
5.20	Calculated potential for 1NN atom displacements in a breathing mode. . . . .	124
6.1	Phonon DOS of vanadium at 293, 873, 1273, and 1673 K. . . . .	129
6.2	Phonon DOS of V-7%Co at 293, 873, and 1273 K. . . . .	131
6.3	Phonon DOS of pure V at 300, 973 and 1323 K, and V-6.25%Pt at 300, 973 and 1323 K, measured with Pharos . . . . .	132
6.4	Phonon DOS of pure V at 300 K and 1273 K, and V-6.25%Nb at 300 K and 1273 K, measured with Pharos . . . . .	133
6.5	Anharmonic contributions to the entropy of vanadium. . . . .	135
6.6	Anharmonic entropy for pure vanadium and V-7%Co. . . . .	136
6.7	Phonon DOS for BCC Ti and Zr at elevated temperatures. . . . .	139
6.8	Phonon DOS of BCC Cr at elevated temperatures. . . . .	140
6.9	Phonon DOS of BCC Nb at elevated temperatures. . . . .	140
6.10	Elastic moduli of vanadium single crystal as function of temperature. . . . .	142
6.11	Shear elastic constant $C_{44}$ of Nb and Nb-Mo single crystals as function of temperature. . . . .	142
6.12	Electronic DOS for BCC V calculated with Wien2k and position of $\Gamma'_{25}$ point. . . . .	143
6.13	Heat capacity components for pure vanadium. . . . .	148
6.14	Ratio of thermal expansion coefficients and quasiharmonic entropy of thermal expansion for V-7%Co versus V. . . . .	149
6.15	Heat capacity components for V-7%Co. . . . .	149
7.1	Diffraction patterns from $Fe_{71}Ni_{29}$ for different stages of transformation. . . . .	155
7.2	Fraction of remaining austenite versus decreasing temperature. . . . .	156
7.3	Time evolution of the austenite fraction at 243 K and 223 K. . . . .	156

7.4	Differential scanning calorimetry profiles for the direct $\gamma \rightarrow \alpha$ and reverse $\alpha \rightarrow \gamma$ martensitic transformations in $\text{Fe}_{71}\text{Ni}_{29}$ . . . . .	158
7.5	Neutron-weighted phonon DOS for $\gamma$ and $\alpha$ - $\text{Fe}_{71}\text{Ni}_{29}$ at room temperature. . . . .	163
7.6	Phonon DOS of $\text{Fe}_{71}\text{Ni}_{29}$ as function of cooling temperature. . . . .	164
7.7	Phonon dispersions for BCC $\text{Fe}_{80}\text{Ni}_{20}$ calculated by Meyer and Entel. . . . .	165
7.8	Phonon dispersions for FCC $\text{Fe}_{70}\text{Ni}_{30}$ measured by Hallman and Brockhouse. . . . .	166
7.9	Partial phonon DOS curves for Fe and Ni in the martensite, at room temperature. . . . .	169
7.10	Magnetisation measurements of Peschard on Fe-28.7%Ni. . . . .	174
7.11	$S^{\text{exp}}(Q, E)$ for $\text{Fe}_{71}\text{Ni}_{29}$ , measured with Pharos. . . . .	177
7.12	$S^{\text{th}}(Q, E)$ for $\text{Fe}_{70}\text{Ni}_{30}$ virtual crystal calculated from Born-von Kármán model. . . . .	182
B.1	Spatial decomposition in APW approach. . . . .	199
E.1	Pure V phonon DOS histogram. . . . .	219
E.2	Interpolated pure V phonon DOS. . . . .	219
E.3	Interpolated pure V phonon DOS. . . . .	221
E.4	Pt partial DOS from Mannheim model. . . . .	221

## List of Tables

4.1	Samples prepared and relevant physical properties. . . . .	55
4.2	Elastic moduli. . . . .	58
4.3	Central force-constants from inversion procedure compared with pure vanadium values. . . . .	74
4.4	Vibrational entropy of alloying and mean phonon energy. . . . .	83
5.1	Relaxed supercell geometries from first-principles calculations. . . . .	99
5.2	Superconductive properties for V-6.25%X alloys. . . . .	115
5.3	Bader charge transfer calculated with Wien2k. . . . .	119
6.1	Vibrational entropy of alloying for 7% Co solutes in V, at the different temperatures for which the phonon DOS measurements were performed. . . . .	138
6.2	Average phonon frequencies and anharmonic heat capacity for V and V-7%Co.151	
7.1	Latent heat and entropy contributions to the $\gamma \rightarrow \alpha$ and $\alpha \rightarrow \gamma$ transformations in Fe <sub>71</sub> Ni <sub>29</sub> . . . . .	170

# Chapter 1

## Introduction

### 1.1 Alloy Thermodynamics

Very extensive experimental efforts have sought to characterize the crystalline phases formed in alloys of various compositions and at varying temperatures, typically extending up to the melting point. Much of that effort is nowadays compounded and readily available in databases such as binary, and to a more restricted extent, ternary phase-diagrams. These empirical observations are generally interpreted in the framework of classical thermodynamics, and can, to a certain extent, be modelled and extended to more complex systems (ternary and quaternary), using semi-empirical approaches [1]. The rationalization of this large body of phenomenological observations is still incomplete, however.

On the one hand, the energetics of fairly complex crystalline phases of alloys have become accessible to theoretical calculations of high accuracy, through the advent of efficient methods to solve the electronic structure problem directly from quantum mechanics. The configurational entropy contributions, beyond the simple point approximation for a purely random distribution of atoms on sites, are also well accounted for, taking into account correlations such as short-range order, thanks to cluster expansions [2, 3, 4].

On the other hand, in building the free energy curve for each phase of a binary alloy, one most often restricts the entropy contributions to the configurational degrees of freedom, in large part because of our lack of knowledge about so-called excess entropy terms. Even when some, or parts, of these terms can be calculated in principle, the difficulty in actually computing them has precluded the emergence of a clear understanding of their size

and variations. Non-configurational degrees of freedom do contribute significantly to the entropy, however, and can induce entropy differences between phases that are significant to thermodynamics. These can induce qualitative changes in phase diagrams, for example. Other sources of entropy exist besides configurational entropy. For a fixed configuration of ions on a given lattice, low energy excitations around that static configuration can be thermally activated and will provide extra entropy. As such, nuclear vibrations, spin-waves or electronic excitations add their own contribution to the entropy of the system. We are concerned in this thesis with the entropic effects of lattice vibrations, or phonons, in transition metal alloys.

## 1.2 Vibrational Entropy

The concept of vibrational entropy is conveniently introduced from the framework of statistical physics, using the notion of phase-space. The phase-space of a system of  $N$  particles (or effective particles) is the  $6N$ -dimensional space of all the coordinates and momenta of the constitutive particles. In the microcanonical description of statistical mechanics, the thermodynamics of the system is fully specified by the function  $\Omega(N, E, V)$ , which gives the number of microstates compatible with the macrostate  $(N, E, V)$  of the system. The classical thermodynamic entropy of the system,  $S$ , is then related to  $\Omega$  through Boltzmann's equation,

$$S = k_{\text{B}} \ln \Omega , \tag{1.1}$$

where  $k_{\text{B}}$  is Boltzmann's constant. Since there are many possible ways to partition the energy of the macroscopic system between its microscopic degrees of freedom, many different microstates are compatible with a given macrostate. It can be shown from quantum mechanical considerations that the volume element associated with one microstate in phase-space is  $h^3$ , where  $h$  is Planck's constant. In the microcanonical description, the representative volume for the system in phase-space,  $\mathcal{V}$ , is proportional to the number of accessible microstates in the ensemble,  $\Omega(N, E, V)$ , and the volume of each microstate  $h^3$ . However, indistinguishability of individual particles introduces a normalization of  $\Omega(N, E, V)$  accord-

ing to the quantum statistics obeyed by the particles, fixed by their spins. In the classical limit, one obtains\*

$$\Omega = \frac{\mathcal{V}}{h^{3N} N!} . \quad (1.2)$$

Thus, entropy can be seen as a measure of the extent of the representative volume of the system in phase-space.

For a collection of particles oscillating around a given configuration, such as nuclei vibrating around their sites on a crystal lattice, the system explores a larger portion of phase-space than if the particles were static. There is thus an entropy associated with the extra extent of phase-space sampled by the system as the constituent particles vibrate. This is the origin of vibrational entropy.

### 1.3 Expected Trends

In a vibrating crystal, the amplitudes of the motions of atoms away from their equilibrium sites depend on the effective force-constants. If the restoring force-constants are large, the amplitudes of vibrations are constrained, and the frequencies high. On the other hand, small force-constants allow for larger displacements, which correspond to a large volume being sampled in phase-space. As a consequence, softer materials have a higher vibrational entropy. For a constant mass of the nuclei, the vibrational entropy of the crystal is a decreasing function of the frequency of its vibration modes.

Changes in the mass of the constituent nuclei, for example in the case of a mass defect, also induce changes in vibrational entropy. A simple harmonic model considering the range sampled by the system in phase-space and taking into account only the mass defect associated with an impurity, without perturbation of the electronic structure, predicts a change in vibrational entropy upon alloying given by

$$\Delta S_{\text{vib}}^{\text{mass}} = \frac{3}{2} c k_{\text{B}} \ln\left(\frac{M_i}{M_{\text{h}}}\right) , \quad (1.3)$$

---

\*more rigorously, for  $N$  particles occupying energy levels  $\{\epsilon_i\}$  according to the distribution  $\{n_i\}$ , the statistical weight associated with indistinguishability is  $w(\{n_i\}) = N! / \prod_p n_p!$ .

where  $M_i$  is the atomic mass of the impurity,  $M_h$  is the atomic mass of the host,  $k_B$  is Boltzmann's constant, and  $c$  is the impurity concentration. In this picture, heavier solutes are thus expected to cause an increase in vibrational entropy, due to a softening of the phonons.

The vibrational entropy of a crystal thus depends both on the mass of the atoms in the crystal and on the restoring force-constants that constrain the nuclei to vibrate around a local equilibrium configuration. The forces on the nuclei are the sum of electrostatic repulsions from other positively charged nuclei and the electrostatic interaction with the negative electronic charge density throughout the crystal. The electronic density is in turn determined by the spatial distribution of point-like nuclear charges.

## 1.4 Overview

Over the last decade, experimental and theoretical investigations have shown that changes in vibrational entropy play an important role in the thermodynamics of solid-state phase transitions [5, 6, 7, 8]. Our recent experimental results have shown that in dilute alloys with a few percent impurities, the vibrational entropy of mixing can be larger in magnitude than the configurational entropy gain due to disorder, and can lead in certain cases to a negative total entropy of mixing [9]. Recent theoretical calculations have also predicted important effects of the vibrational entropy on the solubility limit in dilute alloys [8, 10, 11].

Experimentally, the vibrational entropy difference between two phases of a material can be measured by a number of methods, including calorimetry or inelastic neutron scattering [12, 13, 14]. However, the neutron scattering approach provides more information since it allows measuring the phonon density of states (DOS), which connects the macroscopic thermodynamics of the material with its underlying microscopic lattice dynamics. Calorimetry, on the other hand, gives information mostly about the sum of all entropy contributions, including phonons, magnetism, and electronic excitations, for example.

In this thesis, we first review the concepts underlying our investigations. The theoretical framework of density functional theory is briefly reviewed, followed by a discussion of lattice dynamics in the Born–von Kármán model. The thermal properties of phonons are summarized in the harmonic and anharmonic cases. The inelastic neutron scattering tech-

nique, which constituted the backbone of the experimental work performed, is presented succinctly.

The thesis then presents our results and findings. The first aspect of vibrational entropy investigated in this work is associated with the introduction of impurities. Vanadium is the host crystal on which our efforts have been focused, and different impurities from the transition metals are considered. The different dilute vanadium alloys investigated were studied both experimentally and by means of computer simulations. We find for the first time a clear trend with the chemical properties of the impurity atoms. We believe this trend offers a significant insight into the systematics of vibrational entropy in binary alloys. Also, vibrational entropy is strongly reduced upon alloying with late transition metal impurities. In the case of Pt solutes, this reduction overcomes the gain in configurational entropy, so the total entropy of mixing is negative. Such a large effect, for only a few percent impurities, has surprised the alloy thermodynamics community.

The second aspect considered is the temperature dependence of the phonon modes. Vanadium and dilute V-based alloys are studied, in the light of previous investigations on pure vanadium and other BCC transition metals. It is shown that impurities disrupt the anomalous temperature-dependence observed in pure vanadium. Differential scanning calorimetry was used to evaluate the respective contributions of phonons and electrons, and interpreted in terms of phonon-phonon and electron-phonon interactions.

Finally, the effect of vibrational entropy on the  $\gamma - \alpha$  martensitic transformation in  $\text{Fe}_{71}\text{Ni}_{29}$  is investigated. The phonons and vibrational entropy in this material were monitored across the martensitic transformation upon cooling. The difference in phonon entropy between the high and low temperature phases is substantial. Additional calorimetry work for both the direct and reverse transformations identified a large additional contribution from magnetism in the reverse transformation.

## Chapter 2

### Theoretical Background

#### 2.1 Hamiltonians and Densities

We review in this section some fundamental aspects of solid-state theory and the more specialized framework of density functional theory. More details on this subject can be found in [15]. A shorter account is also given in [16].

##### 2.1.1 Condensed-Matter Hamiltonian

We start with the general many-body hamiltonian describing a system of interacting electrons and nuclei:

$$\begin{aligned} \hat{H} = & -\sum_i \frac{\hbar^2}{2m_e} \nabla_i^2 - \sum_{I,i} \frac{Z_I e^2}{|\mathbf{r}_i - \mathbf{R}_I|} + \frac{1}{2} \sum_{i \neq j} \frac{e^2}{|\mathbf{r}_i - \mathbf{r}_j|} \\ & - \sum_I \frac{\hbar^2}{2M_I} \nabla_I^2 + \frac{1}{2} \sum_{I \neq J} \frac{Z_I Z_J e^2}{|\mathbf{R}_I - \mathbf{R}_J|}, \end{aligned} \quad (2.1)$$

where the uppercase (resp. lowercase) subscripts label the nuclei (resp. electrons),  $M_I$  is the nuclear mass,  $m_e$  the electronic mass,  $Z_I$  the atomic number of ion  $I$  and  $\mathbf{R}_I$  and  $\mathbf{r}_i$  are the nuclear and electronic positions, respectively. We have absorbed the spin index for the electrons into the symbol  $\mathbf{r}_i$ . This hamiltonian operates on many-body states in the Hilbert space of the system, such as many-body wave functions  $\psi(\{\mathbf{R}_I, \mathbf{r}_i\})$  in position representation. Also, we require that the wave function  $\psi$  is antisymmetric under the exchange of electrons. We recognize in this hamiltonian the canonical kinetic and potential

energy operators for nuclei and electrons:

$$\begin{aligned}
\hat{T}_n &= -\sum_I \frac{\hbar^2}{2M_I} \nabla_I^2 \\
\hat{T}_e &= -\sum_i \frac{\hbar^2}{2m_e} \nabla_i^2 \\
\hat{V}_{n-n} &= \frac{1}{2} \sum_{I \neq J} \frac{Z_I Z_J e^2}{|\mathbf{R}_I - \mathbf{R}_J|} \\
\hat{V}_{e-n} &= -\sum_{I,i} \frac{Z_I e^2}{|\mathbf{r}_i - \mathbf{R}_I|} \\
\hat{V}_{e-e} &= \frac{1}{2} \sum_{i \neq j} \frac{e^2}{|\mathbf{r}_i - \mathbf{r}_j|}, \tag{2.2}
\end{aligned}$$

where  $\hat{T}_n$  is the kinetic energy of the nuclei,  $\hat{T}_e$  is the kinetic energy of the electrons,  $\hat{V}_{n-n}$  is the Coulombic repulsion energy of the nuclei,  $\hat{V}_{e-n}$  is the Coulombic attraction between electrons and nuclei and, finally,  $\hat{V}_{e-e}$  is the electron-electron interaction. The hamiltonian of Eq. 2.1 is too hard to solve directly and a series of approximations are called for to reduce this problem to a manageable one.

### 2.1.2 Born-Oppenheimer Approximation

Usually the first simplification is to use the Born-Oppenheimer, or adiabatic, approximation. Considering the very small mass ratio of the electron and nuclei,  $m_e/M$ , one can perform a series expansion of  $\hat{H}$  in this parameter and apply perturbation theory. We focus for now on the zero-th order term in this expansion; higher-order terms relevant to the electron-phonon interaction will be discussed later. At this order:

$$\hat{H} = \hat{T}_e + \hat{V}_{e-e} + \hat{V}_{e-n} + \hat{V}_{n-n}, \tag{2.3}$$

so only the static positions of the nuclei intervene. We can effectively consider the nuclear configuration  $\{\mathbf{R}_I\}$  as a set of external parameters for the problem of determining the electronic quantum states. Physically, this amounts to saying that the nuclei move much slower than the electrons and thus, at any given time, the electron states correspond to the instantaneous nuclear configuration. With this point of view,  $\hat{V}_{e-n}$  is seen as an “external

potential,"  $\hat{V}_{\text{ext}}$ , imposed on the electrons for a fixed configuration of the nuclei. Next,  $\hat{V}_{\text{n-n}}$  is just a constant and thus has no relevance to the electronic problem. Leaving this last term aside, we obtain the electronic hamiltonian:

$$\hat{H}_e = \hat{T}_e + \hat{V}_{e-e} + \hat{V}_{\text{ext}} . \quad (2.4)$$

### 2.1.3 Density Functional Theory

The electronic hamiltonian for a specified external potential (Eq. 2.4) is still very difficult to solve. Chief among the difficulties facing us is the fact that this is still a *many-body* problem:  $\hat{H}$  operates on electronic wave functions  $\psi(\{\mathbf{r}_i\})$ , that depend on the  $3N$  spatial coordinates of the  $N$  electrons in the system (and also on their spin coordinates). Besides, the electrons are *interacting*, which precludes us from treating them as independent particles. Traditionally, the electron-electron interaction is broken down into exchange interaction and correlation.

A considerable simplification can be performed following the important results of Hohenberg and Kohn and of Kohn and Sham, published in two papers in 1964 and 1965 [17, 18]. Hohenberg and Kohn [17] showed that the problem above can be recast into a problem that depends only on the electronic *density*,  $\rho(\mathbf{r})$ , rather than the many-body wave function. This is a tremendous advance since  $\rho(\mathbf{r})$  only depends on *one* three-dimensional position. The possibility to recast the problem in this manner stems from two very general theorems introduced by Hohenberg and Kohn (HK).

The first HK theorem states that the external potential  $\hat{V}_{\text{ext}}$  is uniquely determined from the ground state density of the many-body interacting system. Conversely, the specification of  $\hat{V}_{\text{ext}}$  determines  $\hat{H}_e$ , and thus the ground state and its density  $\rho_0(\mathbf{r})$ . We conclude that there is a *one to one* relationship between the ground state density  $\rho_0(\mathbf{r})$  and the external potential  $\hat{V}_{\text{ext}}$  for the electrons. Because the hamiltonian fully describes the system, an additional consequence is that every property of the system is determined from  $\rho_0(\mathbf{r})$ . Mathematically, this is expressed by writing the observables  $\hat{\mathcal{O}}$  of the system as functionals of the electronic density:

$$\langle \hat{\mathcal{O}} \rangle = \langle \psi | \hat{\mathcal{O}} | \psi \rangle = \mathcal{O}[\rho] ,$$

where  $\mathcal{O}[\rho]$  is a real-valued functional of continuous functions on  $\mathbb{R}^3$ ,  $\mathcal{O} : \mathcal{C}(\mathbb{R}^3) \rightarrow \mathbb{R}$ .

The second HK theorem states that there *exists* a universal functional for the energy  $E[\rho]$ , which can be *uniquely* defined, provided the external potential  $\hat{V}_{\text{ext}}$ . The density that minimizes this functional is the ground state density and the energy at the minimum, the ground state energy. More specifically, applying the first theorem to the hamiltonian itself, we write:

$$E = \langle \hat{H} \rangle = H[\rho] = E_{V_{\text{ext}}}[\rho] = F_{\text{HK}}[\rho] + \int \rho(\mathbf{r})V_{\text{ext}}(\mathbf{r}) d^3r , \quad (2.5)$$

where  $F_{\text{HK}}[\rho] = \langle \psi | \hat{T}_e + \hat{V}_{e-e} | \psi \rangle$  is universal for any many-electron system. The 2<sup>nd</sup> theorem stipulates that  $E_{V_{\text{ext}}}[\rho]$  reaches its minimum for  $\rho = \rho_{\text{GS}}$  and that  $E_{V_{\text{ext}}}[\rho_{\text{GS}}] = E_{\text{GS}}$ .

Using these results, the original eigenvalue problem for the solution of the Schrödinger equation corresponding to the electronic hamiltonian (2.4) can be replaced by a minimization problem for  $E_{V_{\text{ext}}}[\rho]$ . One could try solving this minimization problem using the Rayleigh-Ritz procedure, for example. There is one problem, however, as an explicit expression for  $F_{\text{HK}}[\rho]$  has not yet been found and its expression for the many-body problem might be hopelessly complicated. The procedure devised by Kohn and Sham [18] overcomes this difficulty.

### 2.1.4 Kohn-Sham Equations

The approach of Kohn and Sham for determining the ground state density of the many-body problem is to introduce an auxiliary hamiltonian for independent particles, the Kohn-Sham hamiltonian. This *ansatz* rests upon the assumption that the independent particle system has the same ground state density as the interacting particle system. We start by regrouping the terms in  $F_{\text{HK}}$ :

$$F_{\text{HK}} = T_0 + E_{\text{H}} + E_{\text{xc}} , \quad (2.6)$$

where  $T_0$  is the kinetic energy functional for independent electrons,  $E_{\text{H}}$  is the Hartree classical Coulomb interaction energy

$$E_{\text{H}}[\rho] = \frac{1}{2} \int \frac{\rho(\mathbf{r})\rho(\mathbf{r}')}{|\mathbf{r} - \mathbf{r}'|} d^3r d^3r' , \quad (2.7)$$

and  $E_{\text{xc}}$  is the exchange-correlation energy defined as the difference between the kinetic and potential interaction energies of the true interacting many-body electron system and those of the fictitious independent electron gas, with electron-electron interaction limited to the Hartree contribution:

$$E_{\text{xc}}[\rho] = \langle \hat{T}_e \rangle - T_{\text{ni}}[\rho] + \langle \hat{V}_{e-e} \rangle - E_{\text{H}}[\rho], \quad (2.8)$$

where the subscript “ni” stands for “non-interacting.” As is apparent from its definition,  $E_{\text{xc}}[\rho]$  contains all the difficult parts about the interactions in the real system, and an exact expression for this term is not known. Nevertheless, several approximations for exchange and correlation have been developed that allow for realistic results in solid-state DFT calculations, such as the local density approximation (LDA) and a number of generalized gradient approximations (GGA). Supposing  $E_{\text{xc}}$ , or a model thereof, is known, Eq. 2.5 can be reformulated as an effective single-particle hamiltonian by using a Rayleigh-Ritz approach to convert the variational minimization into an eigenvalue problem, as first done by Kohn and Sham. The single-particle Kohn-Sham (KS) hamiltonian for a given external potential reads:

$$\hat{H}_{\text{KS}} = \hat{T}_{\text{ni}} + \hat{V}_{\text{H}} + \hat{V}_{\text{xc}} + \hat{V}_{\text{ext}}, \quad (2.9)$$

with  $\hat{V}_{\text{xc}}$  the functional derivative of the exchange-correlation functional:

$$\hat{V}_{\text{xc}} = \frac{\delta E_{\text{xc}}[\rho]}{\delta \rho}, \quad (2.10)$$

and similarly for the Hartree potential. The determination of the ground state density for the true system of  $N$  interacting electrons then reduces to solving an effective one-particle Schrödinger equation

$$\hat{H}_{\text{KS}}\phi_i = \epsilon_i\phi_i \quad (2.11)$$

for the  $N$  lowest-energy states  $\{\phi_i\}_{1 \leq i \leq N}$  and then using the fact that the model independent-particle density is the same as that of the interacting system:

$$\rho_{\text{GS}}(\mathbf{r}) = \rho_{\text{ni}}(\mathbf{r}) = \sum_{i=1}^N \phi_i^*(\mathbf{r}) \phi_i(\mathbf{r}) . \quad (2.12)$$

The set of equations (2.11) for  $1 \leq i \leq N$  constitutes the celebrated Kohn-Sham equations. This eigenvalue problem is finally tractable and can be solved by expanding the single-electron wave functions  $\phi_i$  on some basis and diagonalizing the KS hamiltonian matrix expressed in this basis. One additional layer of complexity arises, however, as both  $\hat{V}_{\text{H}}$  and  $\hat{V}_{\text{xc}}$  entering in (2.11) depend on  $\rho$ , which is the quantity we seek to determine. We are thus faced with a self-consistency problem, which we can solve iteratively. Starting with some estimate for the density,  $\rho_{n=0}$ , such as a superposition of atomic densities in a solid,  $\hat{V}_{\text{H}}$  and  $\hat{V}_{\text{xc}}$  are calculated, the eigenvalue problem (2.11) is solved and a new density  $\rho_{n+1}$  is obtained via (2.12). This cycle is iterated until self-consistency is reached, *e.g.*  $\int |\rho_{n+1}(\mathbf{r}) - \rho_n(\mathbf{r})| d^3r \leq Q_{\text{tol}}$ , with  $Q_{\text{tol}}$  some tolerance on the charge difference. Another approach is to solve the minimization problem for  $E[\rho]$  using a variational approach with orthonormalization constraints for the Kohn-Sham orbitals, using for example a conjugate gradient method [19].

Numerous schemes have been devised and implemented to solve the Kohn-Sham equations. Broad classes can be distinguished, based on the basis set used to expand the Kohn-Sham wave functions or the treatment of core electrons. Different flavors of DFT also arise from the approximation used in the representation of the exchange-correlation functional. We review some of these implementations in an appendix.

## 2.2 Lattice Dynamics

We review in this section some fundamental aspects of lattice dynamics, as described in the model established by Born and von Kármán. This model has been a cornerstone of solid-state physics since its introduction almost a century ago. It is presented extensively in the seminal book of Born and Huang [20]. Other accounts of this theory and its extensions can be found in [21, 22, 23].

In the harmonic approximation, the nuclear potentials are parabolic, and the Ehrenfest theorem allows us to treat the system classically, by identifying particles with the center of their wavepacket [24]. In the following, we present a classical derivation for the vibration modes and finally present a connection with the quantum-mechanical concept of a phonon.

### 2.2.1 Born–von Kármán Model

#### Atomic force-constants and equations of motion

We consider a crystal generated by the infinite repetition in space of a parallelepipedic unit cell defined by three non-coplanar vectors  $\mathbf{a}_1$ ,  $\mathbf{a}_2$ , and  $\mathbf{a}_3$ . The vectors  $\mathbf{a}_1$ ,  $\mathbf{a}_2$ , and  $\mathbf{a}_3$  are the lattice vectors of the crystal. We label each unit cell by a triplet  $l$  of integers:  $l = (l_1, l_2, l_3)$ . The equilibrium position of the origin of the unit cell  $l$  is denoted

$$\mathbf{x}(l) = l_1\mathbf{a}_1 + l_2\mathbf{a}_2 + l_3\mathbf{a}_3 . \quad (2.13)$$

If there are  $r > 1$  atoms per unit cell, we assign an index  $\kappa = 1, 2, \dots, r$  to the atoms of the basis and write their mass  $M_\kappa$ . We describe the atomic equilibrium positions with respect to the origin of a unit cell with basis vectors  $\{\mathbf{x}(\kappa), \kappa = 1, 2, \dots, r\}$  so that the equilibrium position of atom  $\kappa$  in cell  $l$  is then given by  $\mathbf{x}(l\kappa) = \mathbf{x}(l) + \mathbf{x}(\kappa)$ . Thermal fluctuations induce displacements in the atomic positions; we write  $\mathbf{u}(l\kappa)$  the displacement vector of atom  $(l\kappa)$  from its equilibrium position  $\mathbf{x}(l\kappa)$ , and  $u_\alpha(l\kappa)$ ,  $\alpha = x, y, z$ , the corresponding cartesian components. The instantaneous position  $\mathbf{R}(l\kappa)(t)$  of atom  $(l\kappa)$  at time  $t$  is then

$$\mathbf{R}(l\kappa)(t) = \mathbf{x}(l\kappa) + \mathbf{u}(l\kappa)(t) . \quad (2.14)$$

The total potential energy  $V$  for the nuclei is assumed to be a function of the instantaneous positions of all the atoms in the crystal

$$V = V(\{\dots, \mathbf{R}(l\kappa), \dots, \mathbf{R}(l'\kappa'), \dots\}) \quad (2.15)$$

and it can then be expanded in a Taylor series of the atomic displacements:

$$V = V_0 + \sum_{l\kappa\alpha} \Phi_\alpha(l\kappa)u_\alpha(l\kappa) + \frac{1}{2} \sum_{l\kappa\alpha} \sum_{l'\kappa'\beta} \Phi_{\alpha\beta}(l\kappa; l'\kappa')u_\alpha(l\kappa)u_\beta(l'\kappa') + \dots \quad (2.16)$$

In the harmonic approximation of lattice dynamics, we use only the terms of the series explicitly written above, and neglect terms of order three and higher in the displacements. The coefficients of the Taylor series are the derivatives of the potential with respect to the displacements:

$$\begin{aligned} \Phi_\alpha(l\kappa) &= \left( \frac{\partial V}{\partial u_\alpha(l\kappa)} \right)_0 \\ \Phi_{\alpha\beta}(l\kappa; l'\kappa') &= \left( \frac{\partial^2 V}{\partial u_\alpha(l\kappa) \partial u_\beta(l'\kappa')} \right)_0, \end{aligned} \quad (2.17)$$

where the subscript zero means that derivatives are evaluated in the equilibrium configuration (all displacements equal to zero) and  $V_0$  is the static potential energy of the crystal. Because the force on any particle must vanish in the equilibrium configuration, we have

$$\Phi_\alpha(l\kappa) = 0 \quad \forall \alpha, l, \kappa. \quad (2.18)$$

The hamiltonian for the nuclei is given by  $H = T + V$  where  $T = \sum_{\kappa,l} \mathbf{p}_{\kappa,l}^2 / 2M_\kappa$  is the kinetic energy of the crystal. Following the harmonic approximation we obtain

$$H = \sum_{\kappa,l} \frac{\mathbf{p}_{\kappa,l}^2}{2M_\kappa} + V_0 + \frac{1}{2} \sum_{l\kappa\alpha} \sum_{l'\kappa'\beta} \Phi_{\alpha\beta}(l\kappa; l'\kappa')u_\alpha(l\kappa)u_\beta(l'\kappa'). \quad (2.19)$$

We can rewrite the last term as a matrix product, and obtain

$$H = \sum_{\kappa,l} \frac{\mathbf{p}_{\kappa,l}^2}{2M_\kappa} + V_0 + \frac{1}{2} \sum_{l\kappa} \sum_{l'\kappa'} \mathbf{u}^T(l\kappa) \mathbf{\Phi}(l\kappa; l'\kappa') \mathbf{u}(l'\kappa'), \quad (2.20)$$

where we have defined the  $3 \times 3$  matrix  $\mathbf{\Phi}$  by

$$\mathbf{\Phi}(l\kappa; l'\kappa') = [\Phi_{\alpha\beta}(l\kappa; l'\kappa')] . \quad (2.21)$$

The matrix  $\Phi(l\kappa; l'\kappa')$  is the force-constant matrix associated with the bond  $(l\kappa; l'\kappa')$ . If  $(l, \kappa) \neq (l', \kappa')$ , then the components of the force-constant matrix are given by the second-order derivatives of the potential as in Eq. 2.17. On the other hand, if  $(l, \kappa) = (l', \kappa')$ , then  $\Phi$  is the so-called self force-constant matrix, whose expression is derived from the requirement that there is no force on the crystal as it undergoes a constant uniform translation:

$$\Phi(l\kappa; l\kappa) = - \sum_{(l', \kappa') \neq (l, \kappa)} \Phi(l\kappa; l'\kappa') . \quad (2.22)$$

A number of relations on the force-constant tensors  $\Phi(l\kappa; l'\kappa')$  can be derived from requirements that there be no overall translation or rotation of the crystal, and from the symmetries of the crystal structure.

From the quadratic approximation of the hamiltonian, one can derive the equations of motion for all the atoms in the crystal:

$$M_\kappa \ddot{\mathbf{u}}(l\kappa) = - \sum_{l', \kappa'} \Phi(l\kappa; l'\kappa') \mathbf{u}(l'\kappa') \quad \forall l, \kappa . \quad (2.23)$$

It is then convenient to impose periodic boundary conditions on the crystal. If we write  $N_x^{\text{cell}}$  ( $N_y^{\text{cell}}$ ,  $N_z^{\text{cell}}$ ) the number of unit cells in the crystal in the x (y, z) direction, and  $N^{\text{cell}} = N_x^{\text{cell}} N_y^{\text{cell}} N_z^{\text{cell}}$  the total number of unit cells, we then have  $3 \times r \times N^{\text{cell}}$  equations of motion to solve. We can seek the solutions under the form of plane waves of wave vector  $\mathbf{q}$ , angular frequency  $\omega_{\mathbf{q}j}$ , and polarization  $\mathbf{e}(\kappa, \mathbf{q}j)$ :

$$\mathbf{u}_\alpha(l\kappa, \mathbf{q}j) = \frac{1}{2\sqrt{N M_\kappa}} \{ A(\mathbf{q}j) e_\alpha(\kappa, \mathbf{q}j) \exp(i(\mathbf{q} \cdot \mathbf{x}(l\kappa) - \omega_{\mathbf{q}j} t)) + \text{c.c.} \} , \quad (2.24)$$

where  $A(\mathbf{q}j)$  are amplitudes and c.c. denotes the complex-conjugate term.

The periodic boundary conditions cause the set of possible wave vectors  $\{\mathbf{q}\}$  to be discrete, although the typically large number of unit cells in the crystal translates into a very fine mesh of  $\mathbf{q}$ -points in reciprocal space. For each value of the wave vector  $\mathbf{q}$ , there are  $3 \times r$  vibration modes of the crystal, corresponding to *a priori* different polarization vectors  $\mathbf{e}(\kappa, \mathbf{q}j)$  and angular frequencies  $\omega_{\mathbf{q}j}$  ( $1 \leq j \leq 3r$ ). The number of physically distinct wave vectors is  $N^{\text{cell}}$ , so that the total number of degrees of freedom for the system is

$3rN^{\text{cell}}$ , as required. As a side note, we point out that in a physical finite crystal 6 of these degrees of freedom actually correspond to translations and rotations of the whole crystal, so  $(3rN^{\text{cell}} - 6)$  degrees of freedom effectively qualify as internal lattice vibrations. Although this is a minor point for bulk crystals where  $N^{\text{cell}} \gg 1$ , it may become important in the case of very small crystallites. In the present model, these degrees of freedom are “clamped.”

### The Dynamical Matrix and its Eigenvalue Problem

The substitution of the propagating-wave displacements of Eq. 2.24 in the equations of motion effectively corresponds to taking a space–Fourier transform of the right-hand side in Eq. 2.23, and leads to the introduction of the “dynamical matrix”, the Fourier transform of the interatomic force-constant tensor. After simplifying by the oscillatory time dependence, we are left with an eigenvalue problem for  $\omega^2$ , with the corresponding eigenvectors being the polarization vectors of the lattice vibrations. The polarization vectors  $\mathbf{e}(\boldsymbol{\kappa}, \mathbf{q}j)$  for all the atoms in the basis ( $1 \leq \kappa \leq r$ ) and their associated angular frequencies  $\omega_{\mathbf{q},j}$  can be calculated by diagonalizing the dynamical matrix  $\mathbf{D}(\mathbf{q})$ . More explicitly, the  $(3r \times 3r)$  dynamical matrix  $\mathbf{D}(\mathbf{q})$  is constructed from  $(3 \times 3)$  submatrices  $\mathbf{D}(\kappa\kappa', \mathbf{q})$ , which are the Fourier transforms of the force-constant matrices  $\Phi(\kappa l, \kappa' l')$ :

$$\mathbf{D}(\mathbf{q}) = \begin{pmatrix} \mathbf{D}(11, \mathbf{q}) & \dots & \mathbf{D}(1r, \mathbf{q}) \\ \vdots & \ddots & \vdots \\ \mathbf{D}(r1, \mathbf{q}) & \dots & \mathbf{D}(rr, \mathbf{q}) \end{pmatrix},$$

with

$$\mathbf{D}(\kappa\kappa', \mathbf{q}) = \frac{1}{\sqrt{M_{\kappa}M_{\kappa'}}} \sum_{l'} \Phi(0 \kappa, l' \kappa') e^{i\mathbf{q} \cdot (\mathbf{x}(l') - \mathbf{x}(l))}, \quad (2.25)$$

where we took  $l = 0$  since the summation is over all values of  $l'$  and the crystal is infinite, periodic, and the origin cell is arbitrary\*. By similarly collecting the polarization vectors into a vector of size  $3r$ , we can rewrite our system of differential equations for the plane

---

\*Ziman calls this the “cosmological principle” for the lattice [25]

waves in the form of an eigenvalue problem:

$$\mathbf{D}(\mathbf{q})\mathbf{e}(\mathbf{q}j) = \omega_{\mathbf{q}j}^2 \mathbf{e}(\mathbf{q}j), \quad (2.26)$$

where

$$\mathbf{e}(\mathbf{q}j) = \begin{pmatrix} \mathbf{e}(1, \mathbf{q}j) \\ \vdots \\ \mathbf{e}(r, \mathbf{q}j) \end{pmatrix}.$$

It can be shown that the  $(3r \times 3r)$  dynamical matrix  $\mathbf{D}(\mathbf{q})$  is hermitian (for any value of  $\mathbf{q}$ ), and thus is fully diagonalizable. The  $3r$  eigenvectors and eigenvalues of the dynamical matrix evaluated at a particular wave vector  $\mathbf{q}$  then correspond to the  $3r$  eigenmodes of vibration of the crystal for that wave vector. Since  $\mathbf{D}(\mathbf{q})$  is hermitian, its eigenvalues are real and thus the angular frequencies  $\omega_{\mathbf{q}j}$  are either real or purely imaginary. The case of purely imaginary frequencies leads to exponential divergence of the displacements in the past or the future and this case must be ruled out from mechanical stability conditions (although this formalism is valid to predict wavevectors  $\mathbf{q}$  leading to mechanical instabilities, *e.g.*, at martensitic transitions). Also, the eigenvectors can be chosen to form a complete orthonormal set and, thus, any nuclear displacement field can be expressed as a linear combination of these vectors.

### Normal Modes and Phonons

One can introduce normal modes  $Q(\mathbf{q}j)$  by rewriting the displacements as

$$\mathbf{u}(l\kappa, \mathbf{q}j) = \frac{1}{\sqrt{N M_\kappa}} \sum_{\mathbf{q}j} \mathbf{e}(\kappa, \mathbf{q}j) \exp(i \mathbf{q} \cdot \mathbf{x}(l\kappa)) Q(\mathbf{q}j), \quad (2.27)$$

such that

$$Q(\mathbf{q}j) = \frac{1}{2} [A(\mathbf{q}j) \exp(-i\omega_{\mathbf{q}j}t) + A^*(-\mathbf{q}j) \exp(i\omega_{\mathbf{q}j}t)]. \quad (2.28)$$

After introducing the conjugate normal momenta  $P(\mathbf{q}j) \equiv \dot{Q}(\mathbf{q}j)$ , it can be shown that the hamiltonian can be written

$$H = \frac{1}{2} \sum_{\mathbf{q}j} P^*(\mathbf{q}j)P(\mathbf{q}j) + \omega_{\mathbf{q}j}^2 Q^*(\mathbf{q}j)Q(\mathbf{q}j) \quad (2.29)$$

and the normal modes verify equations of motion for uncoupled harmonic oscillator:

$$\ddot{Q}(\mathbf{q}j) + \omega_{\mathbf{q}j}^2 Q(\mathbf{q}j) = 0. \quad (2.30)$$

The formulation of the problem in terms of the normal modes can be quantized with the canonical correspondence for position and momentum operators. Based on the normal mode operators, one can introduce the operators  $\hat{b}_{\mathbf{q}j}$  and  $\hat{b}_{\mathbf{q}j}^\dagger$ :

$$\begin{aligned} \hat{b}_{\mathbf{q}j} &= \frac{1}{\sqrt{2\hbar\omega_{\mathbf{q}j}}} [\omega_{\mathbf{q}j}Q(\mathbf{q}j) + iP^*(\mathbf{q}j)] \\ \hat{b}_{\mathbf{q}j}^\dagger &= \frac{1}{\sqrt{2\hbar\omega_{\mathbf{q}j}}} [\omega_{\mathbf{q}j}Q^*(\mathbf{q}j) - iP(\mathbf{q}j)]. \end{aligned} \quad (2.31)$$

The operators  $\hat{b}(\mathbf{q}j)$  and  $\hat{b}^\dagger(\mathbf{q}j)$  satisfy the commutation relations for annihilation and creation operators, respectively. In the occupation number representation (second quantization), they annihilate or create a quantum of excitation for the mode  $s = (\mathbf{q}j)$ :

$$\begin{aligned} \hat{b}_s |\dots, n_s, \dots\rangle &= \sqrt{n_s} |\dots, n_s - 1, \dots\rangle \\ \hat{b}_s^\dagger |\dots, n_s, \dots\rangle &= \sqrt{n_s + 1} |\dots, n_s + 1, \dots\rangle. \end{aligned} \quad (2.32)$$

The hamiltonian assumes the form of a sum of uncoupled quantum harmonic oscillators in terms of these operators:

$$\hat{H} = \sum_s \hbar\omega_s \left[ \frac{1}{2} + \hat{n}_s \right], \quad (2.33)$$

where  $\hat{n}_s = \hat{b}_s^\dagger \hat{b}_s$  is the number operator

$$\hat{n}_s |\dots, n_s, \dots\rangle = n_s |\dots, n_s, \dots\rangle. \quad (2.34)$$

Within this description, we define the concept of a phonon as a quantum of excitation of mode  $s = (\mathbf{q}j)$ . A purely quantum-mechanical attribute of this description is that, as appears in Eq. 2.33, even when the phonons are all in their ground state (zero temperature), the system possesses  $\frac{1}{2}\hbar\omega$  of energy per mode, corresponding to zero-point motion. We recall that phonons so defined are quasi-particles obeying Bose-Einstein statistics.

### Calculation of the phonon density of states

We define the phonon density of states (DOS)  $g(\omega)$  as the function giving the number of states  $(\mathbf{q}j)$  of frequency  $\omega$ , or in a continuous description, the number of states whose frequency is between  $\omega$  and  $\omega + d\omega$ :

$$\begin{aligned} g(\omega) &= \frac{1}{3rN} \sum_{\mathbf{q} \in \text{BZ}} \sum_{1 \leq j \leq 3r} \delta(\omega - \omega_{\mathbf{q}j}) \\ &= \frac{\Omega}{3r(2\pi)^3} \sum_j \int_{\text{BZ}} \delta(\omega - \omega_{\mathbf{q}j}) d^3q, \end{aligned} \quad (2.35)$$

where we used the fact that the  $\mathbf{q}$ -point grid is fine in the first Brillouin zone (BZ) to go from the first to the second expression ( $\Omega$  is the volume of the unit cell in real space). With this definition,  $g$  is normalized:

$$\int_0^\infty g(\omega) d\omega = 1, \quad (2.36)$$

To calculate the phonon density of states (DOS) of the crystal, we need to diagonalize the dynamical matrix at a large number of points in the first BZ. The diagonalization of  $\mathbf{D}(\mathbf{q})$  returns  $3r$  eigenvalues of frequency  $\omega_{\mathbf{q}j}$  ( $1 \leq j \leq 3r$ ) at each  $\mathbf{q}$ -point. By sampling all the  $\mathbf{q}$ 's inside the first Brillouin zone of the reciprocal lattice (or its symmetry-irreducible portion), we get a list of all the vibration frequencies of the crystal, thus defining  $g(\omega)$  through Eq. 2.35. The number of  $\mathbf{q}$ -points to sample is prohibitive, however. A practical solution consists in partitioning the frequency axis into bins and populating these bins according to the number of states whose frequency fall into them. This is equivalent to considering  $g(\omega)$  as a histogram.

Different computational algorithms can be used to populate this DOS histogram. In

general, the number of sampling  $\mathbf{q}$ -points (and matrix diagonalizations to perform) to get good statistics in the histogram varies inversely with the bin-width of the histogram. For a given bin-size, we can adopt different schemes for sampling reciprocal space. Two elementary approaches consist in picking  $\mathbf{q}$  at random (a Monte Carlo approach), or on a regular grid. In the computations presented in this thesis, the random sampling has usually been used, for it presents the advantage of avoiding systematic sampling of high-symmetry directions with degenerate phonon modes. In the Monte Carlo approach, we need to define the volume to sample. Technically, one only needs to sample the symmetry-irreducible portion of the first BZ. However, we adopted an extended zone scheme view and sampled a very large volume (*e.g.*, a cube) so that the boundary effects (owing to partial sampling of BZ intersected by the boundary surface) were minimized.

### 2.2.2 Electron-Phonon Interaction

Finally, we emphasize that both the formalism of density functional theory and the Born–von Kármán model of lattice dynamics rest on the Born-Oppenheimer approximation. It is the Born-Oppenheimer approximation that allows one to treat the electronic and nuclear problems as decoupled. Although well founded in principle, the adiabatic approximation precludes us from treating such effects as the electron mass-enhancement at low temperature in metals, which gives rise to an increase in electronic specific heat, for example. The electron-phonon interaction can be reintroduced in the theory with a perturbative treatment. Some ingredients of this description are given in an appendix.

## 2.3 First-Principles Phonon Calculations

In this section, we give a brief overview of current approaches for calculating phonons from first-principles simulations.

### 2.3.1 Frozen Phonons

This approach draws on the adiabatic approximation to calculate the energy of displacement of the nuclei (or ions) in the potential provided by the electrons. One picks a phonon

mode for the system (wavelength and mode index) and applies a displacement field to the nuclei corresponding to this phonon. The displacements correspond to the polarization vector for the phonon considered,  $\mathbf{e}(\mathbf{q}j)$ , multiplied by the periodic oscillation,  $\sin(\mathbf{q} \cdot \mathbf{R}_{l\kappa})$ , and a displacement amplitude,  $u$ . By calculating the total energy for a set of displacement configurations (varying the values of  $u$ ), one obtains the “deformation potential” for this phonon. This potential curve is typically parabolic around the equilibrium configuration (small  $u$ ), but for larger displacements, anharmonic components in the potential become more important. One can then extract the frequency for this phonon mode from the potential energy curve. For example in the case of a parabola, the frequency is  $\sqrt{K/M}$ , with  $K$  the second-derivative of the potential and  $M$  the nuclear mass.

The advantage of this method is that it provides the potential for the atomic displacements and it is not limited to the harmonic approximation. Studies of anharmonicity for selected phonon modes in transition metals have been performed with this method [26, 27, 28]. The obvious disadvantage of the frozen-phonon method is its computational cost. For calculating long-wavelength modes, one needs to setup a supercell that can be quite large. Also, the method is rather cumbersome, since the phonon modes are calculated one at a time, and a special supercell is needed for each one. Obviously, the method is limited to phonon modes whose displacement pattern are commensurate to the supercell used. The calculation of the entire phonon dispersions along several directions, or even worse the phonon DOS, would be very tedious and probably too demanding computationally for a true *ab initio* approach.

### 2.3.2 Hellmann-Feynman Forces

The Hellmann-Feynman or ‘direct’ method is based on the calculation of *forces*, rather than the total energy. The essence of this method is based on the evaluation of forces on nuclei in a quantum-mechanical description of the system, which is done with use of the Hellmann-Feynman theorem [29, 15].

If we consider the ground state energy  $E_\lambda$  and wave function  $\psi_\lambda$  to be parameterized by

some quantity  $\lambda$ , the change in  $E_\lambda$  incurred by a change in  $\lambda$  is given by

$$\frac{\partial E_\lambda}{\partial \lambda} = \langle \psi_\lambda | \frac{\partial \hat{H}}{\partial \lambda} | \psi_\lambda \rangle, \quad (2.37)$$

since the ground state energy is extremal with respect to variations of the wave function and the terms of the form  $\langle \partial \psi_\lambda / \partial \lambda | \hat{H} | \psi_\lambda \rangle$  vanish. The force on the nucleus  $I$  at  $\mathbf{R}_I$  is thus

$$\mathbf{F}_I = -\frac{\partial E}{\partial \mathbf{R}_I} = -\langle \psi | \frac{\partial \hat{H}}{\partial \mathbf{R}_I} | \psi \rangle. \quad (2.38)$$

Feynman [29] showed this to be just the electrostatic force on the displaced nucleus:

$$\begin{aligned} \mathbf{F}_I &= -\int \rho(\mathbf{r}) \frac{\partial V_{\text{ext}}(\mathbf{r})}{\partial \mathbf{R}_I} d^3r - \frac{\partial V_{\text{n-n}}}{\partial \mathbf{R}_I} \\ &= \int \rho(\mathbf{r}) \frac{(\mathbf{r} - \mathbf{R}_I) Z_I e}{|\mathbf{r} - \mathbf{R}_I|^3} d^3r + \frac{1}{2} \sum_{J \neq I} \frac{(\mathbf{R}_I - \mathbf{R}_J) Z_I Z_J e^2}{|\mathbf{R}_I - \mathbf{R}_J|^3}. \end{aligned} \quad (2.39)$$

This theorem is very useful as it provides us with an expression for the force on the nucleus from the electronic density  $\rho(\mathbf{r})$  directly. Using DFT, we can calculate the electronic ground state density for a nuclear configuration with a displaced nucleus  $\mathbf{R}(l\kappa) = \mathbf{x}(l\kappa) + \mathbf{u}(l\kappa)$  and thus, we can obtain the force on the nucleus from first principles.

The direct method for phonon simulations has its foundation in the calculation of the Hellmann-Feynman forces. The argument given above to calculate the force on a displaced atom can be generalized to compute the force on all atoms  $\kappa'$  in the crystal unit cell upon displacement of atom  $\kappa$ . The direct method typically proceeds with assuming that forces are linear with the displacement amplitude (Hooke's law), which is equivalent to the harmonic model for the nuclear potential, although this is not an intrinsic limitation. With this assumption, we can directly obtain the interatomic force-constants as the proportionality factor. With the interatomic force-constants in hand, we can calculate the phonon dispersions and density of states with the Born-von Kármán model, as described above.

In principle, one off-symmetry displacement of an atom is sufficient to determine all the force-constants involving this atom, which makes the direct method much more efficient than the frozen-phonon approach. There is one pitfall, however. In typical DFT simulations, periodic boundary conditions are used to replicate the crystal unit cell. If we displace

one of the atoms in the basis  $(l, \kappa)$ , all the periodic images of this atom  $\{l' \neq l, \kappa\}$  are also displaced, producing extra “image forces” on other basis atoms. The forces calculated are thus cumulant forces, instead of the true Hellmann-Feynman forces. This can be corrected for, however [30]. More severely, the range of interactions that can be calculated depends directly on the size of the supercell. Also, displacements in off-symmetry directions make the DFT calculation more costly and it may be more favorable to replace them by several high-symmetry displacements. Although the direct method is much more efficient than the frozen-phonon approach to treat the harmonic lattice dynamics with DFT, its main drawback is the need to use rather large supercells for materials with long-ranged interatomic interactions.

Pioneering examples of first-principles phonon computation with this approach can be found in [31, 32]. We performed phonon DOS calculations using the direct method, as implemented in the computer programs “Phonon” and “Phon”, and using the electronic-structure code VASP [33] to compute the Hellmann-Feynman forces. A presentation of the “Phonon” computer program implementation of the direct method can be found in [30]. The alternative software implementation provided by “Phon” is described in [34]. Our results from first-principles calculations for FCC Al, BCC Cr and BCC Fe are shown in figure 2.1, where they are compared with phonon DOS curves we obtained using a Born–von Kármán model and interatomic force-constants (derived from triple-axis neutron scattering measurements) reported in the literature. As can be seen in this figure, the results of our calculations with the direct method are in very good agreement with the experimental phonon DOS. The deviations between the *ab-initio* and experimental DOS in the case of Cr and Fe are consistent with the higher temperature at which the measurements were conducted.

### 2.3.3 Linear Response

The linear response approach to the calculation of perturbations allows one to compute the dynamical matrix  $D(\mathbf{q})$  and phonon frequencies  $\omega_j(\mathbf{q})$  at a selected set of  $\mathbf{q}$ -points without the need for supercells. It is based essentially on the computation of the derivatives (at arbitrary order) of the total energy with respect to perturbations, such as atomic displacements

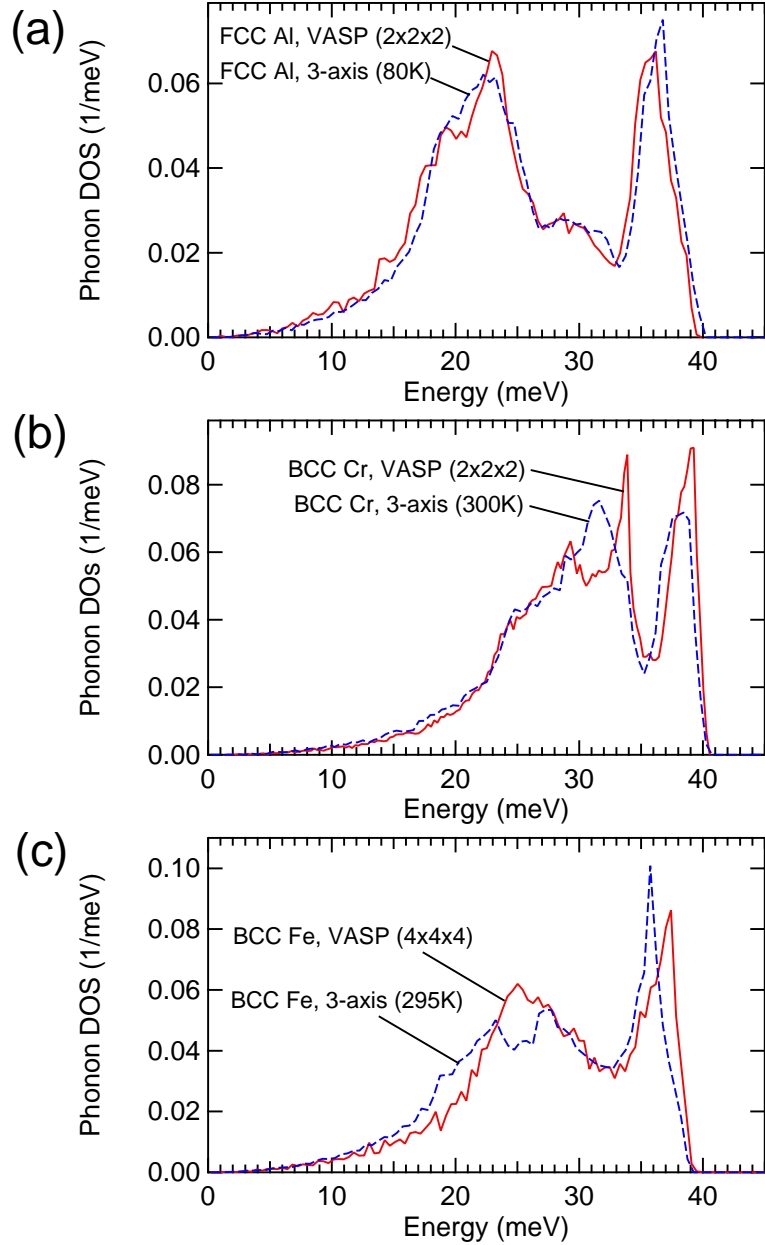


Figure 2.1: Phonon DOS of FCC Al (a), antiferromagnetic BCC Cr (b) and ferromagnetic BCC Fe (c), calculated from first-principles with the direct method, using VASP [33] and Phonon [30] (Al, Cr), or Phon [34] (Fe). The *ab-initio* results are compared to phonon DOS curves that were obtained with Born–von Kármán models, using experimental interatomic force-constants reported in the literature [35, 36, 37]. The first-principles calculation for FCC Al used a  $2 \times 2 \times 2$  repetition of the cubic unit cell (32 atoms). The calculation for BCC Cr (spin-polarized, antiferromagnetic) used a  $2 \times 2 \times 2$  cubic supercell (16 atoms). The calculation for BCC Fe (spin-polarized, ferromagnetic) used a  $4 \times 4 \times 4$  repetition of the rhombohedral primitive unit cell (64 atoms).

in the case of phonons. The derivatives are obtained from the formalism of perturbation theory applied onto the general DFT, thereby creating the so-called density functional perturbation theory (DFPT). DFPT relies on the “ $2n + 1$  theorem” of perturbation theory to obtain the  $(2n + 1)$  order derivatives of  $E$  from  $n$ -order perturbed wave functions. This formalism is discussed in details in [19, 38, 39, 40]. Applications to the calculation of phonons in transition metals are presented in [41, 42].

The linear-response method is quite general. Many physical properties are derivatives of the total energy, or of a suitable thermodynamic potential, with respect to perturbations. For example, perturbations might be atomic displacements, dilations or contractions of the unit cell, or an external electric field. The corresponding first order derivatives of the energy would then be the forces on the nuclei, the stresses and the dipole moment. Second-order derivatives would include the dynamical matrix, elastic constants, the dielectric susceptibility, the Born effective charge tensors and internal strains, while third-order derivatives would include the non-linear dielectric susceptibility, phonon-phonon interactions and Grüneisen parameters [19]. Implementations of DFPT are found in several computer programs, such as Abinit [43] and PWscf [44].

### 2.3.4 Molecular Dynamics

Finally, we briefly comment on molecular dynamics (MD), which also gives access to vibrational properties. In classical molecular dynamics, one numerically integrates Newton’s equations of motion (EOM) for an ensemble of particles, provided a set of initial conditions for positions and velocities, and with some model for interparticle interactions. By integrating the EOM with a fine time-step and for many steps, we can get a good sampling of the dynamics of the system (through the ergodic principle), which are recorded in a run history. Various properties can be calculated from such a run; in particular, the phonon DOS can be computed as the Fourier transform of the velocity autocorrelation function. The MD approach is a powerful one, as it can be applied to liquids or amorphous solids and not just crystalline solids. It also offers a realistic way to investigate effects of temperature, and it has been applied with some success to the case of transition metals. Examples of studies for transition metals relevant to this thesis can be found in [45, 46, 47].

Historically important potentials used in these simulations are the Morse, Lennard-Jones, and Born-Mayer potentials, among others. Embedded-atom potentials have been more successful for metals. Since these potentials are, to a large extent, empirical, these types of simulations do not qualify as “first-principles”. New developments have allowed to carry the MD technique into the realm of first-principles simulations, following the introduction by Car and Parinello of a novel approach to solve the quantum MD problem [48]. In the approach of Car and Parinello, a fictitious lagrangian for both nuclei and electrons is introduced, which is solved simultaneously for the classical coordinates of the nuclei and the quantum-mechanical degrees of freedom of the electrons. Although this reformulation has offered a great improvement in the feasibility of solving the quantum MD equations, the main difficulty is that it is still computationally very expensive, in particular for metals.

## 2.4 Thermal Properties

We review in this section the connection between vibrational and electronic properties and the thermodynamics of crystals and alloys. We start by recalling a number of relations for thermodynamical properties of phonons, without deriving them. Derivations for these standard results can be found in many textbooks, *e.g.*, [49, 50, 51, 52].

### 2.4.1 Harmonic Oscillators

#### Classical Harmonic Oscillator

A classical one-dimensional harmonic oscillator of mass  $M$  and force-constant  $k$  has a natural frequency

$$\omega = \sqrt{k/M} . \quad (2.40)$$

Its potential energy is

$$E_{\text{pot}}(x) = \frac{1}{2}kx^2 = \frac{1}{2}M\omega^2x^2 . \quad (2.41)$$

From the equipartition theorem, in equilibrium, the average potential and kinetic energies are equal,

$$\overline{E}_{\text{pot}} = \overline{E}_{\text{kin}} = \frac{1}{2}k_{\text{B}}T, \quad (2.42)$$

such that  $\overline{x^2}$  only depends on the temperature  $T$  and the force-constant  $k$ :

$$\overline{x^2} = \frac{k_{\text{B}}T}{M\omega^2} = \frac{k_{\text{B}}T}{k}. \quad (2.43)$$

The heat capacity is

$$C = \frac{\partial E}{\partial T} = \frac{\partial(\overline{E}_{\text{pot}} + \overline{E}_{\text{kin}})}{\partial T} = k_{\text{B}}, \quad (2.44)$$

which recovers the law of Dulong and Petit, according to which the classical, high-temperature limit for the heat capacity of solids is  $3k_{\text{B}}$  per atom.

### Harmonic Phonons

Consider a quantum harmonic oscillator of natural frequency  $\omega$ . Its thermal occupation factor at temperature  $T$  is given by the Bose-Einstein distribution

$$n(\hbar\omega, T) = \frac{1}{\exp(\hbar\omega/k_{\text{B}}T) - 1}, \quad (2.45)$$

with  $k_{\text{B}}$  the Boltzmann constant. In thermal equilibrium, the energy associated with a harmonic phonon with frequency  $\omega = \omega_{\mathbf{q}j}$  is

$$E(\mathbf{q}j) = (n(\mathbf{q}j) + 1/2)\hbar\omega_{\mathbf{q}j}, \quad (2.46)$$

where  $n(\mathbf{q}j) = n(\hbar\omega(\mathbf{q}j))$ , and for a harmonic crystal:

$$E_{\text{har}}(T) = \sum_{\mathbf{q}j} E(\mathbf{q}j) = 3N \int_0^{\omega_{\text{max}}} \hbar\omega (n(\hbar\omega, T) + 1/2) g(\omega) d\omega, \quad (2.47)$$

with  $g(\omega)$  the phonon DOS. The entropy of a particular harmonic phonon of frequency  $\omega$  is given by the general formula for the entropy of non-interacting bosons [52]:

$$S_{\text{har}}(\mathbf{q}j, T) = k_{\text{B}} [(n + 1) \ln(n + 1) - n \ln n], \quad (2.48)$$

where we wrote  $n$  for  $n(\hbar\omega_{\mathbf{q}j}, T)$ . Thus, we obtain the entropy per atom for the harmonic crystal:

$$S_{\text{har}}(T) = \sum_{\mathbf{q}j} S_{\text{har}}(\mathbf{q}j, T) = 3k_{\text{B}} \int_0^{\omega_{\text{max}}} [(n+1) \ln(n+1) - n \ln n] g(\omega) d\omega, \quad (2.49)$$

with  $g(\omega)$  normalized to unity. For harmonic vibrations, the heat capacities at constant pressure or constant volume are equal:  $C_P = C_V = C_{\text{har}}$ . They can be obtained from the relation

$$C_{\text{har}} = \frac{\partial E_{\text{har}}}{\partial T} = T \frac{\partial S_{\text{har}}}{\partial T}. \quad (2.50)$$

For a single mode ( $\mathbf{q}j$ ), we obtain

$$C_{\text{har}}(\mathbf{q}j, T) = \left( \frac{\hbar\omega_{\mathbf{q}j}}{k_{\text{B}}T} \right)^2 \frac{\exp(\hbar\omega_{\mathbf{q}j}/k_{\text{B}}T)}{[\exp(\hbar\omega_{\mathbf{q}j}/k_{\text{B}}T) - 1]^2}, \quad (2.51)$$

and for the harmonic solid, per atom,

$$C_{\text{har},T} = \int_0^{\omega_{\text{max}}} C_{\text{har}}(\omega, T) g(\omega) d\omega. \quad (2.52)$$

### 2.4.2 Anharmonicity

In the theory of lattice dynamics presented above, the interatomic potential was truncated at the quadratic order. This has allowed us to identify uncoupled vibration modes of the crystal, or phonons, that depend only the force-constants, *i.e.* the second-order derivatives of the nuclear potential energy. In particular, the phonon frequencies so-derived do not depend explicitly on the amplitudes of the vibrations, nor on the temperature. The harmonic approximation stems from the proposition that the displacements of the nuclei away from their equilibrium positions are small and that higher order terms in the expansion of the potential are negligible. Although these conditions are verified in many solids at low temperature, they tend to become less valid as the amplitude of the displacements increases at high temperatures, or in the vicinity of a martensitic phase transition. Some fundamental thermophysical properties are even completely unaccounted for by the harmonic approximation. If this model were valid, there would be no thermal expansion and

the thermal conductivity would be infinite, in the absence of phonon-phonon scattering. Also, force-constants and elastic constants would not vary with temperature or pressure and, as previously mentioned, the heat capacities at constant pressure and constant volume would be equal.

If one keeps a description of vibrations in terms of phonons, small deviations from the harmonic case can be treated in perturbation theory and the result is a shift in phonon frequencies [50]:

$$\tilde{\omega}(\mathbf{q}j) = \omega(\mathbf{q}j) + \Delta(\mathbf{q}j) - i\Gamma(\mathbf{q}j), \quad (2.53)$$

with  $\omega(\mathbf{q}j)$  the harmonic frequency of mode  $(\mathbf{q}j)$ . The frequencies  $\tilde{\omega}(\mathbf{q}j)$  are called “renormalized” phonon frequencies. The term  $-i\Gamma(\mathbf{q}j)$  expresses that the phonons are now damped, as  $(\mathbf{q}j)$  is not a true eigenstate of the anharmonic hamiltonian and is not stationary. In the case of weak anharmonicity,  $\Gamma/\omega \ll 1$  and the lifetime of the state is long enough that it is still meaningful to label it as a phonon state  $(\mathbf{q}j)$ . The shifted frequencies (2.53) are the frequencies measured in a neutron scattering experiment [50, 53, 51, 52]. In the following, it is assumed that the phonon width  $\Gamma$  is small and the focus is on the energy shift  $\Delta$ .

In the case of a one-dimensional oscillator, the anharmonicity of the potential can be expressed

$$V(x) = \frac{1}{2}M\omega^2x^2 + V_3x^3 + V_4x^4, \quad (2.54)$$

where higher order terms are neglected. The harmonic case  $V_3 = V_4 = 0$  yields the energy eigenstates  $E_n = (n + 1/2)\hbar\omega$ , but including the effect of small terms  $V_3$  and  $V_4$  in second-order perturbation theory gives a shift [50]:

$$\Delta E_n = \langle n|V_4x^4|n\rangle + \sum_{n' \neq n} \frac{|\langle n|V_3x^3 + V_4x^4|n'\rangle|^2}{E_{n'} - E_n}, \quad (2.55)$$

since  $\langle n|V_3x^3|n\rangle = 0$  because the integrand  $V_3|\psi_n(x)|^2x^3$  is odd in  $x$ . On the other hand, the contribution of  $V_4x^4$  in the last term is smaller than that of  $V_3x^3$  and it can be dropped.

From this,  $V_3$  and  $V_4$  contribute to the same order in perturbation and both must be kept to leading order. The renormalized phonon frequencies (without damping) can thus be written

$$\tilde{\omega}(\mathbf{q}j) = \omega_0(\mathbf{q}j) + \Delta_2(\mathbf{q}j) + \Delta_3(\mathbf{q}j) + \Delta_4(\mathbf{q}j), \quad (2.56)$$

with  $\omega_0(\mathbf{q}j)$  the harmonic frequencies at some reference volume and temperature (usually 0 K or 300 K) and where  $\Delta_3$  and  $\Delta_4$  are shifts due to explicitly anharmonic potentials, while  $\Delta_2$  is the shift due to the change in force-constants upon thermal expansion or application of pressure.  $\Delta_2$  represents the softening of the parabolic potentials with the increase in volume incurred by thermal expansion or their stiffening with applied external pressure. When only  $\Delta_2$  is retained in Eq. 2.56, one speaks of the quasiharmonic approximation.

### Quasiharmonic Approximation

The change in frequency of a particular phonon mode  $\mathbf{q}j$  is related to the change in volume  $V$  through the Grüneisen parameter  $\gamma_{\mathbf{q}j}$ :

$$\gamma_{\mathbf{q}j}(V, T) = -\frac{\partial \ln \omega_{\mathbf{q}j}(V, T)}{\partial \ln V}. \quad (2.57)$$

It is cumbersome to consider a specific Grüneisen parameter for each phonon mode since the full phonon spectrum needs to be taken into account for thermodynamic purposes. A thermodynamic Grüneisen parameter is then generally defined as:

$$\gamma_G(V, T) = \frac{3\alpha V B_T}{C_V} = \frac{3\alpha V B_S}{C_P}, \quad (2.58)$$

with  $\alpha$  the coefficient of linear thermal expansion,  $V$  the specific volume,  $B_T$  and  $B_S$  the isothermal and isentropic bulk moduli, respectively, and  $C_V$  and  $C_P$  the heat capacity at constant volume and constant pressure, respectively. The approximation of  $\gamma_{\mathbf{q}j}$  by  $\gamma_G$  is not always firmly justified, as substantial deviations of  $\gamma_{\mathbf{q}j}$  may exist between different phonon modes. It is often adopted for convenience, however. In first approximation,  $\gamma_{\mathbf{q}j}$  (or  $\gamma_G$ ) is a constant around ambient conditions, *i.e.*, it does not depend on the magnitude of the change in  $V$  for small compression/expansion around the reference volume, and the only

$T$ -dependence is usually assumed to come through the dependence of the reference volume on temperature  $V = V(T, P)$ . Although this may be inappropriate in the case of explicit anharmonicity, we concentrate for now on the thermodynamic consequences that can be expected from the softening of phonons in the quasiharmonic approximation.

Thermal expansion yields a difference between the heat capacities at constant pressure and constant volume. From standard thermodynamic equalities, one can show that

$$C_P - C_V = 3\alpha\gamma_G C_V T = 9\alpha^2 V B_T T. \quad (2.59)$$

Integrating this relation, the quasiharmonic change in entropy associated with thermal expansion between  $T_1$  and  $T_2$  is obtained:

$$\Delta S^{\text{qh}}(T_1, T_2) = 9V \int_{T_1}^{T_2} \alpha^2 B_T dT. \quad (2.60)$$

The quasiharmonic entropy defined this way takes into account the shift  $\Delta_2$  in phonon frequencies. Since it is defined from a macroscopic relation, however, phonons may not be the only degrees of freedom that contribute. In particular, in a metal, electrons also contribute to the entropy and in this case

$$\Delta S^{\text{qh}}(T_1, T_2) = \Delta S_{\text{ph}}^{\text{qh}}(T_1, T_2) + \Delta S_{\text{el}}^{\text{xp}}(T_1, T_2), \quad (2.61)$$

where we use the subscript ‘xp’ to refer to the effect of thermal expansion on the electronic entropy.

### Beyond the Quasiharmonic Approximation

An attempt to describe thermodynamic effects related to the amplitudes of phonon displacements requires one taking into account the explicit anharmonic shifts  $\Delta_3$  and  $\Delta_4$  in the renormalized phonon frequencies in Eq. 2.56. An important result concerning the thermodynamics of anharmonic crystals is that, in leading order in perturbation theory, the vibrational entropy is still given correctly by its harmonic expression, but with phonon frequencies given by their renormalized values. This was proven first by Barron [54] with

perturbation theory and was also shown to be valid at all orders of self-consistent phonon theory by Hui and Allen [55]. The vibrational entropy is the only thermodynamic function for which this procedure applies, however. In particular, the result does not hold for the free energy or the heat capacity [52, 50]. The anharmonic phonon entropy is

$$S_{\text{ph}}^{\text{anh}} = S_{\text{ph}}^{\text{qh}} + S_{\text{ph}}^{(3)} + S_{\text{ph}}^{(4)} = \tilde{S}_{\text{har}} \equiv S_{\text{har}}(\{\tilde{\omega}_{\mathbf{q}j}\}) . \quad (2.62)$$

It should be emphasized that this result is only established up to leading order in perturbation theory and may not hold when the anharmonicity is large.

Another important result is that the renormalized phonon frequencies are the frequencies measured in neutron scattering experiments. Thus, the true anharmonic entropy is experimentally accessible. It also follows that the entropy due to explicit anharmonicity in the nuclear potential,  $S_{\text{ph}}^{(3)} + S_{\text{ph}}^{(4)}$ , is accessible by comparing  $S_{\text{ph}}^{\text{anh}}$  and  $S_{\text{ph}}^{\text{qh}}$ , provided the electronic entropy and its volume dependence are available.

The argument can be made more specific with the help of a generalized notation. First, we recognize that the anharmonic shifts in phonon frequencies,  $\Delta_2$ ,  $\Delta_3$ , and  $\Delta_4$  yield a redistribution of the area under the density of states, so we can write

$$\tilde{g}(\omega) = g^{(0)}(\omega) + \delta g^{(2)}(\omega) + \delta g^{(3)}(\omega) + \delta g^{(4)}(\omega) , \quad (2.63)$$

where we added a symbolic zero superscript on the harmonic phonon DOS for explicitness. Second, the expressions (2.49) and (2.62) for the phonon entropy show that it is a functional of the phonon DOS, which motivates the notation

$$S[\tilde{g}_T, T] = S_{\text{ph}}^{\text{har}}(\{\tilde{\omega}_{\mathbf{q}j}(T)\}) , \quad (2.64)$$

where the second argument,  $T$ , denotes the temperature in the Bose-Einstein thermal population. Also, we point out that this functional is linear with respect to the first argument (linearity of integration). With this notation, the difference in phonon entropy between  $T_1$  and  $T_2$ , in leading order in perturbed phonon frequencies, is

$$S_{\text{ph}}^{\text{anh}}(T_2) - S_{\text{ph}}^{\text{anh}}(T_1) = S[\tilde{g}_{T_2}, T_2] - S[\tilde{g}_{T_1}, T_1]$$

$$\begin{aligned}
&= \{S[g_{T_2}^{(0)}, T_2] - S[g_{T_1}^{(0)}, T_1]\} \\
&+ \{S[g_{T_2}^{(2)}, T_2] - S[g_{T_1}^{(2)}, T_1]\} \\
&+ \{S[g_{T_2}^{(3,4)}, T_2] - S[g_{T_1}^{(3,4)}, T_1]\} .
\end{aligned} \tag{2.65}$$

The second grouping on the right corresponds to the quasiharmonic change in phonon entropy owing to thermal expansion between  $T_1$  and  $T_2$ :

$$S[g_{T_2}^{(2)}, T_2] - S[g_{T_1}^{(2)}, T_1] = \Delta S_{\text{ph}}^{\text{qh}}(T_1, T_2) , \tag{2.66}$$

and the last grouping is the explicitly anharmonic contribution to the change in phonon entropy between the two temperatures:

$$S[g_{T_2}^{(3,4)}, T_2] - S[g_{T_1}^{(3,4)}, T_1] = \Delta S_{\text{ph}}^{(3,4)}(T_1, T_2) . \tag{2.67}$$

Since the harmonic component of the phonon DOS is independent of temperature, we also have  $g_{T_1}^{(0)} = g_{T_2}^{(0)}$ . We now consider the case where  $T_1$  is a low-temperature and  $T_2$  some high temperature. We make the approximation that the low temperature phonon DOS is harmonic,  $\tilde{g}_{T_1} = g_{T_1}^{(0)} = g_{T_2}^{(0)}$ . This is expected to be approximately valid for  $T_1 \sim 300$  K and should be better at lower temperatures. With this approximation, we obtain the result

$$S[\tilde{g}_{T_2}, T_2] - S[\tilde{g}_{T_1}, T_2] = \Delta S_{\text{ph}}^{\text{qh}}(T_1, T_2) + \Delta S_{\text{ph}}^{(3,4)}(T_1, T_2) , \tag{2.68}$$

which allows us to evaluate the explicitly anharmonic contribution from the experimental phonon DOS curves at temperatures  $T_1$  and  $T_2$  and the knowledge of the quasiharmonic effect, obtained from the classical thermal expansion formula (corrected for the electronic part), Eq. 2.60. The physical signification of the left-hand side in (2.68) is clear: it is the difference between the phonon entropy obtained from the measured high-temperature DOS and the phonon entropy that would be obtained at high temperature, if the solid were harmonic.

### 2.4.3 Electronic Entropy

In metals, the Fermi level falls in the conduction band and empty electronic states are accessible to electrons at any temperature  $T > 0$ . An electronic entropy  $S_{\text{el}}$  is associated with the excitations of electrons with temperature:

$$S_{\text{el}}(T, V) = -k_{\text{B}} \int_{-\infty}^{\infty} [(1 - f_{T,E}) \ln(1 - f_{T,E}) + f_{T,E} \ln(f_{T,E})] n_V(E) dE, \quad (2.69)$$

where  $f_{T,E}$  is the Fermi distribution function and  $n_V(E)$  is the electronic density of states at energy  $E$  [52]. Using density functional theory,  $n_V(E)$  can be calculated for different volumes of the crystal, and the change in  $S_{\text{el}}$  with thermal expansion can be evaluated. A simple procedure is to calculate  $S_{\text{el}}$  at a low-temperature volume,  $V_{\text{low}}$ , and a high-temperature volume,  $V_{\text{high}}$ , and interpolate at intermediate temperatures

$$S_{\text{el}}(T) = S_{\text{el}}(T, V_{\text{low}}) \left( \frac{T_{\text{high}} - T}{T_{\text{high}} - T_{\text{low}}} \right) + S_{\text{el}}(T, V_{\text{high}}) \left( \frac{T - T_{\text{low}}}{T_{\text{high}} - T_{\text{low}}} \right). \quad (2.70)$$

In practice,  $S_{\text{el}}$  can be large at elevated temperatures, with values on the order of  $1 k_{\text{B}}/\text{at}$ . at  $T_{\text{fus}}$  in transition metals (see, *e.g.* [56]). The change in  $S_{\text{el}}$  with thermal expansion is small, however  $S_{\text{el}}^{\text{xp}}(T_{\text{fus}}) \sim 0.05 k_{\text{B}}/\text{at}$ .

## Chapter 3

# Inelastic Neutron Scattering

### 3.1 Introduction

Thermal neutrons represent a valuable probe of condensed matter, and their use has considerably increased since the early work of Brockhouse and Shull\*. The strength of neutrons is that they are well suited to the study of both static and dynamic properties of matter. Not only is the wavelength of thermal neutrons of the same order as the interatomic distances in solids, but the energy and momenta of thermal neutrons match well those of a range of low-energy excitations, such as phonons and magnons. These favorable properties, together with the advent of facilities producing beams of thermal neutrons (nuclear reactors or spallation sources) have spun the development of a host of techniques to investigate countless aspects of condensed matter.

Neutrons interact with the nuclei in the sample through nuclear forces. Since the neutron has a magnetic moment, it can also interact with the spin distribution of the sample. We thus have two fundamental types of interactions, leading to nuclear or magnetic scattering processes. In this thesis, we are mostly concerned with nuclear scattering processes, for which we present an overview of the theory. More detailed accounts of the theory of thermal neutron scattering can be found in the books of Squires [14] and Lovesey [13].

The principal aspect of neutron scattering that interests us is the opportunity of probing phonon modes in metals and alloys. Thermal neutrons corresponding to a temperature of

---

\*Bertram N. Brockhouse and Clifford G. Shull shared the 1994 Nobel prize in physics for the development of neutron spectroscopy and neutron diffraction, respectively.

293 K, or equivalently of energy  $E = 25.3$  meV, have a wavelength  $\lambda = 1.798$  Å and, correspondingly, a wave vector  $k = 2\pi/\lambda = 3.49$  Å<sup>-1</sup>. This wavelength matches well the lattice parameters of crystals, and thus the wave vector has about the same size as the width of the Brillouin zone. This energy scale also corresponds well to phonon energies in many materials. By comparison, IR or visible photons match excitation energies in molecules or crystals but, owing to their small wave vector, they can only sample vibration modes close to the center  $\Gamma$  of the Brillouin zone. Besides, the modes accessible by Raman scattering and infrared spectroscopy are limited by selection rules, although these are often complementary between the two techniques. X-ray photons, on the other hand, can interact with phonons throughout the Brillouin zone, but the energy they gain or lose in this interaction is much smaller than their incident energy (by a factor of  $10^6$ ). Such minute energy changes are difficult to detect. Inelastic x-ray scattering has undergone tremendous progress with the advent of synchrotron radiation sources, however, and measurements of phonon dispersions and densities of states are nowadays possible, with conventional or nuclear-resonant inelastic x-ray scattering techniques. Although neutron scattering is still the central technique in phonon investigations, neutron and x-ray scattering offer some interesting complementarities. One illustrative example applies to the measurement of the phonon DOS in binary alloys. Inelastic neutron scattering can provide a total phonon DOS for the alloy, but this DOS is usually weighted by the different strengths with which the constituent nuclei scatter the neutrons. This constitutes the infamous “neutron-weighting” problem. For elements exhibiting Mössbauer isotopes, nuclear-resonant inelastic x-ray scattering allows one to measure the partial phonon DOS for the resonant nucleus, and thus gives a way to determine both contributions to the total DOS and correct for neutron-weighting.

We consider the general scattering event depicted in figure 3.1, where an incident neutron of wave vector  $\mathbf{k}_i$  is scattered by the sample into a final state of wave vector  $\mathbf{k}_f$ , transferring a momentum  $\mathbf{Q} = \mathbf{k}_i - \mathbf{k}_f$  to the sample. The incident and final neutron energies are  $E_i = \hbar^2 \mathbf{k}_i^2 / 2m$  and  $E_f = \hbar^2 \mathbf{k}_f^2 / 2m$ , where  $m$  denotes the mass of the neutron, and the energy transferred to the sample is  $E = E_i - E_f = \hbar^2 (\mathbf{k}_i^2 - \mathbf{k}_f^2) / 2m$ . The scattering angle  $\Phi$  verifies  $\cos(\Phi) = \mathbf{k}_i \cdot \mathbf{k}_f / \|\mathbf{k}_i\| \|\mathbf{k}_f\|$ . One notes from figure 3.1 that, for a fixed incident neutron energy  $E_i$  and a constant scattering angle  $\Phi$ , the magnitudes of the momentum

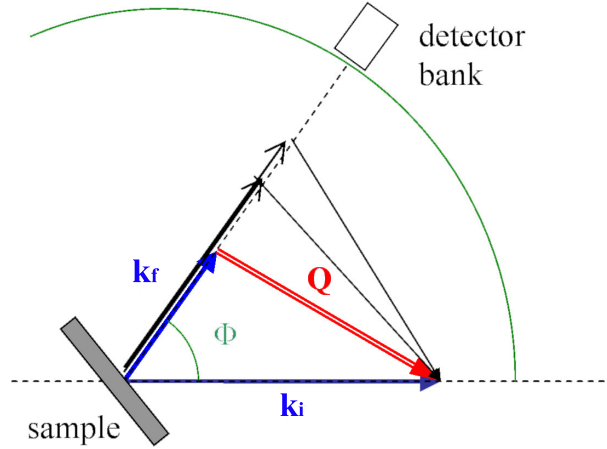


Figure 3.1: Neutron scattering geometry.

transfer  $Q$  and energy transfer  $E$  vary with the final wave vector of the neutron. The relationship between  $E$  and  $Q$  gives rise to kinematic conditions on the scattering, which are of experimental importance.

## 3.2 Scattering Cross-Section

### 3.2.1 General Case

The central quantity in a scattering experiment is the cross-section. We can determine the cross-section from the probability that the system (neutron+sample) undergoes a transition from the initial state  $(\mathbf{k}_i, \lambda_i)$  to the final state  $(\mathbf{k}_f, \lambda_f)$  as the neutron traverses the scattering potential  $V$  in the sample. In this discussion,  $\lambda$  denotes an aggregate quantum number for the state of the sample. For experimental reasons, we are interested in the scattering cross-section corresponding to neutrons being scattered into final states  $\mathbf{k}_f$  within a small solid angle  $d\Omega$  around the direction  $\hat{\Omega}$ . This differential cross-section is expressed in terms of the rate  $W$  of scattering events  $(\mathbf{k}_i, \lambda_i) \rightarrow (\mathbf{k}_f, \lambda_f)$  and the flux  $\mathcal{F}$  of incident neutrons as [14]:

$$\left(\frac{\partial\sigma}{\partial\Omega}\right)_{\lambda_i\rightarrow\lambda_f} = \frac{1}{\mathcal{F}} \frac{1}{d\Omega} \sum_{\mathbf{k}_f \in d\Omega} W_{(\mathbf{k}_i, \lambda_i) \rightarrow (\mathbf{k}_f, \lambda_f)}. \quad (3.1)$$

Using Fermi's golden rule, we can express the transition rate in terms of the matrix element of the scattering potential  $V$  coupling the initial and final states:

$$\sum_{\mathbf{k}_f \in d\Omega} W_{(\mathbf{k}_i, \lambda_i) \rightarrow (\mathbf{k}_f, \lambda_f)} = \frac{2\pi}{\hbar} \rho_{\mathbf{k}_f} |\langle \mathbf{k}_f \lambda_f | V | \mathbf{k}_i \lambda_i \rangle|^2, \quad (3.2)$$

where  $\rho_{\mathbf{k}_f}$  is the density of final states within  $d\Omega$ , per unit energy. Working out  $\rho_{\mathbf{k}_f}$  from the energy relation for free final particles  $E_f = \hbar^2 \mathbf{k}_f^2 / 2m$  and using the fact that  $\mathcal{F}$  is proportional to the velocity of incident neutrons and thus to  $k_i$ , one obtains

$$\left( \frac{\partial \sigma}{\partial \Omega} \right)_{\lambda_i \rightarrow \lambda_f} = \frac{k_f}{k_i} \left( \frac{m}{2\pi \hbar^2} \right)^2 |\langle \mathbf{k}_f \lambda_f | V | \mathbf{k}_i \lambda_i \rangle|^2. \quad (3.3)$$

We also obtain the double differential cross-section for scattering of neutrons into final states within  $d\Omega$  and of energy between  $E_f$  and  $E_f + dE$ , by requiring that the energy of the system (neutron + sample) be conserved:

$$\left( \frac{\partial^2 \sigma}{\partial \Omega \partial E} \right)_{\lambda_i \rightarrow \lambda_f} = \frac{k_f}{k_i} \left( \frac{m}{2\pi \hbar^2} \right)^2 |\langle \mathbf{k}_f \lambda_f | V | \mathbf{k}_i \lambda_i \rangle|^2 \delta((E_{\lambda_i} + E_i) - (E_{\lambda_f} + E_f)). \quad (3.4)$$

### 3.2.2 Phonon Scattering

We recall in this section the results that can be derived in the case of neutrons scattering off the phonon excitations in a crystalline sample. A pictorial representation of a phonon creation process is given in figure 3.2. In this inelastic scattering process, a phonon of wave vector  $\mathbf{q} = \mathbf{Q}$  and energy  $\hbar\omega = E_i - E_f$  is created, raising the occupation number of such phonons in the crystal from  $n_{\mathbf{q}\omega}$  to  $n_{\mathbf{q}\omega} + 1$ .

The phonon scattering processes occur through the neutron-nucleus interaction, which is conventionally described by an isotropic delta function, or Fermi pseudopotential:

$$V(\mathbf{r}) = \frac{2\pi \hbar^2}{m} b \delta(\mathbf{r}), \quad (3.5)$$

where  $b$  is the scattering length. If we consider a Bravais lattice, this potential is replicated

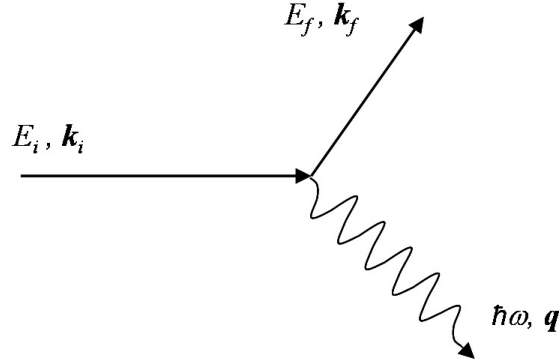


Figure 3.2: Scattering process for creation of one phonon.

at each site of the lattice:

$$V(\mathbf{r}) = \sum_l \frac{2\pi\hbar^2}{m} b_l \delta(\mathbf{r} - \mathbf{R}_l). \quad (3.6)$$

The scattering of the neutron between the asymptotic plane wave states  $\mathbf{k}_i$  and  $\mathbf{k}_f$  by this potential involves the matrix element  $\langle \mathbf{k}_f | V | \mathbf{k}_i \rangle$ , which corresponds to taking the space-Fourier transform of  $V$ . The matrix element is then rewritten as  $\sum_l b_l \langle \lambda_f | \exp(i\mathbf{Q} \cdot \mathbf{R}_l) | \lambda_i \rangle$ , with  $\mathbf{Q} = \mathbf{k}_i - \mathbf{k}_f$ . The cross-section is then best evaluated with the position operators  $\mathbf{R}_l$  expressed in Heisenberg representation. Reasoning that we do not actually measure the cross-section for the transition  $\lambda_i \rightarrow \lambda_f$ , but rather between the sets of sample states  $E_{\lambda_i}$  and  $E_{\lambda_f}$ , and expressing the delta function for conservation of energy with help of its time Fourier transform, one can rewrite Eq. 3.4 as

$$\begin{aligned} \left( \frac{\partial^2 \sigma}{\partial \Omega \partial E} \right) &= \frac{k_f}{k_i} \frac{1}{2\pi\hbar} \sum_{l,l'} b_l b_{l'} \\ &\times \int_{-\infty}^{\infty} \langle \exp(-i\mathbf{Q} \cdot \mathbf{R}_{l'}(0)) \exp(i\mathbf{Q} \cdot \mathbf{R}_l(t)) \rangle \exp(-i\omega t) dt, \end{aligned} \quad (3.7)$$

where the brackets denote thermal averages and  $\hbar\omega = E_i - E_f$  is the energy transferred to the sample. The quantity in brackets represents a space-time correlation function for the displacements projected along the momentum transfer.

Two categories of scattering processes can be distinguished at this point: coherent scat-

tering processes, in which the phases in the scattering by each center preserve the coherency of the neutron wave, and incoherent scattering processes, in which the coherency is lost. In the coherent case, the neutron waves scattered from each center can produce interference effects, and these effects build up over the whole sample. On the other hand, in the incoherent case, the randomness in the phase of each scattered wave prevents any macroscopic interference and the scattering intensity is effectively a sum of scattering intensities from each nucleus. In the case of coherent scattering, we take the Fourier transform of the correlation functions between different atoms at different times, whereas in the incoherent case, each atom is considered separately and the correlation function is for that same atom at different times. The respective cross-sections are given by:

$$\left(\frac{\partial^2 \sigma}{\partial \Omega \partial E}\right)_{\text{coh}} = \frac{\sigma_{\text{coh}}}{4\pi} \frac{k_f}{k_i} \frac{1}{2\pi\hbar} \sum_{l,l'} \times \int_{-\infty}^{\infty} \langle \exp(-i\mathbf{Q} \cdot \mathbf{R}_{l'}(0)) \exp(i\mathbf{Q} \cdot \mathbf{R}_l(t)) \rangle \exp(-i\omega t) dt \quad (3.8)$$

$$\left(\frac{\partial^2 \sigma}{\partial \Omega \partial E}\right)_{\text{inc}} = \frac{\sigma_{\text{inc}}}{4\pi} \frac{k_f}{k_i} \frac{1}{2\pi\hbar} \sum_l \times \int_{-\infty}^{\infty} \langle \exp(-i\mathbf{Q} \cdot \mathbf{R}_l(0)) \exp(i\mathbf{Q} \cdot \mathbf{R}_l(t)) \rangle \exp(-i\omega t) dt, \quad (3.9)$$

where  $\sigma_{\text{coh}} = 4\pi\bar{b}^2$  and  $\sigma_{\text{inc}} = (\bar{b}^2 - \bar{b}^2)$  are the total coherent and incoherent cross-sections, with the bar denoting averages over all nuclei in the sample. One should keep in mind that even a Bravais lattice can be an incoherent neutron scatterer, as different spin-states of the same isotope can lead to incoherency. Isotopic disorder is an additional source of incoherency. Neutron diffraction and dispersion curve measurements exploit the coherent scattering (in a time-averaged way for diffraction) to reveal  $Q$ -structure, while measurements on incoherent scattering samples can only access the  $E$ -dependence.

In the case of a vibrating lattice, the nuclear scattering potentials oscillate periodically around the equilibrium lattice positions and these oscillations are described by normal modes of vibrations, which have been discussed in chapter 2. The displacement operator for the atom in cell  $l$  of a Bravais lattice is expressed in terms of the phonon creation and

annihilation operators,  $\hat{b}_s^\dagger$  and  $\hat{b}_s$ , respectively ( $s = (\mathbf{q}, j)$ ), as

$$\hat{\mathbf{u}}_l = \left( \frac{\hbar}{2MN^{cell}} \right)^{1/2} \sum_s \frac{\mathbf{e}_s}{\sqrt{\omega_s}} (\hat{b}_s \exp(i\mathbf{q} \cdot \mathbf{R}_l) + \hat{b}_s^\dagger \exp(-i\mathbf{q} \cdot \mathbf{R}_l)). \quad (3.10)$$

The scattering cross-sections of (3.9) involve the instantaneous nuclear positions  $\mathbf{R}_l(t) = \mathbf{x}_l + \mathbf{u}_l(t)$ . After introducing the operators  $U = -i\mathbf{Q} \cdot \mathbf{u}_0(t)$  and  $V = i\mathbf{Q} \cdot \mathbf{u}_l(t)$ , both cross-sections can be shown to involve the correlation function  $\langle \exp U \exp V \rangle$ , while a static structure factor can be pulled out of the time integral. One can then show that, for a Bravais crystal of harmonic oscillators,

$$\langle \exp U \exp V \rangle = \exp\langle U^2 \rangle \exp\langle UV \rangle, \quad (3.11)$$

where the first factor on the right corresponds to the well-known Debye-Waller factor. The factor  $\exp\langle UV \rangle$  can be expanded as a Taylor series:

$$\exp\langle UV \rangle = 1 + \langle UV \rangle + \frac{1}{2!} \langle UV \rangle^2 + \dots \quad (3.12)$$

Because of the time Fourier transform in (3.9), the first term gives a non-zero contribution to  $\partial^2 \sigma / \partial \Omega \partial E$  only if  $\omega = 0$ , which is the case of elastic scattering. In the coherent case, we are then left with the static structure factor for diffraction, multiplied by the Debye-Waller factor. On the other hand, the elastic incoherent cross-section is just proportional to the Debye-Waller factor. The higher-order terms in the decomposition of  $\exp\langle UV \rangle$  correspond to inelastic scattering processes. The first order term represents processes where one phonon is created or annihilated and the  $p$ -th order term, processes where  $p$  phonons are involved.

We now focus our discussion on the incoherent inelastic cross-section for one-phonon scattering. The evaluation of  $\langle UV \rangle$  with the expression (3.10) brings about products of phonon creation and annihilation operators, which reduce to occupation numbers upon thermal averaging. We are then left with two terms:

$$\begin{aligned} \left( \frac{\partial^2 \sigma}{\partial \Omega \partial E} \right)_{\text{inc, 1phonon}} &= \frac{\sigma_{\text{inc}} k_f}{4\pi k_i} \frac{1}{2M} \exp\langle U^2 \rangle \sum_s \frac{(\mathbf{Q} \cdot \mathbf{e}_s)^2}{\omega_s} \\ &\times \{ \langle n_s + 1 \rangle \delta(\omega - \omega_s) + \langle n_s \rangle \delta(\omega + \omega_s) \}, \end{aligned} \quad (3.13)$$

where the first and second delta functions correspond respectively to the creation and annihilation of one phonon of energy  $\hbar\omega$ . The sum over modes  $s$  brings about the phonon density of states and after further simplification, one obtains the incoherent neutron scattering cross-section for a one-phonon creation process, originally derived by Placzek and van Hove [12]:

$$\left( \frac{\partial^2 \sigma}{\partial \Omega \partial E'} \right)_{+1 \text{ phonon}}^{\text{inc}} = \frac{\sigma^{\text{inc}}}{4\pi} \frac{k_f}{k_i} \frac{3N}{2M} e^{-2W} \times \frac{Q^2}{3\omega} g(\hbar\omega) \langle n(\omega) + 1 \rangle, \quad (3.14)$$

where  $\exp(-2W) = \exp\langle U^2 \rangle$  is the Debye-Waller factor and  $g(\hbar\omega)$  is the normalized phonon DOS. Since phonons are Bosons,  $\langle n(\omega) \rangle$  is the Bose-Einstein distribution.

### 3.3 Scattering Function

A more general formulation of neutron scattering was derived by van Hove [57] in terms of correlation functions. All the information on the system available from a neutron scattering experiment is encoded in the time-dependent pair-correlation function for the scattering centers,  $G(\mathbf{r}, t)$  (also called the van Hove correlation function). The scattering intensity is related to the Fourier transform in time and space of  $G(\mathbf{r}, t)$ , also called the scattering function  $S(\mathbf{Q}, \omega)$ :

$$S(\mathbf{Q}, \omega) = \frac{1}{2\pi\hbar} \int G(\mathbf{r}, t) \exp(i(\mathbf{Q} \cdot \mathbf{r} - \omega t)) d^3r dt. \quad (3.15)$$

The relations between  $S(\mathbf{Q}, \omega)$  and the cross-sections for coherent and incoherent scattering are [14]:

$$\begin{aligned} \left( \frac{\partial^2 \sigma}{\partial \Omega \partial E} \right)_{\text{coh}} &= \frac{\sigma_{\text{coh}}}{4\pi} \frac{k_f}{k_i} S_{\text{coh}}(\mathbf{Q}, \omega) \\ \left( \frac{\partial^2 \sigma}{\partial \Omega \partial E} \right)_{\text{inc}} &= \frac{\sigma_{\text{inc}}}{4\pi} \frac{k_f}{k_i} S_{\text{inc}}(\mathbf{Q}, \omega), \end{aligned} \quad (3.16)$$

where  $S_{\text{inc}}(\mathbf{Q}, \omega)$  in the incoherent case corresponds to  $G(\mathbf{r}, t)$  limited to self-correlations.

## 3.4 Time-of-Flight Neutron Spectrometer

### 3.4.1 Principle

The time-of-flight (TOF) neutron spectrometer corresponds directly to the pictorial scattering experiment of figure 3.1. A schematic of a direct-geometry chopper spectrometer, as found most commonly at a spallation source, is shown in figure 3.3. A pulsed source delivers neutrons to a moderator, in which the neutrons thermalize through multiple collisions with the medium, exiting with a maxwellian velocity distribution representative of the moderator temperature. The spectrum typically also contains epithermal neutrons of higher energy that were not fully equilibrated. A port passes a beam of neutrons, which is monochromatized by a pair of rotating choppers ( $t_0$  and  $E_0$  rotors in figure 3.3), whose synchronized opening times only let through neutrons of a chosen energy. This energy selection rests on the energy-velocity relationship for the free neutrons,  $E = \frac{1}{2}mv^2$ . The neutrons are incident on a sample and some of them are scattered, transferring momentum and energy, and the scattered neutrons are collected by a set of detectors covering possibly a large angular range. Typically, the detectors are  $^3\text{He}$ -filled tubes, which produce a charge after capture of the neutron and a low-energy nuclear reaction. This type of detector does not offer energy discrimination. Instead, knowing the time of the initial neutron pulse, the velocity of the scattered neutrons is determined from their arrival time on the detector, the time at which they were impinging on the sample, and knowledge of the sample-detector distance. This velocity is converted to energy with the energy-velocity relationship. In this time-of-flight approach, the final energies are most accurately measured when the sample-to-detector flight path is long. However, because of spatial and monetary constraints, the surface that can be covered with detectors is finite and there is thus a trade-off between the length of the flight path and the solid-angle coverage.

Another important parameter in neutron scattering experiment is the relatively low flux of neutron sources, especially when compared to x-ray sources. Because the density of neutrons in the beam is low (with particle densities on the order of a magnitude of a good vacuum), the dimensions of the beam tend to be large to compensate. This results in the need for large samples, with typical transverse sizes on the order of a few centimeters.

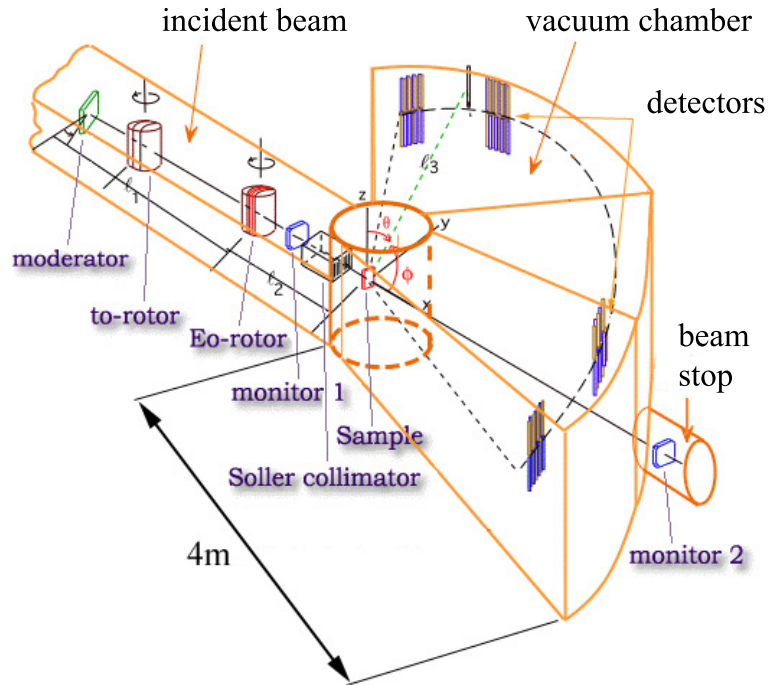


Figure 3.3: Direct-geometry time-of-flight neutron spectrometer.

Another aspect, resulting from this sample size, is that one needs to minimize multiple scattering events. Because the elastic cross-section is typically much larger than its inelastic counterpart (see examples below), multiple scattering events mostly involve several elastic scattering events or a combination of one elastic scattering and one inelastic scattering. Since the neutrons involved in an extra elastic scattering event travel extra distances inside the sample, they will reach the detector with a delay, thus appearing to have an extra energy loss. Multiple scattering is difficult to correct for and as a result one tries to limit the number of such processes by having samples that are thin enough. A typical working value is to make samples that scatter 10% of the incident neutrons, limiting double elastic scattering events to less than 1%. This has the unfortunate consequence that most of the already scarce incident neutrons are wasted. Such limitations are intrinsic to the neutron time-of-flight approach, until detectors with sufficient energy resolution are devised.

### 3.4.2 Sampling Region

Among the many different neutron scattering techniques, time-of-flight neutron spectrometry stands out as the best method to measure the phonon density of states. This technique allows one to sample large regions of  $\mathbf{q}$ -space (the reciprocal space of the sample). In the case of coherently scattering nuclei, the phonon dispersions can be accessed as well as the DOS. The possibility of collecting data over a large swath of reciprocal space at once is in fact the main strength of this technique, whereas more detailed studies of excitations at specific points in the Brillouin zone are perhaps best undertaken with a triple-axis spectrometer.

From the incident and final neutron energies and the scattering angle  $\Phi$ , the momentum transfer  $Q$  can be determined. In practice, one most often works with polycrystalline samples and only the magnitude of the momentum transfer is relevant,

$$Q = \left\{ \frac{1}{2.072} (2E_i (1 - \cos \Phi \sqrt{1 - \hbar\omega/E_i}) - \hbar\omega) \right\}^{1/2}, \quad (3.17)$$

where  $Q$  is in  $\text{\AA}^{-1}$  and the energies are in meV. The  $Q(\Phi, E)$  relation for the low-resolution medium-energy chopper spectrometer (LRMECS) instrument at the intense pulsed neutron source (IPNS) at Argonne National Laboratory is shown in figure 3.4, for different scattering angles covered by the detector bank.

From figure 3.4, one can see that the relevant range of phonon energies for a vanadium crystal is sampled with momentum transfer ranging from close to  $0 \text{\AA}^{-1}$  up to about  $8 \text{\AA}^{-1}$ . A spherical sampling region with such range is compared to the size of the first Brillouin zone for the vanadium reciprocal lattice in figure 3.5. In this figure, the sphere denotes the volume sampled by the neutrons and the central thick square is the Brillouin zone of the fcc reciprocal lattice. One can see on this figure that many Brillouin zones are sampled.

## 3.5 Data Analysis

Figure 3.6 presents typical results for  $S(E)$  obtained on a TOF instrument, after summing the data over  $\Phi$ . The first thing to note is the relative intensity of the elastic scattering (central peak) and inelastic scattering (side shoulders). As seen in the inset, the elastic scattering dominates by a factor of approximately 20 in this case. Also of interest is the

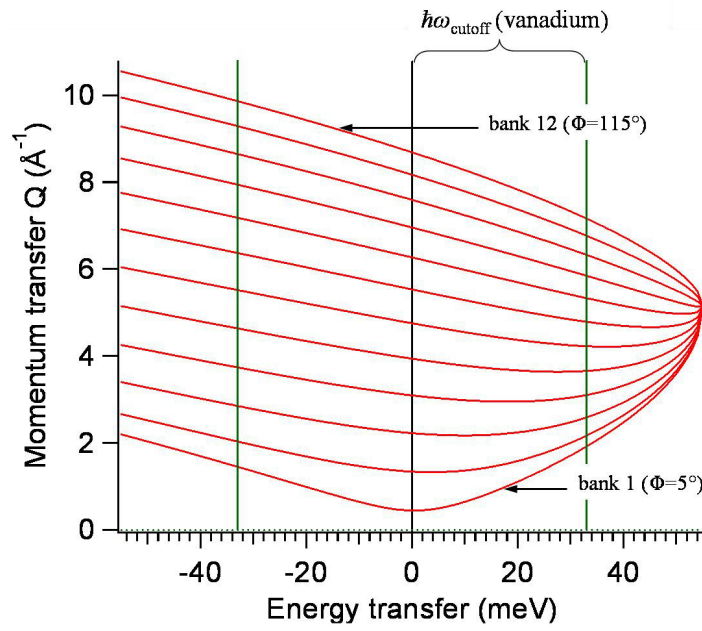


Figure 3.4: Scattering kinematics for LRMECS instrument with  $E_i = 55$  meV.

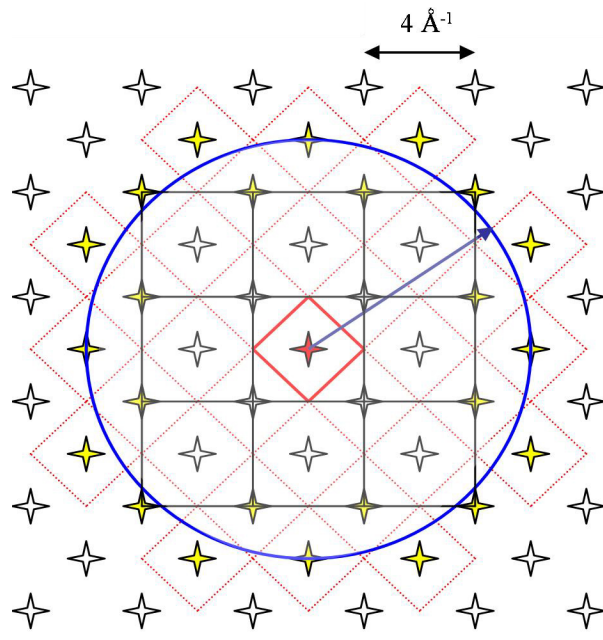


Figure 3.5: Sampling volume in reciprocal space for vanadium single crystal. Estimated for LRMECS instrument with  $E_i = 55$  meV.

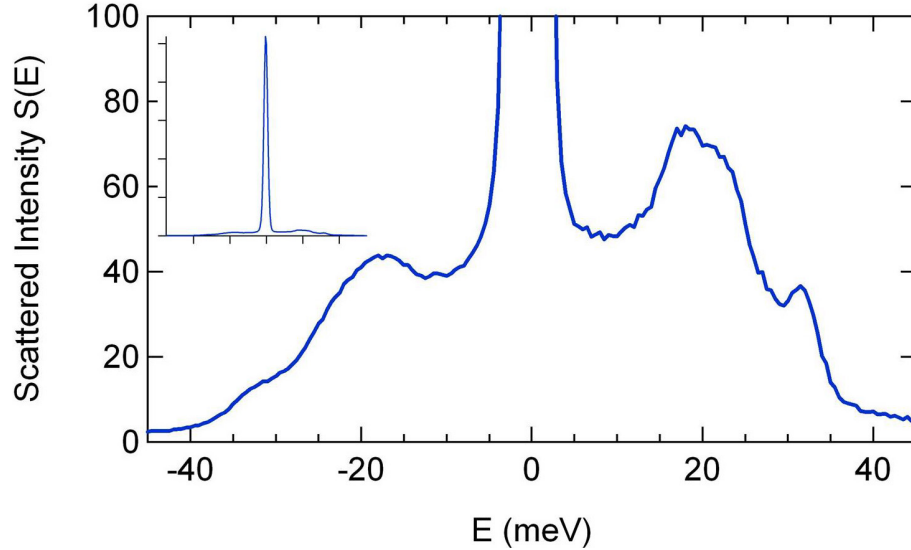


Figure 3.6: Scattering intensity  $S(E)$  for  $\text{Fe}_{71}\text{Ni}_{29}$  sample. Data measured on Pharos instrument at LANSCE.

symmetry observed in the data between positive energy transfers (phonon creation) and negative energy transfers (phonon annihilation). This symmetry is the direct consequence of the detailed balance principle. Considering two states between which the sample can transition, and assuming the *a priori* probabilities for an incident neutron to induce either transition (up or down in energy) to be equal, then the ratio of the cross-section for the two scattering events will be the ratio of the probabilities for the sample to be in either state initially. Thus the phonon annihilation process (down in sample energy) is less likely and

$$S(\mathbf{Q}, -E) = \exp(-E/k_{\text{B}}T) S(\mathbf{Q}, E). \quad (3.18)$$

Features on the negative energy transfer side are also broader, which is an effect of energy resolution. Because neutrons gain energy in these processes, their final velocities are higher and timing errors represent larger errors in energy.

### 3.5.1 Background

The first correction to apply to the data is to subtract a constant background due to extraneous events in the detector, as well as the signal due to the sample holder and sample

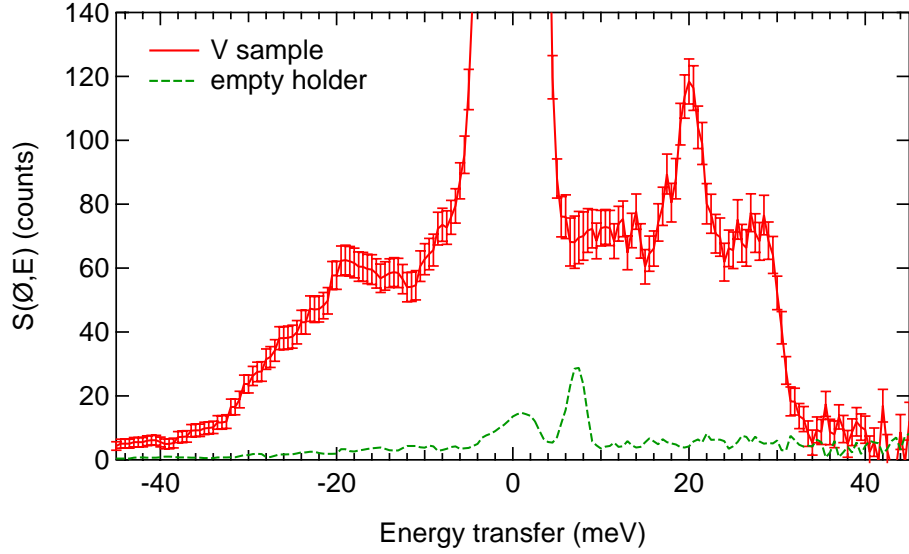


Figure 3.7: Scattering intensity  $S(\Phi, E)$  from V sample and empty holder. The data correspond to a constant scattering angle  $80^\circ \leq \Phi \leq 90^\circ$ . Data measured on LRMECS instrument at IPNS.

environment. A comparison of signal from the sample and from a typical aluminum encasing in a dispex environment is shown in figure 3.7. The peak around 7 meV in the background corresponds to diffraction from an Al window in the sample well, yielding a delayed elastic peak.

One can also note on this graph that  $S(\Phi, E)$  tends to a constant at low energy transfer, as expected from Eq. 3.14, since  $g \sim E^2$  and  $n(E) \sim kT/E$  at low  $E$ , so  $S(\Phi, E) \sim \text{constant}$ . The error bars in this graph represent counting statistics in the detector channels.

Once the background correction is performed, one can obtain the phonon DOS from the scattered intensity using Eq. 3.14, by dividing out the Bose-Einstein thermal occupation and the Debye-Waller factor as well as other prefactors. However, the Debye-Waller factor is not known *a priori*. Nevertheless it can be calculated from an estimated DOS, as

$$\begin{aligned}
 2W &= \frac{1}{3}Q^2\langle u^2 \rangle \\
 &= \frac{Q^2\hbar}{2M} \int_0^{\omega_{\max}} \coth(\hbar\omega/2kT)g(\omega)/\omega d\omega, \quad (3.19)
 \end{aligned}$$

with  $\langle u^2 \rangle$  the mean thermal displacement, in the approximation of a cubic Bravais crystal.

We can thus envisage an iterative solution converging on the Debye-Waller factor. An additional correction for multiphonon scattering is often needed and it can also be applied in this iterative scheme, as we now discuss.

### 3.5.2 Multiphonon Scattering

The cross-section for a one-phonon creation process is given by Eq. 3.14 and a similar expression for the one-phonon annihilation process. However, the experimentally measured cross-section also contains contributions from higher-order scattering events (for both annihilation and creation processes), which cannot be neglected at higher scattering vectors:

$$\left(\frac{\partial^2\sigma}{\partial\Omega\partial E}\right)_{\text{inelastic}}^{\text{inc}} = \sum_{n=1}^{\infty} \left(\frac{\partial^2\sigma}{\partial\Omega\partial E}\right)_{n\text{-phonon}}^{\text{inc}}. \quad (3.20)$$

We use the multiphonon correction procedure of Bogdanoff and Fultz [58], which we summarize below. The incoherent inelastic  $n$ -phonon double differential scattering cross-section is given, for TOF spectra measured at constant scattering angle, by:

$$\begin{aligned} \left(\frac{\partial^2\sigma}{\partial\Omega\partial E}\right)_{n\text{-phonon}}^{\text{inc}} &= \frac{\sigma^{\text{inc}} k_f N}{4\pi\hbar k_i n!} e^{-2W} \\ &\times \left(\frac{\hbar\kappa^2}{2M\omega}\right)^n P(\omega)^{(n)} \\ P(\omega) &= g(\hbar\omega)\langle n(\omega) + 1 \rangle - g(-\hbar\omega)\langle n(-\omega) \rangle, \end{aligned} \quad (3.21)$$

where the symbolic power notation  $f^{(n)}$  means the sequential convolution of  $n$  instances of the function  $f$ . Extracting the neutron-weighted phonon DOS thus involves a correction for multiphonon scattering, which contributes to the measured signal mostly at higher momentum transfers, as well as corrections for the Debye-Waller factor and the Bose-Einstein thermal occupation function. This is accomplished through an iterative procedure that calculates the  $n$ -phonon contributions to the scattering for each one of the angle banks, fits the sum of these contributions to the data and subtracts the  $n \geq 2$  phonon scattering contribution to obtain the single phonon spectrum from each bank. The multiphonon cross-section of Eq. 3.20 was truncated after the 5-th order in  $n$ , the  $n$ -phonon contribution to this sum becoming vanishingly small as  $n$  increases beyond small values. From the single-phonon

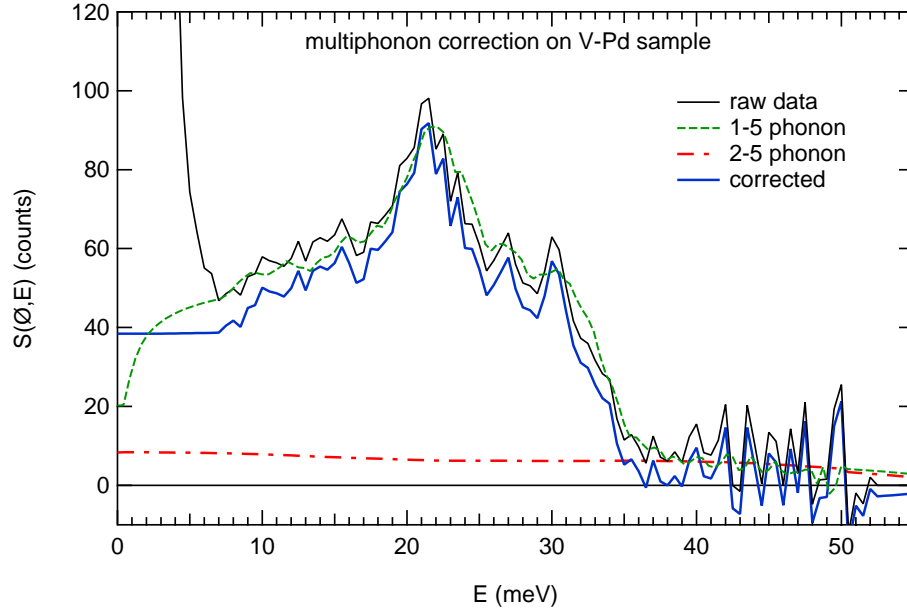


Figure 3.8: Multiphonon scattering correction for V-6.25%Pd sample at 295 K. The data correspond to a constant scattering angle  $80^\circ \leq \Phi \leq 90^\circ$ . Data measured on LRMECS instrument at IPNS.

scattering, the next iteration of the DOS is easily obtained by applying a correction for thermal occupation and taking into account the Debye-Waller factor, itself evaluated from the previous iteration of the DOS. This procedure is iterated until convergence is reached on the Debye-Waller factor and the DOS itself, yielding self-consistency between all the computed quantities. Convergence is often achieved in three or four iterations.

Results for a V-6.25%Pd polycrystalline sample are shown in figure 3.8. As seen in this example, the multiphonon contribution is mostly featureless, owing to the convolution products of (3.21). For the materials studied in this thesis, the correction is relatively minor at low temperatures, but becomes significant above room temperature.

### 3.5.3 Instrument Resolution

Typical instrument energy resolution functions are plotted in figure 3.9. One can see that instrument resolution gets worse with higher incident neutron energies. Also, the Pharos instrument has a better resolution than LRMECS because of its longer sample-to-detector flight path and higher-frequency Fermi chopper.

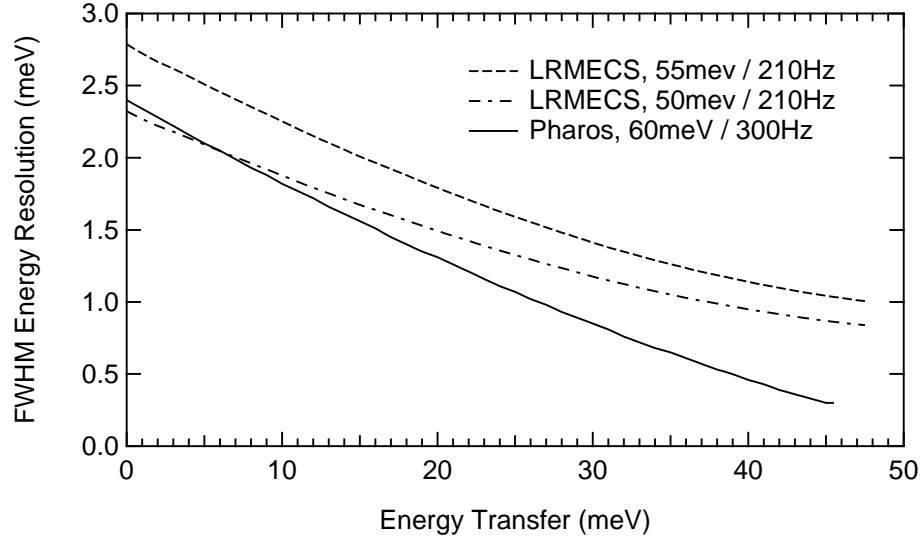


Figure 3.9: Energy Resolution for LRMECS and Pharos spectrometers. The resolution is the full width at half maximum (FWHM) of the line shape, for the instrument in the specified operating conditions.

### 3.5.4 Neutron-Weighting

Neutron-weighting is a thorny problem in time-of-flight neutron scattering investigations of alloys. Because different isotopes have different neutron cross-sections, the modes corresponding to the elements of higher cross-section are overemphasized over those of elements with lesser neutron scattering power, resulting in a weighting of the partial DOS components. We call this measured DOS a generalized phonon DOS (gDOS). In the incoherent scattering regime for an ordered structure, the weight associated with the vibrations of a given species in the crystal is  $(\sigma_{inc}/M) \exp(-2W)$ , with  $\sigma_{inc}$  the incoherent neutron scattering cross-section of the species,  $M$  its atomic mass and  $\exp(-2W)$  the Debye-Waller factor for this atom of the unit cell [13],[14]. Hence, the neutron-weighted phonon DOS is rigorously defined as

$$g_{NW}(E) \propto \sum_{\kappa} g_{\kappa}(E) \exp(-2W_{\kappa}) \exp(2W) \frac{\sigma_{\kappa}}{M_{\kappa}}, \quad (3.22)$$

where  $g_{\kappa}(E)$ ,  $\exp(-2W_{\kappa})$ ,  $\sigma_{\kappa}$  and  $M_{\kappa}$  are the partial phonon DOS, Debye-Waller factor, total scattering cross-section, and mass for atom  $\kappa$  in the basis. The Debye-Waller factor is an

explicit function of  $g_\kappa(E)$ . The term  $\exp(-2W)$  is the average Debye-Waller correction; this is calculated from the self-consistent neutron-weighted DOS. The factor  $\exp[2(W - W_\kappa)]$  is very close to unity, with a deviation typically smaller than a few percent.

Currently, there exists no general method to correct for the effects of neutron-weighting. Generally, we cannot solve the problem thus formulated as the number of undetermined variables is larger than the number of available equations. However, additional information can be obtained on the different components of the DOS, which sometimes involved well-chosen approximations. Several approaches have been adopted in this thesis, through computational modelling as well as by combining data from other techniques. These will be discussed in the following chapters.

## Chapter 4

# Effects of Alloying on Phonons in Vanadium

### 4.1 Introduction

Vanadium is an ideal element for measuring a phonon DOS since it scatters neutrons incoherently, and it has a cubic crystal structure (BCC). There is in this case a direct relationship between the inelastic neutron scattering cross-section and the phonon DOS, as discussed in chapter 3. These properties make polycrystalline vanadium especially suitable for phonon DOS measurements using a time-of-flight (TOF) neutron spectrometer.

Our interest in the phonons in V and its alloys is not fueled only by mere convenience, however. Several known properties of vanadium make it an interesting material in which to study phonons. First, V is one of the elements with the highest superconducting transition temperature ( $T_c = 5.3\text{K}$ ), which reveals the importance of electron-phonon interactions in this metal. Also, the elastic constants in BCC transition metals are known to vary systematically upon alloying, with a good correlation to the average electronic density per atom [59, 60, 61, 62]. This trend has been interpreted in terms of the electronic structure of BCC transition metals [63]. Also, some of the elastic constants in vanadium exhibit an anomalous temperature dependence [64], similarly to the other metals of column 5, Nb and Ta [65, 66], which is suppressed upon alloying [67]. The origin of this anomaly has also been traced to the electronic structure [66]. Since there is some correlation between the interatomic force-constants and the elastic moduli, it is interesting to see whether this behavior carries over to the phonon DOS, which is the central quantity in phonon thermodynamics. In this chapter, we concentrate on the effect of alloying on phonons at low (room) temperature.

The high-temperature phonon properties will be the topic of chapter 6.

Previous measurements of the phonon DOS in vanadium-based alloys have indicated a strong sensitivity of the phonons to impurities in vanadium. Neutron scattering measurements of the phonon DOS have been reported for the V-rich alloys V-Pt, V-Ta, V-W, V-Ni, and V-U [68, 69, 70, 71, 72], all in solid-solution with a few percent solutes. Although quite interesting, these older measurements focused on the dynamics of resonance modes and lacked the reliability necessary to allow for the investigation of phonon thermodynamics. In particular, the phonon densities of states for pure V show marked deviations between the different results reported.

In the following, we report a systematic investigation of phonons and vibrational entropy in dilute V-X alloys for a large number of solute elements and we examine the emerging chemical trends. A clear trend is observed for solutes across the  $d$ -series: impurities to the left of vanadium induce a softening of the phonon modes while those to the right cause a stiffening that is gradually increasing with their number of  $d$ -electrons. This trend is robust and applies to large and heavy impurities of the  $4d$ - and  $5d$ -series as well as those of the  $3d$ -series. This trend goes against what might be expected based on mass considerations. For heavy impurities such as Pd and Pt, one might expect an overall softening of the phonon modes in the alloy, but this is not observed and instead there is a large overall stiffening of the phonon DOS. Our results thus show that the mass effect is small compared to the effect of the changes in the interatomic force-constants due to the rearrangement of the electronic structure. The difference in electronegativity between the impurity and the host is identified as a good parameter to parameterize the stiffening in the phonon DOS and the vibrational entropy of alloying. Electronegativity differences point to the role of charge transfer, which is investigated using first-principles calculations in the following chapter.

## 4.2 Experimental Details

### 4.2.1 Sample Preparation and Characterization

The alloys investigated and some of their relevant properties are listed in table 4.1. The samples were prepared from slugs of vanadium of 99.8% purity or better, and alloying

elements of purity better than 99.9%. The elemental components were weighed with a precision scale to obtain the desired compositions. Several ingots were synthesized for each material by arc-melting the elemental metals under ultra-high-purity Ar atmosphere. A Ti getter ingot was melted in the chamber to remove trace amounts of oxygen. Each sample ingot was flipped in the crucible and melted thoroughly several times to ensure good homogeneity. The mass loss upon arc-melting was measured on each ingot and found to be small to negligible in all cases. From the measured mass loss, we estimated an upper bound on the deviation to the nominal alloy compositions listed in table 4.1 of at most 0.2%. The samples showed no trace of surface oxidation. The ingots were subsequently cold-rolled to the desired thickness in order to produce neutron scattering samples with 10% total scattering cross-section, with the exception of V-Zr and V-Hf samples, which were crushed to form granules of the appropriate size. The elemental vanadium control sample was prepared by directly rolling the pure V shots. All the alloys were then recrystallized at 1000° C for an hour under Ar atmosphere and quenched into ice-brine. There was only minimal surface oxidation on the samples after heat treatment, which was easily removed on all the cold-rolled samples by a slight mechanical polishing. The Rockwell hardness, measured before and after heat treatment on several of the alloys (V-Ni, V-Pd, V-Pt), showed a large softening characteristic of recrystallization.

X-ray diffractometry with Co  $K\alpha$  radiation was performed on all samples using an Inel CPS-120 position sensitive detector. The diffraction patterns showed that all samples were BCC solid solutions with no chemical long-range order. Lattice parameters were obtained from x-ray diffraction patterns measured with a Philips X'Pert series diffractometer using a Cu  $K\alpha$  x-ray source. The densities of the samples were measured using Archimedes' method, from which a second value of lattice parameter was derived. The experimental lattice parameters are plotted in figure 4.1.

Our results indicate almost no change in lattice parameter for the alloys V-6.25%Pd and V-6.25%Pt. This is in good agreement with the XRD results of Daumer *et al.*, who found almost no change in lattice parameters for the solid-solutions V-10%Pd and V-10%Pt [73]. Our results for V-6.25%Nb and V-6.25%Ta are also in good agreement with the values reported by these authors, after a correction for the difference in composition. For impurities

Table 4.1: Samples prepared and relevant physical properties.

X	$c_X$ (% at.)	$M_X$ (a.u.)	$r_m^{\text{BCC}}$ ( $\text{\AA}$ )	$\chi$ Pauling	$a(\rho)$ ( $\text{\AA}$ )	$a$ (XRD) ( $\text{\AA}$ )	$\sigma_X^{\text{scat}}/M_X$ (barn)
	0	50.94	1.310	1.63	$3.032 \pm 0.002$	3.029	0.100
Ti	6.25	47.87	1.422	1.54	$3.045 \pm 0.003$	3.039	0.091
Cr	6.25	51.99	1.248	1.66	$3.020 \pm 0.002$	3.017	0.067
Fe	6.25	55.85	1.240	1.83	$3.008 \pm 0.002$	3.011	0.208
Co	6.25	58.93	1.219	1.88	$3.007 \pm 0.002$	3.009	0.096
Co	2.00	58.93	1.219	1.88	$3.022 \pm 0.002$	— — —	0.096
Ni	6.25	58.69	1.213	1.91	$3.013 \pm 0.002$	3.012	0.316
Zr	6.25	91.22	1.558	1.33	— — —	— — —	0.071
Nb	6.25	92.91	1.428	1.60	$3.051 \pm 0.003$	— — —	0.067
Pd	6.25	106.42	1.339	2.20	$3.030 \pm 0.004$	3.026	0.042
Hf	6.25	178.49	1.537	1.30	— — —	— — —	0.057
Ta	6.25	180.95	1.427	1.50	$3.047 \pm 0.005$	— — —	0.033
Pt	6.25	195.08	1.350	2.28	$3.034 \pm 0.004$	[3.024]	0.060

along the  $3d$ -series, the lattice parameter  $a$  shows first a linear contraction from Ti to V to Cr, followed by a plateau for Fe and Co and finally a slight increase in  $a$  from V-6.25% Co to V-6.25%Ni. We also plotted in figure 4.1 the lattice parameters for more concentrated V-Cr alloys derived from the density measurements of Lenkkeri *et al.* as the thick dashed line [61]. For all concentrations of Cr in V the lattice parameter varies linearly, which is not the observed behavior for later transition metal impurities at the constant alloy concentration of 6.25%. This explicitly shows the difference between a rather homogeneous system such as V-Cr, which exhibits a linear trend as function of composition, and the more dilute V-X system we investigate, in which effects are more localized and dependent on the properties of the impurity element.

A comparison of the lattice parameter in the V-6.25%X alloys with the metallic radii  $R_m$  for the pure elements in BCC coordination determined by Teatum and Gschneider [74] reveals a good correspondence. The relative difference in  $R_m$  between the solutes and vanadium is plotted in figure 4.2. As seen in this figure, the contraction of  $R_m$  along the  $d$ -series explains in part the trend observed in the lattice parameter of the random solid-solutions. A good estimate of the lattice parameter in the alloy is given by dividing this  $\Delta R_m/R_m$  of the solute by 16 to get the average change in size per atom in the solution (Vegard's law). The result of this calculation is indicated by the crosses in Fig. 4.1.

#### 4.2.2 Elastic Moduli

The elastic moduli were measured using an ultrasound pulse-echo technique on the annealed samples. The shear modulus  $G = \rho c_T^2$  and bulk modulus  $B = \rho c_L^2 - \frac{4}{3}G$  were obtained from measurements of the transverse ( $c_T$ ) and longitudinal ( $c_L$ ) sound velocities, which were performed using 5 MHz transducers. The sound velocities and elastic moduli could not be obtained in this way for the V-Zr and V-Nb alloys, because the samples for these alloys were prepared in the form of coarse-grained powders. Results for  $B$  and  $G$  are listed in Table 4.2. Two sets of measurements were performed with different ultrasonic setups. The second set of measurements is considered more accurate since it used an oscilloscope with a higher sampling rate. Figure 4.3 shows the relative change in moduli for solutes across the  $3d$ -series.

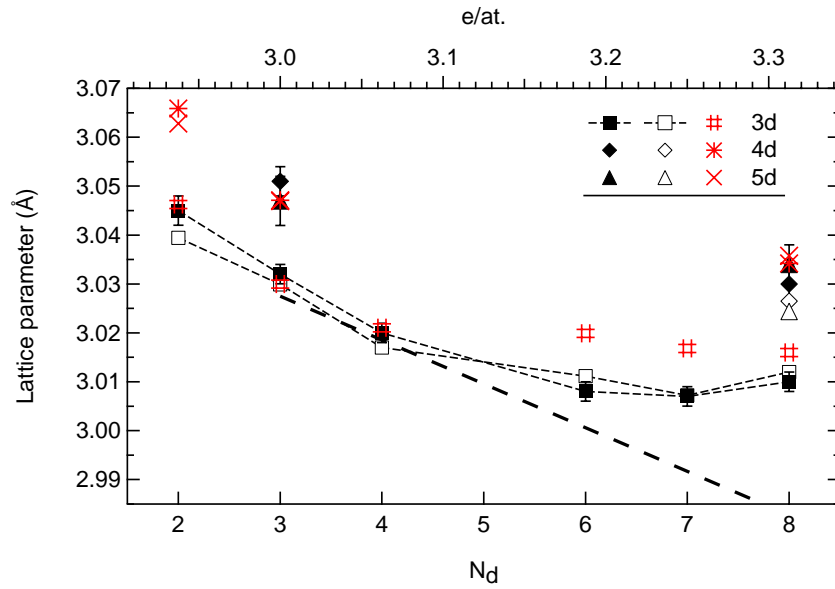


Figure 4.1: Experimental lattice parameters. Solid symbols: density measurements, open symbols: XRD. Crosses and stars: values calculated from the metallic radii of Teatum [74]. Thick dashed line: density measurements of Lenkkeri *et al.* on V-Cr alloys [61], plotted versus electron concentration  $e/at.$

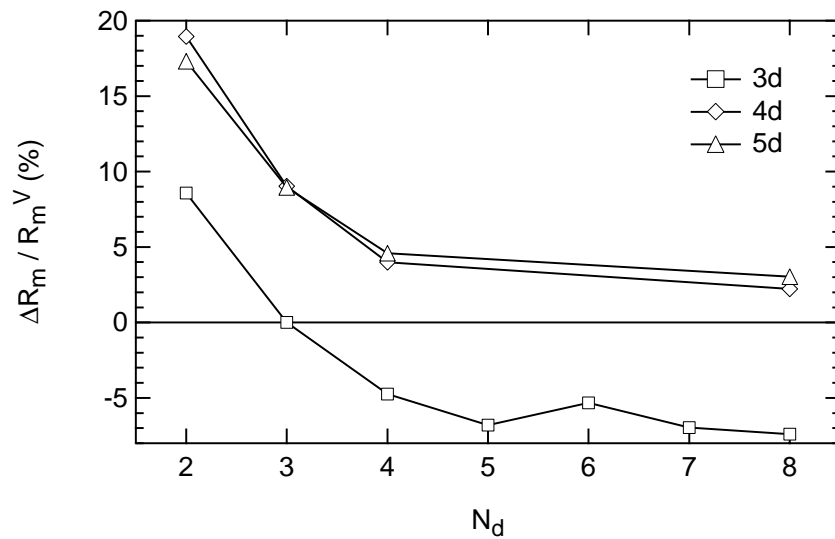


Figure 4.2: Metallic radius of transition metals with BCC coordination, after Teatum and Gschneider [74].

Table 4.2: Elastic moduli.

composition	set 1		set 2	
	$G$ (GPa)	$B$ (GPa)	$G$ (GPa)	$B$ (GPa)
V	$46.0 \pm 0.7$	$149 \pm 7$	$48.1 \pm 0.2$	$163 \pm 1$
$V_{93.75}Ti_{6.25}$	-	-	$45.2 \pm 0.3$	$163 \pm 1$
$V_{93.75}Cr_{6.25}$	-	-	$49.2 \pm 0.3$	$176 \pm 2$
$V_{93.75}Fe_{6.25}$	-	-	$51.7 \pm 0.3$	$172 \pm 1$
$V_{93.75}Co_{6.25}$	-	-	$52.5 \pm 0.4$	$173 \pm 2$
$V_{93}Co_7$	$51.3 \pm 1.1$	$154 \pm 8$	-	-
$V_{93.75}Ni_{6.25}$	$48.6 \pm 0.9$	$163 \pm 8$	$50.8 \pm 0.3$	$168 \pm 1$
$V_{93.75}Nb_{6.25}$	-	-	$47.1 \pm 0.2$	$165 \pm 1$
$V_{93.75}Pd_{6.25}$	$53.4 \pm 0.9$	$150 \pm 6$	$56.2 \pm 0.3$	$168 \pm 1$
$V_{93.75}Ta_{6.25}$	-	-	$49.6 \pm 0.3$	$178 \pm 2$
$V_{93.75}Pt_{6.25}$	$59.3 \pm 1.0$	$167 \pm 7$	$61.7 \pm 0.4$	$176 \pm 2$

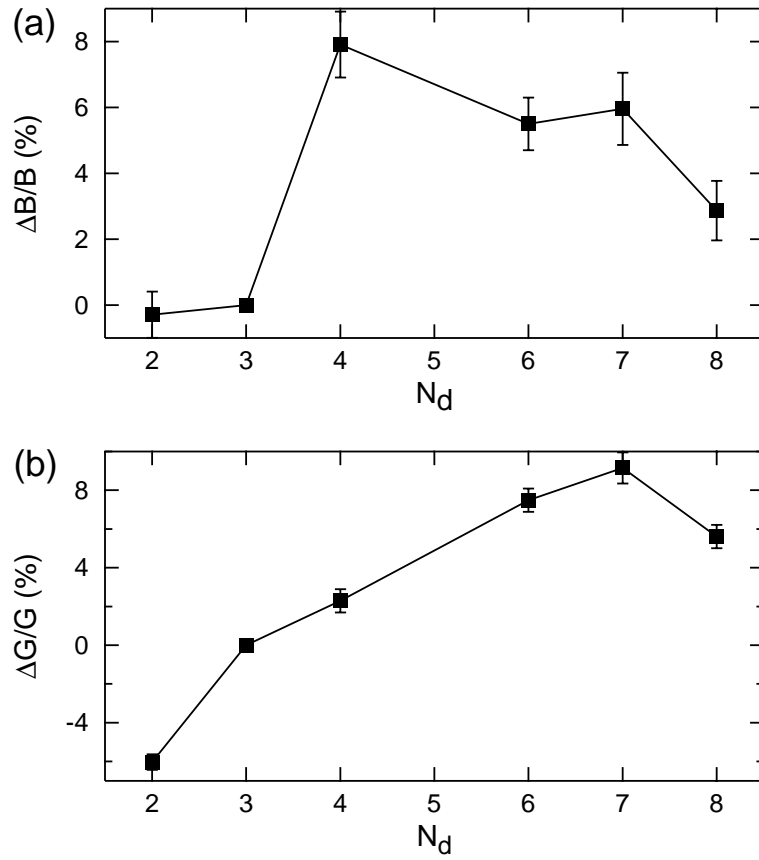


Figure 4.3: Change in bulk and shear moduli in V-6.25%X upon alloying. (a) Change in bulk modulus  $B$  for solutes across the  $3d$ -series, (b) change in shear modulus  $G$  for impurities across the  $3d$ -series. Error bars are experimental errors from ultrasonic measurements.

A clear trend is observed in the shear modulus  $G$  for alloys of vanadium with  $3d$ -series impurities. For Ti impurities, the shear modulus is softer by about 6%, while for impurities with more  $d$ -electrons than vanadium, the shear modulus stiffens. This stiffening in  $G$  increases with the number of  $d$ -electrons of the impurity up to Co impurities, for which 9% stiffening is observed, then decreases in the case of Ni, which induces about 6% stiffening. A similar trend is seen in the variation of the bulk modulus  $B$ , with Ti inducing softening, while elements to the right of vanadium induce a stiffening of the alloy bulk modulus. The stiffening of  $B$  is very similar to that observed for  $G$  in the case of Fe, Co and Ni solutes. On the other hand, in the alloy  $V_{93.75}Cr_{6.25}$ , the stiffening seems much larger for  $B$  than for  $G$ , but it could be due to experimental inaccuracies, and it is still compatible with the trend observed for other solutes.

Down the Ni column, we observe a large and systematic increase in  $G$ , with 10% increase from  $V_{93.75}Ni_{6.25}$  to  $V_{93.75}Pd_{6.25}$  and again from  $V_{93.75}Pd_{6.25}$  to  $V_{93.75}Pt_{6.25}$ . On the other hand,  $B$  only shows a modest increase down this column.

### 4.2.3 Inelastic Neutron Scattering

Time-of-flight inelastic neutron scattering spectra were measured with the LRMECS chopper spectrometer, at the IPNS spallation neutron source at Argonne National Laboratory. Additional measurements for V, V-Nb and V-Pt were performed on the Pharos chopper spectrometer at the Los Alamos Neutron Science Center (LANSCE). The neutron scattering samples were assembled by tiling the specimens into mosaic plates of uniform thickness of dimension 7.5 cm by 10 cm (5 cm by 7 cm for Pharos), and encasing them in neutron-transparent thin-walled aluminum pans. The samples were mounted directly onto the sample holder of the spectrometer, and positioned at 45 degrees with respect to the incident beam (in transmission geometry) to minimize self-shielding. For our samples, this configuration resulted in about 10% scattering of incident neutrons for both elastic and inelastic processes, the probability of scattering through inelastic processes being much smaller, however. All measurements were conducted under vacuum with the samples at room temperature. The detector coverage of the LRMECS spectrometer ranges from  $3^\circ$  to  $117^\circ$ , allowing measurements over a wide range of momentum and energy transfers. The

detector coverage on Pharos is even larger, extending from  $-10^\circ$  to  $145^\circ$ . In our first experiment on LRMECS, for the measurement of V, V-Ni, V-Pd, and V-Pt samples, the instrument choppers were set to produce a monochromatic incident energy of  $E_i = 55$  meV. In the second LRMECS experiment, during which the remaining alloys were measured, the incident energy was  $E_i = 50$  meV. At these incident energies, the scattered neutrons measured correspond to a momentum transfer  $k$  varying between about 0.5 and  $9 \text{ \AA}^{-1}$  at zero energy transfer. This corresponds to an average sampling in reciprocal space covering many Brillouin zones of the reciprocal lattice for all the samples. During the Pharos experiments, the incident energies were set to  $E_i = 75$  meV (V-Pt) and  $E_i = 70$  meV (V-Nb). The range of momentum transfers sampled in the Pharos runs exceeds that in the LRMECS measurements. The LRMECS instrumental energy resolutions for the two incident energies are plotted in figure 3.9. The FWHM energy resolution of the LRMECS spectrometer in the run conditions is about 2.5 meV at the elastic line, smoothly decreasing to about 1.0 meV at 40 meV energy transfer. Typically, data were acquired on each sample (alloys and V control sample) for about 8 hours to ensure good statistics. The background scattering from the empty Al pan was measured for the same amount of time. The response from the  $^3\text{He}$  detector tubes was calibrated with a standard procedure using a pure vanadium sample illuminated with a “white” neutron beam, without the Fermi chopper.

## 4.3 Data Analysis

### 4.3.1 Density of States

The time-of-flight neutron spectra were first normalized with respect to the cumulated incident intensity and corrected for detector efficiency as well as time-independent background following standard procedures. The detector counts were summed into 7 angle banks, corresponding to  $10^\circ$  scattering angle ranges, covering the range  $50^\circ$  to  $117^\circ$ . The contribution to the background due to the Al sample container and sample environment was subtracted using the data collected on the empty sample pan. Only the positive part of the spectra was conserved, corresponding to energy gained by the sample, since the statistics and energy resolution on this side of the elastic line were much better. The data below 7 meV are dom-

inated by the large elastic scattering peak, which was stripped by keeping the data constant at low energy, as the neutron scattering function is proportional to  $g(\hbar\omega)/\omega^2$  and thus tends to a constant in the limit of low energy transfer  $\hbar\omega \rightarrow 0$ . The neutron-weighted phonon density of states was determined in all cases following the procedure described chapter 3. The final phonon DOS curves were all normalized to unity.

### 4.3.2 Neutron-Weighting

The data were analyzed in the virtual crystal and incoherent-scattering approximations to obtain the neutron-weighted phonon DOS. We expect the incoherent scattering approximation to be valid in the case of random substitutional alloys of vanadium. First, the vanadium host crystal scatters neutrons almost purely incoherently, its coherent cross-section accounting for less than  $4 \times 10^{-3}$  of its total neutron scattering cross-section [75]. Second, the impurity elements, although their scattering cross-sections have a coherent component [75], only contribute to the incoherent signal, since they are distributed randomly, thus preventing any global interference between the scattered neutron waves. Because of this, one should be careful to consider the total scattering cross-section for the impurities,  $\sigma_{\text{scat}} = \sigma_{\text{coh}} + \sigma_{\text{inc}}$ .

Table 4.1 summarizes the neutron scattering properties of the elements present in our samples. As seen in this table, the neutron-weight ratios,  $\sigma/M$  for the solute atoms deviate from the value for vanadium by a factor of 3 on either side. This neutron-weighting can affect the inelastic energy spectra measured experimentally, if the partial DOS for the impurity differs markedly from that for the host, as discussed in chapter 3. However, for the low concentrations of substitutional impurities considered here, the overall bias compared to the true phonon DOS is expected to be small. Nevertheless, a correction for this effect was performed for the alloys potentially affected the most. A quantitative estimate of this effect on the measured vibrational entropy is thus derived.

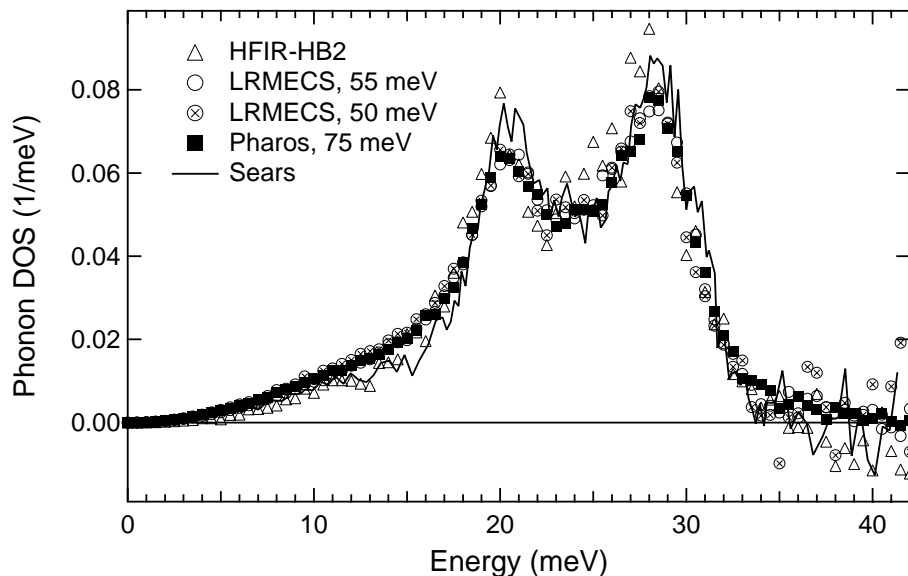


Figure 4.4: Pure Vanadium phonon DOS. Comparison of different measurements and published results of Sears [76].

## 4.4 Phonon DOS

### 4.4.1 Pure Vanadium

The results of our measurements for the phonon density of states of pure vanadium are shown in figure 4.4, where they are compared with the previous measurement of Sears [76] and the measurement of Bogdanoff *et al.* [77]. As can be seen in this figure, the results of our different measurements for pure vanadium on Pharos and LRMECS yielded phonon DOS curves that are in very good agreement with each other, as well as with the previous measurement of Sears, carried with a triple-axis spectrometer in constant- $Q$  mode [76]. The phonon DOS for pure V measured by Bogdanoff *et al.* [77] using the HFIR-HB2 triple-axis spectrometer at Oak Ridge National Laboratory shows more scatter, but it is nevertheless in good agreement with our time-of-flight results.

### 4.4.2 Trend Across the 3d-Series

Our result for the vanadium phonon DOS and the neutron-weighted phonon DOS of V-6.25%X, with X a 3d-series solute, are shown in figure 4.5. The average phonon frequencies

for all the alloys are listed in table 4.4.

The neutron-weighted phonon DOS curves for these alloys show a systematic stiffening from the case of V-6.25%Ti to the case of V-6.25%Ni. In the case of Ti impurities, the phonon DOS is softer than in pure V. All modes appear shifted to lower energies, with a maximum shift of about 2 meV, on the lower energy side of the transverse peak. The longitudinal peak and the cutoff frequency appear shifted down by about 1 meV. In the case of Cr, Fe, Ni, and Co impurities, the phonon DOS is stiffer than in pure vanadium and this stiffening is gradually increasing along the  $3d$ -series. The upward energy shift affects all the modes in these alloys and the cutoff shift goes from about 1 meV in the case of Cr to about 2.5 meV in the case of Ni. Another observed trend is that impurities that induce the larger shifts of the phonon DOS also affect its shape the most and in particular the transverse and longitudinal peaks appear to coalesce for the impurities with higher atomic number (Fe, Co, Ni).

#### 4.4.3 Trend Down the Ti Column

Our measurements for the alloys of vanadium with Ti, Zr, and Hf are shown in figure 4.6. All these solutes induce a softening in the phonon DOS, compared with pure V. The softening increases when going down the column from Ti to Hf. This is best seen at low energies, between 8 and 17 meV and around the cutoff energy. Since these impurities are isoelectronic, this trend can be associated with the increase in mass of the impurity down the column, as well as the increase the size of the impurity, which induces a larger average lattice parameter for the alloy (0.3% increase in the case of Ti, see table 4.1). Also, in the case of Zr and even more so for Hf, the partial phonon DOS for the impurities is likely to exhibit a resonance mode at low energies, due to the high impurity/host mass ratio (1.8 and 3.5, respectively). We discuss such resonance modes for Pd and Pt impurities (mass ratios of 2.1 and 3.8, respectively) below.

#### 4.4.4 Trend Down the V Column

Figure 4.7 shows our results for the phonon DOS of the isoelectronic alloys V-Nb and V-Ta. Niobium and tantalum impurities have a remarkably small effect on the vanadium

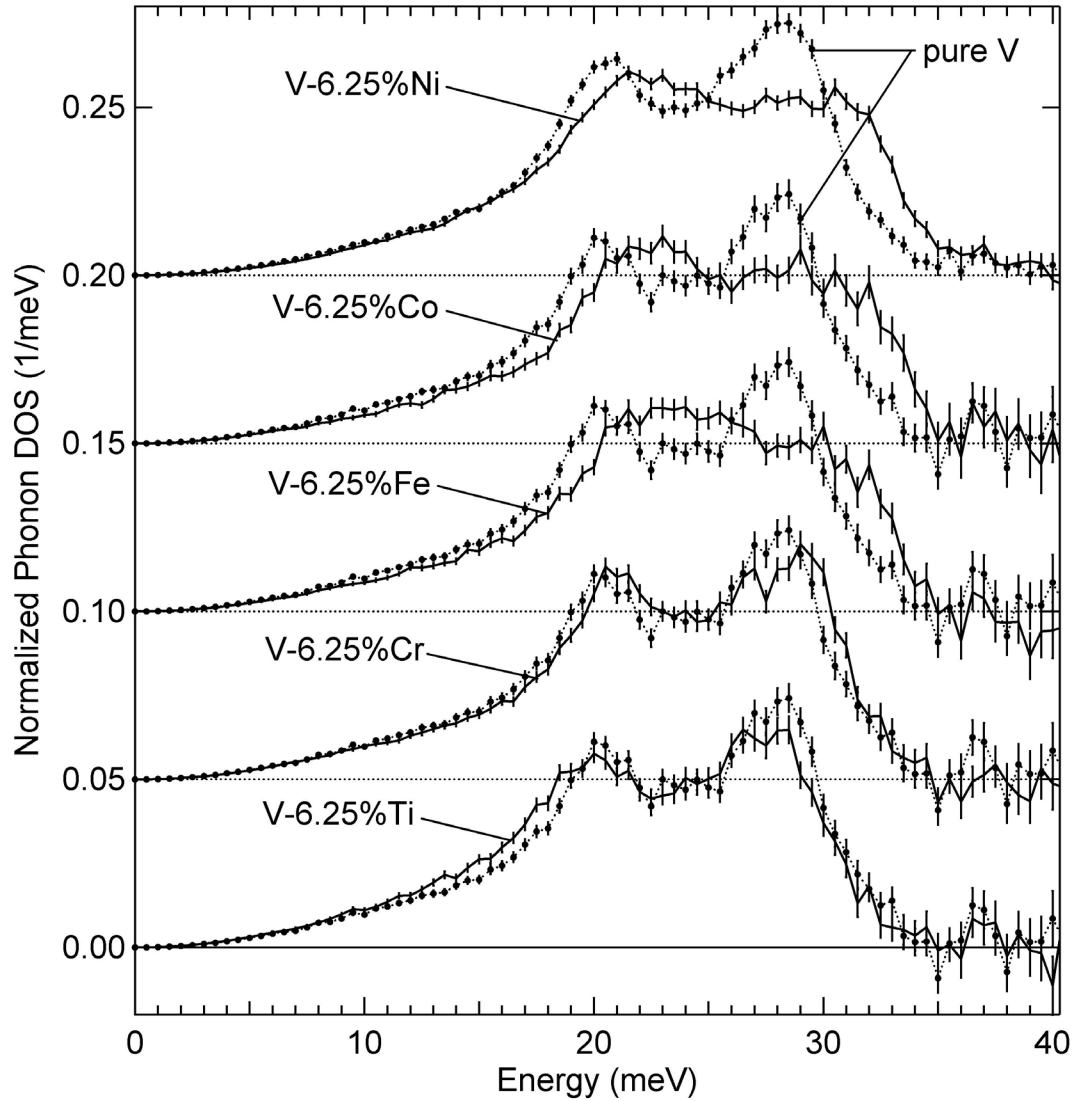


Figure 4.5: Neutron-weighted Phonon DOS for impurities across the  $3d$ -series measured on LRMECS. Broken traces: pure vanadium, solid lines: V-6.25%X.  $E_i = 50$  meV, except for top curves where  $E_i = 55$  meV.

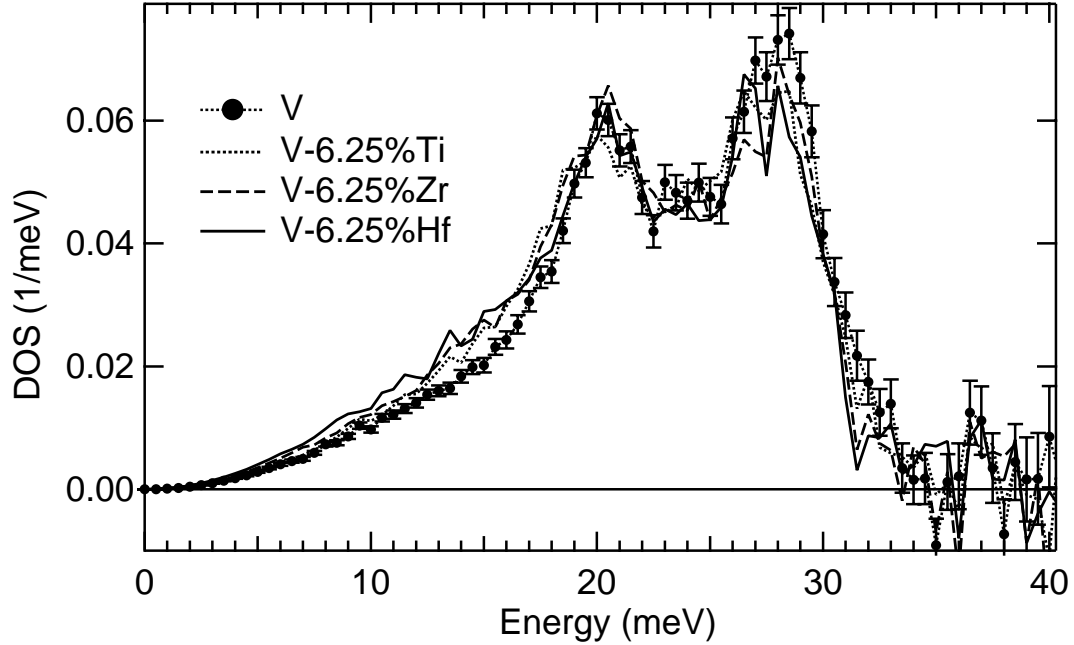


Figure 4.6: Neutron-weighted Phonon DOS for impurities down the Ti column measured on LRMECS,  $E_i = 50$  meV.

phonon DOS. Nb induces a slight softening of about 0.5 meV at the cutoff as well as on the low-energy side of the transverse peak. On the other hand, Ta solutes seem to have no detectable effect on the V phonon DOS, within our experimental error bars. This is surprising considering the impurity/host mass ratio in excess of 3.5 in this case. However, it is possible that this is an artifact due to the stronger neutron-weighting for Ta impurities, with Ta modes scattering neutrons three times more weakly than vanadium modes (see the  $\sigma^{\text{scat}}/M$  ratios in Table 4.1). Nevertheless, the overall effect of Ta solutes on the phonon DOS appears to be very weak.

#### 4.4.5 Trend Down the Ni Column

Ni, Pd and Pt impurities have the strongest effect on the V phonon DOS. The curves plotted in figure 4.8 are the neutron-weighted DOS curves for V-6.25%Ni, V-6.25%Pd, V-6.25%Pt and V. Ni, Pd and Pt impurities induce a large stiffening of the vanadium phonon DOS, which is gradually increasing from the case of Ni to that of Pd and Pt. The shift of the cutoff is about 2.5 meV in the case of Ni and almost 4 meV in the case of Pt. The pure V

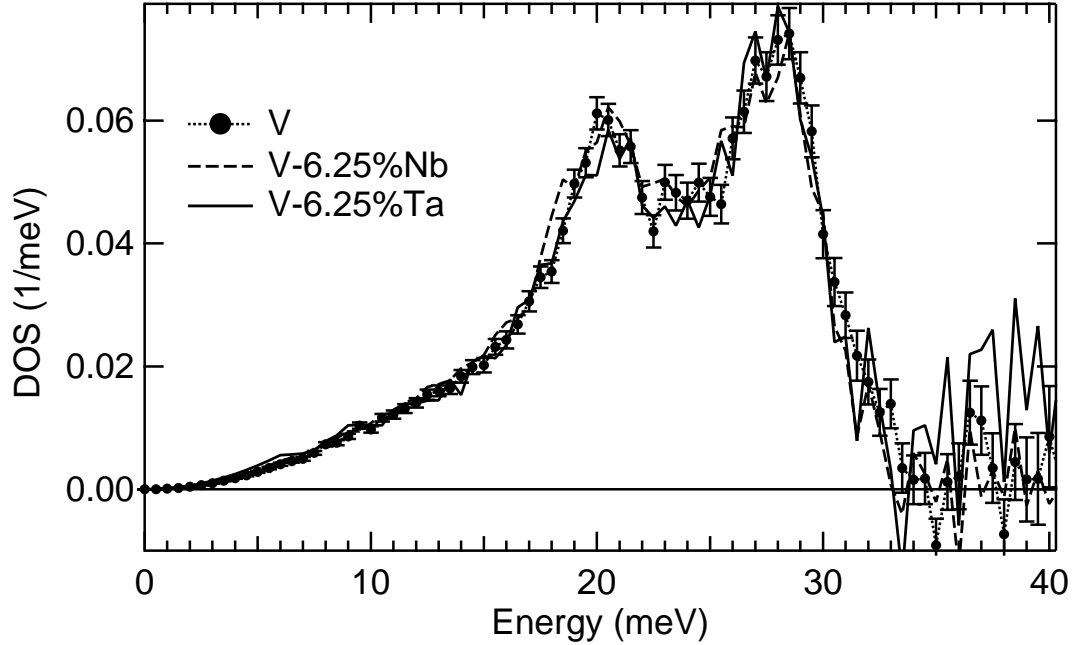


Figure 4.7: Neutron-weighted Phonon DOS for impurities down the V column measured on LRMECS,  $E_i = 50$  meV.

and V-6.25%Pt measurements using Pharos are shown in figure 4.9. As can be seen on this figure, the agreement between the LRMECS and Pharos measurements is excellent. In all the alloys down the column, the shift affects the full DOS rather uniformly, although there is also some restructuring of the phonon spectrum, with the transverse and longitudinal peaks coalescing in the alloys. Also, we show below using a Born–von Kármán lattice dynamics model that Pd and Pt impurities exhibit resonance modes around 12 meV. However, these modes only affect a small portion of the total DOS for impurity concentrations of 6.25%. Hence the neutron-weighting does not affect the general shape of the total phonon DOS significantly and has a minor effect on the calculated vibrational entropy, as discussed in the following.

#### 4.4.6 Concentration Dependence in V-Co

We investigated the dependence of the phonon DOS on the concentration of Co impurities. The V-Co system is particularly suitable for this type of study, as it is almost free of neutron-weighting, and Co impurities induce a significant distortion of the phonon DOS. The alloys

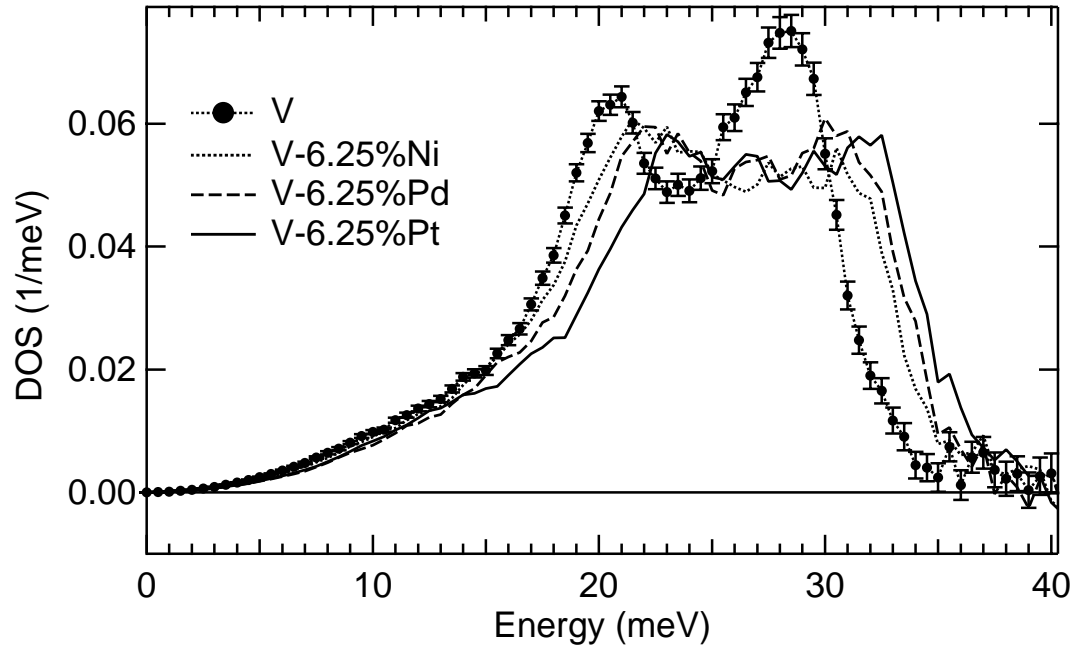


Figure 4.8: Neutron-weighted Phonon DOS for impurities down the Ni column measured on LRMECS,  $E_i = 55$  meV.

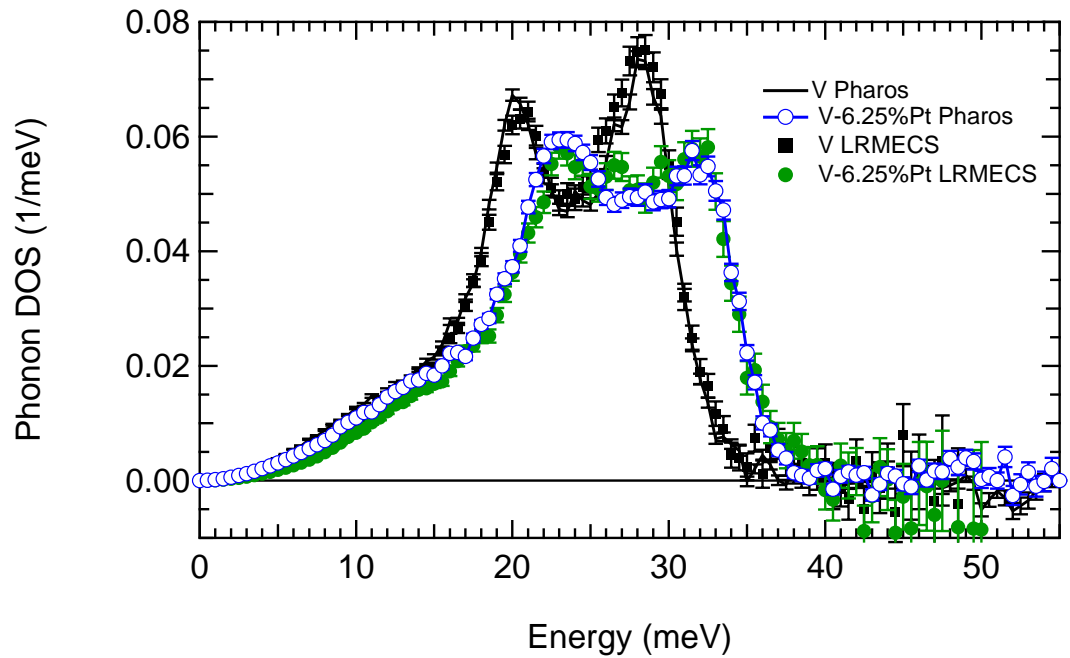


Figure 4.9: Neutron-weighted Phonon DOS for V and V-6.25%Pt measured on LRMECS ( $E_i = 55$  meV) and Pharos ( $E_i = 75$  meV).

V-6.25%Co and V-2.0%Co were measured on the LRMECS time-of-flight spectrometer, together with the reference V sample, while the alloy V-7.0%Co and a pure V reference were measured with the HB-2 triple-axis spectrometer at HFIR (Oak Ridge National Laboratory). The triple-axis data are unpublished results measured by P.D. Bogdanoff, B. Fultz *et al.* with the experimental conditions described in [77]. The phonon DOS for the alloys and control samples are shown in figure 4.10. As seen in this figure, the addition of Co impurities in V causes a gradual stiffening of the phonons. The data from LRMECS show that the stiffening increases in proportion to the impurity concentration. The data for V-7.0%Co show a much bigger stiffening than those for V-6.25%Co. Although we cannot rule out the possibility of stronger impurity dependence of the DOS from 6.25% to 7.0% impurity, this seems rather unlikely considering the small difference in overall concentration. Besides, the random solid-solutions will present concentration fluctuations that will make the two materials locally very similar. It is possible that a small amount of a second phase is present in the V-7.0%Co alloy, but we think that the difference comes in part from the different sampling of reciprocal space between the time-of-flight and triple-axis measurements.

## 4.5 Born–von Kármán Inversions

Fitting a Born–von Kármán lattice-dynamics model to the data allowed us to calculate phonon DOS curves for the alloys free of neutron-weighting and their corresponding difference in vibrational entropy with pure vanadium. The refined atomistic lattice dynamics model also provides valuable insight into the change in interatomic force-constants upon alloying, identifying the origin of the change in vibrational entropy. We conducted such a Born–von Kármán analysis on the alloys V-6.25%Ni, V-6.25%Pd and V-6.25%Pt, which exhibit the biggest effect of impurities on the phonon DOS. Also, these samples present possibly the strongest neutron-weighting effect in the series of alloys we studied, so the quantitative assessment of neutron-weighting on the phonon DOS and vibrational entropy is of particular interest.

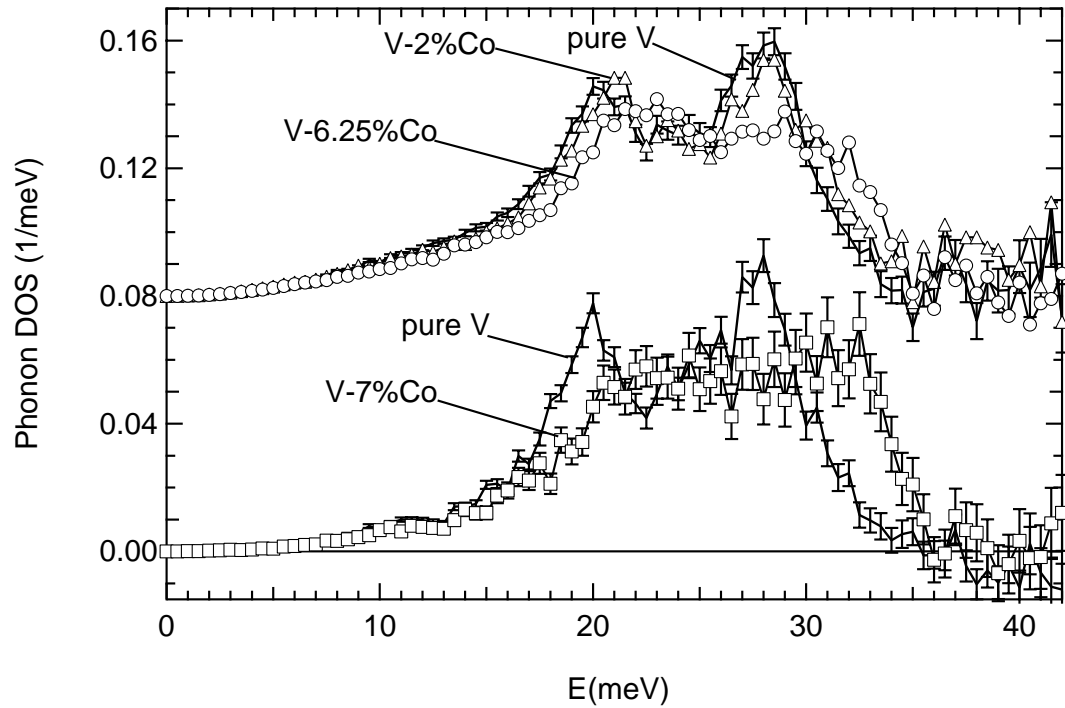


Figure 4.10: Phonon DOS for V-Co alloys of different composition. The top curves are from measurements on the LRMECS time-of-flight spectrometer,  $E_i = 50$  meV. The bottom curves are from unpublished measurements by P.D. Bogadanoff and B. Fultz on the HB-2 triple-axis spectrometer at HFIR.

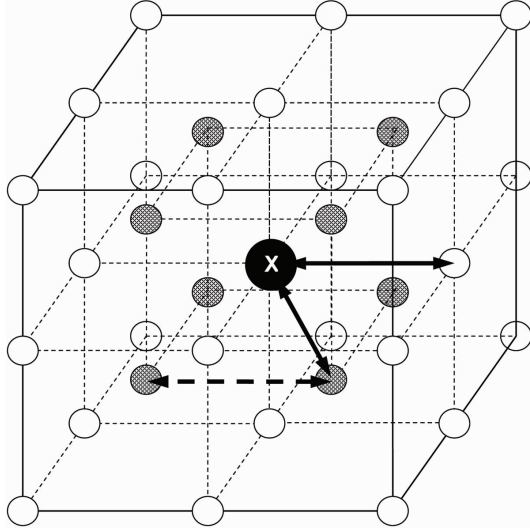


Figure 4.11: Supercell model used in lattice dynamics inversions. The central black circle is the solute atom X. Small dark atoms are 1NN vanadium atoms. Arrows indicate the bonds whose force-constants were optimized in the simulation. Solid arrows: X-V force-constants. Dashed arrow: V1-V1 force-constants.

#### 4.5.1 Lattice Dynamics Model and Fitting Procedure

The lattice dynamical model we employed to calculate the phonon DOS was based on a 16-atom cubic  $V_{15}X_1$  supercell made out of 8 BCC V unit cells, with the central V atom substituted by an impurity atom X ( $X = \text{Ni, Pd, Pt or Co}$ ), as illustrated in Fig. 4.11. The 8 vanadium atoms that are first-nearest-neighbors (1NN) to the impurity were treated separately from the 7 other, more distant, vanadium atoms. Three sets of independent force-constants were used in the model, corresponding to three types of bonds: X-V bonds, V1-V1 bonds (both vanadium atoms 1NN to the impurity), and V-V or V1-V bonds (at most one vanadium atom 1NN to the impurity). All bonds were included up to 5NN, if present. X-X type bonds correspond to higher-distance bonds (6NN) and were not included. The consistency of this model was checked by reproducing the DOS of pure BCC vanadium, upon setting the mass of the impurity atom equal to that of vanadium and setting all the force-constants equal to their pure V values.

This supercell model allowed us to compute both the true phonon DOS and the neutron-weighted phonon DOS by applying the neutron weights discussed above to the different

modes. The DOS curves were calculated from a random sampling of  $\vec{q}$  points in reciprocal space, covering a sphere of arbitrarily large radius in order to minimize the effect of partial sampling of the farthest Brillouin zones. A convergence study lead us to use  $1 \times 10^3$  random  $\vec{q}$  points for DOS calculations with the supercell model, whose dynamical matrix  $\mathcal{D}(\vec{q})$  has 48 eigenvalues at each  $\vec{q}$  point. The calculated gDOS histograms were binomially smoothed to match the experimental instrument average energy resolution. Our fitting procedure employed an implementation of Powell’s algorithm [78] to optimize the tensorial interatomic force-constants  $\Phi_{\alpha,\beta}^{\kappa,\kappa'}$  by minimizing the deviation between the calculated and experimental DOS curves, as evaluated through the generalized  $\chi^2$ :

$$\chi^2 = \sum_{i=i_{\min}}^{i_{\max}} \frac{(g_i^{\text{exp}} - g_i^{\text{calc}})^2}{(\sigma_i^{\text{exp}})^2}, \quad (4.1)$$

with  $\sigma_i^{\text{exp}}$  the experimental error bars.

The experimental DOS curves were fit by optimizing the 6 parameters corresponding to 1NN and 2NN X-V force-constants and 2NN V1-V1 force-constants, while all remaining force-constants were constrained to their pure vanadium values. To identify and discard possible local minima solutions, we conducted the fitting procedure for 20 different starting guesses in the parameter space, which were obtained from the pure V force-constants by applying a random deviation with a spread equal to half the value of each force-constant.

In all our simulations, we used as pure vanadium force-constants the values published by Colella *et al.*, which were obtained by fitting V dispersion curves measured by diffuse inelastic x-ray scattering [79]. For consistency, the experimental DOS of pure vanadium was also inverted, using a primitive BCC unit cell and the same procedure followed for the  $V_{15}X_1$  supercells. This inversion up to 4NN bonds yielded a force-tensor in very good agreement with that published by Colella *et al.*

#### 4.5.2 Minimization Results

We present here our minimization results for the force-constants and the corresponding DOS and partial DOS curves. Some of the guesses for the force-constants were trapped in local minima in the parameter space during the fitting procedure. For this reason, initial

guesses that converged towards bad fits, with peaks at either much higher energies than the cutoff energy or at very low energies were discarded. The average and standard deviation for each force-constant was calculated from the remaining population. Partial and total supercell DOS curves were then calculated from these.

### Minimized Force-Constants

Assuming a central potential, longitudinal and transverse force-constants were calculated from their optimized tensorial counterparts according to [21]:

$$\Phi_{\alpha\beta}^{x\text{NN}} = (L^{x\text{NN}} - T^{x\text{NN}}) \frac{r_\alpha r_\beta}{r^2} + \delta_{\alpha\beta} T^{x\text{NN}} \quad (4.2)$$

where  $L^{x\text{NN}}$  and  $T^{x\text{NN}}$  are the longitudinal and transverse stiffnesses for  $x^{\text{th}}$  NN bonds, and  $r$  and  $r_\alpha$  are the magnitude and  $\alpha$  component of the bond vector. Results are listed in table 4.3. The central 1NN X-V force-constants are plotted versus the relative change in metallic radius in figure 4.12.

The elastic constants  $c_{11}$ ,  $c_{12}$  and  $c_{44}$  and the elastic moduli  $B = (c_{11} + 2c_{12})/3$  and  $G = c_{44}$  were calculated from the minimized tensorial force-constants, using the Born-Huang relations (see [20]), which were evaluated up to 3NN bonds for a BCC lattice:

$$\begin{aligned} c_{11} &= \frac{2}{a} (\Phi_{xx}^{1\text{NN}} + \Phi_{xx}^{2\text{NN}} + 4\Phi_{xx}^{3\text{NN}}) \\ c_{12} &= \frac{2}{a} (2\Phi_{xx}^{1\text{NN}} - \Phi_{xy}^{1\text{NN}} - \Phi_{yy}^{2\text{NN}} + 2(2\Phi_{xy}^{3\text{NN}} - \Phi_{xx}^{3\text{NN}} - \Phi_{zz}^{3\text{NN}})) \\ c_{44} &= \frac{2}{a} (\Phi_{xx}^{1\text{NN}} + \Phi_{yy}^{2\text{NN}} + 2(\Phi_{xx}^{3\text{NN}} + \Phi_{zz}^{3\text{NN}})) \end{aligned} \quad (4.3)$$

The derivation of these relations is given in an appendix. Supercell alloy averages for  $B$  and  $G$  were then obtained by taking into account the fraction of bonds of X-V or V-V type for bonds up to 3NN (in this calculation, the V-V bonds in the 1NN shell around the impurity are considered identical to more distant V-V bonds):

$$B = \sum_{i=1}^3 f_{i\text{NN}} B_{i\text{NN}}^{\text{XV}} + (1 - f_{i\text{NN}}) B_{i\text{NN}}^{\text{V}}$$

Table 4.3: Central force-constants from inversion procedure compared with pure vanadium values from [79].

$\Phi(N/m)$	V*	V-Pt	V-Pd	V-Ni
$\dagger$ X-V L1	25.4	$84 \pm 8$	$75 \pm 3$	$-2 \pm 5$
$\dagger$ X-V T1	3.63	$-7 \pm 7$	$-13 \pm 3$	$22 \pm 3$
$\dagger$ X-V L2	6.49	$21 \pm 9$	$11 \pm 2$	$8 \pm 11$
$\dagger$ X-V T2	-2.15	$0 \pm 12$	$-1 \pm 2$	$1 \pm 7$
$\ddagger$ V1-V1 L2	25.4	$21 \pm 11$	$21 \pm 3$	$26 \pm 7$
$\ddagger$ V1-V1 T2	3.63	$3 \pm 4$	$3 \pm 1$	$-11 \pm 2$

\*R. Colella and B.W. Batterman, Phys. Rev. B **1**, 3913 (1970).

$\dagger$ impurity-vanadium bond.

$\ddagger$ vanadium-vanadium bond in 1NN shell around impurity.

$$G = \sum_{i=1}^3 f_{i\text{NN}} G_{i\text{NN}}^{\text{XV}} + (1 - f_{i\text{NN}}) G_{i\text{NN}}^{\text{V}}, \quad (4.4)$$

with  $f_{i\text{NN}}$  the fraction of X-V type bonds amongst  $i$ -th NN bonds. The bond fractions can be obtained from enumerating the number of bonds of each type within our supercell. One finds:  $f_{1\text{NN}} = \frac{1}{8}$ ,  $f_{2\text{NN}} = \frac{1}{7}$ , and  $f_{3\text{NN}} = \frac{2}{11}$ .

Some clear trends can be observed in our force-constant minimization results. The most important trend is the very large change in the 1NN impurity-host force-constants, notably the longitudinal force-constant  $L1$  of 1NN X-V bonds. This force-constant is much larger in V-Pt and V-Pd than it is in pure V, while it is much smaller in V-Ni. This result indicates that  $L1$  increases or decreases dramatically as one replaces the central V atom by a larger (Pd, Pt) impurity atom, or a smaller (Ni) one. A similar effect is observed on  $L2$ , with an apparently comparable magnitude, although the numerical noise in the inversion results makes comparisons more difficult in this case. Conversely, the transverse stiffness  $T1$  clearly follows an opposite trend, decreasing as the size of the impurity atom gets larger. The trend in  $L1$  is expected from the shape of the binding energy vs. separation curve for a metal, such as described by the universal equation of state of Rose *et al* [80]. In effect, as the size of the impurity substituted for the host vanadium atom increases, the X-V bond is put

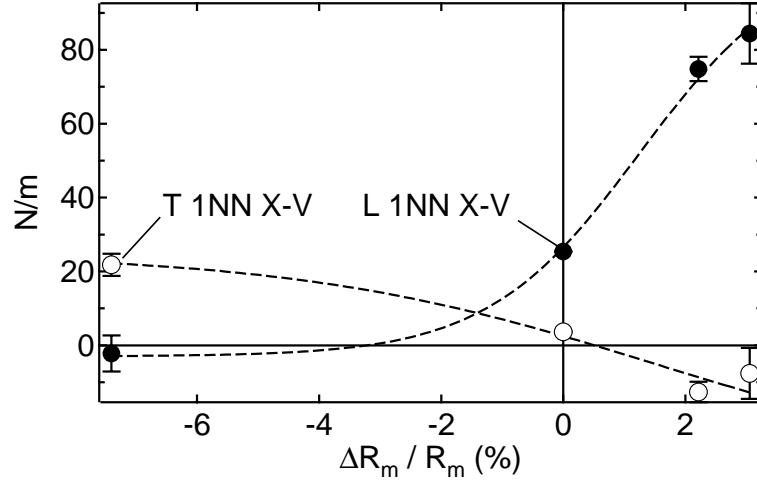


Figure 4.12: Longitudinal and transverse force-constants from optimized lattice dynamics model. The horizontal axis is the relative change in metallic radius between impurity and host. The central force-constants are calculated using Eq 4.2. Lines are drawn to guide the eye.

under compression, so the longitudinal stiffness of the bond increases. The converse effect in  $T1$  is less intuitive at first. A simple physical argument can nevertheless be made to explain the trend in  $T1$ . The densely-packed  $\langle 111 \rangle$  rows of atoms are put in compression by the introduction of large impurities, which drives an instability with respect to lateral displacements of the atoms. The result is a negative  $T1$  transverse force-constant. This mechanism has previously been invoked to explain the lattice dynamics of crystals with interstitial impurities [81]. The magnitude of the change in  $L1$  and  $T1$  can be compared to the difference in metallic radius between the host and impurity atom, and a good correlation is found between those two quantities (see Fig 4.12). It is helpful to recall, however, that the relaxation of atomic positions around the impurity atom is not at all taken into account in our lattice dynamics model. It is possible that, in reality, the shift in bond length is distributed over a longer distance than just the 1NN shell around the impurity, so that the X-V1 bond lengths would be less affected. Also, the magnitude of the change in  $L1$  seems very large for a 2% increase in impurity metallic radius, which might indicate that an additional effect is at play. We will discuss these points further in following sections.

A test of the force-constants obtained from the lattice-dynamics inversion procedure is to

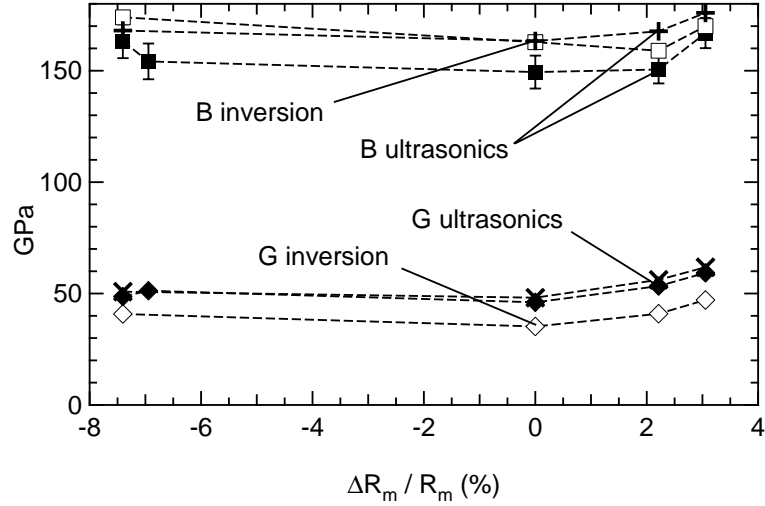


Figure 4.13: Bulk modulus  $B$  and shear modulus  $G$  measured by ultrasound pulse-echo technique and calculated from phonon DOS inversion procedure. Crosses are for second set of measurements in table 4.2.

compare the elastic moduli  $B$  and  $G$ , obtained from Eq. 4.3 and 4.4, with the experimental values from ultrasound measurements. Both values are plotted in Fig 4.13. As can be seen in this figure, the experimental and calculated results are in good agreement, although the calculated value of  $G$  is consistently underestimated by about 20%. The trends in both  $G$  and  $B$  are very well reproduced, as can be seen in a plot of  $\Delta G/G$  and  $\Delta B/B$  (see Fig. 4.14). The systematic deviation between the calculated and experimental values of  $G$  has two possible explanations. First of all, we calculated the shear modulus from  $G = c_{44}$ , which is not entirely appropriate for a polycrystalline material, although this yields a convenient estimate. A more accurate value for a random polycrystalline solid could be obtained from the arithmetic mean of the Voigt and Reuss shear moduli, which take into the elastic anisotropy parameter of the single crystal [61, 50]. Secondly, the Born-Huang equations for determining the elastic constants from the interatomic force-constants in the long-wavelength limit are known to converge slowly with the range of interactions taken into account [20, 23], so a better agreement should be obtained by extending Eq. 4.3 to interactions beyond 3NN bonds.

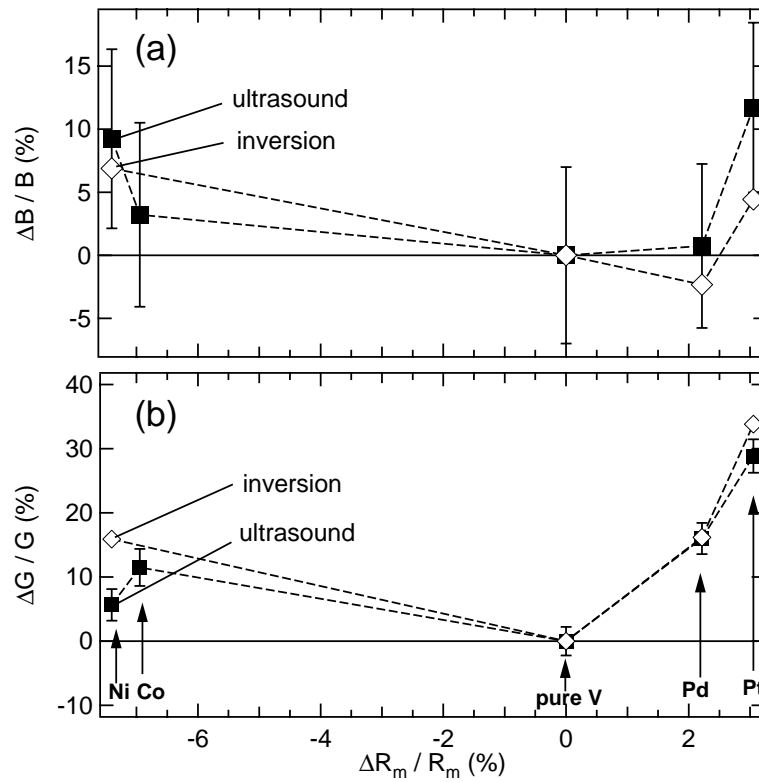


Figure 4.14: Relative change in bulk modulus  $B$  (panel a) and shear modulus  $G$  (panel b), measured by ultrasound pulse-echo technique and calculated from phonon DOS inversion procedure.

### Calculated Partial and Total DOS Curves

From the minimized values of tensorial force-constants, we used the same supercell model to calculate the total and partial DOS curves for V-Ni, V-Pd and V-Pt. These calculated DOSes were convolved with the resolution function for LRMECS (Fig. 3.9,  $E_i = 55$  meV) and are shown in figure 4.15. The most striking feature is the low-energy resonance mode observed in the Pt and Pd impurity partial DOS curves. For both types of impurities, this resonance is observed around 12 meV and accounts for most of the impurity vibration modes. Such impurity resonance modes have been predicted and experimentally observed before; they are known to occur when the mass ratio between impurity and host atoms is large. Although the critical value of this mass ratio for the appearance of a resonance mode depends on the bonding between impurity and host, a critical ratio of two is a general estimate [81, 21]. In both V-Pt and V-Pd, an extra impurity peak is observed at high energies, slightly above the cutoff energy of pure vanadium, while practically no modes are present at intermediate energies. The high-energy peak can be attributed to a local vibration mode, involving simultaneous displacements of the impurity and its nearest neighbors. Within the framework of the Mannheim theory of impurity vibrations, the coexistence of resonance and local modes has been predicted to occur in the case of heavy impurities that are strongly bound to the host lattice [81]. For both V-Pt and V-Pd also, the pDOS curves for 1NN, 2NN and 3NN vanadium atoms around the impurity are very similar. The 3NN pDOS is similar to the DOS curve for pure vanadium and shows that the vibrations of 3NN atoms are only slightly affected by the impurity. On the other hand, the 1NN pDOS shows an important stiffening in both cases, and due to the fact that the 1NN atoms represent 8 out of the 16 atoms in the supercell, this accounts for most of the stiffening observed in the experimental total DOS curves. The stiffening in the 2NN pDOS is smaller but present in both cases. For the 1NN and 2NN, the pDOS stiffening is more important in the case of the Pt impurity than in the case of the Pd impurity, which can perhaps be attributed to the larger size of the Pt impurity atom. In the case of Ni impurities, the impurity pDOS does not show any resonance mode and is similar to the pDOS of the surrounding V atoms. This is consistent with the mass of Ni being only 15% heavier than that of V.

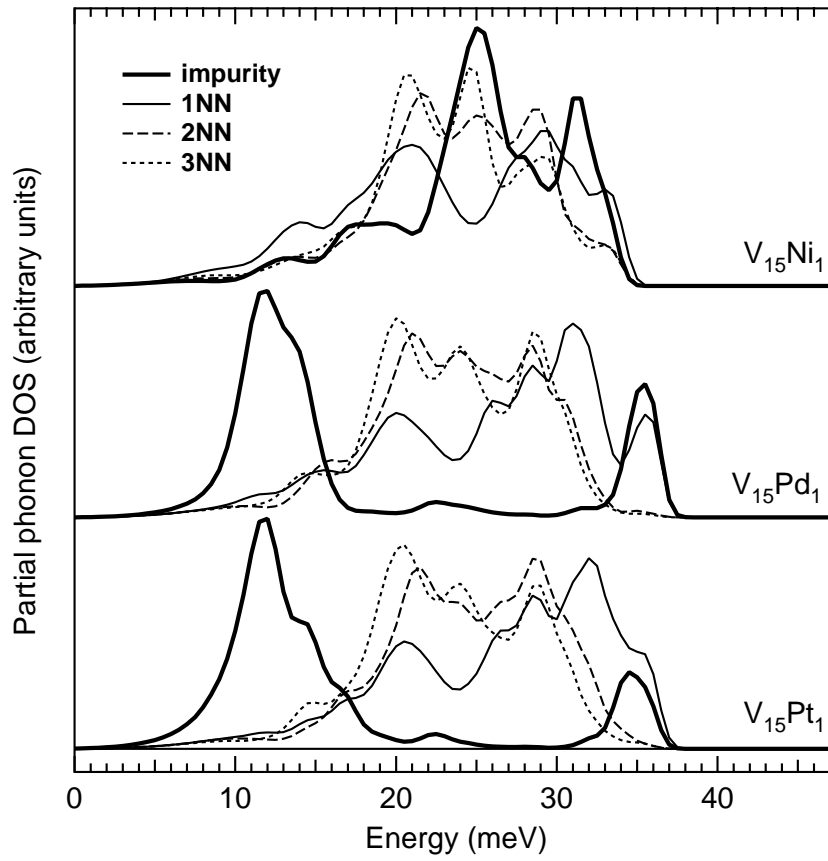


Figure 4.15: Partial phonon DOS for the solute atom and its V neighbors. The partial DOS are obtained from the optimized supercell force-constants.

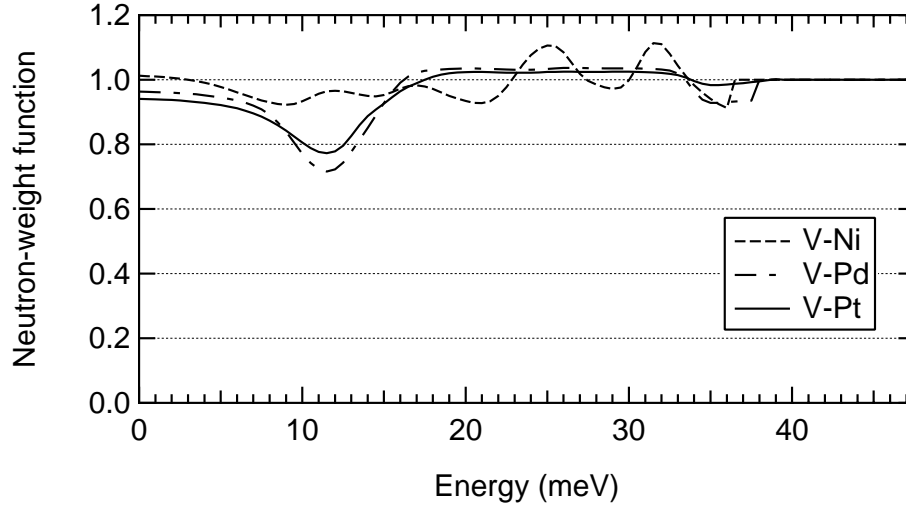


Figure 4.16: Neutron-weight function derived from partial phonon DOS.

### Neutron Cross-Section De-Weighting

One can see from the values in table 4.1 that the ratios of phonon scattering intensities of the impurity elements to those of the vanadium matrix atoms range between 3.1 in the case of Ni to 0.4 in the case of Pd. For impurity concentrations of 6.25%, the overall bias compared to the true phonon DOS is expected to be reasonably small, but a correction was nevertheless performed to obtain accurate values of vibrational entropy.

From the individual pDOS curves we constructed both the total DOS and the neutron-weighted total DOS curves of the alloys  $V_{93.75}Ni_{6.25}$ ,  $V_{93.75}Pd_{6.25}$  and  $V_{93.75}Pt_{6.25}$ . The ratio of these then gave us a neutron-weight distribution, which we used to correct the experimental DOS curves, by dividing out the neutron-weighting. The so-obtained neutron-weighting functions are shown in figure 4.16.

The corrected experimental DOS curves as well as the DOS curves resulting from our minimization procedure are presented in figure 4.17. One can see on this figure that the Pd and Pt resonance modes are more prominent once corrected for the neutron-weighting, as expected from the fact their  $\sigma/M$  ratios are smaller than for V. The overall effect on the total DOS is small in all cases, however.

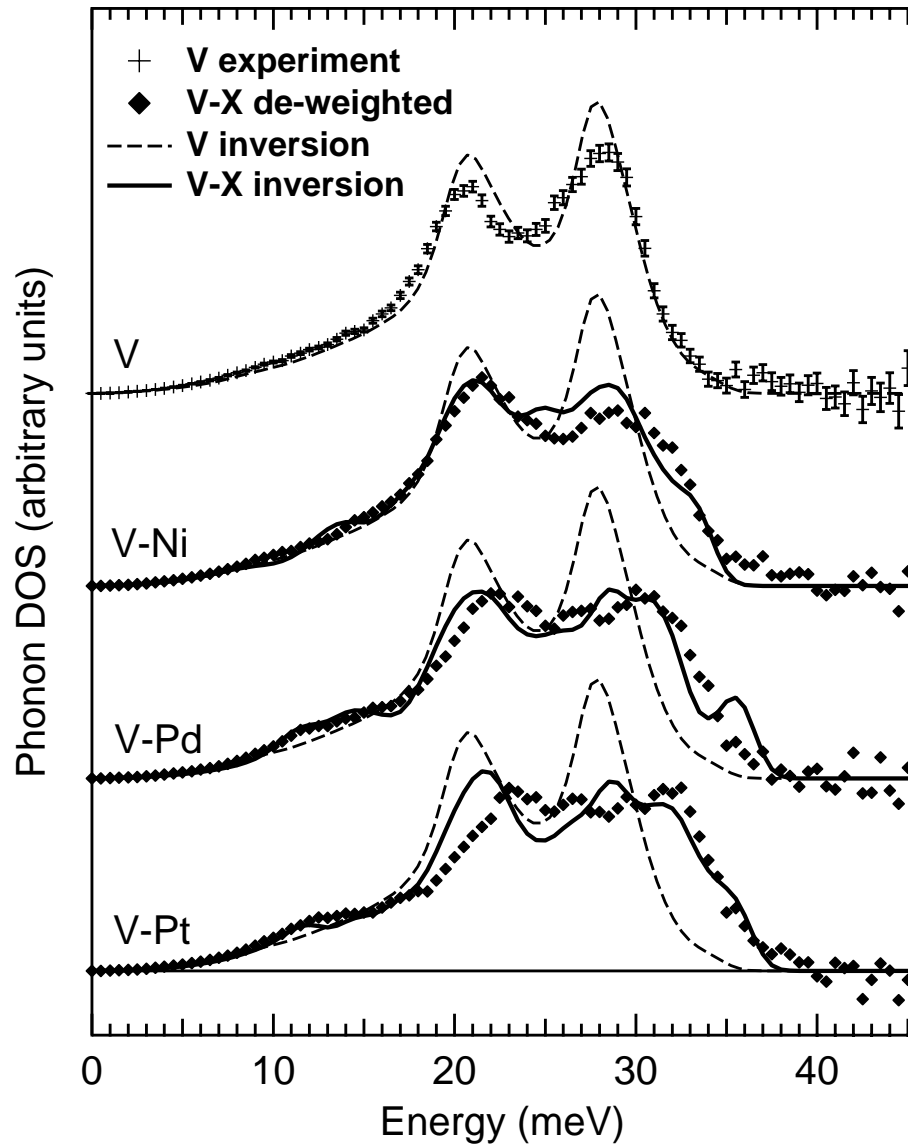


Figure 4.17: Experimental phonon DOS and Born–von Kármán phonon DOS obtained from the inversion procedure described in the text.

## 4.6 Vibrational Entropy

### 4.6.1 Trend with Alloying Element

The vibrational entropy  $S_{\text{vib}}$  is given by

$$S_{\text{vib}} = 3k_{\text{B}} \int_0^{E_{\text{max}}} [(n+1)\ln(n+1) - n\ln(n)] g(E) dE, \quad (4.5)$$

where  $n_E$  is the Bose-Einstein distribution and  $g(E)$  is the DOS, both for the same temperature. The vibrational entropy of alloying is then defined as  $S_{\text{vib}}^{\text{al}} = S_{\text{vib}}^{\text{V-X}} - S_{\text{vib}}^{\text{V}}$ . For each alloy, the DOS used in Eq. 7.5 was the experimental neutron-weighted DOS curve. The cutoff energy  $E_{\text{max}}$  was estimated visually from the DOS. It was checked that small changes in  $E_{\text{max}}$  around the estimated value ( $\pm 1$  meV) did not significantly affect the value of  $S_{\text{vib}}$ . The Results for room-temperature are listed in Table 4.4.

The vibrational entropy of alloying follows a clear trend as function of the solute element, as can be seen in Fig. 4.18. For elements to the left of vanadium in the periodic table,  $S_{\text{vib}}^{\text{al}}$  is positive, corresponding to the softening of the phonons upon alloying, while elements to the right of vanadium yield a negative  $S_{\text{vib}}^{\text{al}}$  by the reverse effect. The trend in vibrational entropy is mirrored in the plot of the average phonon frequency of figure 4.19.

The vibrational entropies of alloying are large for impurities down the Ti column and for impurities at the end of the transition metal series, which have an important difference in their number of  $d$ -electrons and their electronegativity, compared with the host vanadium atoms.  $S_{\text{vib}}^{\text{al}}$  also increases in magnitude with the mass and size of the impurity. This is observed both for solutes from column IV, which have increasing positive values of  $S_{\text{vib}}^{\text{al}}$ , from Ti to Zr and Hf, and also for solutes from column VIIIc, which yield decreasing negative values from Ni to Pd and Pt. Chromium and impurities that are isoelectronic with vanadium (Nb, Ta), have smaller effects on  $S_{\text{vib}}$ . The effect seen for impurities from either end of the transition metal series are comparable in magnitude with the positive configurational entropy of mixing,  $S_{\text{cf}}^{\text{mix}} = -k_{\text{B}}[c\ln c + (1-c)\ln(1-c)]$ , which for 6.25% impurities gives an entropy gain  $S_{\text{vib}}(0.0625) = 0.23k_{\text{B}}/\text{at}$ .

Table 4.4: Vibrational entropy of alloying and mean phonon energy.

composition	$\langle \hbar\omega \rangle$ ( <i>meV</i> )	$E_{cut}$ ( <i>meV</i> )	$S_{vib}^{al}$ N.W.* ( $k_B/at$ )	$S_{vib}^{al}$ cor.† ( $k_B/at$ )	$S_{vib}^{mix}$ cor.† ( $k_B/at$ )
pure V	$22.9 \pm 0.2$	35	na	na	na
V <sub>93.75</sub> Ti <sub>6.25</sub>	22.3	35	$0.08 \pm 0.01$	na	na
V <sub>93.75</sub> Cr <sub>6.25</sub>	23.1	35	$-0.04 \pm 0.01$	na	na
V <sub>93.75</sub> Fe <sub>6.25</sub>	23.6	36	$-0.09 \pm 0.01$	na	na
V <sub>93.75</sub> Co <sub>6.25</sub>	23.9	36	$-0.12 \pm 0.01$	na	na
V <sub>93.75</sub> Ni <sub>6.25</sub>	23.7	36	$-0.09 \pm 0.01$	$-0.08 \pm 0.01$	$-0.08 \pm 0.01$
V <sub>93.75</sub> Zr <sub>6.25</sub>	22.0	35	$0.12 \pm 0.02$	na	na
V <sub>93.75</sub> Nb <sub>6.25</sub>	22.4	35	$0.05 \pm 0.01$	na	na
V <sub>93.75</sub> Pd <sub>6.25</sub>	24.5	38	$-0.17 \pm 0.01$	$-0.15 \pm 0.01$	$-0.019 \pm 0.01$
V <sub>93.75</sub> Hf <sub>6.25</sub>	21.9	35	$0.14 \pm 0.02$	na	na
V <sub>93.75</sub> Ta <sub>6.25</sub>	22.6	35	$0.01 \pm 0.02$	na	na
V <sub>93.75</sub> Pt <sub>6.25</sub>	25.1	40	$-0.24 \pm 0.01$	$-0.21 \pm 0.01$	$-0.27 \pm 0.01$

\*from neutron-weighted phonon DOS

†from corrected phonon DOS

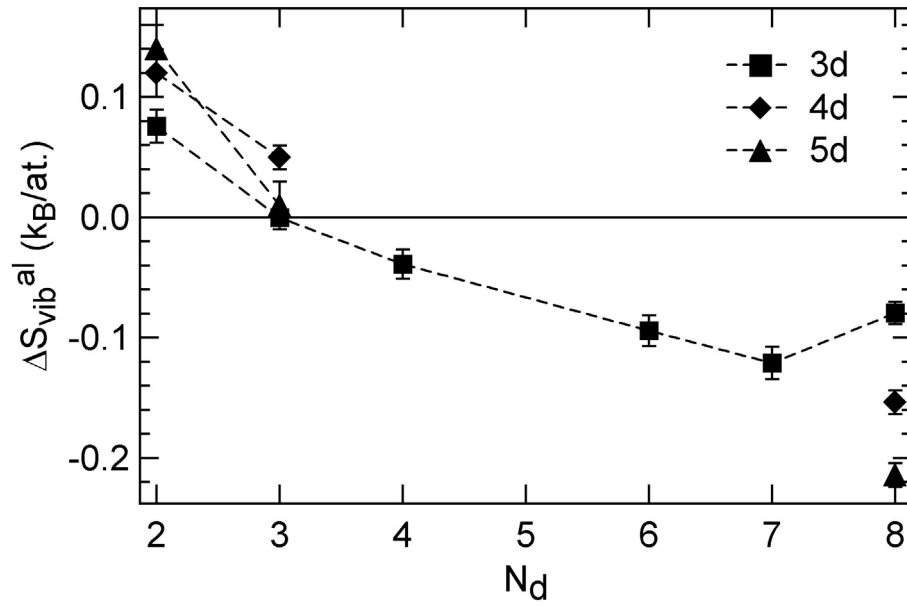


Figure 4.18: Neutron-weighted vibrational entropy of alloying (de-weighted values in the case of Ni, Pd, and Pt impurities).

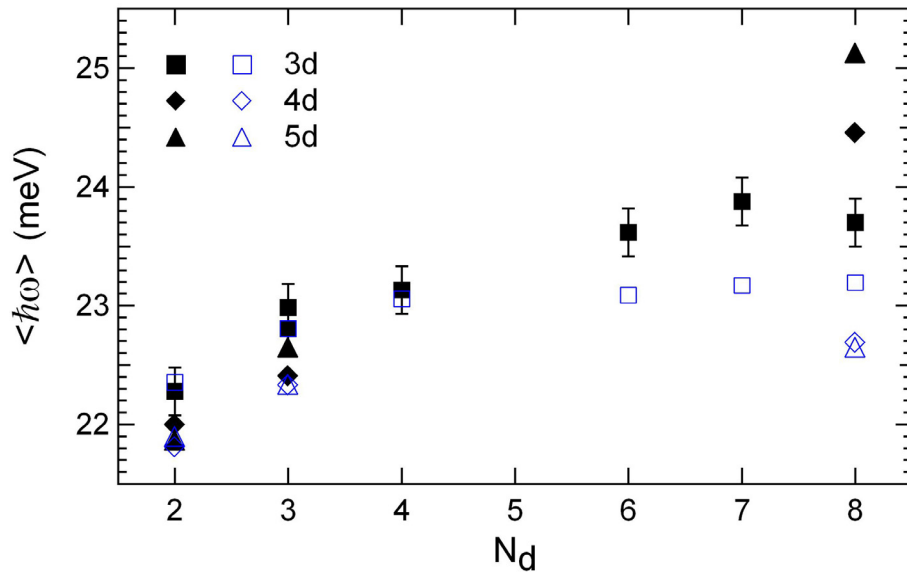


Figure 4.19: Average phonon energy. Solid symbols: from experimental phonon DOS. Open symbols: estimate from Grüneisen parameter and impurity metallic radius.

### 4.6.2 Effect of Neutron-Weighting

The effect of neutron-weighting on the calculated vibrational entropy can be estimated by comparing the values of vibrational entropy obtained from the neutron-weighted and de-weighted phonon DOS. The phonon DOS for V-Ni, V-Pd, and V-Pt were analyzed using the Born–von Kármán lattice dynamics inversion procedure described above, which allowed correction for the effect of neutron-weighting. The neutron-weighted and corrected vibrational entropies of alloying for these alloys are listed in Table 4.4. The effect of neutron-weighting is potentially largest when the alloy components have very different ratios of cross-section over mass. However, even in this case, neutron-weighting only has an effect if the different species have sufficiently different partial densities of states. The alloy V-Pd shows the largest possible neutron-weighting, owing to the resonant nature of the Pd pDOS and the Pd neutron scattering cross-section, which yields a scattering intensity ratio compared with vanadium of 0.4. Even in the case of Pd impurities, one can see that the effect of neutron-weighting on the vibrational entropies listed in Table 4.4 is of modest magnitude, comparable to the statistical error due to counting statistics on the phonon DOS itself. The same is true for Ni and Pt impurities. It was shown above that most of the stiffening of the DOS is due to the stiffened pDOS curves for the 1NN vanadium atoms around the impurities. Most of the entropy change is associated with the vibrations of these 1NN vanadium atoms, and is not affected by neutron-weighting.

### 4.6.3 Vibrational Entropy of Mixing

The difference in entropy between the pure elements and the alloy, is the vibrational entropy of mixing:

$$S_{\text{vib}}^{\text{mix}} = S_{\text{vib}}^{\text{V}_{1-x}\text{X}_x} - ((1-x)S_{\text{vib}}^{\text{V}} + xS_{\text{vib}}^{\text{X}}). \quad (4.6)$$

This analysis conserves the number of atoms before and after alloying, and is representative of an entropy for a closed thermodynamic system. We computed this quantity for the V-Ni, V-Pd, and V-Pt alloys, using the de-weighted phonon DOS curves and published experimental phonon DOS curves for FCC Ni, Pd, and Pt [82, 83, 84]. Results are listed in

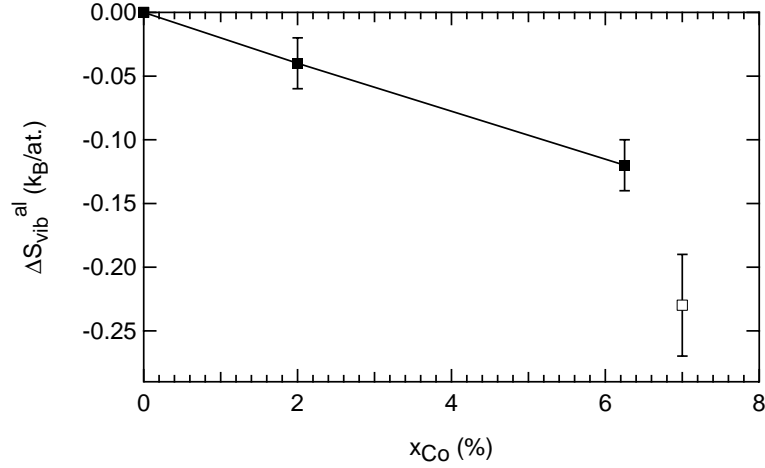


Figure 4.20: Neutron-weighted vibrational entropy of alloying for V-Co alloys with different Co concentrations. Solid symbols: LRMECS data. Open symbol: HFIR-HB2 data.

Table 4.4. Because the vibration frequencies in pure Pd and Pt are lower than in V,  $S_{\text{vib}}^{\text{mix}}$  is more negative than  $S_{\text{vib}}^{\text{al}}$  in these cases. In the case of Pt solutes, the vibrational entropy of mixing ( $-0.27k_{\text{B}}/\text{at}$ ) is even larger in magnitude than the configurational entropy gain ( $+0.23k_{\text{B}}/\text{at}$ ), which makes the total entropy of mixing impurities negative in this case (the electronic entropy turns out to augment this effect, as discussed in the following).

#### 4.6.4 Concentration Dependence in V-Co

The vibrational entropies of alloying for V-Co obtained from the phonon DOS curves of figure 4.10 are shown in figure 4.20. Co has almost the same  $\sigma/M$  as V, so these vibrational entropies are almost free of neutron-weighting. For the data from LRMECS for Co concentrations  $x_{\text{Co}} \leq 6.25\%$ ,  $S_{\text{vib}}^{\text{al}}$  varies linearly with  $x_{\text{Co}}$ . The data point for  $x_{\text{Co}} = 7\%$  does not fall exactly on the same line, but the error bars on this value are larger and the discrepancy might be attributed in part to the different technique used in this measurement, as discussed above.

#### 4.6.5 Connection with Elastic Constants

As can be seen from figures 4.19 and 4.18, the vibrational entropy of alloying is directly related to the change in average phonon energy upon alloying. This is expected since in first

approximation, an average phonon energy or Debye frequency can describe the vibrational entropy fairly well, as  $S_{\text{vib}} \simeq k_{\text{B}}(3 + \langle \ln(k_{\text{B}}T/\hbar\omega) \rangle)$  in the high-temperature limit. We also observe a high degree of correlation between the shear elastic constants and the vibrational entropy, as seen in figure 4.3. The shear modulus  $G$  appears closely correlated to the mean phonon energy and vibrational entropy, while the trend in the bulk modulus  $B$  is not quite as clear. This is best seen in figure 4.21. This is expected from simple considerations in, for example, a Debye model [50]. In the Debye model of atomic vibrations, the density of states is proportional to  $\omega^2/C_{\text{D}}^3$ , with  $C_{\text{D}}$  the Debye average sound velocity:

$$\frac{3}{C_{\text{D}}^3} = \frac{1}{C_{\text{L}}^3} + \frac{2}{C_{\text{T}}^3}, \quad (4.7)$$

where  $C_{\text{L}}$  and  $C_{\text{T}}$  are, respectively, the longitudinal and transverse sound velocities. Typically,  $C_{\text{L}}$  is larger than  $C_{\text{T}}$ , and in the case of V alloys  $C_{\text{L}}/C_{\text{T}} \sim 2$  so that the second term in the right-hand side of Eq. 4.7 is about 16 times larger than the the first term. Equation 4.7 thus shows that the shear modulus is more important than the bulk modulus (in the Debye model) in estimating the average phonon frequency and vibrational entropy. This is also observed experimentally, at least qualitatively.

## 4.7 Chemical Trends

The effects observed on the vanadium phonon DOS upon alloying of 6.25% transition metal impurities are large and follow some systematic trends, as discussed above. The systematic stiffening of the phonon DOS for solutes across the transition metal series is opposite to the effect of increasing solute mass. This indicates that the mass effect is a smaller effect and that the main effect is due to changes in interatomic force-constants, associated with changes to the electronic structure of the crystal upon introduction of the impurities. Two types of factors can influence this change in the electronic structure: first, the size of the impurity atoms (metallic radius  $R_{\text{m}}$ ), and second, their atomic electronic properties, such as their number of  $d$ -electrons,  $N_{\text{d}}$ , and electronegativity,  $\chi$ .

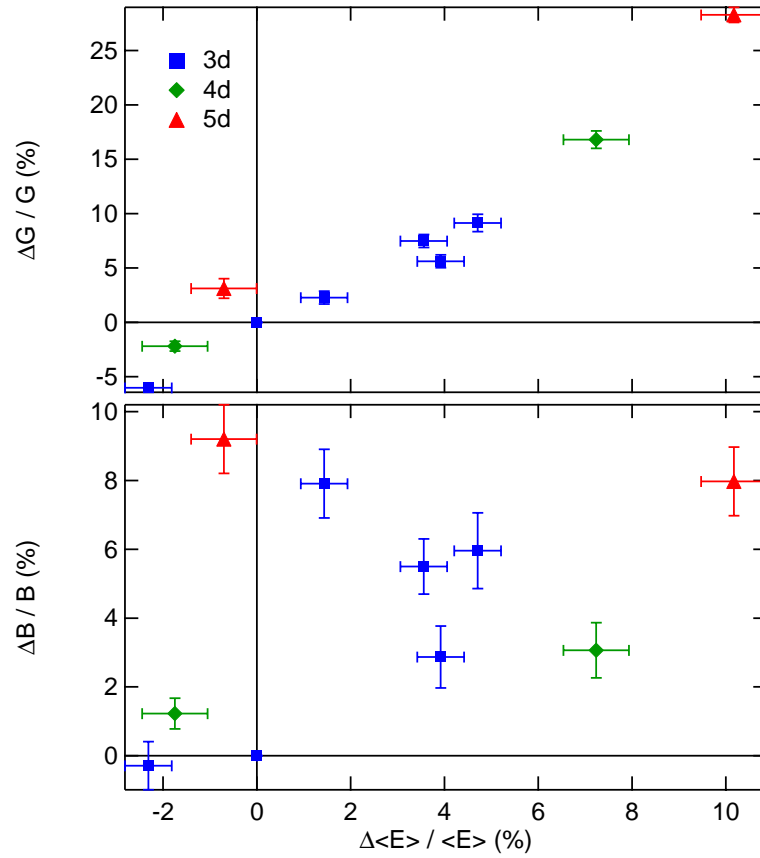


Figure 4.21: Change in shear modulus  $G$  and bulk modulus  $B$ , plotted versus the change in average phonon energy  $\langle E \rangle$ , for V-6%X alloys, with X a 3d, 4d or 5d impurity.

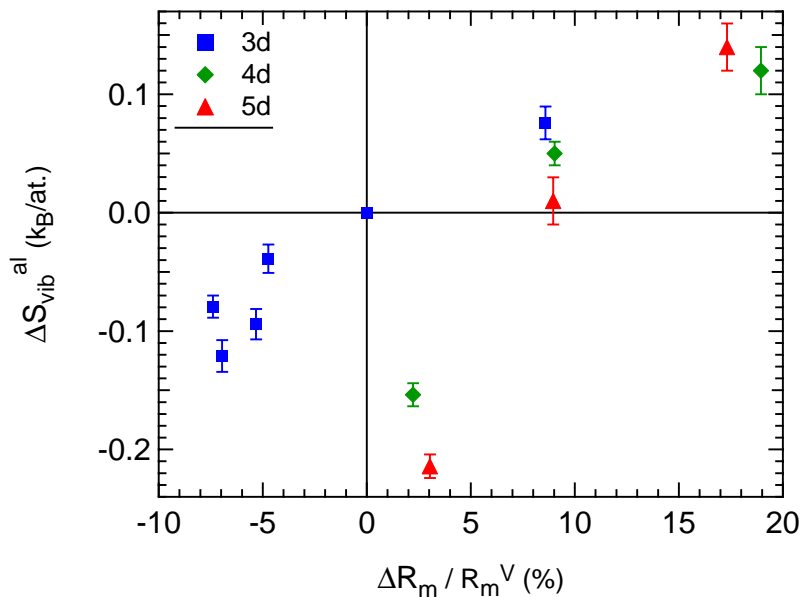


Figure 4.22: Neutron-weighted vibrational entropy of alloying plotted against relative change in metallic radius between host and impurity. Metallic radii are from Table 4.1.

#### 4.7.1 Effect of Metallic Radius

The vibrational entropy of alloying is graphed against the relative change in metallic radius in figure 4.22. There is a generally fair correlation between the two quantities, with most points falling into the lower-left and upper-right quadrants. This is not surprising. Vibrational entropy tends to increase as the average lattice parameter increases and phonons soften. More quantitative assessments using the Grüneisen parameter are given below. More recent models, such as the “bond-stiffness vs. bond-length” model, have developed similar considerations, seeking a linear relationship between the interatomic force-constants and the length of a given chemical bond [8]. However, this model does not give predictions for chemical trends, when one component of the bond is systematically varied as studied here. Two points in the lower portion of figure 4.22 are not following the same metallic radius trend observed in the rest of the alloys. These correspond to Pd and Pt impurities. Pd and Pt solutes do not alter substantially the lattice parameter of the alloy, yet they produce the largest phonon stiffening.

The effect of the impurity metallic radius on the average lattice parameter was seen to

account for the experimental trend of Fig. 4.1. In a similar fashion, one can calculate the effect of the impurity metallic radius on the average phonon frequency, using the Grüneisen parameter  $\gamma_G$  (Eq. 2.58). Using our measured bulk modulus and reported values for the heat capacity  $C_P$  and linear coefficient of thermal expansion  $\alpha$  at 300 K [85, 86], we obtained  $\gamma_G = 1.23$  for V at 300 K. The change in average phonon frequency is then obtained from

$$\frac{\Delta\langle\omega\rangle}{\langle\omega\rangle} \simeq -3c\gamma_G \frac{\Delta R_m}{R_m}, \quad (4.8)$$

with  $c$  the concentration (1/16). Results are shown together with the experimental values in figure 4.19. One can see on this figure that the values predicted from  $R_m$  in this model are in good agreement with experimental results for impurities in columns adjacent to V. However, the agreement is poor for impurities from the late transition metals. The predicted effect is much too small for Fe, Co, and Ni solutes and in the case of Pd and Pt a softening is predicted instead of the strong observed stiffening. This illustrates limitations of these atomic size considerations.

#### 4.7.2 Effect of Electronegativity

Figure 4.23 shows a correlation plot of  $\Delta S_{\text{vib}}^{\text{al}}$  with the difference in electronegativity between solute and host atoms on the Pauling scale,  $\Delta\chi_{\text{Pauling}}$ . This graph shows that  $\Delta S_{\text{vib}}^{\text{al}}$  varies linearly with the electronegativity of the solute, even for the large and heavy solutes of the 4d and 5d rows. The correlation with electronegativity for our 6.25% solute concentrations, weighted with experimental error bars, is  $\Delta S_{\text{vib}}^{\text{al}} = -0.34(\pm 0.06)\Delta\chi$ . This correlation is successful both across the 3d row and down three columns of the periodic table. The charge transfer between solutes and host vanadium atoms, as quantified by the Pauling electronegativity scale, accounts surprisingly well for the trends observed in the phonon DOS. This result prompted us to investigate charge transfer effects in these alloys using first-principles calculations. Results are discussed in the next chapter.

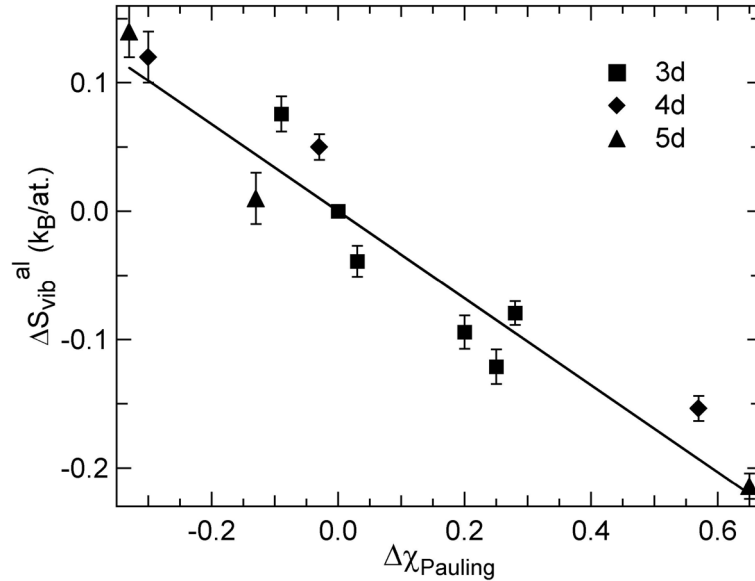


Figure 4.23: Neutron-weighted vibrational entropy of alloying plotted against Pauling's electronegativity of the solutes. The line is a fit to the data.

### 4.7.3 Comparison with Trends for BCC Transition Metals

We can compare the present results to previous observations for BCC transition metals. It has been shown that the phonon dispersions of BCC transition metals exhibit systematic trends correlating with their number of  $d$ -electrons [87, 88]. The BCC lattice exhibits inherent instabilities for deformations toward the HCP lattice and the  $\omega$  structure, which leads to the occurrence of both types of martensitic transformations in Sc, La, Ti, Zr and Hf [89, 90, 91, 92, 93]. The instability toward the  $\omega$  transformation appears as a pronounced dip in the dispersions at the  $L\ 2/3[111]$  point, or  $\omega$ -point. This weakness is understood as a geometric feature of the BCC lattice [87]. The displacement of the ions in this phonon mode corresponds to motions of dense rows of atoms in the  $[111]$  directions that do not alter the 1NN distance between ions. Because the 1NN interactions are strongest and they do not come into play in this displacement pattern, the corresponding energy is particularly low. This feature is also present in BCC alkali metals and was reproduced in theoretical calculations [94]. The BCC to HCP martensitic transformations in the elements of groups 3 and 4 are also explained in terms of precursor modes corresponding to a mechanical weakness of the BCC lattice. In this case, the precursor mode involved is the N-point

( $1/2[110]$ ) transverse phonon,  $T_{[1\bar{1}0]}$ . As was shown by Petry [87], the group 3 and 4 BCC elements exhibit a valley of low-energy, strongly damped modes along the low-symmetry  $[2\xi\xi\xi]$  direction, which connects the  $L\ 2/3[111]$  and  $T_{[1\bar{1}0]}1/2[110]$  modes. These low-energy modes contribute an increase in vibrational entropy, which stabilizes the BCC phase at high temperatures.

The dip at the  $\omega$ -point in the  $L[111]$  phonon branch is progressively suppressed as the number of  $d$ -electron increases. Petry has related this observation to the strengthening of directional bonding with the filling of the  $d$ -band, which leads to “cross-locking” of  $[111]$  rows of atoms [87, 88]. Directional bonding also stabilizes the  $T_{[1\bar{1}0]} [110]$  transverse phonon branch. As a result, the BCC phase is mechanically stabilized at lower temperatures for more filling of the  $d$ -band. This strong stiffening of the phonons is observed as one goes from group 5 to group 6 elements, with an increase in nominal  $d$ -band filling from 3 to 4 (or number of valence electrons per atom between  $5 e/at$  and  $6 e/at$ ). For example, the cutoff energy of the phonon DOS increases from 21 meV to 28 meV between Ta and W [95], from 27 meV to 33 meV between Nb and Mo [96], and from 33 meV to 40 meV between V and Cr [36] (magnetism also intervenes in the latter case, but it is believed to yield a softening, not a stiffening).

The  $d$ -band filling has also been invoked to explain the composition dependence of the elastic moduli in BCC transition metal alloys [61, 62, 60, 65, 66, 67, 63]. In the simplest of approximations, that of a free-electron metal, one can relate the bulk modulus  $B$  to the electron density  $n$  through (see ref. [49])

$$B = \frac{\hbar^2 \pi^{4/3}}{3^{1/3} m} n^{5/3} . \quad (4.9)$$

In the transition metals, the electronic structure is more complex. In the Friedel model, one considers a rectangular electronic DOS to approximate the  $d$ -band, while the  $sp$  band is neglected altogether. The only free parameters are then the bandwidth  $W$  and the number of  $d$ -electrons  $N_d$  (the height of the rectangular DOS is fixed to  $10/W$ , since there are 10  $d$  states to accommodate). In this model, the cohesive energy is proportional to  $N_d(10 - N_d)$ ; it is an inverted parabola peaking at  $N_d = 5$ . The bulk modulus exhibits an essentially similar behavior, but the modulation by the change in lattice parameter (and thus electron

density) across the  $d$ -band gives it a more linear dependence with  $N_d$  for  $N_d < 5$  [97]. The predicted shape of  $B(N_d)$  reproduces well the experimental values of bulk modulus for the pure elements, independently of their crystal structure.

Measurements on Ti-V-Cr and Zr-Nb-Mo alloys have found a generally linear dependence of the bulk modulus with  $e/at$  [61, 62, 59, 60] in the range of  $4e/at$  to  $5.8e/at$ , in good agreement with the simple model of Friedel. For more Cr-rich V-Cr alloys, the magnetism yields a sudden decrease in  $B$ . The shear modulus  $G$  and single crystal shear elastic constant  $c_{44}$  present a more complex behavior, however. At room-temperature, the dependence of  $G$  and  $c_{44}$  on  $e/at$  goes from weak to much stronger, with a pronounced cusp at around  $5.4e/at$  [61, 62, 60, 67]. This behavior is even more pronounced at low temperatures, where  $c_{44}$  goes from a decrease with  $e/at$  to a strong increase, at around this composition. This feature has been attributed to the crossing of the  $\Gamma_{25'}$  point in the band structure at a band-filling of about  $5.4e/at$ , corresponding to a topological change of the Fermi surface [64]. More will be said about this in chapter 5.

The rigid-band model is rather successful at describing both the temperature and electron-concentration dependence of the elastic constants of Ti-V-Cr and Zr-Nb-Mo alloys, as well as some features of their phonon dispersions. However, it is expected that the rigid band model is limited to “homogeneous” alloys and will not be valid for alloys with components that are not neighbors in the periodic table. In the case of V-6.25%X alloys, the rigid band model describes well the elastic constants for Ti and Cr impurities. But for later transition metal impurities such as Fe, Co, Ni, Pd, and Pt, it does not work so well. We observe a stronger dependence of the elastic constants and phonons on the type of solute than would be predicted by a mere band-filling. One should keep in mind that with 6.25% solutes, the range of electron concentration sampled is small, between  $4.9375e/at$  and  $5.3125e/at$ . We observed a downward curvature of  $B$  and  $G$  from Co to Ni impurities, for example, which would not be expected based on rigid-band filling only. Most prominently, the behavior of  $G$  and the phonons for solutes changing from Ni to Pt (at constant  $e/at$ ) is unaccounted for.

The emerging picture is thus as follows. For solutes having a similar number of  $d$ -electrons as the vanadium atoms of the host crystal, the alloy is rather homogeneous,

thus the rigid-band model is valid and provides some account of the observed stiffening of the phonons and elastic constants. On the other hand, for solutes from the end of the transition metal series, the alloy is not homogeneous and the rigid-band model fails. The chemical nature of the impurities then becomes more important than the average electron concentration in predicting the change in the vibrational and elastic properties. We have shown that the difference in electronegativity between the impurities and the host atoms is a good parameter to predict the sign and magnitude of the change in vibrational entropy, in the case of semi-dilute vanadium alloys.

## 4.8 Summary

The phonon density of states and vibrational entropy were investigated in a series of dilute vanadium alloys V-6.25%X, with X a transition metal impurity. Systematic chemical trends were identified in the behavior of the phonons as function of the alloying solute. Impurities to the left of V induce a stiffening of the phonons and a positive vibrational entropy of alloying, while elements to the right of V produce the reverse effect. The impurity mass was shown to be of minor importance to the observed effect, even for impurities four times as massive as the host. The mass effect could be more relevant in concentrated alloys, however. The vibrational entropy of alloying correlates in part with the metallic radius of the impurity, at least for solutes not too different chemically from the host. For late transition metal impurities, the trend with metallic radius fails. On the other hand, we show that the vibrational entropy of alloying exhibits a strong correlation with the electronegativity of the solutes. A linear relationship is found between the two quantities, which is robust for solutes from the 3*d*-, 4*d*- and 5*d*-series. To date the systematics of the vibrational entropy of alloying have remained elusive, so this electronegativity correlation should be of interest to the alloy community. Tests of its applicability to other metallic systems would be very interesting.

## Chapter 5

### First-Principles Simulations of V-X Alloys

#### 5.1 Introduction

We performed first-principles electronic structure calculations to determine the origin of the experimentally observed effects in V-6.25%X alloys. The calculations were carried out with density functional theory, using full electronic potentials and linearized augmented plane-waves plus local orbitals (FP-LAPW+LO) method, as implemented in the software package Wien2k [98, 99]. Additional density functional theory calculations were performed using the computer program VASP [33, 100], within the projector-augmented wave (PAW) representation [101, 102]. Descriptions of these implementations of density functional theory are presented in an appendix.

Calculations on pure BCC vanadium used a two-atom simple cubic unit cell, or a  $2 \times 2 \times 2$  supercell (16 atoms), or a  $3 \times 3 \times 3$  supercell (54 atoms), based on repetitions of the two-atom cell. The random substitutional solid-solutions were modelled using the  $2 \times 2 \times 2$  and  $3 \times 3 \times 3$  supercells, with the central vanadium atom replaced in each case by an impurity atom X, yielding the compositions  $V_{15}X_1$  (V-6.25%X) and  $V_{53}X_1$  (V-1.85%X), respectively.

#### 5.2 Simulation Parameters

##### 5.2.1 Wien2k

We used the PBE-96 parameterization of the generalized-gradient approximation by Perdew, Burke and Ernzerhof for the exchange-correlation functional [103]. We used the Brillouin

zone sampling scheme of Monckhorst and Pack (MP) [104] and carried out convergence studies for the grid mesh size. For the simple BCC unit cell, we calculated total energies with grids comprising between 20 and 560 sampling points in the irreducible portion of the Brillouin zone (IBZ), corresponding to  $7 \times 7 \times 7$  and  $27 \times 27 \times 27$  MP grids, respectively. For the  $2 \times 2 \times 2$  supercells, we used  $\mathbf{k}$ -point grids with 35 (MP- $10 \times 10 \times 10$ ) to 286 points in the IBZ (MP- $21 \times 21 \times 21$ ). The calculations for the  $3 \times 3 \times 3$  supercells used 20 points in the IBZ.

Wien2k calculations were performed with atomic sphere radii  $R_{\text{MT}} = 2.2$  atomic units (a.u.) for all atoms in the unit cells considered. A convergence study on the  $2 \times 2 \times 2$  pure vanadium supercell lead us to use a plane wave energy cutoff  $R_{\text{MT}}K_{\text{max}} = 7.0$ , corresponding to a kinetic energy cutoff  $E_{\text{cut}} = 138$  eV. This gave satisfactory convergence, when taking into account the important error cancelling when comparing pure vanadium with the alloy supercells. Additional calculations on the relaxed supercells were performed with an increased  $R_{\text{MT}}K_{\text{max}} = 8.0$ , which did not affect the calculated properties.

In the case of the magnetic impurities Fe, Co and Ni, spin-polarized calculations were performed on the relaxed  $2 \times 2 \times 2$  supercells, indicating no magnetization on the impurity atom, and subsequent simulations were performed with the non-spin-polarized model. Sample input files for Wien2k simulations are presented in appendices.

### 5.2.2 VASP

The VASP calculations were carried within the PAW formalism with the Perdew-Wang 1991 (PW91) GGA exchange-correlation functional. We used the Monckhorst-Pack Brillouin zone sampling with a mesh of  $16 \times 16 \times 16$  points for the  $2 \times 2 \times 2$  supercells, as suggested by a convergence study. This mesh reduces to 120 independent  $\mathbf{k}$ -points in the IBZ. The partial occupancies for the wave functions were determined from the Methfessel-Paxton method, with an energy smearing width of 0.2 eV. A typical input file for VASP calculations is shown in the appendix.

## 5.3 Geometry Relaxation

### 5.3.1 Procedure

Upon introduction of an impurity atom, the host crystal relaxes its volume and geometry to accommodate the stresses. For a substitutional impurity, these are due to the difference in metallic radius and electronic structure between the solute and the host. The total energy of the supercell was minimized with respect to the volume of the supercell and the position of the atoms in the basis in order to calculate the equilibrium volume and strains in the alloys. The theoretical equilibrium volume for pure vanadium was calculated with both the Wien2k and VASP simulation codes and converged with respect to both the  $\mathbf{k}$ -point grid and kinetic energy cutoff. In Wien2k, the positions of all ions in the supercell were relaxed using the provided “PORT” algorithm, which minimizes the calculated forces on the ions at a fixed cell volume by displacing the nuclei. The volume was then optimized with fixed fractional ionic coordinates and a final optimization of the ion positions was performed at this optimum volume. In this last step, the changes in ion coordinates were very small. A typical energy-volume curve with relaxed ion coordinates is shown in figure 5.1 for the case of  $V_{15}Ti_1$ . A Murnaghan equation of state [105] is fitted to the calculated energy-volume data in order to determine the equilibrium lattice parameter:

$$E(V) = E_0 + \frac{B_0 V}{B'_0} \left( \frac{(V_0/V)^{B'_0}}{B'_0 - 1} + 1 \right) - \frac{B_0 V_0}{B'_0 - 1} \quad (5.1)$$

with  $V_0 = a_0^3/2$  the zero-pressure atomic volume (there are two atoms per unit cell),  $B_0$  the zero-pressure bulk modulus and  $B'_0$  the bulk modulus pressure derivative, which is assumed constant. The geometry relaxation was performed within Wien2k for both the  $2 \times 2 \times 2$  and  $3 \times 3 \times 3$  supercells.

In the VASP simulations, the geometry relaxation was performed with a script that let the code optimize the ion coordinates for a set of increasing lattice parameters. The calculations were conducted with an energy cutoff increased by 30% to minimize the effect of Pulay stress. The results were then fit to Eq. 5.1. Figure 5.2 compares the energy-volume curves calculated with VASP and Wien2k. As can be seen in this figure, the two

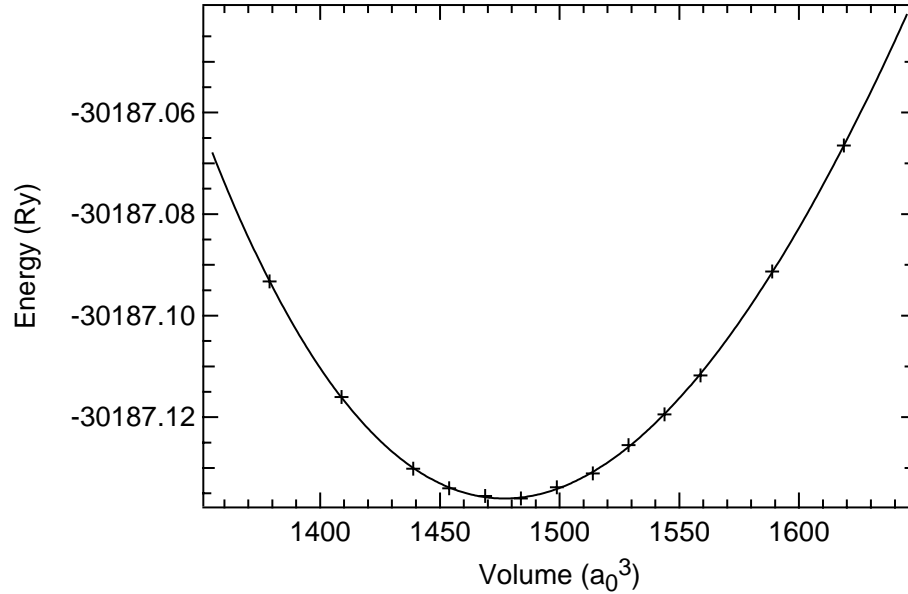


Figure 5.1: Typical energy-volume curve for the  $V_{15}X_1$  supercells calculated with Wien2k. Here for  $V_{15}Ti_1$ , with relaxed ionic positions. The line is a fit to the Murnaghan equation of state.

calculations are in very good agreement. The slight energy difference can be attributed to the ionic positions, held fixed at all volumes in Wien2k, in addition to general differences in the two simulation codes.

### 5.3.2 Results

The results of supercell geometry optimizations are summarized in table 5.1. Since the supercells have  $O_h$  point symmetry, the directions of impurity-host bonds are constrained to  $\langle 111 \rangle$ ,  $\langle 200 \rangle$  and  $\langle 220 \rangle$  directions for the 1-st, 2-nd, and 3-rd nearest-neighbor bonds, respectively. The free parameters are the bond-lengths and lattice parameters. Our results are given in table 5.1.

A comparison with the experimental results listed in table 4.1 shows that the calculated lattice parameters are too small by about 1%. Additional calculations on pure V within the local density approximation (LDA) in VASP predicted an even smaller lattice parameter, about 4% smaller than the experimental value. Discrepancies of 1% are considered small with current implementations of density functional theory. Besides, this error is systematic

Table 5.1: Relaxed supercell geometries from first-principles calculations.  $L_1$ ,  $L_2$  and  $L_3$  are the 1-st, 2-nd, and 3-rd nearest-neighbor bond lengths;  $a$  is the equivalent BCC lattice parameter.

system	VASP		Wien2k		Wien2k			
	$2 \times 2 \times 2$		$2 \times 2 \times 2$		$3 \times 3 \times 3$			
	$a(\text{\AA})$	$L_1(\text{\AA})$	$a(\text{\AA})$	$L_1(\text{\AA})$	$a(\text{\AA})$	$L_1(\text{\AA})$	$L_2(\text{\AA})$	$L_3(\text{\AA})$
V-Ti	3.015	2.653	3.013	2.653	3.004	2.676	3.003	4.247
pure V	2.996	2.594	2.996	2.595	2.996	2.595	2.996	4.237
V-Cr	2.989	2.561	2.986	2.557	2.994	2.544	3.009	4.225
V-Mn			2.980	2.543	2.993	2.538	3.010	4.223
V-Fe	2.978	2.547	2.973	2.546	2.992	2.547	3.002	4.219
V-Co	2.978	2.565	2.973	2.562	2.991	2.568	2.988	4.220
V-Ni	2.982	2.592	2.980	2.588	2.993	2.601	2.969	4.229
V-Zr			3.036	2.722				
V-Nb			3.020	2.659				
V-Pd	3.002	2.650	2.998	2.641	2.998	2.664	3.008	4.230
V-Hf			3.036	2.714				
V-Ta			3.023	2.666				
V-Pt	3.002	2.643	2.998	2.634	2.998	2.654	3.007	4.239

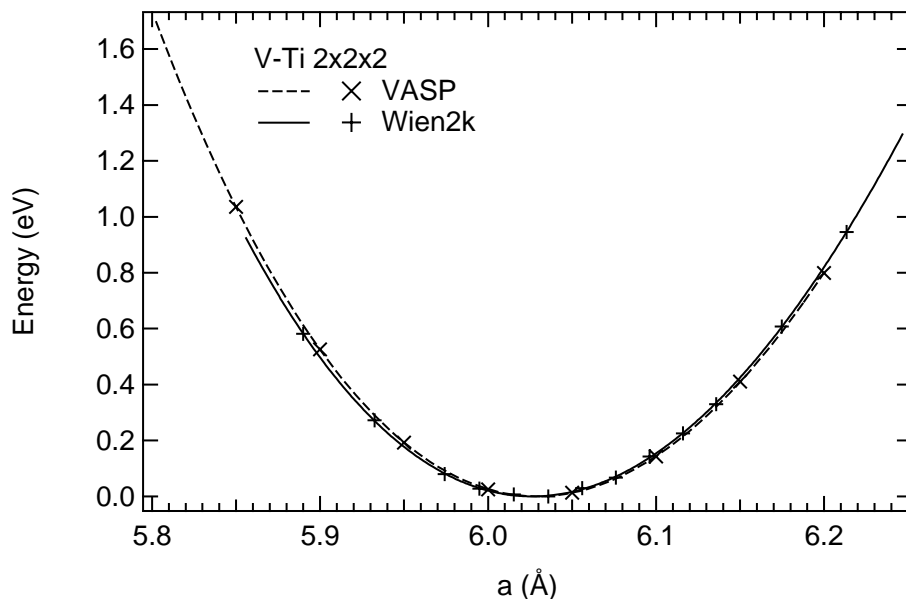


Figure 5.2: Comparison of volume relaxation curves from Wien2k and VASP for  $V_{15}Ti_1$ . The lines are fits to the Murnaghan equation of state.

and can be overcome by looking at the relative change in lattice parameter  $\Delta a/a$  between pure vanadium and the alloys. This quantity is plotted in figure 5.3. As seen on this figure, there is good agreement between the experimental and calculated change in lattice parameter. This indicates that the relaxation effect upon introduction of the impurities is captured well by the DFT simulations. The deviations are not much larger than the experimental uncertainties, except in the case of V-6.25%Ti, for which  $\Delta a/a$  is overestimated by about 50% in both the FP-LAPW and PAW calculations. Both types of simulations reproduce well the overall trend across the  $3d$ -series, with first a linear contraction, followed by an upward curvature of  $\Delta a/a$ .

This trend is due mostly to the change in 1NN bond length, as we will now discuss. Figure 5.4 shows the calculated change in 1NN bond length  $\Delta L_1/L_1$  for the  $3d$ -series. The values of  $\Delta L_1/L_1$  obtained from FP-LAPW and PAW calculations are in very good agreement and present a similar behavior as  $\Delta a/a$ . The magnitude of the change is much larger however, as physically expected. The upward curvature for later transition metal impurities is also stronger in  $\Delta L_1/L_1$  than in the lattice parameter, with almost no net change in 1NN bond length in the case of Ni impurities. This indicates that for Ni, the

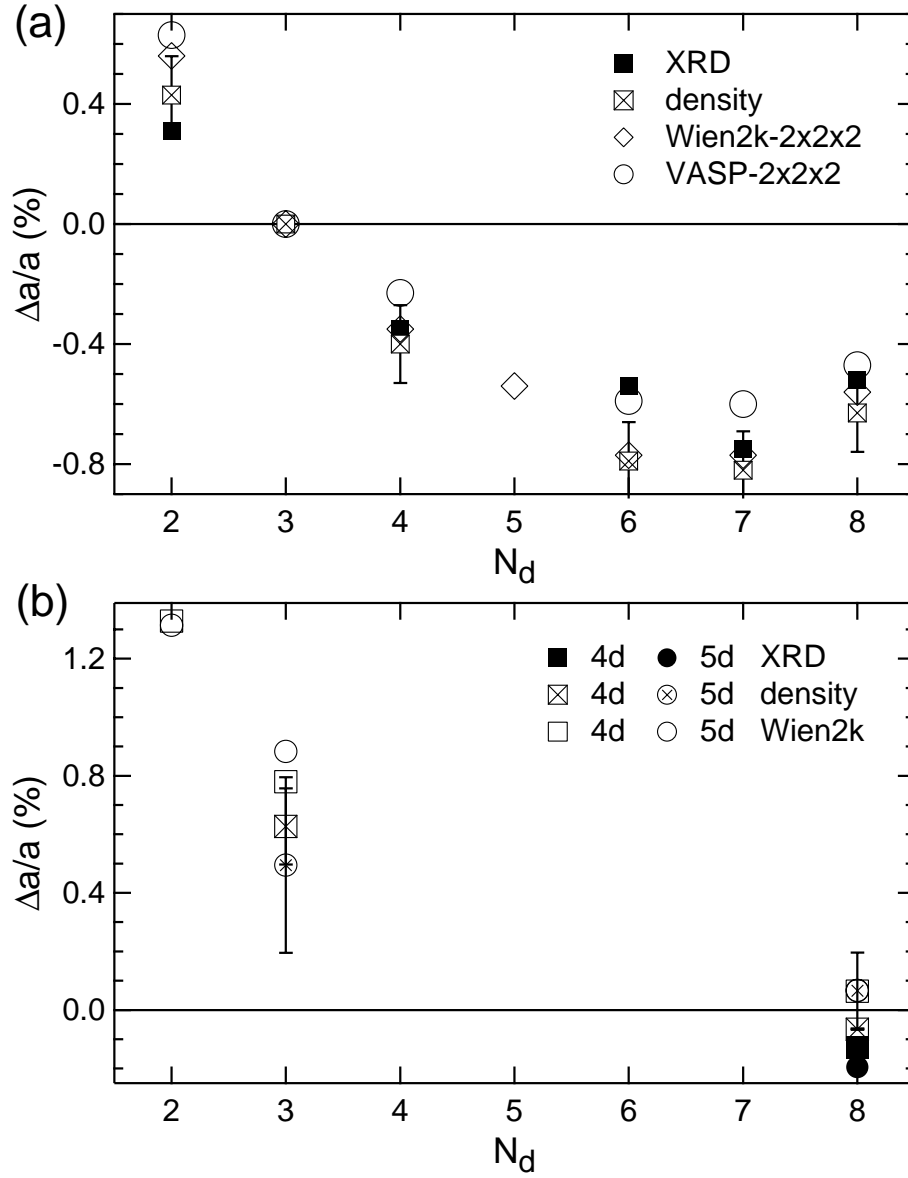


Figure 5.3: Relative change in lattice parameter between V-6.25%X alloys and pure V. (a): impurities in the 3d-series, (b): impurities in the 4d and 5d-series.  $N_d$  is the formal number of  $d$  electrons of the impurity.

relaxation involves predominantly further NN shells. The values of  $L_{1NN}$  calculated on the  $3 \times 3 \times 3$  supercells are close to those obtained on the  $2 \times 2 \times 2$  supercells, which shows that the impurity-impurity interactions are relatively weak for a concentration of 6.25%, when the impurities are separated by 6-th NN bonds as in the case of the ordered  $2 \times 2 \times 2$  structure. The positions of 2NN and 3NN atoms around the impurity in the  $2 \times 2 \times 2$  supercell are constrained by symmetry, so we used  $3 \times 3 \times 3$  supercells to investigate the relaxation of these shells. The results are plotted in figure 5.5. This figure clearly shows that the relaxation predominantly occurs in the 1NN bonds, at least for earlier transition metal impurities up to Fe. For these elements, the relaxation in  $L_{1NN}$  is more than four times larger than in  $L_{2NN}$  or  $L_{3NN}$ . For Co impurities, this ratio decreases to about three and in the case of Ni the relaxation affects mostly  $L_{2NN}$ . For the other impurities of the Ni-column, Pd and Pt, the relaxation in the 1NN shell is sizeable, with 2.6% and 2.3% increase in 1NN bond lengths for Pd and Pt impurities, respectively. The strain is also positive for 2NN bonds in the case of Pd and Pt impurities (about 0.4% increase). In all cases, the strains decay to negligible levels beyond the 3NN shell.

An interesting aspect is the alternating sign in the strain as the distance from the impurity increases, for impurities in the  $3d$ -series. This feature may be related to Friedel oscillations in the electronic density. However, Singh *et al.* have also reported predictions of such oscillations in the strain around impurities in V [106], based on purely mechanical considerations of lattice forces. Singh *et al.* used an analytical potential for interionic interactions in transition metals developed by Wills and Harrison [107] and performed calculations of the strain induced by transition metal impurities (Ti, Cr, Mn, Fe, Nb, Mo, Ta, W) in vanadium with the Kanzaki lattice statics method [108]. The strains they calculated show trends similar to our results, but are much smaller in magnitude, by about a factor of three. Also, the calculations of Singh *et al.* predict a maximum strain at the 2NN shell for all the impurities they considered (except W), which disagrees with our results. It is likely that their results suffer from the stringent approximations that were used, in particular the neglect of charge transfer between the solute and host atoms as well as the central potential approximation and the inclusion of ion-ion interactions only up to 2NN. Also, the electric field gradient around the impurities calculated by the same authors in

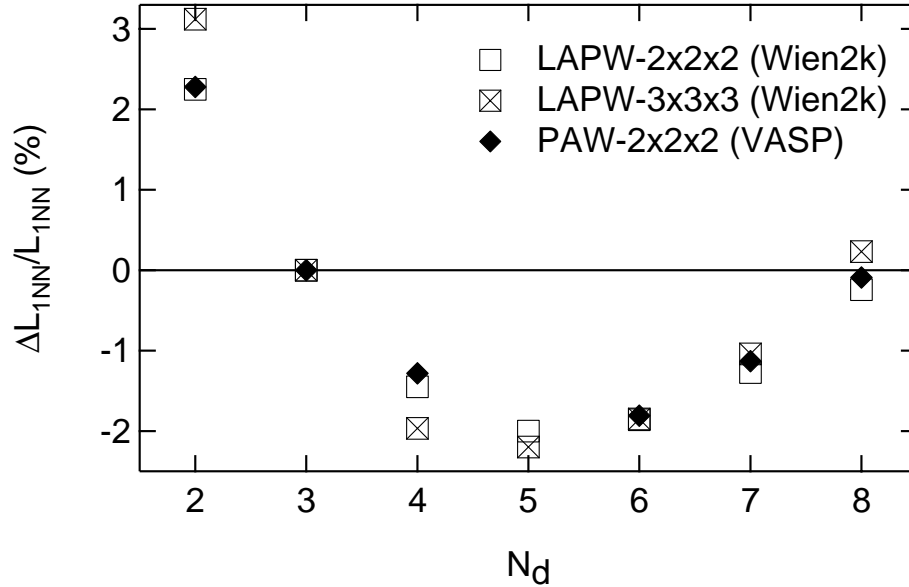


Figure 5.4: Impurity-host 1NN bond-length calculated for different supercells.

a subsequent study are not in very good agreement with experimental results [109]. This discrepancy also illustrates the difficulty of making reliable predictions for transition metals using simple analytical potentials.

## 5.4 Electronic Structure

The electronic density of states (DOS) was computed with Wien2k on the relaxed  $2 \times 2 \times 2$  supercells, using a Monkhorst-Pack grid of  $21 \times 21 \times 21$  k-points (286 points in the IBZ). The electronic densities of states for pure vanadium and the alloys with  $3d$ -series elements are shown in figure 5.6. The electronic DOS in this discussion includes the factor of two for both up and down spins. As can be seen in this figure, the electron DOS shows a systematic behavior as the impurity element changes from Ti to Ni. For early transition metal impurities, the conduction band is shifted to lower energies with no change of shape to first order, hence exhibiting a “rigid-band” behavior. Early theoretical considerations have predicted that upon introduction of dilute impurities in a metal, the electron DOS is

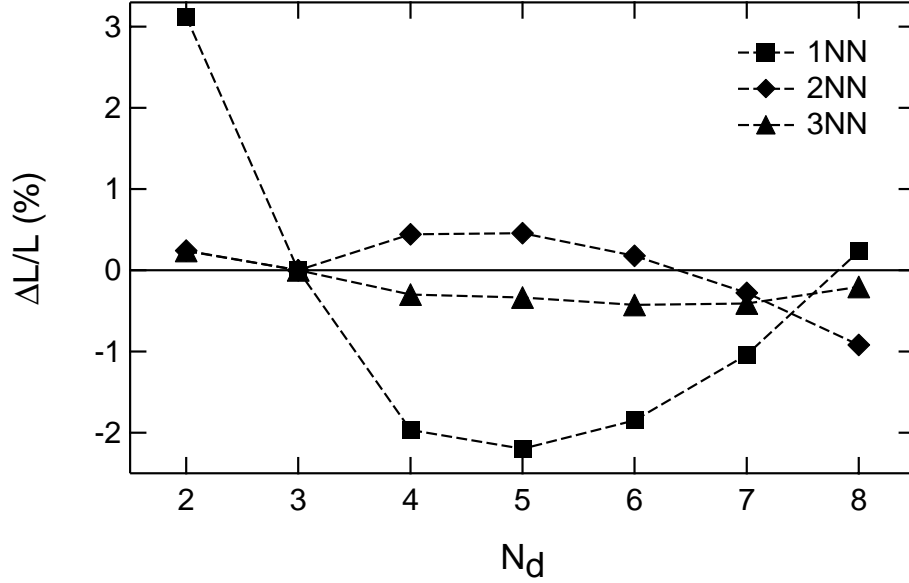


Figure 5.5: Impurity-host bond-length for 1NN, 2NN and 3NN bonds in Wien2k 3x3x3 supercells.

modified up to second order only by a rigid energy shift  $\Delta E$ :

$$n(E) \simeq n_0(E - \Delta E) + \mathcal{O}_2(V_p), \quad (5.2)$$

where  $V_p$  is the perturbing potential due to the introduction of the impurity and  $\Delta E$  is the average of the perturbation potential:

$$\Delta E \simeq \mathcal{V}^{-1} \int_{\mathcal{V}} V_p d\tau + \mathcal{O}_2(V_p), \quad (5.3)$$

with  $\mathcal{V}$  the volume of the system. The reader can refer for example to Friedel's treatment in [110]. Alternatively, in the rigid-band picture, this energy shift upon introduction of impurities with extra  $d$ -electrons can be seen as a simple filling of the  $d$ -band. The energy shift in the case of Ni solutes is about 0.2 eV. From the integrated electron DOS for pure V, one finds that this requires about one-third of an electron, in good agreement with the 5/16 extra electrons per atom introduced by the Ni solutes. However, one cannot expect this argument to be valid for impurities that are very different to the host, such as the  $4d$  and  $5d$  elements. One can also notice on fig. 5.6 that the rigid-band description starts to fail for

later transition metal impurities, with the appearance of new features, such as states filling the pseudo-gap (see for example the  $e_g$  peak for Fe, Co and Ni in Fig. 5.8) and a generally more “wiggly” density of states. However, some of these features are associated with the ordered nature of the supercell used in the simulation and one expects the electron DOS for the random solid solution to be more washed out.

Another important feature of the electronic structure of an alloy is the electronic structure at the Fermi level,  $n(E_F)$ . This quantity determines for example the electronic specific heat, given at low temperatures by [49]

$$\begin{aligned} C_{\text{el}}(T \sim 0) &= \gamma T, \\ \gamma &= \frac{\pi^2}{3} k_B^2 n(E_F). \end{aligned} \quad (5.4)$$

In the case of metals with a significant electron-phonon coupling, there is an additional factor  $(1 + \lambda)$ , corresponding to an effective mass enhancement factor for the electrons [53]. At higher temperatures this simple linear temperature behavior of  $C_{\text{el}}(T)$  (with or without electron-phonon coupling) starts to break down as the Fermi distribution populates states at energies sufficiently high above  $E_F$  that the actual shape of  $n(E)$  has to be taken into account. More on this will be said in chapter 6. The quantity  $n(E_F)$  also influences the electron-phonon coupling parameter  $\lambda$ , as discussed in the next section. Because the Fermi level in pure V sits on the shoulder of the  $t_{2g}$  peak below the pseudo-gap, the filling of the band in this region yields a decrease of the electron density at the Fermi level. We will describe this more quantitatively below.

For an alloy, it is interesting to consider the local density of states on an atom, for the different species present [97, 111]. In the simulation code Wien2k, this quantity is readily available, and already decomposed into orbital angular momentum components, inside the atomic spheres. In Fig. 5.8, we plot the local  $d$ -density of states on the impurity atoms (sphere of radius  $R_{\text{MT}} = 1.164 \text{ \AA}$ ). One can see that the  $d$ -states of the impurity are shifting to lower energy with increasing  $Z$  and that their width is narrowing, indicating more atomic-like orbitals. The lower center of gravity of the impurity  $d$ -states tends to induce a charge transfer from the host vanadium atoms to the impurity [97]. We will present below

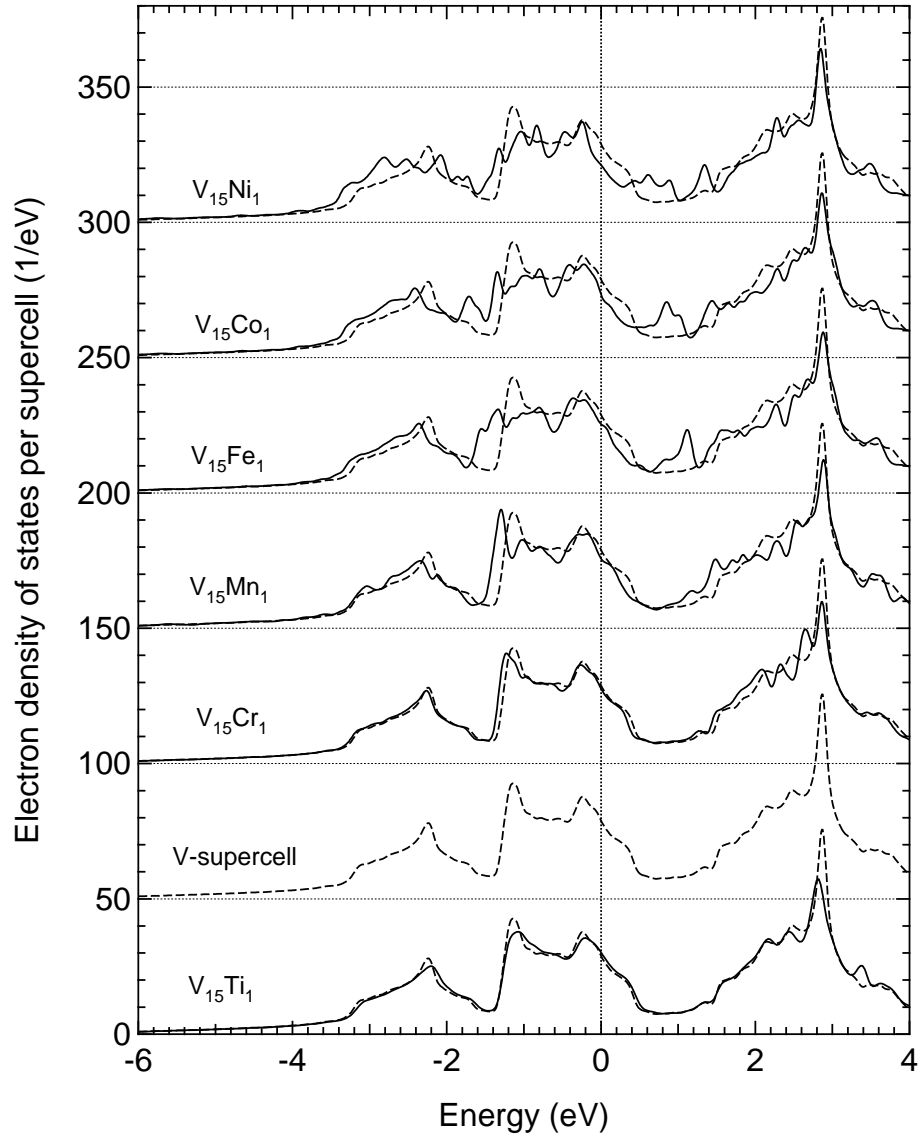


Figure 5.6: Electronic density of states for pure vanadium and the relaxed  $V_{15}X_1$   $2 \times 2 \times 2$  supercells for  $3d$  impurities, calculated with Wien2k. Broken curves: pure vanadium; solid curves:  $V_{15}X_1$ . The Fermi level is taken as origin of energy.

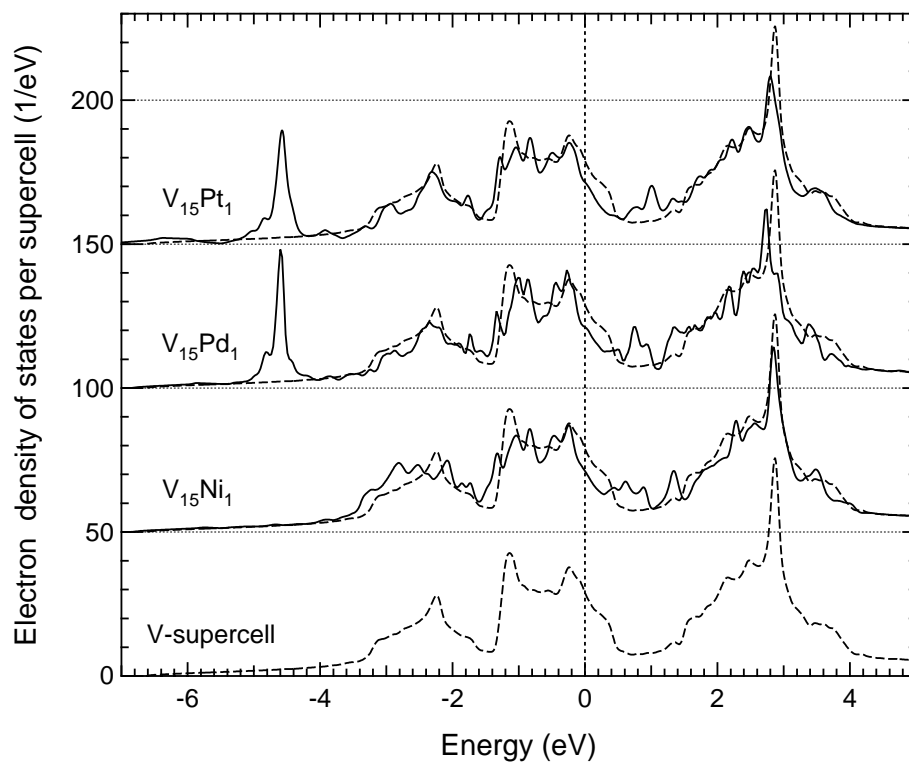


Figure 5.7: Electronic density of states for pure vanadium and the relaxed  $V_{15}X_1$   $2 \times 2 \times 2$  supercells for column VIII impurities, calculated with Wien2k. Broken curves: pure vanadium; solid curves:  $V_{15}X_1$ . The Fermi level is taken as origin of energy.

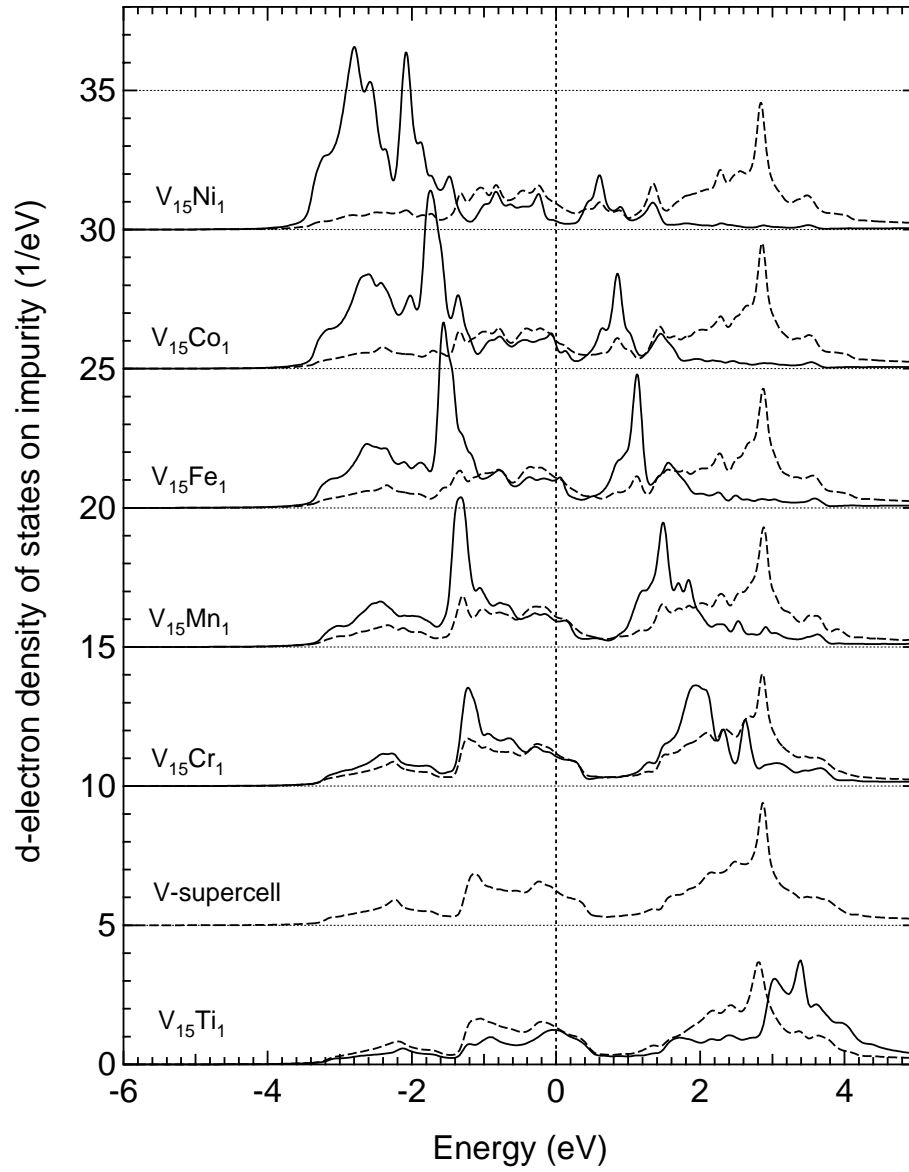


Figure 5.8: Local  $d$ -electron density of states on impurity calculated with Wien2k ( $2 \times 2 \times 2$  supercells), for  $3d$  impurities. Broken curves: pure vanadium; solid curves:  $V_{15}X_1$ . The Fermi level is taken as origin of energy.

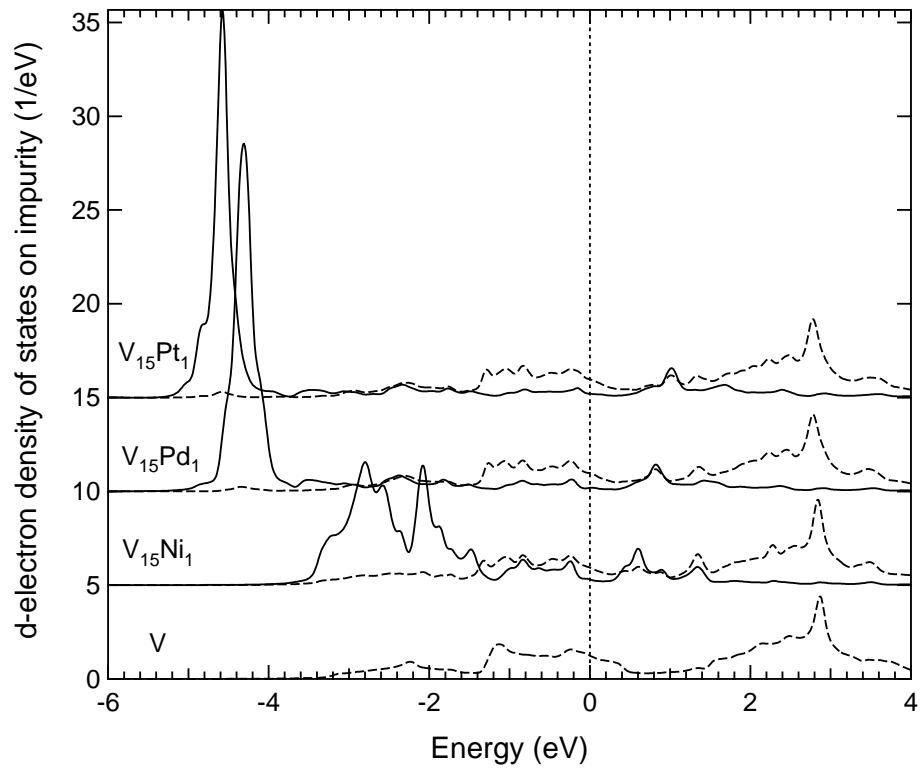


Figure 5.9: Local  $d$ -electron density of states on impurity calculated with Wien2k ( $2 \times 2 \times 2$  supercells), for column VIII impurities. Broken curves: pure vanadium; solid curves:  $V_{15}X_1$ . The Fermi level is taken as origin of energy.

quantitative calculations of the charge transfer. Figures 5.7 and 5.9 show the electron DOS and local  $d$ -electron DOS respectively for the alloys V-Ni, V-Pd and V-Pt. The same trends described in the above discussion are observed, with the impurity  $d$ -levels shifting to even lower energies and becoming more localized as one goes down this column of the periodic table.

## 5.5 Electronic Topological Transition

It is generally accepted that the rigid-band model holds well for metallic alloys of elements that are neighbors in the periodic table. Our simulations support this view in the case of V-6.25%Ti, V-6.25%Cr and V-6.25%Mn alloys. It has been discussed in chapter 4 that the elastic constant  $C_{44}$  in BCC alloys of V-Cr presents an anomaly for a band-filling corresponding to about  $5.4 e/\text{atom}$ . This anomaly has been ascribed to an electronic topological transition [64, 66]. Electronic topological transitions (ETT) correspond to topological changes in the Fermi surface, such as a sheet of the surface disappearing or two portions becoming disconnected or merging. These can arise when the volume is changed through increasing external pressure, for example, although the conditions would have to be extreme. They are more commonly known to arise with alloying, which simply changes the band-filling in a rigid-band model [112]. Although their effects are currently not fully understood, ETTs have been related to anomalies in the elastic constants, the thermal expansion coefficient, phonon dispersions, and thermodynamic properties [112, 113, 114].

We investigated the Fermi surface of BCC V for different band-fillings. The band-fillings correspond to different compositions of a V-Cr alloy, in the rigid-band model. The Fermi surface was computed starting from the Wien2k self-consistent density and potential, and performing a band structure calculation with  $10^4$   $\mathbf{k}$ -points in the Brillouin zone. The calculation was performed with the software Xcrysden [115]. Results are illustrated in figure 5.10. High-symmetry points and directions for the BCC lattice Brillouin zone are labelled in Fig. 5.11.

For pure V ( $5 e/at$ ), the Fermi surface is composed of an octahedron at  $\Gamma$ , ellipsoids at N and a multiply connected “jungle-gym” manifold. As the band-filling increases, the octahedron sheet thins down to a cross and disappears at about  $5.4 e/at$ , while the “jungle-

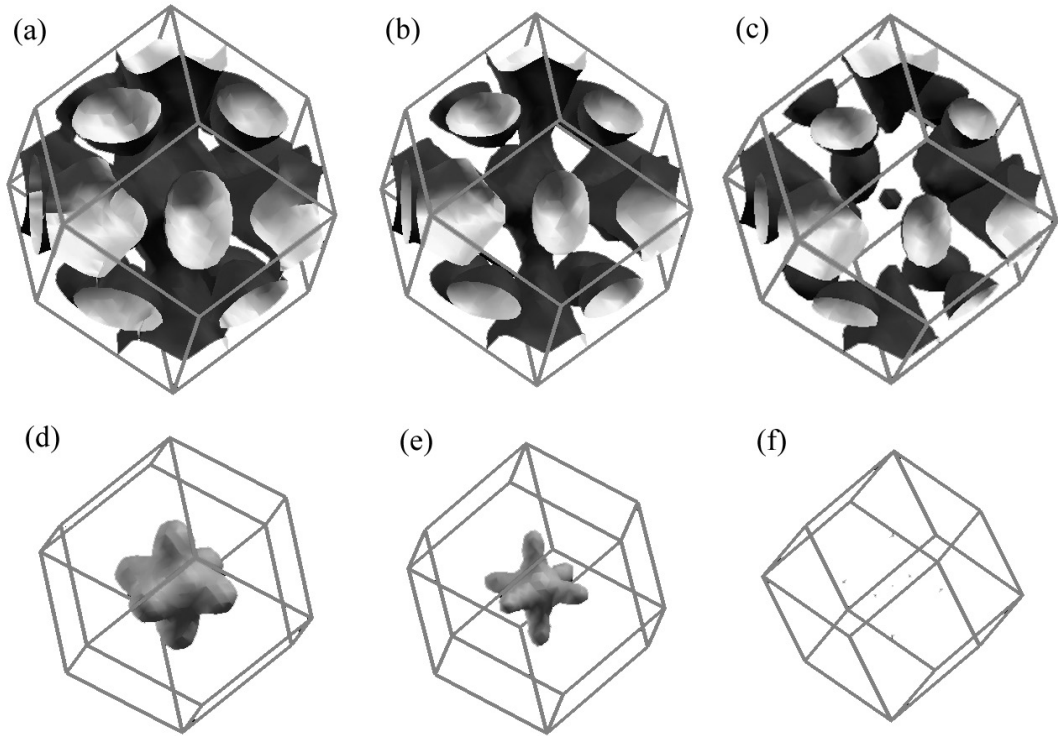


Figure 5.10: Topological transition in Fermi surface of V-Cr alloys. The Fermi surface is calculated with Wien2k for bcc V, with different values of band-filling. (a), (b), (c): Jungle-gym and N-point ellipsoids for 5, 5.2, and  $5.4 e/at$ , respectively. (d), (e), (f): octahedron sheet at the same respective electron concentrations as (a), (b), and (c).

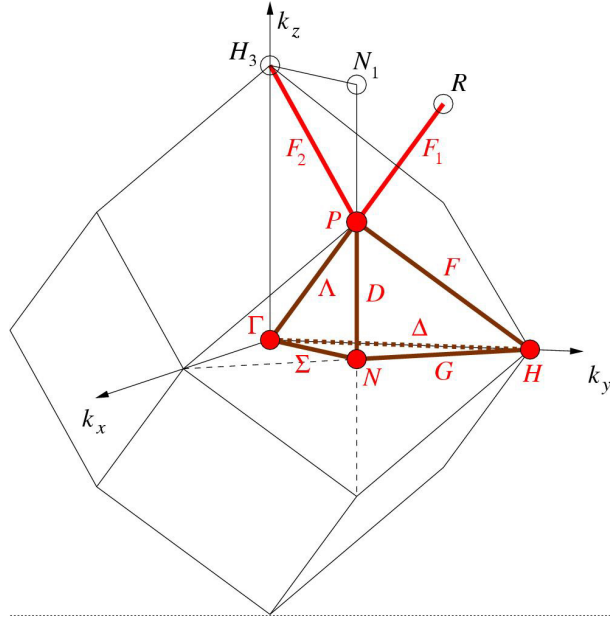


Figure 5.11: Brillouin zone for BCC lattice.

gym” sheet of the Fermi surface becomes disconnected and breaks down into a small pocket at  $\Gamma$  and a “star” around  $H$ . This topological transition corresponds to a large decrease in the area (and number of states) of the Fermi surface. This could lead to an important change in the wave vectors spanning by the Fermi surface sheets that may consequently affect the electron-phonon coupling. A similar ETT has been reported in Nb-Mo alloys, also at  $5.4 e/at$ , and has been correlated to a decrease in electron-phonon coupling strength with increasing number of valence electrons [112].

## 5.6 Superconductivity and Electron-Phonon Coupling

Vanadium is a superconductor at low temperatures. The transition temperature  $T_c = 5.3$  K is one of the highest for pure elements [116]. In the BCS theory of superconductivity, the electron-phonon coupling is the mechanism responsible for pairing of the electrons in Cooper pairs. The strength of the interaction between electrons and phonons, as quantified by the parameter  $\lambda$ , is related to the electronic density at the Fermi level as well as the average phonon energy. In the McMillan theory of strong-coupled superconductors [117],

the electron-phonon coupling constant  $\lambda$  is given by

$$\lambda = \frac{n(E_F)\langle I^2 \rangle}{M\langle \omega^2 \rangle}, \quad (5.5)$$

where  $n(E_F)$  is the electron density at the Fermi level,  $\langle I^2 \rangle$  is the average over the Fermi surface of the square of the electron-phonon interaction matrix element,  $M$  is the nuclear mass, and the average phonon frequency square  $\langle \omega^2 \rangle$  is defined by

$$\langle \omega^2 \rangle = \frac{\int d\omega \omega \alpha^2 F(\omega)}{\int d\omega \alpha^2 F(\omega)/\omega}, \quad (5.6)$$

with  $\alpha^2 F(\omega)$  the direction-averaged Éliashberg coupling function. The superconducting transition temperature in McMillan's theory is estimated as

$$T_c = \frac{\theta}{1.45} \exp \left[ \frac{-1.04(1 + \lambda)}{\lambda - \mu^*(1 + 0.62\lambda)} \right], \quad (5.7)$$

where  $\mu^*$  is the effective Coulomb repulsion potential for the electrons and  $\theta$  is a representative average phonon temperature, such as the Debye temperature or the temperature corresponding to the average phonon energy. This formula was slightly revised by Allen and Dynes [118], but it will serve our purpose here.

As mentioned in the previous section, because of the negative slope in  $n(E)$  at the Fermi level, the introduction of impurities raises or decreases  $n(E_F)$  when the solutes have fewer or more  $d$ -electrons than vanadium, respectively. The results of our calculations of  $n(E_F)$  with Wien2k, using  $10^4$   $\mathbf{k}$ -points, are shown in figure 5.12. The decrease in  $n(E_F)$  appears approximately linear with the number of  $d$ -electrons of the impurity,  $N_d$ . In fig. 5.13, we compare the relative change in the calculated  $n(E_F)$  with the same experimental quantity, deduced from low-temperature measurements of the electronic specific heat. The agreement is good, although our calculations predict slightly smaller effects upon alloying. For impurities in the Ni column, the decrease in  $n(E_F)$  is about 20%. This electronic contribution to the change in the electron-phonon coupling  $\lambda$  (cf Eq. 5.5) can be compared to the phonon contribution coming from the factor  $\langle \omega^2 \rangle$ . From the values listed in table 5.2, we see that the phonon effect on  $\lambda$  is comparable to that of  $n(E_F)$ .

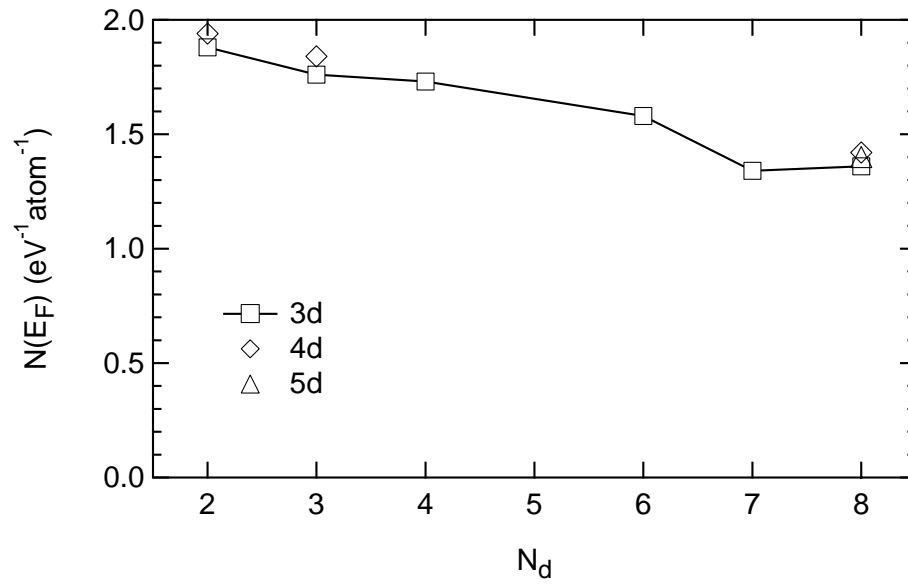


Figure 5.12: Electronic density at the Fermi level calculated with Wien2k.

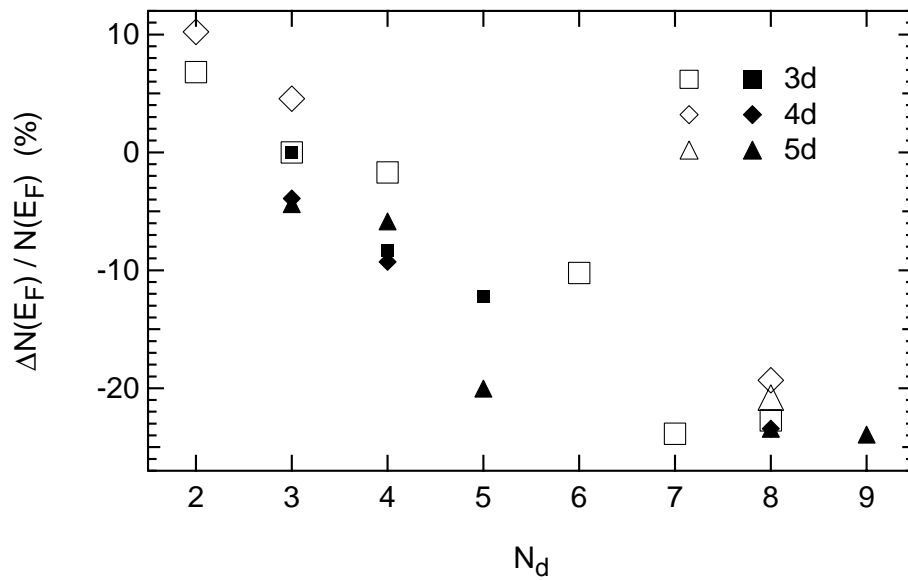


Figure 5.13: Change in electronic density at the Fermi level upon alloying. Open symbols: Wien2k calculation for  $2 \times 2 \times 2$  supercells; full symbols: experimental results (see text).

Table 5.2: Superconductive properties for V-6.25%X alloys.

X	$T_c^\ddagger$ (K)	$T_c$ ref.	$\langle \hbar\omega \rangle^*$ (meV)	$n(E_F)^\dagger$ (eV <sup>-1</sup> at. <sup>-1</sup> )	$\lambda$
Ti	6.00	[119]	22.3	1.88	0.71
V	5.30	[73]	22.9	1.76	0.68
Cr	3.74	[73]	23.1	1.73	0.61
Mn	3.31	[73]	-	-	-
Fe	2.07	[120]	23.6	1.58	0.52
Co	-		23.9	1.34	-
Ni	-		23.7	1.36	-
Zr	5.36	[119]	22.0	1.94	0.69
Nb	4.54	[73]	22.4	1.84	0.65
Mo	3.62	[73, 121]	-	-	-
Tc	2.93	[122]	-	-	-
Ru	0.80	[123]	-	-	-
Rh	0.55	[123]	-	-	-
Pd	2.22	[73]	24.5	1.42	0.53
Hf	5.18	[119]	21.9	-	0.68
Ta	4.42	[73, 120]	22.6	-	0.64
W	4.20	[73]	-	-	-
Re	2.46	[73]	-	-	-
Os	0.96	[124]	-	-	-
Pt	2.22	[73]	25.1	1.40	0.52
Au	1.71	[73]	-	-	-

<sup>‡</sup>Extrapolated to 6.25% impurity concentration

\*From phonon DOS measurement

<sup>†</sup>From Wien2k simulations

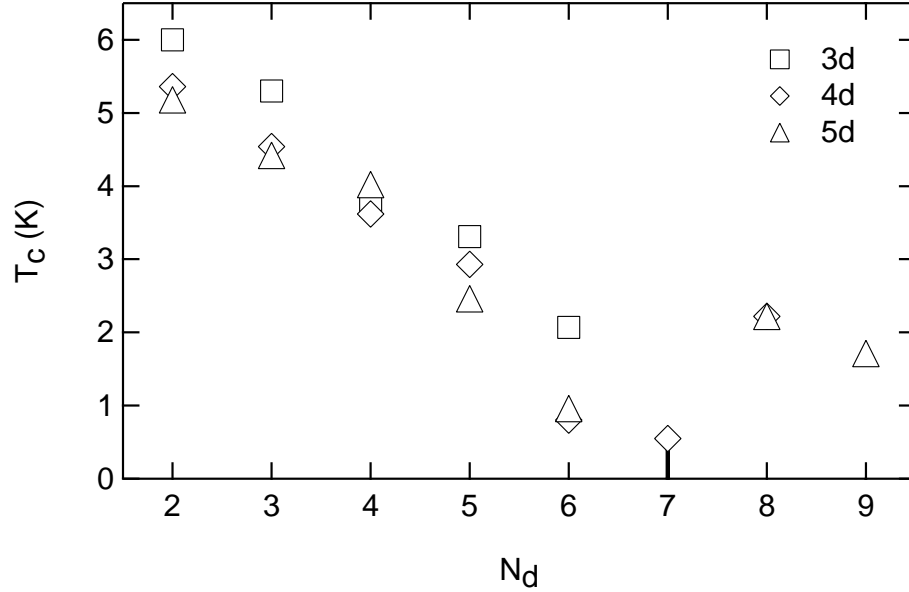


Figure 5.14: Estimated superconducting critical temperature for V-6.25%X.

Using published measurements of  $T_c$  for V-X alloys with impurity concentrations less than 10% (typically 5% and 10% impurities), we linearly extrapolated the value of  $T_c$  for alloys V-6.25%X. Our results are summarized in table 5.2 and shown in figure 5.14. We extracted values of  $\lambda$  from these critical temperatures for the alloys whose phonon DOS we measured. We used Eq. 5.7, in which we set  $\theta = \hbar\langle\omega\rangle/k_B$  and used  $\mu^* = 0.13$ , a value commonly used for transition metals. Results are listed in table 5.2 and plotted in figure 5.15. The fractional variation of  $\lambda$  for all the impurities exceeds 20%, which may have significant effects on the electron-phonon coupling in these alloys.

## 5.7 Electronic Entropy

The electronic entropy at finite temperature is associated with the availability of unoccupied states above the Fermi level and is given by

$$S_{\text{el}} = -k_B \int_{-\infty}^{\infty} [(1 - f_{T,E})\ln(1 - f_{T,E}) + f_{T,E}\ln(f_{T,E})] n(E) dE, \quad (5.8)$$

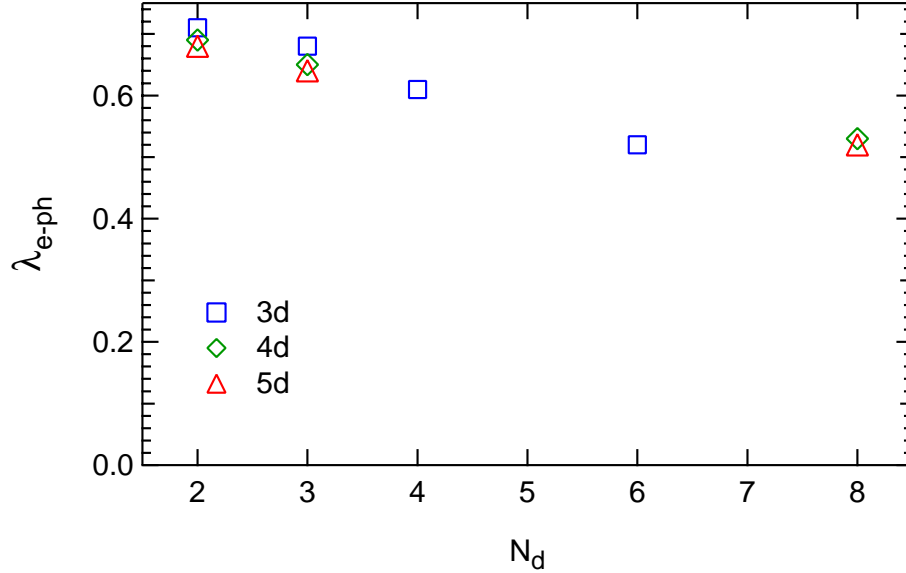


Figure 5.15: Electron-phonon coupling strength for V-6.25%X.

where  $f_{T,E}$  is the Fermi distribution function and  $n(E)$  is the electronic density of states at energy  $E$  [52]. Using the electronic densities of states obtained from FP-LAPW simulations for the relaxed  $2 \times 2 \times 2$  supercells, we calculated the difference in electronic entropy between the pure vanadium and the alloys  $V_{15}X_1$ , or electronic entropy of alloying at temperature  $T$ ,  $\Delta S_{el}^{al}(T)$ . Our results for  $T = 295$  K are plotted in figure 5.16. Comparing these results with the vibrational entropy of alloying  $\Delta S_{vib}^{al}(295 \text{ K})$  of figure 4.18, one can see that  $\Delta S_{el}^{al}$  is much smaller than  $\Delta S_{vib}^{al}$  for the alloys investigated, with the exception of V-6.25%Ni. In this case,  $\Delta S_{el}^{al}$  is about half of  $\Delta S_{vib}^{al}$ , while in all other cases, it is smaller by a factor of five or more. The thermodynamic contribution of  $\Delta S_{el}^{al}(T)$  is thus expected to be small at low temperatures, although it may play a more important role at high temperatures, as we will discuss in the next chapter. Also, in the case of the dilute vanadium alloys investigated,  $\Delta S_{el}^{al}$  follows a similar trend as its vibrational counterpart, with a positive contribution for solutes to the left of V in the periodic table and an increasingly negative contribution for those to the right. This extra contribution to the total entropy of alloying thus augments the vibrational contribution.

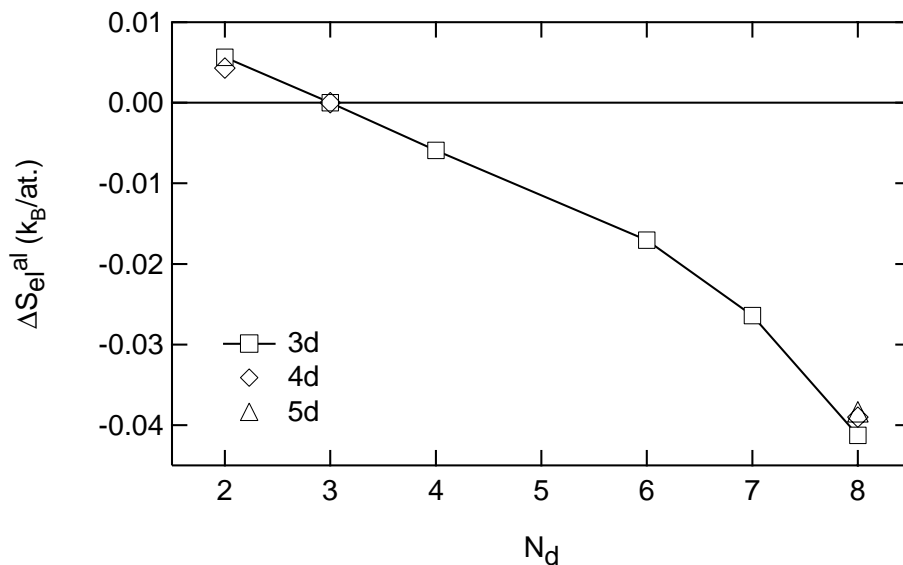


Figure 5.16: Electronic entropy of alloying at 295 K for  $V_{15}X_1$  relaxed supercells.

## 5.8 Charge Transfer

Chapter 4 reported an experimental correlation of the phonon frequencies with the Pauling electronegativity of the solutes. We investigated this further by performing first-principles charge transfer calculations. The concept of atomic charges is one of interest to chemists and solid-state physicists, as it is helpful for a simple description of solids and molecules and it naturally arises in a variety of contexts. There is, however, no unique way of ascribing the electron density in a condensed-matter system (or a molecule) to the atoms that compose it. Many different definitions of atomic charges have been given, inspired by different models, and they are unfortunately not equivalent. Some methods for partitioning the electrons between the atoms adopt orbital-projection schemes, the most widespread being the Mulliken population analysis. Other approaches partition the electronic density based on topology (Bader analysis) or the geometrical configuration of the nuclei (Voronoi analysis) [125, 126]. Another method uses the relative contribution of each atom to the superposition of atomic densities, before any bonding redistributes the charge, to determine the contribution associated with the atom (Hirshfeld analysis). These schemes are all based on the notion of static charges attached to host nuclei. Another class of models focuses on the change in polarization upon displacements of the atoms, introducing the concept of

Table 5.3: Bader charge transfer (in number of electrons) calculated with Wien2k.

	$N_d$	$\chi_{\text{Pauling}}$	$\chi_{\text{Watson}}$	X	V1nn*	V2nn*	V3nn*
Ti	2	1.54	1.38	-0.565	0.442	0.140	0.002
V	3	1.63	1.62	0.000	0.000	0.000	0.000
Cr	4	1.66	1.69	0.477	-0.375	-0.098	-0.008
Mn	5	1.55	1.74	0.929	-0.763	-0.123	-0.051
Fe	6	1.83	1.93	1.130	-0.934	-0.141	-0.074
Co	7	1.88	1.95	1.190	-1.013	-0.133	-0.092
Ni	8	1.91	2.09	1.125	-0.979	-0.114	-0.097
Zr	2	1.33	1.37	-0.421	0.360	0.103	-0.051
Nb	3	1.6	1.69	0.198	-0.088	-0.070	-0.022
Pd	8	2.2	2.22	1.440	-1.152	-0.248	-0.080
Hf	2	1.3	1.4	-0.375	0.333	0.071	-0.029
Ta	3	1.5	1.74	0.327	-0.157	-0.147	-0.004
Pt	8	2.28	2.28	1.864	-1.446	-0.388	-0.087

\*Taking into account the multiplicity

dynamical charges (*e.g.*, Born dynamical charges) [127, 128].

In analyzing the electronegativity correlation discussed in the previous section, we concentrate on the charge analysis introduced by Bader [125], as it provides a well-defined way of partitioning the whole crystal into atomic volumes in which the charge can be integrated. In this approach, the atomic charges are defined based on the topological properties of the electronic density,  $\rho(\mathbf{r})$ . Atoms are defined as the basins delimited by surfaces of zero charge-flux  $\nabla\rho(\mathbf{r}_S) \cdot \mathbf{n}(\mathbf{r}_S) = 0$ , where  $\mathbf{n}(\mathbf{r}_S)$  is the unit vector normal to the surface at point  $\mathbf{r}_S$  on the Bader surface  $S$ . The Bader surfaces are also constrained to go through the critical points (saddle points) between atoms.

The Bader charge analysis is readily implemented in the Wien2k package, while in the VASP calculations, the additional software of Henkelman *et al.* was used to analyze the VASP output density files [129]. Our results for the alloys V-6.25%X with solutes in the

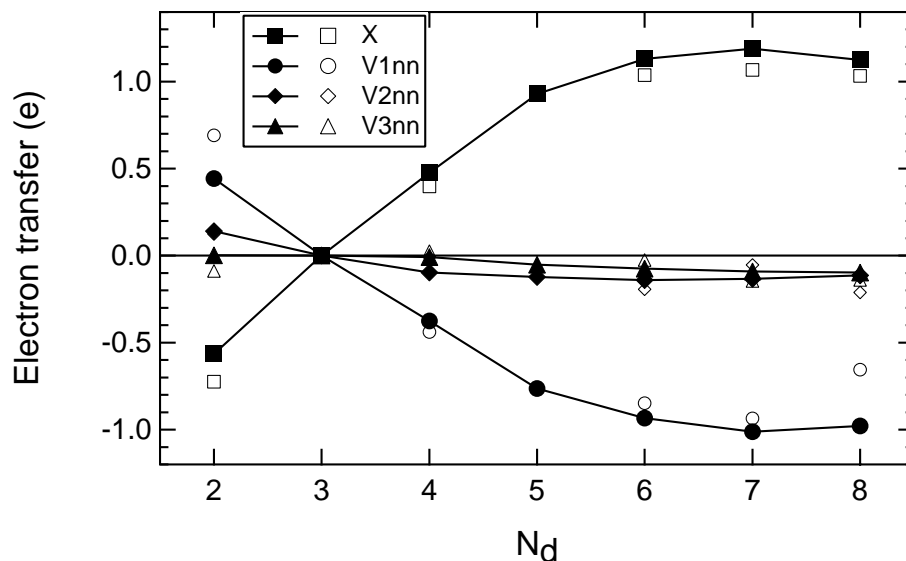


Figure 5.17: Charge transfer onto each atom for impurities across the  $3d$ -series, calculated from first principles using the Bader charge analysis. Solid symbols: Wien2k calculation, open symbols: VASP calculation and Bader analysis with software of Henkelman *et al.* [129].

$3d$ -series are shown in figure 5.17. All Wien2k charge transfer results are listed in table 5.3. A clear trend is observed: Ti ( $N_d = 2$ ) loses some of its valence charge to the surrounding host V atoms ( $N_d = 3$ ), while impurities to the right of V increasingly gain electrons from their V neighbors. The charge transfer to the impurity atom rises linearly from a negative value in  $V_{15}Ti_1$  (loss of electrons) to positive values for Cr and Mn solutes, and subsequently tapers off for Fe, Co and Ni impurities. This behavior is mirrored in the charge transfer to 1NN vanadium atoms around X, while further V neighbors do not participate much in the charge redistribution. In the plot of Fig. 5.17, the charge transfer to each atom type is weighted by the multiplicity of the atom in the supercell. The complementarity of the weighted charge transfer for impurity and 1NN vanadium atoms indicates that the charge redistribution is confined to the 1NN shell around the impurities. Mention should be made of the magnitude of the calculated charge transfers. The values we obtained are very large (plus or minus one electron for Fe, Co, Ni solutes). However, it is known that the Bader charge determination scheme tends to overestimate charge transfer when compared to other

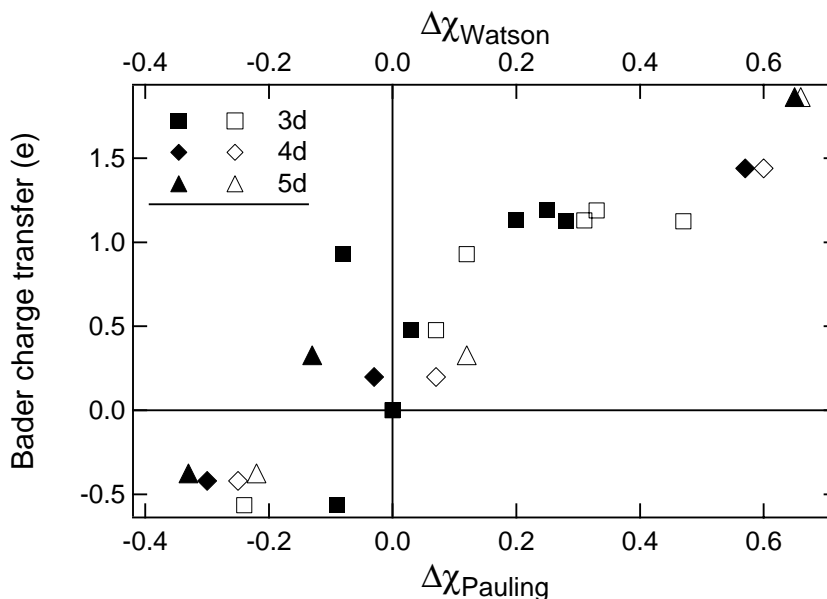


Figure 5.18: charge transfer on impurity calculated with the Bader analysis (Wien2k), plotted against the impurity-host difference in electronegativity on the Pauling (solid symbols) and Watson (open symbols) scales.

methods, such as the Mulliken or Hirshfeld charge analyses [126]. To the extent that charge transfers can only be compared for a given definition of atomic charges, we do not have to worry about this point. In any case, it is expected that the bonding in the physical system is not fully ionic.

Figure 5.18 shows the calculated transfer of charge to the impurity, in the Bader sense, plotted against the difference of electronegativity between impurity and host atoms, on the Pauling and Watson scales. The Watson electronegativity scale is derived from experimental observations of Mössbauer isomer shifts and electronic structure calculations in transition metals [130, 131]. We observe a good correlation between the charge transfer and the electronegativity difference between impurity and host on both scales. The correlation with the Watson scale is substantially better, with in particular all points falling either in the lower-left or upper-right quadrants.

Figure 5.19 shows the experimental vibrational entropy of alloying plotted against the calculated charge transfer and the difference in electronegativity of the impurity and the host atoms on the Pauling scale. The Bader charge transfer values are those obtained with

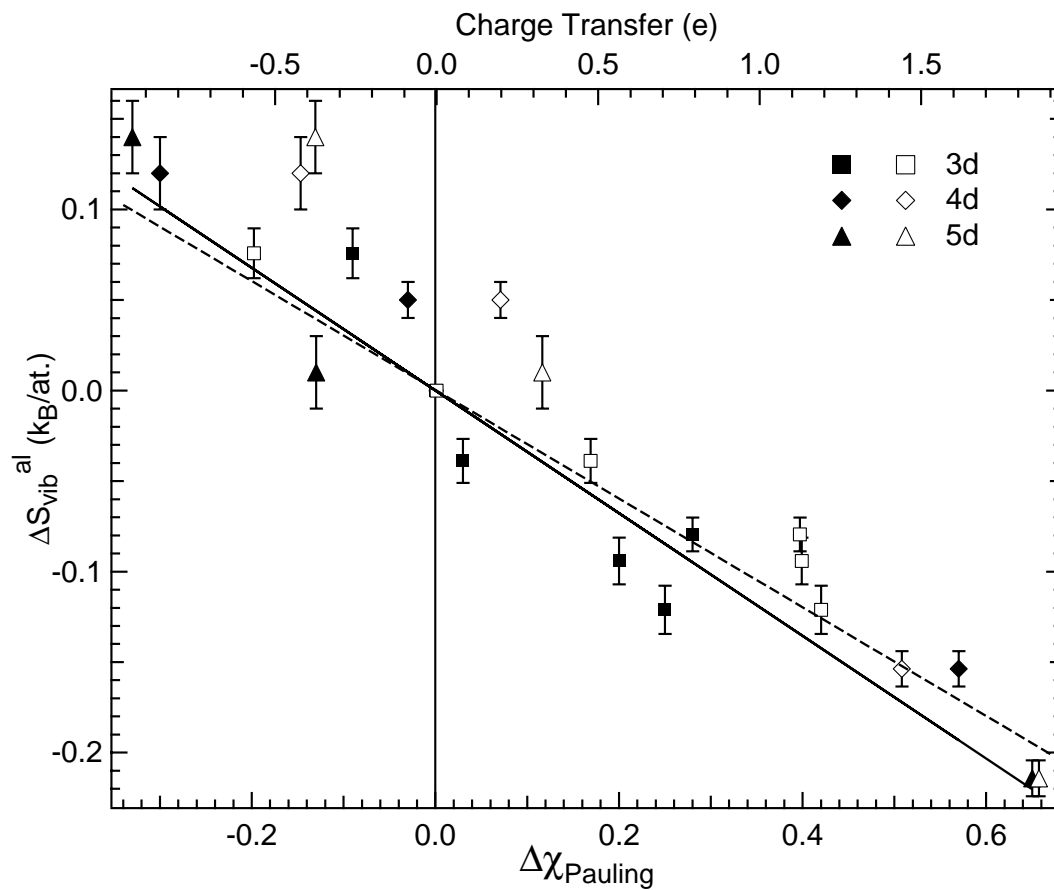


Figure 5.19: Experimental vibrational entropy of alloying plotted against the Bader charge transfer on the impurity calculated with Wien2k (open symbols) and the impurity-host difference in electronegativity on the Pauling scale (solid symbols).

Wien2k on  $2 \times 2 \times 2$  supercells. There is a good correlation between  $\Delta S_{\text{vib}}^{\text{al}}$  and the charge transfer calculated with the Bader analysis, with impurities losing charge to the vanadium atoms inducing a phonon softening (except Nb), while impurities gaining charge from their V neighbors induce a stiffening. This correlation is not as good for large impurities of the  $4d$  series (upper-left quadrant, two most positive values of  $\Delta S_{\text{vib}}^{\text{al}}$ ), but it is possible that size or mass effects for these large solutes influence the phonons differently than the charge transfer.

Thus, it appears that charge transfer effects can explain the experimental trend in the phonons and the vibrational entropy. Large charge transfers between impurity and first-nearest-neighbors produce more ionic bonds, which tend to be stiffer, causing higher-energy phonons. In this electrostatic picture, the charge transfer and the bond length affect the stiffness in opposite ways. Thus, although the V-Ti bond undergoes a charge transfer similar in magnitude to that of the V-Cr bond (but opposite in sign), it should be softer since the bond length is much longer.

## 5.9 Deformation Potential

Over the past 15 years, phonons have become accessible to first-principles calculations. However, *ab-initio* computations of the complete phonon dispersions and density of states remain challenging in the case of transition metals. Early transition metals tend to be especially difficult to treat with the pseudo-potential and plane-wave approach, because they are typically represented with “hard” pseudo-potentials, which require a large number of plane-waves, making the computations costly. We performed test computations on a number of elemental metals within the “direct method” as well as the linear-response approach. We were able to obtain good results for the phonon DOS and dispersions of FCC Al, B2 FeAl, BCC Fe and BCC Cr. However, V and Nb have proven quite a bit harder to tackle. The direct method has consistently failed to produce physical results for long-wavelength phonon modes in Nb and V. For both metals, the direct method tends to predict mechanically unstable transverse modes in the [100] and [110] directions at long wavelengths, but finite k, even for supercells as large as  $6 \times 6 \times 6$ . This difficulty can be traced to the behavior of transverse phonon branches at long wavelengths in BCC metals of

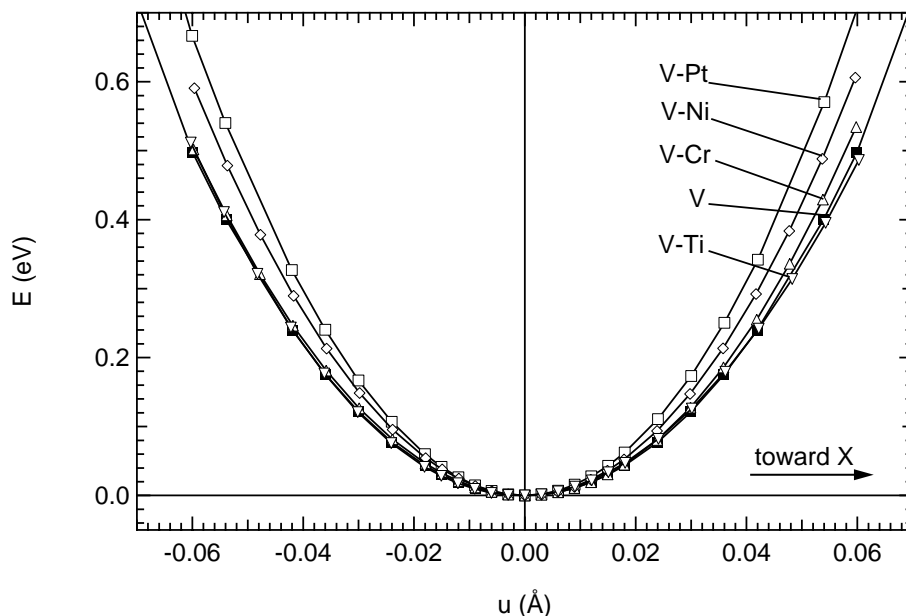


Figure 5.20: Calculated potential for 1NN atom displacements in a breathing mode. The energy is the total supercell energy calculated with VASP. The displacement is counted positive when toward the impurity atom X (1NN shell contraction).

this group. It is known from the experimental dispersion curves and theoretical models that the T[100] and T[110] branches exhibit an anomalous upward curvature in the case of Nb and Ta [132, 96, 133, 134, 135]. Although it is likely that this is also the case in vanadium, as predicted by a few first-principles calculations [135, 136], this is not as well established experimentally, owing to the impossibility of performing coherent neutron scattering experiments on V. The only available dispersion data for V are those measured by Colella and Batterman [79] using thermal diffuse x-ray scattering, and the accuracy of these older measurements is unestablished. Some theoretical investigations based on linear-response DFT have successfully produced phonon dispersions for BCC V, but we are not aware of any phonon calculations on dilute V alloys.

To investigate the change in the interatomic potentials upon introduction of the impurities in V, we resorted to calculations of the deformation potential in a breathing-mode of the 1NN shell around the impurity. We computed the change in total energy of the

$2 \times 2 \times 2$  supercells for 1NN neighbors displaced along the  $\langle 111 \rangle$  directions using VASP with PAW formalism. Owing to the cubic symmetry, all 1NN atoms are displaced toward or away from the impurity by the same amount. This deformation mode is not a proper frozen-phonon, but it allows us to investigate the longitudinal stiffness of the 1NN X-V bond. Results for displacement amplitudes  $u$  up to  $0.06 \text{ \AA}$  (about 2% of  $a$ ) are shown in figure 5.20. The displacement potential for pure V is nearly parabolic over this range of displacements. In the presence of an impurity, the potential exhibits a small amount of asymmetry between positive and negative displacements, as expected. This contributes a small cubic term, but this anharmonicity is small. The potential is increasingly stiffer for Cr, Ni and Pt impurities, whereas Ti induces a small softening for displacements toward the impurity. This trend is in very good agreement with the measured phonon frequencies. A simple fit of parabolas to the displacement potential allows us to estimate the frequencies of this breathing mode. We find an increase in frequency of about 18% for vibrations around the Pt solutes and about 15% around the Ni solutes, compared with the pure V case. This is in good agreement with observed shifts in the frequency of the longitudinal modes, in particular the cutoff frequency.

## 5.10 Summary

Density functional theory calculations were performed on  $V_{15}X_1$  and  $V_{53}X_1$  supercells to model the dilute vanadium solutions investigated experimentally. The predicted lattice parameters agree well with experimental values and the calculated change in lattice parameter between the alloys and the pure host reproduces the experimental trends to within error bars. The strain around the solute atoms was found to occur mostly in the 1NN shell, although it is also significant in the 2NN shell in the case of Co and Ni. The overall trend in the X-V 1NN bond length thus follows that in the lattice parameter. The electronic density calculated on the relaxed supercells showed that the alloys V-Ti, V-Cr and V-Mn behave like in the rigid band model, with minimal deformation of the host electron DOS. On the other hand, late transition metal impurities Fe, Co, Ni, Pd, Pt induce a large restructuring of the electron DOS, with their  $d$ -states being lower in energy than the  $d$ -band in the host V crystal. The electronic density at the Fermi level varies strongly with the impurity, owing to

the large negative slope in  $n(E)$  at  $E_F$  in pure V. This affects the electron-phonon coupling parameter as well as the electronic entropy. The deformation potential for a breathing-mode of the 1NN shell around the impurities was calculated and the same trend is observed as in the phonon measurements. The calculated stiffening of the potential appears to agree broadly with the shift in the experimental frequencies. Within the Bader atomic charge definition, a large charge transfer was found to occur between the solute atoms and their 1NN shell. The trend in the Bader charge transfer behaves linearly with the electronegativity difference between the impurity and the host. This charge transfer offers an explanation for the stiffening of the phonons, as more ionic bonds should be stiffer and induce higher energy phonon modes.

## Chapter 6

# Phonons in Vanadium Alloys at High Temperatures

### 6.1 Introduction

In all early transition metals of groups 3 to 6, the BCC structure is the stable high-temperature phase. From the temperature range over which it is observed, it appears that the BCC phase is stabilized by a larger number of  $d$ -electrons, which has been related to the strengthening of directional bonding [87, 88]. The early transition metals of group 3 and 4 are only stable in the BCC structure at high temperature and undergo martensitic transformations BCC $\rightarrow$ HCP and BCC $\rightarrow$   $\omega$  at low temperatures. The high-temperature stability of the BCC phase for the earlier transition metals is attributed to a stabilization by a large vibrational entropy, owing to low-energy transverse phonons along the [110] and [211] directions (see [88]). On the other hand, the elements of groups 5 and 6 crystallize in the BCC arrangement over the full temperature range of the solid phase, and the melting temperatures for group 6 elements is particularly high. The strengthened directional bonding in these elements increases the mechanical stability of the BCC lattice with respect to martensitic transformations, as evidenced by first-principles frozen-phonon calculations [137, 28, 138, 139].

Another factor is known to stabilize the BCC phase at high-temperatures for elements and alloys with 5 to 6 valence electrons. The electronic density of states of the BCC structure exhibits a pseudo-gap between the low-energy  $t_{2g}$  and high energy  $e_g$  peaks. When the Fermi

level reaches this portion of the DOS with increasing number of  $d$ -electrons, the effect is to effectively lower the occupied states in energy more than in the case of, say, a rectangular  $d$ -band, resulting in an increased cohesive energy. This accounts for the high cohesive energy and melting temperature of Mo and W, and these elements have been likened, at elevated temperatures, to “overheated solids” [140, 141]. As such, they are likely to exhibit large anharmonic effects.

## 6.2 High-Temperature Phonon DOS

### 6.2.1 Pure Vanadium

The phonon DOS of vanadium has been measured up to 1673 K by Bogdanoff, Fultz *et al.*, using triple-axis neutron spectrometry [77]. In the course of this thesis, additional phonon DOS measurements were performed on pure V between 295 K and 1323 K using the Pharos time-of-flight spectrometer at LANSCE. Our results confirm the previous observations of Bogdanoff and coworkers.

The vanadium phonon DOS curves measured by triple-axis spectrometry are shown in Fig. 6.1. The phonon DOS of vanadium is essentially constant up to 1273 K, subject only to broadening. This broadening in energy affects both the transverse and longitudinal peaks. On the other hand, the DOS undergoes a large softening between 1273 K and 1673 K. The phonon broadening is an effect of damping, and the phonon linewidth  $\Gamma$  is related to the damping rate. Anharmonicity is a possible source of such damping, since it causes more frequent phonon scattering events, as was discussed in chapter 2 (see Eq. 2.53). By convoluting the 293 K phonon DOS with the line shape for a damped oscillator to best reproduce the higher-temperature phonon DOS, Bogdanoff and coworkers were able to extract the average quality-factor for the phonons and found that the modes are substantially damped [77].

The results of our V phonon DOS measurements using time-of-flight neutron spectrometry at temperatures of 300 K, 973 K, 1273 K, and 1323 K are shown in figures 6.3(a) and 6.4(a). These phonon DOS curves present an absence of softening up to 1323 K, similarly to the DOS obtained from triple-axis measurements. The softening of the transverse mode

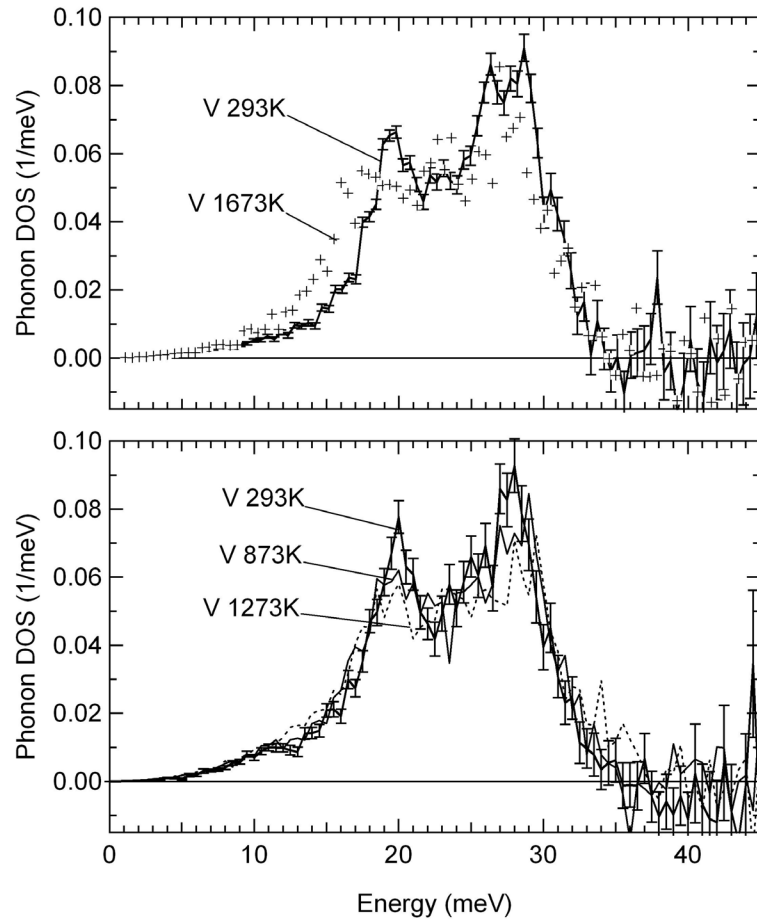


Figure 6.1: Phonon DOS of vanadium at 293, 873, 1273 and 1673 K. Temperatures are as labeled. Measurements at 293, 873, and 1273 K were taken on the triple-axis spectrometer HB2, shown in the bottom half of figure. Measurements taken on the triple-axis spectrometer HB1 at 1673 and again at 293 K are shown in the top half of figure. Adapted from [77]

appears more important in the result of figure 6.3-(a), but this measurement is of lesser statistical quality.

The temperature behavior of the V phonon DOS is inconsistent with what is expected from classical softening upon thermal expansion. Like most materials, vanadium does expand with increasing temperature, and the classical quasiharmonic behavior would suggest that the DOS should soften gradually between 293 K and 1673 K. This is not the observed behavior, however, and it appears that anharmonic effects beyond the quasiharmonic model are at play.

### 6.2.2 Vanadium Alloys

The phonon DOS of vanadium alloys with a few percent of Co, Pt, and Nb impurities at elevated temperatures were investigated. These measurements reveal a trend with the nature of the impurity.

The phonon DOS for the alloy V-7%Co was measured at elevated temperatures by Bogdanoff, Fultz *et al.* (unpublished results). These measurements were conducted with the same triple-axis neutron spectrometry technique used to measure pure V [77]. Results are shown in Fig. 6.2. Contrasting with the anomalous behavior of pure V, the phonon DOS of V-7%Co undergoes a gradual softening between 293 K and 1273 K. The softening is clearly seen in low-energy transverse modes as well as high-energy longitudinal modes, in particular at the cutoff energy. The high-temperature DOS also exhibits a broadening, as can be seen on the tail-like shape of the cutoff. The longitudinal peak appears to gain in intensity at elevated temperatures, however, which could result from a differential softening along independent longitudinal branches in the dispersion curves, or a flattening of the dispersion in a particular direction.

The phonon DOS for V-6.25%Pt and V-6.25%Nb at high temperature were measured with the Pharos time-of-flight spectrometer at LANSCE. Results are shown in figures 6.3(b) and 6.4(b). The temperature-dependence of the phonon DOS for V-6.25%Pt is very similar to that observed in V-7%Co, with a gradual temperature-softening. The softening is larger than in the case of Co impurities, however. The longitudinal peak undergoes an increase in intensity with temperature, similar to V-7%Co. We conclude that Pt and Co impurities

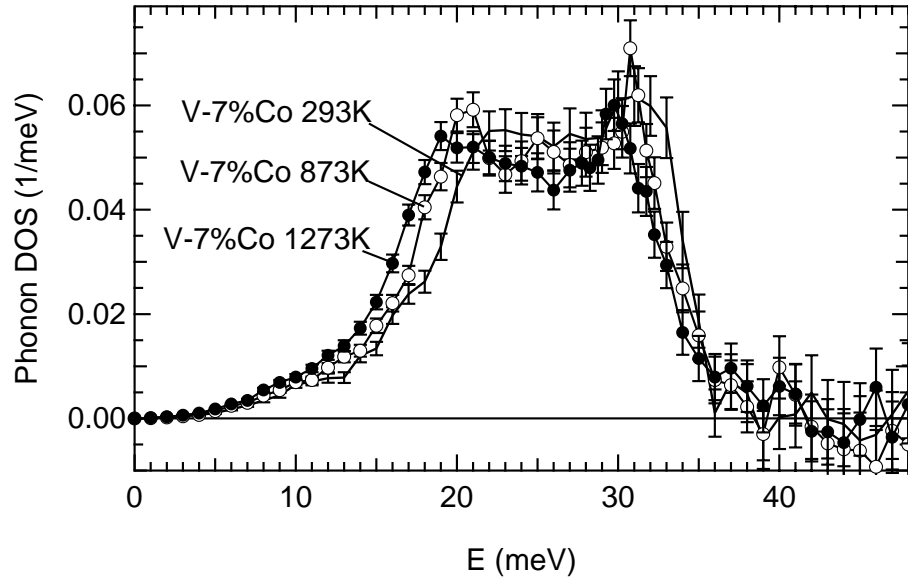


Figure 6.2: Phonon DOS of V-7%Co at 293, 873 and 1273 K, measured with the triple-axis spectrometer HB2. Temperatures are as labeled.

influence the temperature-dependence of the V phonon DOS in the same fashion, with a strong disruption of the anomalous temperature-dependence. We recall that these impurities also had comparable effects on the phonon DOS of V at room-temperature, both causing a large stiffening of the vibrations (see chapter 4). On the other hand, Nb impurities only had a small effect on the phonon DOS at room-temperature and their effect on the temperature-dependence of the phonon DOS is also small, as seen in figure 6.4. The transverse modes are almost unaffected by the Nb solutes, both at 300 K and 1273 K, while the longitudinal modes show only a small excess in softening at 1273 K in the presence of the solutes. A trend in the effect of impurities on the phonon-softening emerges, as Nb is isoelectronic to V, while Co and Pt are both late transition metals.

The anharmonic effects observed in the V phonon DOS can be studied more quantitatively, and contrasted to the behavior of V-Co, using an entropy analysis.

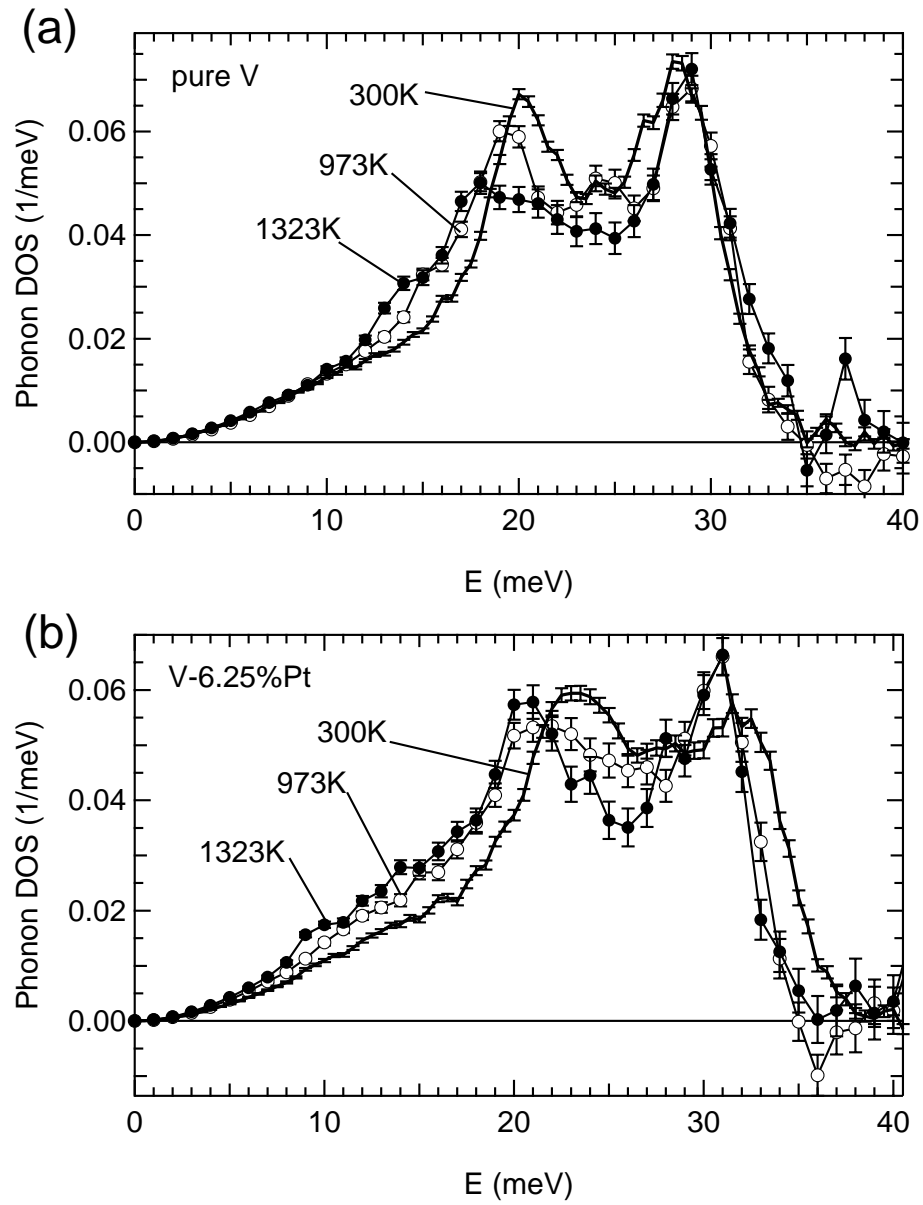


Figure 6.3: (a) Phonon DOS of pure V at 300, 973 and 1323 K, measured with Pharos. (b) Phonon DOS of V-6.25%Pt at 300, 973 and 1323 K, measured with Pharos (LANSCE).

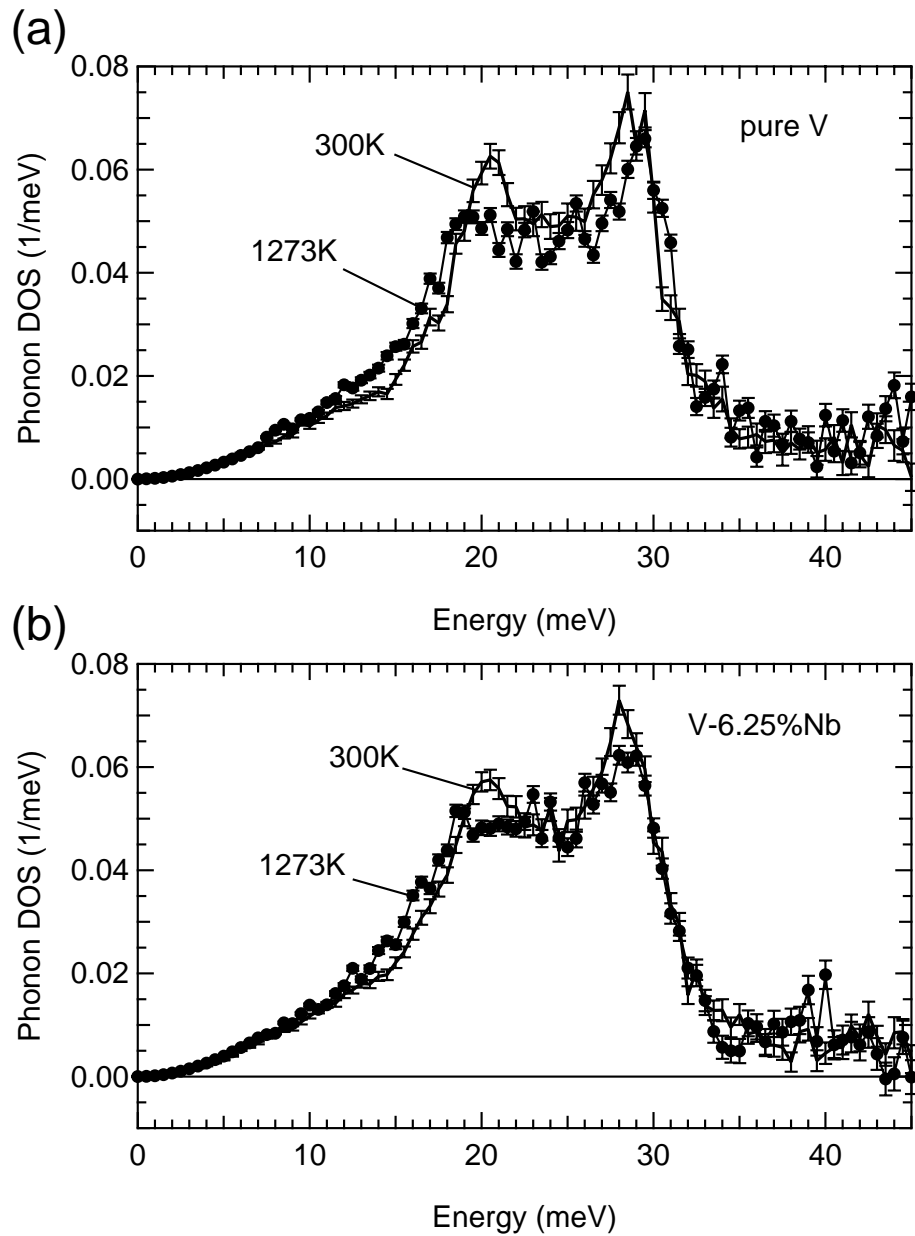


Figure 6.4: (a) Phonon DOS of pure V at 300 K and 1273 K, measured with Pharos. (b) Phonon DOS of V-6.25%Nb at 300 K and 1273 K, measured with Pharos (LANSCE).

## 6.3 High-Temperature Entropy

### 6.3.1 Pure Vanadium

Bogdanoff *et al.* deduced the phonon entropy of pure vanadium at high temperature from their phonon DOS measurements [77]. These authors also compared their results to the predictions of Eriksson, Wills, and Wallace [56], who analyzed the experimental heat capacity and thermal expansion and inferred the phonon entropy after subtracting an electronic contribution obtained from electronic structure calculations. The results of both studies are in good agreement and attribute the anomalous temperature of the phonon DOS to phonon anharmonicity.

The anharmonic entropy analysis adopted by Bogdanoff *et al.* is essentially similar to that described in chapter 2, although the notation used by those authors is slightly different. We illustrate their results with the help of Fig. 6.5, taken from [77]. The crosses in this figure correspond to the anharmonic phonon entropy calculated from the experimental phonon DOS, as in the left-hand side of Eq. 2.68. The thick upward line is the quasiharmonic phonon entropy  $\Delta S_{\text{ph}}^{\text{qh}}$ , obtained from thermal expansion data and corrected for the electronic contribution as in Eq. 2.61, using the electronic structure calculations of Eriksson *et al.* [56]. The difference between the line and the crosses, in the approximation that the phonon modes at 300 K are harmonic, is the contribution of explicit anharmonicity in the interatomic potentials to the entropy,  $\Delta S_{\text{ph}}^{(3,4)}$ . It is plotted as black circles in Fig. 6.5. This contribution is negative and almost exactly cancels out the positive term corresponding to thermal expansion. It represents a stiffening of the phonon modes with increasing temperature at fixed volume.

Eriksson, Wills, and Wallace performed calculations of the electronic entropy  $S_{\text{el}}$  and used heat capacity data, thermal expansion data, as well as harmonic phonon data from the literature to deduce the phonon anharmonicity from the relationship

$$S_{\text{tot}} = S_{\text{el}} + S_{\text{har}} + S_{\text{ph}}^{(2)} + S_{\text{ph}}^{(3,4)}, \quad (6.1)$$

where  $S_{\text{tot}}$  is the total entropy and the terms on the right-hand side are as defined in chapter 2. Their result for the explicit anharmonicity in the entropy,  $S_{\text{ph}}^{(3,4)}$ , is plotted as the

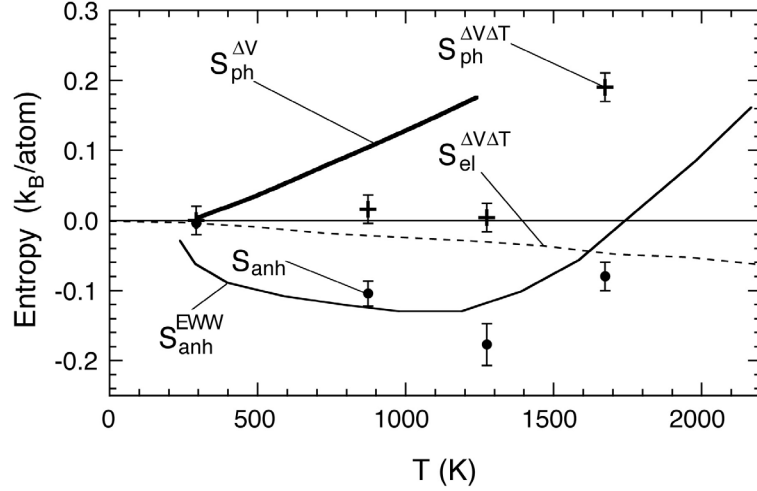


Figure 6.5: Anharmonic contributions to the entropy of vanadium. The bold curve is as computed from Eq. 2.61. Crosses are computed from the phonon DOS of vanadium using Eq. (2.68). The solid circles are the difference between the bold curve and the crosses (the solid circle at 1673 K is obtained by extrapolating the bold curve to higher temperatures). The solid curve is the anharmonic entropy obtained by Eriksson *et al.* [56].

black curve in Fig. 6.5. This curve and the black dots are in good agreement, although the anharmonic component of the entropy was derived by different means, strengthening the proposition that the anomalous  $T$ -dependence of the phonons in V stems from anharmonicity in the displacement potentials.

### 6.3.2 Vanadium Alloys

In this section, the anharmonic phonon entropies of vanadium and V-7%Co are compared. A similar entropy analysis as in the previous section is conducted. However, because the necessary quantities for the alloy were not available from the literature, extra measurements and electronic structure calculations were necessary.

We performed thermal expansion measurements on V and V-7%Co up to 900 K using a Perkin-Elmer TMA-7 thermo-mechanical analyzer. The bulk modulus was obtained for both materials at room-temperature from ultrasonic measurements and densities were measured using Archimedes' method. Using our results for these quantities, we evaluated

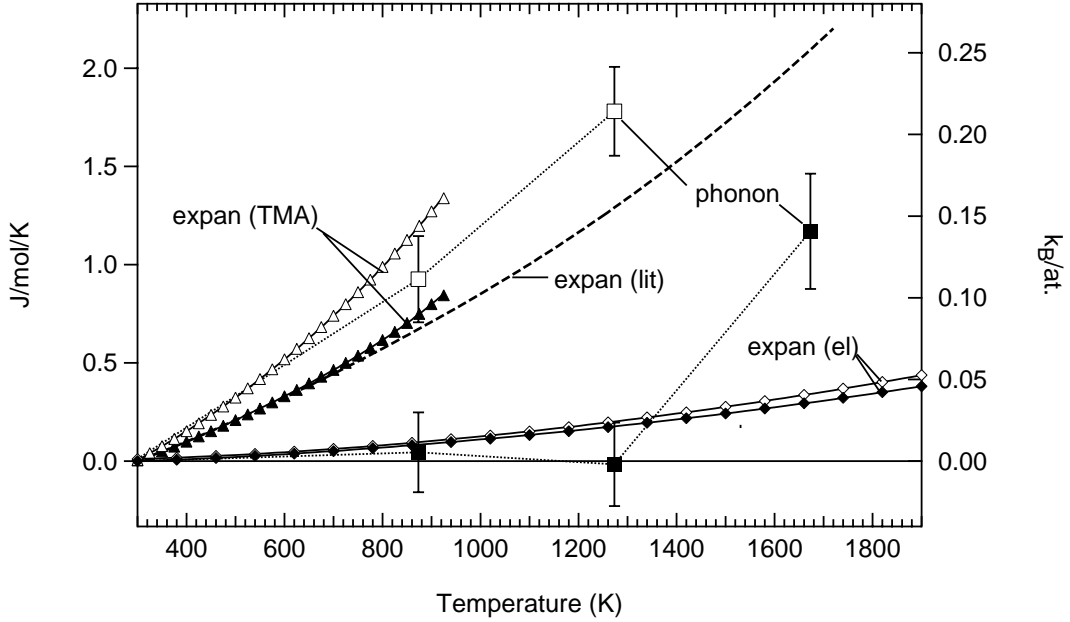


Figure 6.6: Anharmonic entropy for pure vanadium and V-7%Co. Squares represent the anharmonic entropy as defined in Eq. 2.68, triangles represent the anharmonicity contribution due to the expansion against the bulk modulus, as defined in Eq. 2.61. Diamonds represent the electronic entropy of expansion of Eq. 2.61, calculated with Wien2k. Filled symbols: pure V; open symbols: V-7%Co. The dashed line is the same quantity as the filled triangles, evaluated with values taken from the literature.

Eq. 2.60, under the assumption that the bulk modulus does not change with temperature. The resulting quasiharmonic entropy of expansion is plotted as triangles in Fig. 6.6. The quasiharmonic entropy from thermal expansion for vanadium was also evaluated with data taken from the literature. The thermal expansion coefficient used was taken from Touloukian [86], and the temperature-dependent bulk modulus was obtained from the elastic constants measurements of Walker [64], plotted in figure 6.10. The result is plotted as the dashed line in Fig. 6.6. As seen on this figure, the agreement between our thermal expansion measurement for V and the literature result is excellent. The slight quasiharmonic entropy overestimation of our result compared to the literature in the case of V is due to the neglect of the decrease of  $B$  with temperature.

The anharmonic phonon entropy for V-7%Co was derived from the experimental high-

temperature phonon DOS with Eq. 2.68. As can be seen on Fig. 6.6, for V-7%Co, the anharmonic phonon entropy and the quasiharmonic contribution due to thermal expansion are in good agreement, within the error bars on our measurements. The agreement is even better if one considers the small electronic term of Eq. 2.61. This term was calculated with first-principle calculations (Wien2k) on  $V_{15}X_1$  and V  $2 \times 2 \times 2$  supercells, using Eq. 2.70 with  $T_{\text{low}} = 300$  K and  $T_{\text{high}} = 900$  K. It gives a small positive contribution, since thermal expansion decreases the overlap integral and consequently the band-width, increasing the number of electron states per unit energy.

The behavior for V-7%Co is in sharp contrast with the results for pure vanadium, in which the effect of thermal expansion against the bulk modulus predicts a much larger phonon softening and quasiharmonic phonon entropy than is observed. Thus, it appears that most of the phonon frequency shifts with temperature in the case of V-Co are associated with quasiharmonic shifts,  $\Delta_2$ , whereas substantial explicitly anharmonic shifts,  $\Delta_3 + \Delta_4$  (and possibly higher-order terms), are present in the case of pure V. Moreover, in the case of V,  $\Delta_3 + \Delta_4$  is positive, yielding a negative anharmonic entropy  $S^{(3,4)}$ , as discussed above.

This suppression of the anharmonic behavior in V by Co impurities can have several sources. One possible mechanism would be that the impurities disrupt the coherence between phonons and thus suppress the phonon-phonon scattering process, thereby making the material more harmonic. Another possible source is a change of the electron-phonon interaction, as the impurities affect the electronic structure of the host, in particular the electronic density at the Fermi level, and thus the electron-phonon coupling parameter,  $\lambda$  (as discussed in chapter 5).

### 6.3.3 Vibrational Entropy of Alloying

A connection can be established between the temperature-dependent phonon DOS of V and V-7%Co and the temperature dependence of the solubility limit for Co in V.

Because no complete dataset on the Co phonon DOS at high temperatures is available, and because the analysis is complicated by the Co hcp  $\rightarrow$  fcc martensitic phase transition at 673 K, the vibrational entropy of mixing was not calculated and we focus instead on the

Table 6.1: Vibrational entropy of alloying for 7% Co solutes in V, at the different temperatures for which the phonon DOS measurements were performed.

$T$ (K)	$S_{\text{ph}}^{\text{alloying}}$ ( $k_{\text{B}}/\text{atom}$ )
293	$-0.22 \pm 0.03$
873	$-0.13 \pm 0.03$
1273	$-0.02 \pm 0.03$

vibrational entropy of alloying:

$$S_{\text{ph}}^{\text{alloying}}(T) = S_{\text{ph}}^{\text{V-Co}}(T) - S_{\text{ph}}^{\text{V}}(T). \quad (6.2)$$

It is expected that  $S_{\text{ph}}^{\text{alloying}}(T)$  is close to  $S_{\text{ph}}^{\text{mix}}(T)$ , however, since the energy range of the Co phonon DOS is similar to that of V and because there is only 7% Co in the alloy. Our results of  $S_{\text{ph}}^{\text{alloying}}(T)$  for Co in vanadium at different temperatures are listed in Table 6.1. Because the V phonon DOS does not vary much with temperature up to 1273 K while the V-7%Co DOS softens, the stiffening of the DOS induced by the impurities at room temperature is gradually suppressed as temperature increases. This suppression is approximately linear with temperature, and at 1273 K the vibrational entropy of alloying is nearly zero. As a consequence, the total entropy of alloying increases linearly with temperature, since the configurational entropy gain is constant for 7% Co solutes. This gain in entropy with increasing temperature favors the solid-solution over the A15  $\text{V}_3\text{Co}$  phase in equilibrium with it, and therefore contributes to the observed increased solubility limit of Co in V at higher temperatures. Of course, a full account of the temperature dependence of the solubility limit would require to estimate the free energy curves for both phases, and in particular would require consideration of the vibrational entropy for the A15 phase.

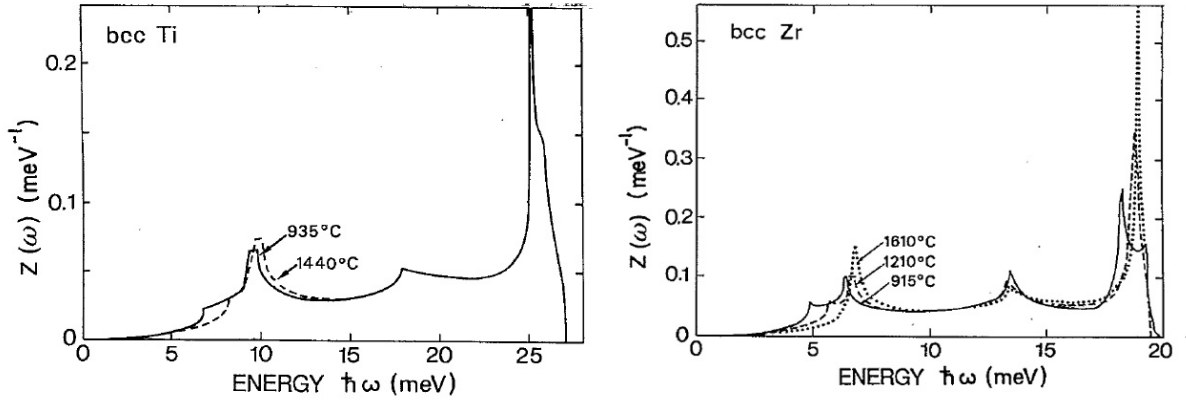


Figure 6.7: Phonon DOS for BCC Ti and Zr at elevated temperatures. Taken from [91, 92].

## 6.4 High-Temperature Properties of BCC Transition Metals

### 6.4.1 Phonon DOS

The phonons in elements of group 5 present an intermediate behavior between those of groups 4 and 6. In the high-temperature BCC phase of group 4 metals, the phonon DOS exhibits a stiffening with temperature. This is particularly pronounced for the transverse modes, while longitudinal modes do not vary much with temperature [91, 92], see figure 6.7. On the other hand, in the BCC metals of group 6, the phonons soften significantly with increasing temperature. This was observed by direct measurements of the phonon dispersions at high temperature in Cr (see [142]; see also Fig. 6.8) and was inferred from a thermodynamic analysis of the heat capacity for Mo and W [141].

Measurements of phonon dispersions in BCC Nb up to 2223K have been performed by Guthoff and coworkers [143]. Their results are shown in Fig. 6.9. From room temperature to 773 K, the phonon DOS of Nb exhibits a stiffening of the transverse modes with little change in the position of the longitudinal peak and cutoff, very much like the behavior observed in the BCC group 4 metals. At temperatures between 773 K and 1773 K, all vibrational modes start to soften, with similarity to the behavior in vanadium. The magnitude of the high-temperature softening in Nb is rather smaller than that expected based on thermal expansion alone, similarly as for V [56, 77].

It thus appears that the softening of phonons expected from thermal expansion is over-

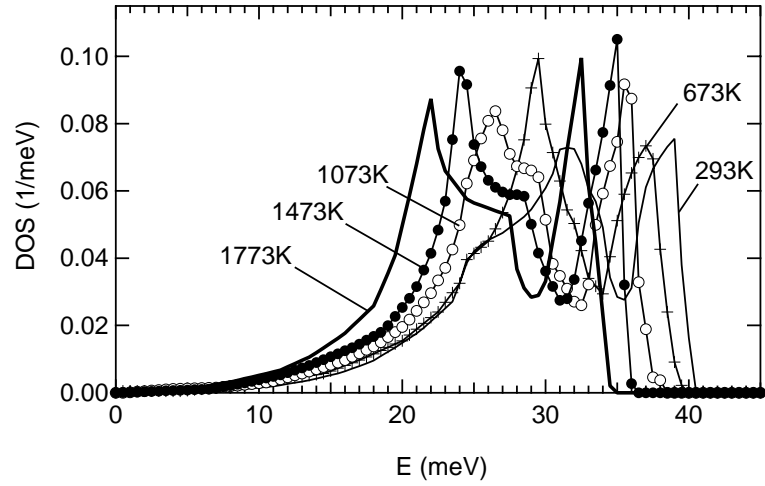


Figure 6.8: Phonon DOS of BCC Cr at elevated temperatures. Adapted from [142].

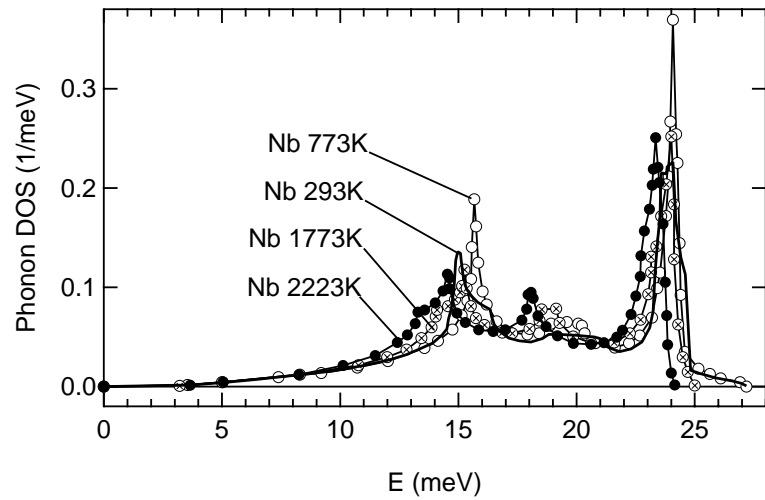


Figure 6.9: Phonon DOS of BCC Nb at elevated temperatures determined by Güthoff *et al.* [143].

come by an intrinsic temperature stiffening (that is, a stiffening with increasing temperature at constant volume) in BCC metals of groups 4 and 5. This intrinsic stiffening appears to dominate over the full temperature range of stability of the BCC phase in group 4 metals, but it is suppressed at very high temperatures in the BCC group 5 metals V and Nb. Between groups 5 and 6, the mechanism responsible for this intrinsic stiffening becomes ineffective and the phonons soften even at moderate temperatures.

#### 6.4.2 Elastic Constants

It is instructive to compare the temperature dependence of phonons in BCC transition metals to the temperature variation of their elastic constants. Room-temperature ultrasonic measurements of elastic constants for BCC transition metals and alloys with varying electron-to-atom ratios,  $e/a$ , have been reported [59, 60, 61, 62]. These were discussed in chapter 4. Several studies have been reported of such measurements in single crystals of V and Nb, as well as single-crystal alloys of V-Cr, Zr-Nb and Nb-Mo at varying compositions and over wide ranges of temperature [65, 66, 64, 67]. These studies have shown that the  $C_{44}$  shear elastic constant exhibits an anomalous temperature variation in V, Nb and Ta and in BCC alloys of composition close to V and Nb. Published results for V and Nb-Mo alloys are shown in figures 6.10 and 6.11, respectively. As seen on these figures,  $C_{44}$  for V and Nb follows a non-monotonic temperature evolution, with first a decrease at low temperatures leading to a local minimum located between 300 K and 800 K, followed by a stiffening that proceeds up to melting in Nb, but reverses around 1500 K in V.

This behavior can be tuned by alloying V and Nb with neighboring elements Cr and Mo, respectively, which form solid-solutions over the whole range of compositions. As seen in Fig. 6.11, the addition of Mo in Nb shifts the position of the local minimum in  $C_{44}$  to lower temperatures. For 33%Mo, the minimum is at 0 K and for concentrations above 56% Mo, the local minimum has disappeared, leaving a normal, monotonic temperature decrease of  $C_{44}$ . The same effect is observed in V-Cr alloys [67]. Through electronic structure calculations, this behavior has been interpreted as a Fermi surface effect [65, 66, 63]. In pure V, the distortion of the unit cell in a trigonal strain corresponding to the  $C_{44}$  elastic constant leads to the opening of a gap around the  $\Gamma_{25'}$  point of the band structure, about 25 mRy

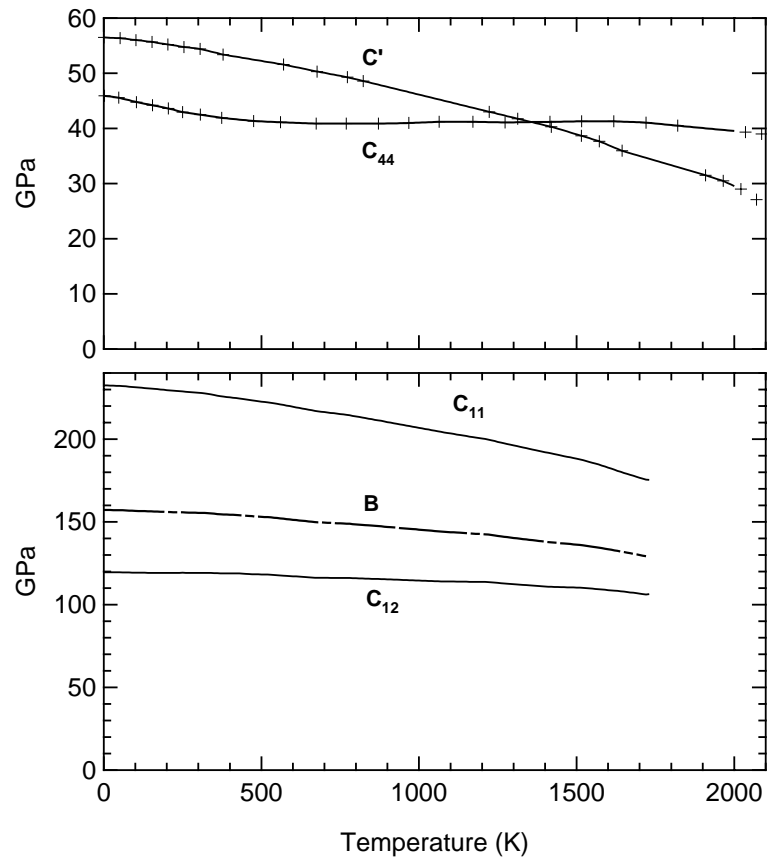


Figure 6.10: Elastic moduli of vanadium single crystal as function of temperature, measured by Walker [64].

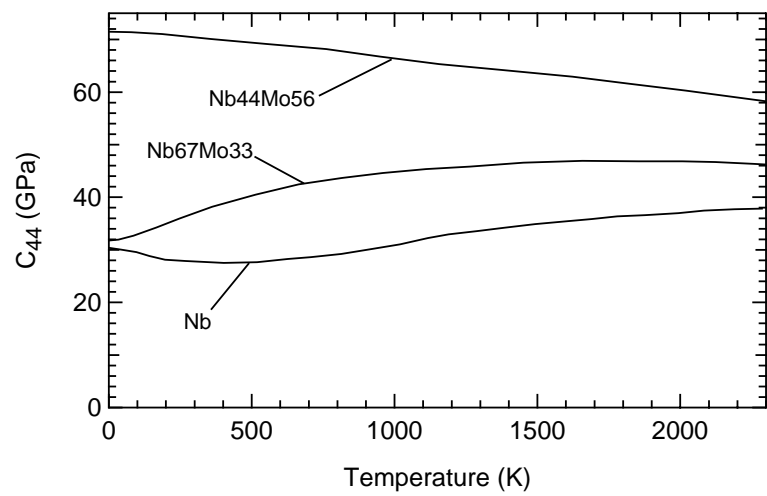


Figure 6.11: Shear elastic constant  $C_{44}$  of Nb and Nb-Mo single crystals as function of temperature, measured by Bujard and coworkers [66].

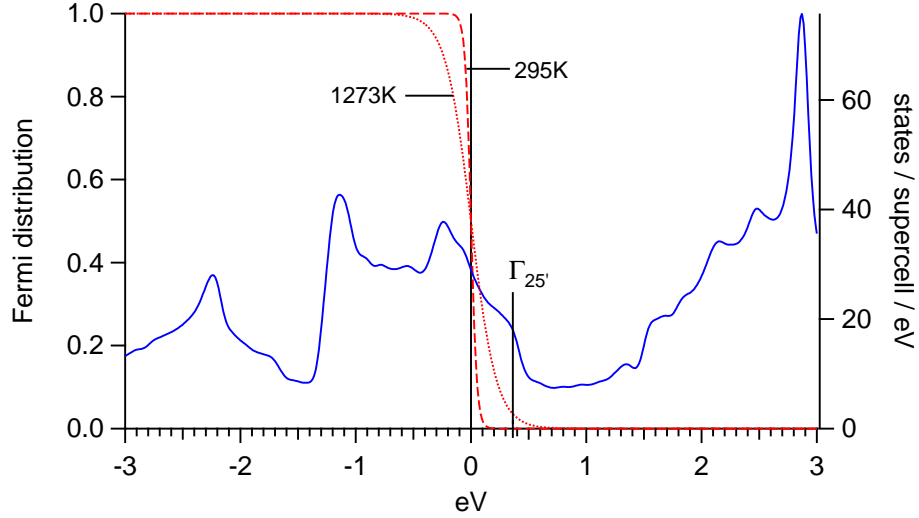


Figure 6.12: Electronic DOS for BCC V calculated with Wien2k and position of  $\Gamma_{25'}$  point.

above the Fermi level, associated with a decrease in the symmetry of the lattice [63]. This has only a small energy cost when the upper band above this gap is unoccupied as is the case in pure V and Nb at low  $T$ . However, it is expected to become more energetically unfavorable when electrons are thermally excited into these states. The position of the  $\Gamma_{25'}$  point in the electronic DOS of BCC V and Fermi distribution for different temperatures are illustrated in Fig. 6.12. Alternatively, in the rigid-band model, the states above  $\Gamma_{25'}$  become filled around  $5.4e/a$  and, at this composition, the stiffening of  $C_{44}$  is shifted to lower temperatures, as band-filling and temperature play similar roles. At higher band-filling and higher temperature, the effect is not as prominent, as Fermi integrals involve the derivative  $(-\partial f/\partial E)$ , which is either not centered on these states or not as sharply peaked [65, 66]. Besides, for band-fillings crossing the  $\Gamma_{25'}$  point, the Fermi surface undergoes an electronic topological transition, as discussed in chapter 5. The significant modifications of the geometry of the Fermi surface during this transition have also been invoked to explain the behavior in the  $C_{44}$  elastic constant [112].

The temperature and composition variations of  $C_{44}$  presents some striking similarities with the variations observed in the phonon DOS, as described above. This is particularly true for the transverse phonon modes, as expected since those have a close connection to shear elastic constants. In particular, the stiffening (or absence of softening) of these

modes at intermediate temperatures follows the same behavior as  $C_{44}$ . Also, the addition of impurities with more  $d$ -electrons (Co and Pt) induces a normal softening, while Nb has almost no effect. Although the addition of Co and Pt solutes is not well described in the rigid-band model, it is interesting that 7% Co or 6.25% Pt correspond to about  $5.3 e/a$ , which is not in bad agreement with the composition at which the anomaly in  $C_{44}$  is suppressed above 300 K. However, we expect that Co and Pt have additional effects, related to the electronic redistribution described in chapter 5. Nevertheless, this similarity between  $C_{44}$  and the phonons strongly suggests the importance of the coupling of the phonons with the Fermi surface in the  $T$ -dependence of the phonons in vanadium and niobium.

## 6.5 Effects of Electron-Phonon Interaction

### 6.5.1 Theoretical Predictions

The possibility of a free energy contribution associated with the electron-phonon coupling has been alluded to in the previous sections. It is well established that the electron-phonon interaction affects thermodynamics at low temperatures [53, 52]. In particular, the electron-phonon interaction gives rise to a mass-enhancement factor  $(1 + \lambda)$  for the electrons, which increases the low-temperature electronic specific heat by the same factor. The non-adiabatic electron-phonon scattering responsible for this mass-enhancement vanishes at higher temperatures, however, and the electronic heat capacity is then correctly given by the band structure expression (the  $T$ -derivative of Eq. 2.69) [53, 50].

The possibility of an electron-phonon interaction contribution to the free energy at high temperatures has been the subject of several contradicting theoretical investigations, and is still debated. Grimvall's calculations for Pb imply that the electron-phonon coupling contribution to the free energy vanishes at temperatures higher than the characteristic phonon frequency [53, 50]. Allen and Hui, on the other hand, calculated the effect of the adiabatic electron-phonon interaction on the heat capacity at elevated temperatures ( $T \geq \theta_D$ ) and predicted a contribution of order of magnitude  $\gamma T$  and of either sign [144]. Wallace, in [52], states that the derivation of Allen and Hui is "grossly overestimating" this heat capacity contribution, because of a neglected double-counting ground state term.

However, in more recent and detailed investigations ([145, 146]), Bock, Coffey, and Wallace isolated the adiabatic and non-adiabatic electron-phonon contributions to the free energy of nearly free electron metals and concluded that, although the non-adiabatic term vanishes at elevated temperatures (in agreement with Grimvall), the adiabatic term increases, and could have effects on the specific heat comparable to those predicted by Allen and Hui. Also, in their more recent study, these authors state that the ground state double-counting correction vanishes at high temperature in the case of the specific heat [146], thus validating Allen and Hui's calculation.

We set out to investigate experimentally the prediction of Allen and Hui. According to those authors, heat capacity measurements at high temperature could be used to discriminate between phonon-phonon and electron-phonon interactions as sources of  $T$ -dependence of the phonon frequencies. This proposition stems from the result, referred to as ‘‘Brooks’ theorem’’ by the authors, that the perturbation of the non-interacting electronic eigenvalue  $\epsilon_{\mathbf{k}n}$  by the addition of an extra phonon in mode  $\mathbf{q}j$  is equal to the change in energy of phonon mode  $\mathbf{q}j$  upon inserting an extra electron in state  $\epsilon_{\mathbf{k}n}$ , or mathematically:

$$\Delta\epsilon_{\mathbf{k}n}(\mathbf{q}j) = \Delta\omega_{\mathbf{q}j}(\mathbf{k}n). \quad (6.3)$$

Using this result, Allen and Hui derive the change in heat capacity of the electrons and phonons, due to the electron-phonon coupling. The change of the phonon heat capacity in this model is due to the temperature-dependence of the Fermi distribution for the electrons, instead of the higher order terms in the deformation potentials in the case of anharmonicity and phonon-phonon scattering. Their result can be summarized as follows. The expression for the change in phonon heat capacity in terms of  $T$ -dependent frequencies due to the electron-phonon coupling turns out to be the same as that due to phonon-phonon coupling and is given by

$$\Delta C_{\text{ph}} = - \sum_{\mathbf{q}j} c_{\text{ph}}^{\text{har}}(\omega_{\mathbf{q}j}) \frac{d \ln \omega_{\mathbf{q}j}}{d \ln T}. \quad (6.4)$$

The change in electronic heat capacity due to the electron-phonon coupling is given by

$$\Delta C_{\text{el}} = - \sum_{\mathbf{kn}} c_{\text{el}}^{\text{n.i.}} (\epsilon_{\mathbf{kn}} - \mu) \frac{d \ln \Delta \epsilon_{\mathbf{kn}}}{d \ln T}, \quad (6.5)$$

with  $c_{\text{el}}^{\text{n.i.}}$  the heat capacity of a non-interacting electron of energy  $\epsilon_{\mathbf{kn}}$  and  $\mu$  the electronic chemical potential. Allen and Hui proceed to show that, following Brooks' theorem,

$$\Delta C_{\text{el}} = \Delta C_{\text{ph}}. \quad (6.6)$$

So, if phonon frequencies are shifting due to phonon anharmonicity alone, the change in heat capacity is given by the phonon term, Eq. 6.4. On the other hand, if the shifts are due to electron-phonon coupling alone, the heat capacity change is given by the sum of the changes in electron and phonon heat capacities  $\Delta C_{\text{el}} + \Delta C_{\text{ph}}$ , and from Eq. 6.6, it is thus twice the change that would be incurred by phonon anharmonicity. This prediction can directly be tested experimentally. A useful simplification of Eq. 6.4 is given by Allen and Hui for  $k_{\text{B}}T > \omega_{\text{max}}$ :

$$\Delta C_{\text{ph}} \simeq -3k_{\text{B}} \frac{d \langle \ln \omega_{\mathbf{q}j} \rangle_T}{d \ln T}, \quad (6.7)$$

per atom, with  $\langle \dots \rangle_T$  the average over modes at temperature  $T^*$ .

## 6.5.2 Heat Capacity Measurements

Heat capacity measurements for pure vanadium and  $\text{V}_{93}\text{Co}_7$  were conducted using a Netzsch 404-C differential scanning calorimeter. Heating rates of 20 K/min were used. The purge gas used was Ar of ultra-high purity, which was circulated through a Ti getter furnace to remove traces of oxygen. This circumvented any observable oxidation on the samples up to the highest temperatures measured (1723 K). Heat capacities for the two materials were obtained by comparison to a measurement of a synthetic sapphire standard. In these runs, the samples (successively sapphire and V or  $\text{V}_{93}\text{Co}_7$ ) were held in a Pt pan with Pt lid, while the reference crucible was an empty Pt holder. A baseline run with empty crucibles

---

\*It can be seen that this expression is equivalent to  $C_P - C_V$  at elevated temperatures.

was conducted before each measurement. Typical results and deviations for pure V are seen in Fig. 6.13. The scatter around the average value is about  $0.2 k_B/\text{atom}$ . Results with somewhat smaller uncertainties were obtained by conducting differential measurements between  $V_{93}Co_7$  and V samples of the same shape, and containing close to the same number of atoms (within a few %). In the differential measurement, the scatter between measurements is about  $0.1 k_B/\text{atom}$  from the average.

### V Heat Capacity

Figure 6.13 shows the different components for the heat capacity at constant pressure of vanadium from 0 K to 1800 K. The figure shows the assessment of Maglic for the total heat capacity of V as the thick dashed line [85]. The harmonic phonon contribution “Cph” was calculated from the V phonon DOS measured at 300 K at Pharos. The non-interacting electronic contribution, “Cel”, was derived from the electronic entropy calculation of Eriksson *et al.* [56] as well as our electronic entropy calculation (Wien2k). The quasiharmonic contribution from thermal expansion “Cexp” is derived from the respective entropy in figure 6.6. The DSC result for the total heat capacity is indicated by the shaded area.

### $V_{93}Co_7$ Heat Capacity

The total constant-pressure heat capacity for V-7%Co was obtained by adding the result of our differential measurement between the alloy and pure V using DSC and the total  $C_P$  of V reported by Maglic [85]. The electronic entropy and specific heat were derived from the electronic DOS for V-6.25%Co calculated with Wien2k. The quasiharmonic heat capacity due to thermal expansion was obtained from the corresponding entropy in Fig. 6.6. Because our thermal expansion measurement is limited to  $T < 925K$ , the heat capacity for thermal expansion was also estimated over a larger range from the literature result for pure V. We observed that the ratio of the thermal expansion coefficients for V-7%Co and V is a constant over the whole range of the measurement ( $1.27 \pm 0.01$ ), see Fig. 6.14. The ratio for the quasiharmonic entropies of thermal expansion, calculated with  $T$ -independent bulk moduli, is also constant over the range of the measurement,  $\Delta S_{V-Co}^{qh}/\Delta S_V^{qh} = 1.57 \pm 0.03$ . This result was extrapolated to higher temperatures, and we assumed that the temperature-

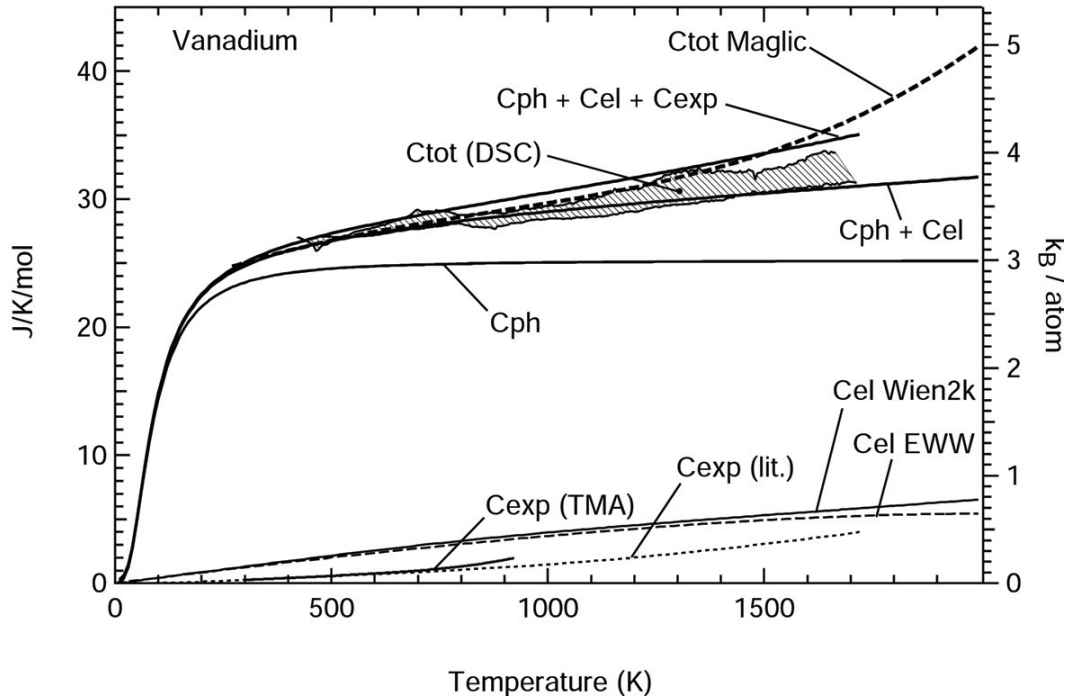


Figure 6.13: Heat capacity components for pure vanadium. Values are at constant pressure.

dependence of the bulk modulus for the two materials is the same (constant bulk modulus ratio). Results are shown in Fig. 6.15.

## Discussion

Our DSC result for the total heat capacity of V is in fair agreement with the recommended value of Maglic [85]. For reasons that are not obvious, there appears to be a systematic underestimation in our DSC measurement, however, by about  $0.2 k_B$  at 1200 K and reaching  $0.5 k_B$  at 1700 K. We will consider the recommended value of Maglic as the reference total heat capacity of V.

The upward curvature observed in  $C_P$  of vanadium at elevated temperatures is a general feature of the heat capacity of early transition metals, although no consensus currently exists on its interpretation. It has been observed in V, Nb, Ta, Cr, Mo, and W [85]. Although the coefficient of thermal expansion exhibits a similar behavior at high  $T$ , the effect observed in the heat capacity is not due only to thermal expansion, as it is still present when one

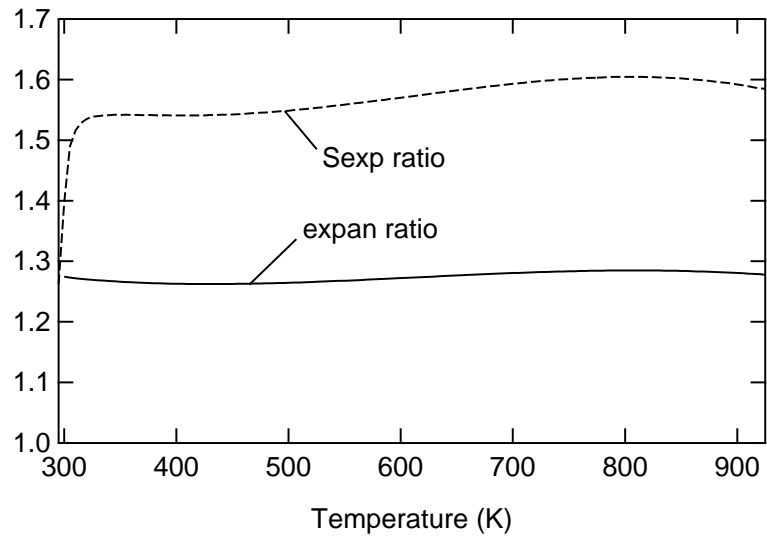


Figure 6.14: Ratio of thermal expansion coefficients and quasi-harmonic entropy of thermal expansion for V-7%Co versus V.

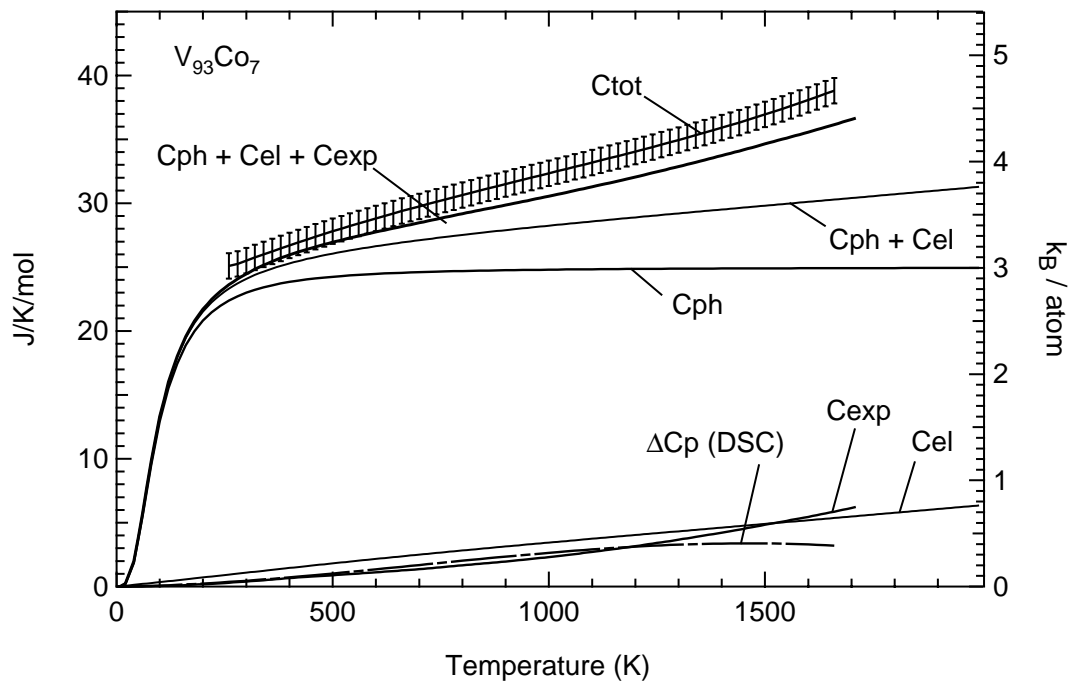


Figure 6.15: Heat capacity components for V-7%Co. Values are at constant pressure.

considers  $C_V$ , as shown by White [147]. The magnitude of the contribution of vacancies to the heat capacity in BCC transition metals has been controversial, but it is generally accepted to be too small to account for the strong non-linear increase in  $C_P$  [147, 148].

Adding the contributions of electrons, harmonic phonons and quasiharmonic phonons for pure vanadium, we obtain a heat capacity (“Cph+Cel+Cexp” in Fig. 6.13) in close agreement with the total heat capacity  $C_P^{\text{tot}}$  of Maglic. However, it is interesting to note that the sum of these contributions is slightly larger than  $C_P^{\text{tot}}$  at low temperatures and then slightly lower at high temperatures, with a crossover around 1500 K. This is reminiscent of the behavior of the phonon DOS and the anharmonic entropy.

In the case of  $V_{93}Co_7$ , “Cph+Cel+Cexp” is following the same temperature dependence as  $C_P^{\text{tot}}$  obtained by adding Maglic’s value for vanadium to our differential DSC measurement, but it is consistently smaller by about  $0.2 k_B/\text{at}$ .

According to the analysis of Allen and Hui, one ought to compare the difference between the curves “Cph+Cel+Cexp” and  $C_P^{\text{tot}}$  to the value of  $\Delta C_{\text{ph}}$  of Eq. 6.7. The results for  $\Delta C_{\text{ph}}$  are given in Table 6.2. The anharmonic entropy of Allen and Hui is small in all cases, not much larger than the error bars on the components and the total heat capacity. Nevertheless, it seems to show the right behavior, with the correct sign and magnitude. It is interesting that it is negative for the range 873 K to 1273 K in pure V (about  $-0.08 k_B/\text{at}$ .) and then becomes larger and positive above 1273 K. Considering the uncertainties in the various components entering our  $C_P$  estimates, it is difficult to assess whether this anharmonic entropy stems from phonon anharmonicity or electron-phonon coupling. The analysis might be more amenable on a material presenting a strong phonon softening or stiffening but would still require careful calorimetry work.

## 6.6 Summary

The temperature-dependence of the phonon DOS of V and dilute V alloys was investigated experimentally with inelastic neutron scattering. Whereas it had been previously shown that the V phonons first present an absence of softening up to 1273 K and subsequently soften more normally, we show that the introduction of a few percent of Co or Pt impurities disrupts this anomalous behaviour. Nb impurities on the other hand do not affect

Table 6.2: Average phonon frequencies and anharmonic heat capacity for V and V-7%Co.

V	293	(583)	873	(1073)	1273	(1473)	1673
$\langle E \rangle$ (meV)	23.0		23.2		23.6		22.6
$\langle \ln E \rangle$	3.10		3.10		3.11		3.08
$\Delta C_{\text{ph}}$ ( $k_{\text{B}}/\text{at.}$ )		0.00		-0.08		0.40	
V-Co	293	(583)	873	(1073)	1273		
$\langle E \rangle$ (meV)	25.2		24.5		23.8		
$\langle \ln E \rangle$	3.19		3.15		3.12		
$\Delta C_{\text{ph}}$ ( $k_{\text{B}}/\text{at.}$ )		0.10		0.25			

the anomaly. The behavior of the phonons with temperature in V and V-rich alloys can be compared to general trends observed in BCC transition metals, suggesting the importance of the electronic structure in determining the temperature-dependence of the lattice vibrations. Careful analyses of the entropy and heat capacity reveal the necessity to account for a multitude of contributions, many of them having similar magnitudes at elevated temperatures. The intrinsically anharmonic components of the entropy and heat capacity, whether stemming from phonon-phonon or electron-phonon interactions, are much smaller, however. The heat capacity analysis derived from Allen and Hui's formalism shows the need for accurate calorimetry measurements and reliable electronic structure calculations.

## Chapter 7

# Vibrational Entropy of the $\gamma - \alpha$ Transformation in $\text{Fe}_{71}\text{Ni}_{29}$

### 7.1 Introduction

Considerable attention has been given to Fe-Ni alloys over the years. Of particular interest is the martensitic transformation occurring upon cooling the face-centered-cubic (FCC) austenite ( $\gamma$ ), which produces body-centered-cubic (BCC) martensite ( $\alpha$ ) of higher specific volume. The temperature at which this transformation occurs is suppressed with increasing Ni content; for Ni concentrations larger than 32%at, the FCC austenite phase is stable down to 0 K, as reported by Owen [149]. The martensitic transformation in the Fe-Ni system has been widely studied, but there has not yet been a quantitative assessment of the entropy contributions to the change in free energy driving the transformation. In displacive phase transitions, the transformation from one crystal structure to another operates through well coordinated movements of atoms, and no long-range diffusion takes place. Thus, there is no change in the configurational entropy of the alloy and it is expected that the vibrational entropy will play the predominant role. The relevance of phonons has already been emphasised in regards to the mechanism of the martensitic transformation, as in the “soft mode” model proposed by Cochran [150].

Magnetic effects in Fe-Ni alloys have also been the subject of many studies, especially the INVAR effect for FCC alloys close to 35%at Ni. Owen [149] reports that the Curie temperature in the FCC phase varies rapidly with Ni content in this range of compositions;

it decreases with decreasing Ni content and it becomes lower than the martensitic transformation start temperature  $M_S$  at 28%at Ni. For Ni concentrations above 28%, the austenite phase is ferromagnetic at the martensitic transformation temperature.

Kaufman and Cohen [151] have shown that the transformation between FCC austenite and BCC martensite in  $\text{Fe}_{71}\text{Ni}_{29}$  is strongly hysteretic. The  $\gamma \rightarrow \alpha$  transformation takes place only upon a large undercooling below the temperature  $T_0$  where the free energies of both phases are equal, while the reverse  $\alpha \rightarrow \gamma$  transformation requires a similarly large overheating above  $T_0$ . The transformation thus takes place out of equilibrium, and this is caused by the large elastic forces of the  $\alpha - \gamma$  transformation.

We investigate the different contributions to the entropy of transformation in the direct  $\gamma \rightarrow \alpha$  and reverse  $\alpha \rightarrow \gamma$  transformations in  $\text{Fe}_{71}\text{Ni}_{29}$  by inelastic neutron scattering and calorimetry. We used inelastic neutron scattering (INS) to measure the phonon density of states (DOS) and the associated vibrational entropy of  $\text{Fe}_{71}\text{Ni}_{29}$  as the alloy undergoes the martensitic transformation. Because the direct and reverse transformations are not in equilibrium and do not happen at the same temperature, their transformation entropies could differ. We found a large discrepancy in the vibrational entropies of the direct and reverse transformations, which we explain in terms of a difference in the magnetic entropy contributions to the  $\alpha \rightarrow \gamma$  and  $\gamma \rightarrow \alpha$  transformations at different temperatures.

## 7.2 Experimental Details

### 7.2.1 Sample Preparation

The samples were prepared from pieces of Fe of 99.98% purity and Ni of 99.9% purity, which were precision-weighted to obtain the alloy of composition  $\text{Fe}_{71}\text{Ni}_{29}$ . Ingots were made by arc-melting under high purity Ar atmosphere. The ingots were flipped in the crucible and melted thoroughly three times to ensure good homogeneity. The mass loss upon arc-melting was negligible, and there was no trace of surface oxidation. We estimate the possible composition variations between ingots were less than 0.2%. The ingots were subsequently cold-rolled to a thickness of 0.4 mm. All specimens were then sealed in evacuated quartz ampoules and recrystallised at a temperature of 1223 K for an hour, then cooled in the

ampoules. The difference in Rockwell hardness as measured before and after heat treatment showed the large softening characteristic of recrystallisation.

### 7.2.2 X-ray Diffractometry

The amount of  $\gamma - \alpha$  martensitic transformation in  $\text{Fe}_{71}\text{Ni}_{29}$  was determined by measuring x-ray diffraction patterns of samples cooled to different temperatures. Strips of samples of 0.4 mm thickness were immersed for 10 minutes in mixtures of ethanol and liquid nitrogen at temperatures ranging from 260 K to 77 K, then warmed in air. In the present alloy,  $M_s$  is below 260 K while  $A_s$  is above 600 K; therefore the phase fraction of martensite in the measured strips should be the fraction achieved by the transformation at the cooling temperature. The x-ray diffractometer used Co  $K\alpha$  radiation and an Inel CPS-120 position sensitive detector. Representative diffraction patterns from the strips after 10 minute coolings are shown in Figure 7.1. The recrystallised starting material is fully austenitic, and the phase fraction of BCC martensite increases with decreasing temperature. At 77 K, the martensite transformation is nearly complete. The austenite phase fraction  $f_\gamma$  was determined from the diffraction patterns using the following formula:

$$f_\gamma = \frac{0.65(I_{311}^\gamma + I_{220}^\gamma)}{I_{211}^\alpha + 0.65(I_{311}^\gamma + I_{220}^\gamma)}, \quad (7.1)$$

as suggested by Fultz and Howe [152]. Our results are plotted in Fig 7.2. The profile of the phase fraction evolution is in good agreement with the results of Kaufman and Cohen [151]. These authors found the  $M_s$  temperature for the onset of the martensitic transformation to be  $243 \pm 10$  K for the composition Fe-29.3%Ni and  $280 \pm 10$  K for the composition Fe-28.0%Ni, while we find  $M_s = 248 \pm 10$  K for the composition Fe-29.0%Ni. Goldman and Robertson [153, 154] report  $M_s = 243$  K for Fe-29%at Ni, also in good agreement with our result. Using the x-ray diffraction measurements, we find that only about 5% austenite remains at 77 K. The time-dependence of the transformation was also investigated at 243 K and 223 K (Fig 7.3). We find a weak time dependence of the transformed fraction, with not much change occurring after about 2 hours. The time dependence may be stronger at higher temperatures.

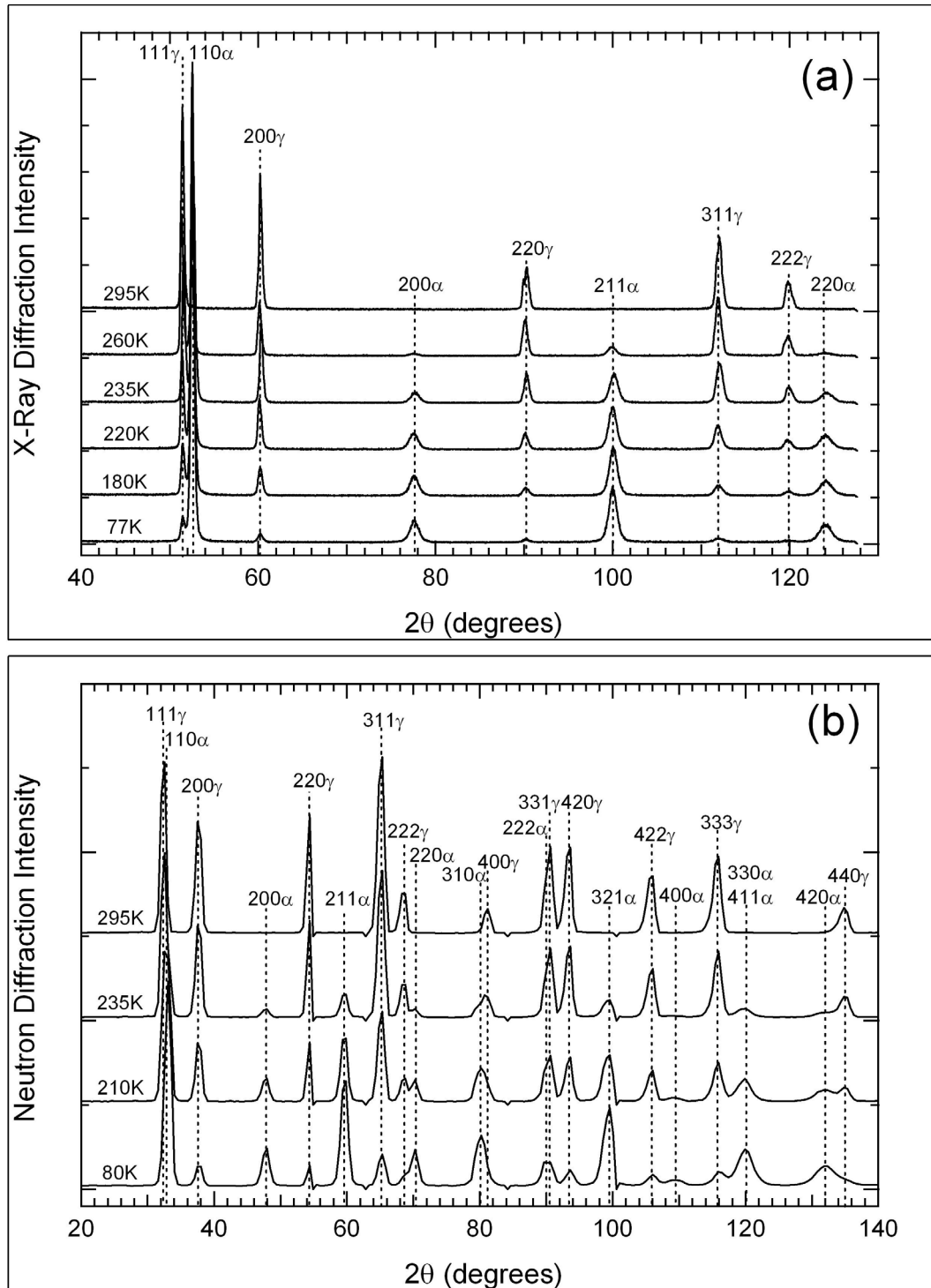


Figure 7.1: Diffraction patterns from Fe<sub>71</sub>Ni<sub>29</sub> at room temperature for transformation stages corresponding to decreasing temperatures. a) X-ray diffraction patterns obtained with Co K $\alpha$  radiation,  $\lambda = 1.790\text{\AA}$ . b) Neutron diffraction patterns from Pharos with 60.05 meV neutrons,  $\lambda = 1.167\text{\AA}$ .

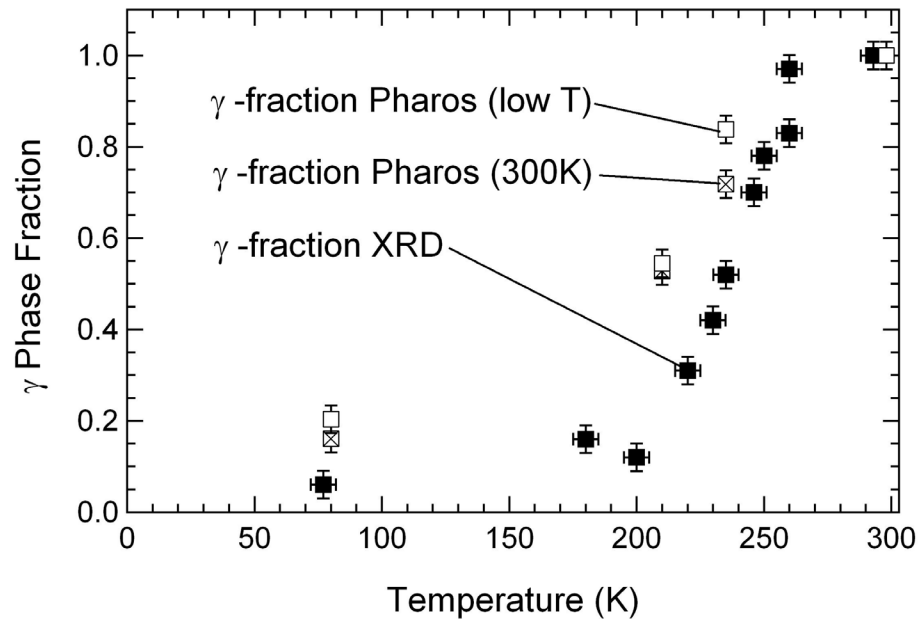


Figure 7.2: Fraction of remaining austenite ( $\gamma$ ) versus decreasing temperature, as obtained from the diffraction patterns of Figure 7.1 with the analysis described in the text.

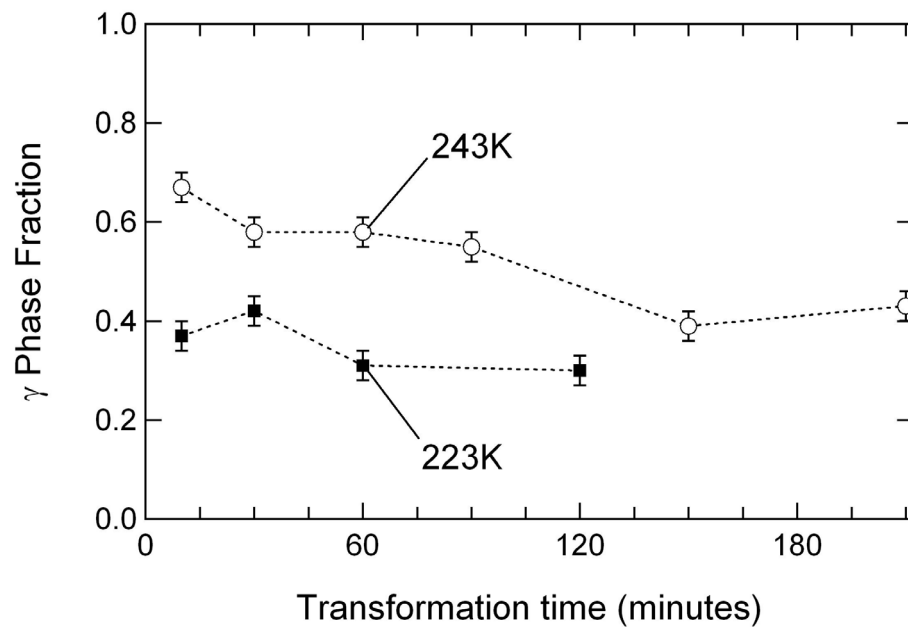


Figure 7.3: Time evolution of the austenite fraction at fixed transformation temperatures of 243 K and 223 K.

### 7.2.3 Calorimetry

Low-temperature differential scanning calorimetry (DSC) measurements of the  $\gamma \rightarrow \alpha$  transformation were performed with a Netzsch STA 449C scanning calorimeter. The  $\alpha \rightarrow \gamma$  measurements were performed with a Perkin-Elmer DSC-7. In all calorimetry runs, the samples were plates of 0.4 mm thickness and about 50 mg mass. The samples were placed in the Pt sample holder and the reference was the empty Pt holder. The  $\gamma \rightarrow \alpha$  measurements were performed by cooling the austenite at rates of  $2 \text{ K min}^{-1}$  and  $5 \text{ K min}^{-1}$  from room temperature to 155 K, a temperature range that includes most of the  $\gamma \rightarrow \alpha$  transformation. The martensite was then brought back to room-temperature and cooled again to obtain a baseline that was subtracted from the measurement. The same procedure was followed to investigate the high-temperature  $\alpha \rightarrow \gamma$  transformation. The starting material in this case was martensite obtained by cooling the alloy to liquid nitrogen temperature and the DSC measurement was performed from room temperature to 823 K at a rate of  $20 \text{ K min}^{-1}$ .

Typical heat capacity difference curves obtained from DSC runs are presented in figure 7.4. The profile of the cooling curve shows that the martensite starts forming below 250 K, and that it occurs in bursts. The first few bursts appeared at 240 K in our samples. These are the larger and sharper bursts, and they are followed by a series of gradually smaller bursts down to 220 K, the transformation appearing continuous thereafter. By comparison, the DSC profile for the reverse transformation is smoother and does not show any sharp bursts.

### 7.2.4 Neutron Scattering

Inelastic neutron scattering spectra were measured on the Pharos time-of-flight chopper spectrometer at the Los Alamos Neutron Science Center. Strips of 0.4 mm thickness of the austenitic alloy were arranged vertically in a cylindrical shape around an aluminum support disk. No material other than the sample obstructed the incident beam. The sample thickness was chosen so that 10% of the incident neutrons were scattered by the sample. The sample was mounted on a closed-cycle helium displacer refrigerator. Spectra were acquired on the sample in the following sequence of temperatures: 300 K, 235 K, 300 K, 210 K, 300 K, 80 K, 300 K. The material in the room temperature runs after various coolings

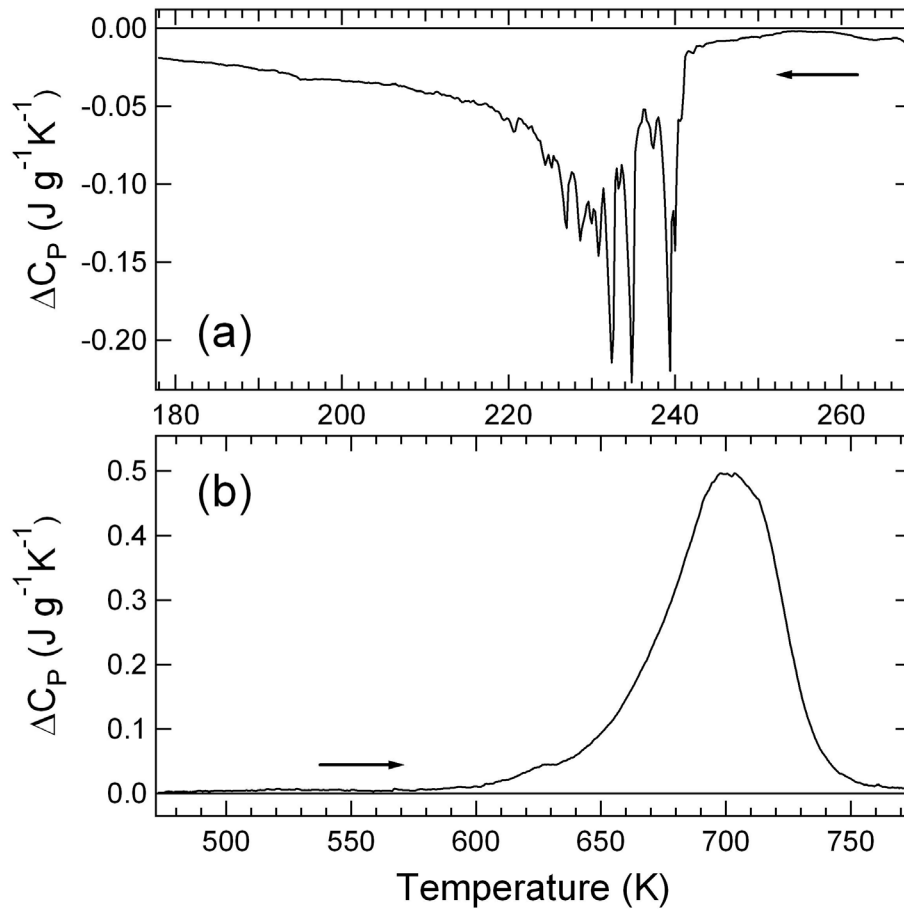


Figure 7.4: Differential scanning calorimetry profiles for the direct  $\gamma \rightarrow \alpha$  (a) and reverse  $\alpha \rightarrow \gamma$  (b) martensitic transformations in  $\text{Fe}_{71}\text{Ni}_{29}$ . Scanning rates were  $5 \text{ K min}^{-1}$  for the direct transformation and  $20 \text{ K min}^{-1}$  for the reverse transformation.

should thus be directly comparable to the material studied by x-ray diffractometry, and this was indeed verified using the elastic scattering portion of our data (see figure 7.1, panel b). For each low-temperature run, the sample was cooled slowly and held until the temperature stabilized, after which data were collected for at least 4 hours. The background signal from the displacer refrigerator and sample environment was measured at room temperature for a comparable time. The Pharos spectrometer covers a range of scattering angles from  $\Phi = -10^\circ$  to  $+145^\circ$  in the scattering plane with 376 position-sensitive  $^3\text{He}$  detector tubes, each with 40 pixels along its 1 m height. The incident neutron energy was 60.05 meV. The scattered neutrons underwent a momentum transfer,  $Q$ , varying between 0 and  $10 \text{ \AA}^{-1}$  at zero energy transfer. This corresponds to a sampling of many Brillouin zones of the reciprocal lattice for both the  $\gamma$ -phase and the  $\alpha$ -phase. The FWHM energy resolution was 2.7 meV at the elastic line (zero energy transfer), decreasing to 0.5 meV at 40 meV of positive energy transfer.

Neutron diffraction patterns were obtained from the elastic portion of the neutron scattering data, and used to monitor in situ the martensitic transformation. The neutron diffraction patterns showed the same trends as the x-ray patterns, as can be seen in figure 7.1, panel b. The same phase-fraction analysis discussed above was applied to these patterns; neutron results are compared to x-ray results in figure 7.2. The  $\gamma$  phase-fraction measured by neutron diffraction is slightly higher than that obtained by XRD at all temperatures, but it is compatible with the same transformation profile. This might reflect a difference in surface and bulk transformation characteristics, but it is known that an isothermal holding below the martensite start temperature  $M_S$  yields a stabilisation of the remaining austenite phase fraction (Kaufman and Cohen [151]), possibly causing the observed shift to lower temperatures. The  $\gamma$  phase fractions measured at room temperature after a cooling of several hours are generally slightly lower than those for the as-cooled sample. This might be explained by the slight time-dependence of the transformed phase fraction at a given temperature, which was measured by XRD (Fig. 7.3). The different values of gamma fractions obtained from neutron and x-ray diffraction might also be explained by the higher penetration of neutrons. In effect, it is possible that the bulk of the 0.4 mm thick samples transforms slower than the surface upon cooling, despite the sample being close to or at

thermal equilibrium at all the temperatures of neutron scattering measurements. Perhaps the strains induced by the transformation of the surface material delay the transformation of the bulk until lower temperatures are reached.

## 7.3 Analysis of the Phonon Density of States

### 7.3.1 Data Reduction

The time-of-flight neutron spectra were first normalized to the cumulated incident intensity and corrected for time-independent background. The response from the  $^3\text{He}$  detector tubes was calibrated with data from a pure vanadium cylinder illuminated with a “white” neutron beam, without a Fermi chopper. The contribution to the background due to the sample environment was subtracted using data collected without any sample mounted on the dispex. The data were rebinned in constant scattering angles  $\Phi$  and energy transfer. The energy bin width was  $\Delta E = 0.5 \text{ meV}$ . They were then summed into 13 slices corresponding to conical shells of  $10^\circ$  width, from  $\Phi = 15^\circ$  to  $\Phi = 145^\circ$ . Because the martensite is ferromagnetic at all temperatures and the austenite is ferromagnetic below room temperature, spin-waves can be excited by neutrons in both phases. Although the intensity from magnetic scattering owing to spin-waves is smaller than the intensity from phonon scattering, it can become large at small momentum transfers  $Q$ . For these reasons, we used only the portion of the scattering data corresponding to  $\Phi$  between  $85^\circ$  and  $145^\circ$ . The data below  $6 \text{ meV}$  are dominated by the large elastic scattering peak. Since the neutron scattering function tends to a constant at small  $E$ , the peak was simply stripped from the data. The phonon density of states (DOS) was determined in the virtual crystal and incoherent approximations, with the procedure described in chapter 3.

### 7.3.2 Neutron-Weight Correction

Because Ni and Fe do not have the same cross-sections for phonon scattering, the resulting phonon DOS is “neutron-weighted.” As discussed in previous chapters, the weighting factor for each species is given by the ratio of neutron scattering cross-section over atomic mass  $\sigma_{\text{scat}}/M$ , which is 1.5 times larger for Ni than for Fe. Thus, the vibrational modes with

large amplitude motions of Ni atoms are overemphasised. The experimentally measured (neutron-weighted) DOS is given by

$$g^{nw}(E) = x_{Fe} \frac{\sigma_{Fe}^{scat}}{M_{Fe}} g_{Fe}(E) + x_{Ni} \frac{\sigma_{Ni}^{scat}}{M_{Ni}} g_{Ni}(E), \quad (7.2)$$

with  $g_{Fe}(E)$  and  $g_{Ni}(E)$  the partial phonon DOS for Fe and Ni atoms, respectively. However, since the integral of the DOS is eventually normalized to unity and since the weighting factor is modest in the present case, the neutron-weighting only affects the shape of the measured DOS if the partial DOS curves of the constituents are markedly different. However, because the atomic masses of Fe and Ni differ only by 5%, we do not expect the two kinds of atoms to follow very different vibrational modes in a random substitutional solid-solution. Hence, the overall shape of the phonon DOS is expected to be at most moderately affected by the neutron-weighting.

Franz *et al.* [155] have performed nuclear-resonant inelastic x-ray scattering experiments on  $^{57}\text{Fe}$ -enriched  $\text{Fe}_{80}\text{Ni}_{20}$  polycrystalline samples. This technique allows the measurement of the partial phonon DOS (pDOS) associated with  $^{57}\text{Fe}$  resonant nuclei, but is insensitive to motions of the Ni atoms. It is in this respect very complementary to the present inelastic neutron-scattering measurements. Using the martensite Fe-pDOS published by these authors, we extracted the Ni partial phonon DOS from our measurement of the 300 K total neutron-weighted DOS using Eq. 7.2, on the assumption that the Fe-pDOS in Fe-29%Ni is comparable to that in Fe-20%Ni. From these Ni and Fe partial DOS contributions, we then obtained the true, unweighted, DOS for the BCC martensite:

$$g(E) = x_{Fe} g_{Fe}(E) + x_{Ni} g_{Ni}(E) \quad (7.3)$$

The ratio of the neutron-weighted DOS to the true DOS for the martensite at room temperature gave us a neutron-weighting distribution for the bcc martensite  $f_{\alpha}^{nw} = g_{\alpha}^{nw} / g_{\alpha}$ . Since the effect of neutron-weighting is not expected to vary strongly with temperature, we used this function to correct the low-temperature martensite DOS  $g_{\alpha,80K}$ . The DOS for the intermediate states of the transformation were then corrected for the neutron-weighting of the martensite phase by subtracting a neutron-weighting enhancement  $\Delta g_{\alpha,T}^{nw} = g_{\alpha,T}^{nw} - g_{\alpha,T}$ , in

proportion to the phase-fraction of martensite determined from our phase-fraction analysis. For example, in the case of the two-phase sample at 210 K,

$$g_{210\text{K}} = g_{210\text{K}}^{nw} - x_{\alpha, 210\text{K}} \Delta g_{\alpha, 80\text{K}}^{nw} . \quad (7.4)$$

The resulting DOS curves were then renormalised to unit area.

## 7.4 Results and Discussion

### 7.4.1 Phonons

Our results for the neutron-weighted phonon DOS curves of martensite and austenite at room temperature are presented in figure 7.5. The martensite has a stiffer phonon DOS than the austenite, with an energy cutoff that is larger by about 2 meV. The transverse and longitudinal modes in the martensite are not as well separated as in the austenite, but all van Hove singularities in the martensite are shifted toward higher energies. The neutron-weighted martensite DOS also displays excess intensity at low energy, which we find to be due to an overweighting of the Ni contribution to low energy modes, as discussed below.

The DOS for the lowest temperature and for the intermediate states of transformation were corrected for neutron-weighting using the procedure described above. Results are plotted in figure 7.6. The DOS curves for the two-phase sample exhibit a smooth evolution from the high-temperature austenite to the low-temperature martensite as the austenite phase fraction diminishes. We do not observe any effect on the two-phase phonon DOS caused by the stresses and strains in the mixed phase samples. Within the statistical errors of our measurements, the total DOS at any degree of transformation is the phase fraction-weighted average of the martensite DOS and austenite DOS. For the martensite, a phonon DOS softening was observed between 80 K and 300 K. This is discussed further below.

Previous neutron scattering measurements were performed on FCC Fe<sub>70</sub>Ni<sub>30</sub> solid-solutions by Hallman and Brockhouse [156], using a triple-axis spectrometer. These authors obtained phonon dispersions along high symmetry directions for the FCC phase at room temperature, and partial dispersions for long wavelength acoustic phonons at 573 K. They obtained tensorial interatomic force-constants up to fifth nearest-neighbors for room

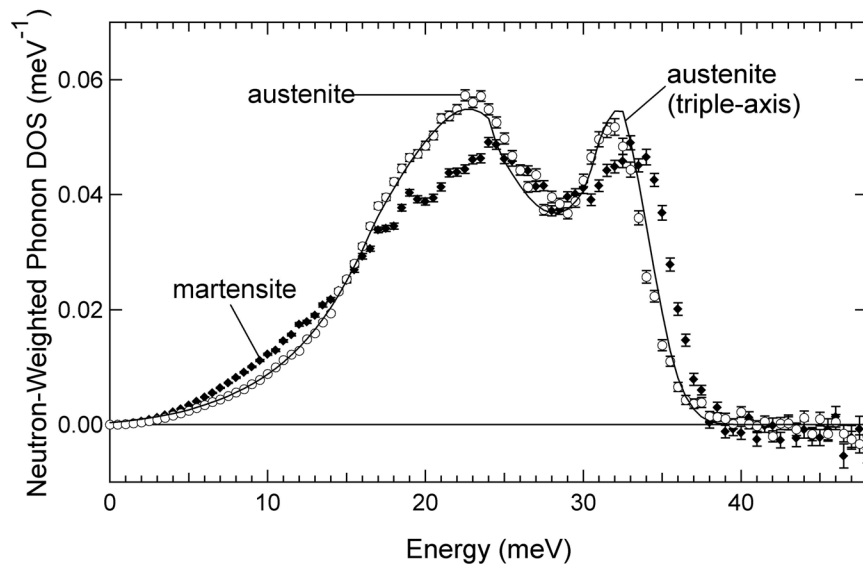


Figure 7.5: Neutron-weighted phonon DOS for  $\gamma$  (white circles) and  $\alpha$  (black diamonds)  $\text{Fe}_{71}\text{Ni}_{29}$  at room temperature, measured by inelastic neutron scattering. The martensite ( $\alpha$ ) result is after cooling the sample to 80 K. The continuous line is the DOS for  $\gamma$ - $\text{Fe}_{70}\text{Ni}_{30}$  obtained by Hallman and Brockhouse (1969), convolved with the Pharos instrument resolution function.

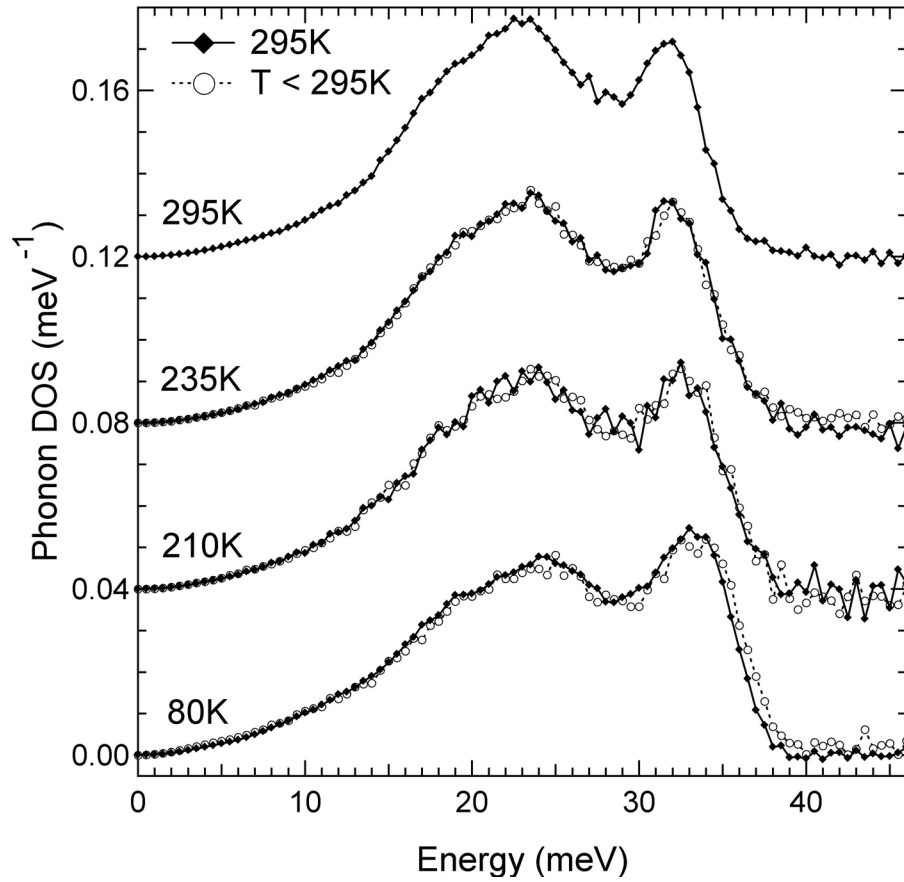


Figure 7.6: Phonon DOS of Fe<sub>71</sub>Ni<sub>29</sub> as function of cooling temperature, corrected for neutron-weighting. White circles: measurements at low temperature. Black diamonds: measurements at room temperature after cooling.

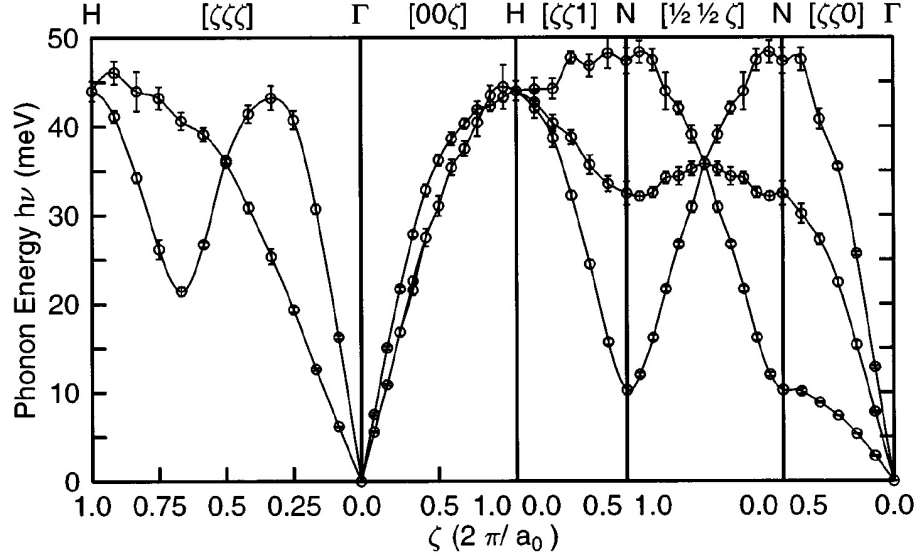


Figure 7.7: Phonon dispersions for BCC  $\text{Fe}_{80}\text{Ni}_{20}$  calculated by Meyer and Entel. The calculation is based on molecular-dynamics with embedded atom potentials [46].

temperature by fitting the experimental dispersions with a Born–von Kármán model, from which they obtained the density of states. The resulting DOS from those authors was convolved with our Pharos resolution function and is compared with our present result in figure 7.5. The agreement is excellent, validating our analysis procedure. The cutoff energy, the positions of the van Hove singularities and the low-energy acoustic behaviour are virtually identical. Because the DOS obtained from force-constants is free of neutron-weighting, the agreement shows that the neutron-weighting in the FCC phase does not affect the shape of the total DOS, and thus the partial DOS curves for Ni and Fe in the FCC phase must be very similar.

We now turn to the analysis of the BCC martensite phonon DOS. In an attempt to elucidate the lattice-dynamical origin of the high-temperature  $\alpha \rightarrow \gamma$  reverse martensitic transformation in  $\text{Fe}_{80}\text{Ni}_{20}$ , Meyer and Entel [46] have performed simulations of phonon dispersions in the BCC phase, using molecular-dynamics with embedded-atom-method potentials. Although the authors report no indication of a soft mode at the martensite-austenite transformation, they predict that [110]- $\text{TA}_1$  phonons at 300 K have very low energies, with a maximum energy at the N point of about 10 meV. Their results are shown in figure 7.7.

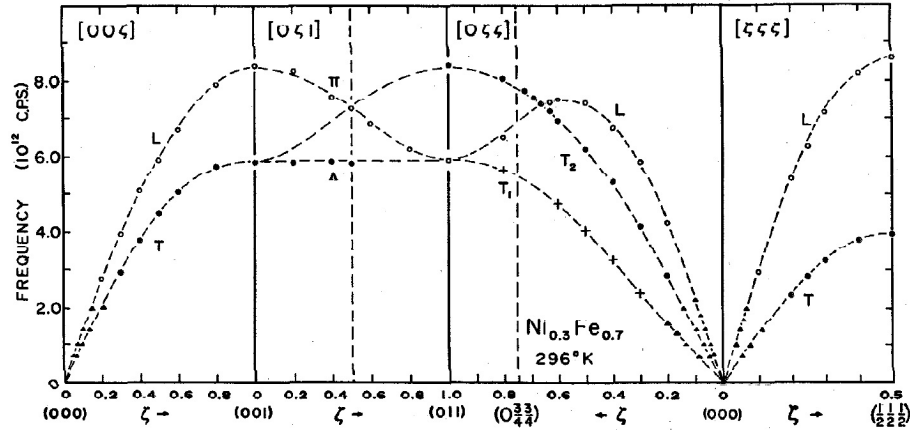


Figure 7.8: Phonon dispersions for FCC  $\text{Fe}_{70}\text{Ni}_{30}$  measured by Hallman and Brockhouse [156].

For comparison, the  $\text{TA}_1$  mode at the N point in pure BCC Fe has an energy of 18.5 meV (Mienkiewicz *et al.* [37]). One should note that the longitudinal phonon frequencies calculated by Meyer and Entel are somewhat overestimated (by as much as 8%), as suggested by the authors and evidenced by their calculations on the pure elements. The authors also found a pronounced softening with temperature of those phonons, with an energy decrease between 300 K and 600 K in excess of 30% along the whole branch. They attribute these low-energy modes to the instability of Ni atoms in the BCC phase. On the other hand, the FCC phase in  $\text{Fe}_{70}\text{Ni}_{30}$  does not show any modes of anomalously low energy and the dispersions are remarkably similar to those of pure FCC Ni (de Wit and Brockhouse [82], Hallman and Brockhouse [156]). The phonon dispersions of  $\text{Fe}_{70}\text{Ni}_{30}$  measured by Hallman and Brockhouse are shown in figure 7.8.

The temperature behavior of the acoustic phonons is also the same in the alloy and pure Ni, with 2.5% average frequency softening from 296K to 573K.

Goldman and Robertson [153] investigated the elastic moduli of austenite and martensite for Fe-29%at Ni using resonant ultrasound pulse techniques. These authors report that at the  $M_S$  temperature the shear modulus  $\mu$  in the martensite is smaller than that in austenite by 15% ( $\mu_\alpha = 55$  GPa,  $\mu_\gamma = 65$  GPa) and that Young's modulus  $E$  in the martensite is also smaller than that in austenite, by 8% ( $E_\alpha = 153$  GPa,  $E_\gamma = 167$  GPa). The shear modulus is directly related to long-wavelength transverse acoustic modes, so this result adds credibility

to the low-energy modes predicted by Meyer and Entel.

Goldman and Robertson's results correspond to a much higher Poisson ratio in the martensite  $\nu_\alpha = 0.39$  than in the austenite  $\nu_\gamma = 0.28$ , for  $T = M_S$ . Also, because of the difference in the Poisson ratio, their results would indicate that the bulk modulus  $B$  follows a trend opposite to that of Young's modulus:  $B_\alpha = 234 \text{ GPa} > B_\gamma = 129 \text{ GPa}$ . The value of  $B_\gamma$  obtained from those authors' results is compatible with the result of Oomi and Mōri, who found  $B_\gamma = 114 \pm 5 \text{ GPa}$  in ferromagnetic fcc  $\text{Fe}_{70}\text{Ni}_{30}$  at  $-30^\circ\text{C}$  with high-pressure measurements [157]. In a high pressure study of  $\text{Fe}_{70}\text{Ni}_{30}$ , Oomi and Mōri [157] found bulk modulus values for the austenite of  $177 \pm 8 \text{ GPa}$  for the paramagnetic state and about  $108 \pm 5 \text{ GPa}$  for the ferromagnetic state, both at 300K. The bulk modulus temperature dependence found by those authors leads to values at  $-30^\circ\text{C}$  of  $183 \pm 8 \text{ GPa}$  and  $114 \pm 5 \text{ GPa}$  for the paramagnetic and ferromagnetic phases, respectively. Since the austenite in Fe–29%at Ni at  $M_S$  is ferromagnetic, the values obtained by Oomi *et al.* and Goldman *et al.* are compatible. These two results may differ because the austenite for 29% Ni is not fully magnetically saturated before the martensitic transformation, thereby increasing its bulk modulus.

Franz *et al.* [155] obtained the Fe-pDOS as a function of temperature from 300 K up to 720 K. Although the resistivity measurements of Kaufmann and Cohen [151] place the  $\alpha \rightarrow \gamma$  start temperature  $A_S$  above 800 K for this composition, Franz *et al.* were able to directly measure the change in Fe-pDOS corresponding to the reverse martensitic transformation. But as the authors point out, the highest temperature they measured corresponds to only a partial transformation to the FCC phase. The features of the Fe-pDOS curves they obtained are similar to our results for the total phonon DOS, with a large softening of the DOS from the  $\alpha$  to the  $\gamma$  phase (in excess of 4 meV at the cutoff), yielding an average Fe-frequency softening  $\langle \hbar\omega_{Fe} \rangle_{\gamma, 720\text{K}}^{\text{Fe}_{80}\text{Ni}_{20}} / \langle \hbar\omega_{Fe} \rangle_{\alpha, 300\text{K}}^{\text{Fe}_{80}\text{Ni}_{20}} = 0.887$ . Using our neutron-weight-corrected DOS, we found an average frequency ratio of austenite to martensite at room temperature  $\langle \hbar\omega \rangle_{\gamma, 295\text{K}}^{\text{Fe}_{71}\text{Ni}_{29}} / \langle \hbar\omega \rangle_{\alpha, 295\text{K}}^{\text{Fe}_{71}\text{Ni}_{29}} = 23.6/24.7 = 0.955$ . Because Franz *et al.* performed their  $\gamma$  phase measurement at 720 K, extra softening is present in their Fe-pDOS compared to the DOS we measured at 295 K. The authors do not report any Fe-pDOS for the  $\gamma$  phase at lower temperatures, although the measurements by Kaufmann and Cohen [151]

place  $M_S$  around 500 K for 20%Ni. While the Fe-pDOS measurement of Franz *et al.* is very interesting in itself, their result for the Fe-pDOS in the martensite at 300 K does not present a strong evidence for the low energy modes predicted by Meyer *et al.* [46] at this temperature.

The Ni-pDOS obtained with the analysis presented above differs markedly from the Fe-pDOS. The dewighted BCC total DOS and the partial DOS for Fe and Ni are shown in figure 7.9. The Ni-pDOS shows an unexpectedly big contribution from low-energy modes, where Ni atoms undergo large amplitude vibrations. On the other hand, it is much lower than the Fe-pDOS above 30 meV. The dewighted total DOS is smaller than its neutron-weighted counterpart at low energies, owing to the overweighting of large amplitude Ni vibrations at low energies. The reverse is true at high energies, where the modes involving mostly Fe contributions were underweighted. The dewighted martensite DOS still shows a small excess of low energy modes between 7 meV and 13 meV, compared with the austenite DOS, although our neutron-weight correction greatly reduced this effect. It thus appears that the phonon DOS for the martensite has more modes at low energies than for the austenite; the consequences for the entropy of transformation are discussed in the next section.

Herper *et al.* have used *ab-initio* techniques to study the FCC  $\rightarrow$  BCT martensitic transformation in ordered L1<sub>2</sub> Fe<sub>3</sub>Ni [158]. Using the frozen-phonon approach, they calculated the phonon softening as function of decreasing temperature in the FCC phase, and ascribed soft-phonon transverse modes in the [110] direction as precursors of the martensitic phase transition. They related the phonon softening along this branch to the increase in the electron-phonon coupling, which the authors expect from the increase in electron density at the Fermi level with decreasing temperature. Although transverse precursor mode softening is generally accepted as a possible mechanism for the FCC to BCT martensitic transformation, no direct evidence for this mechanism can be obtained from our data.

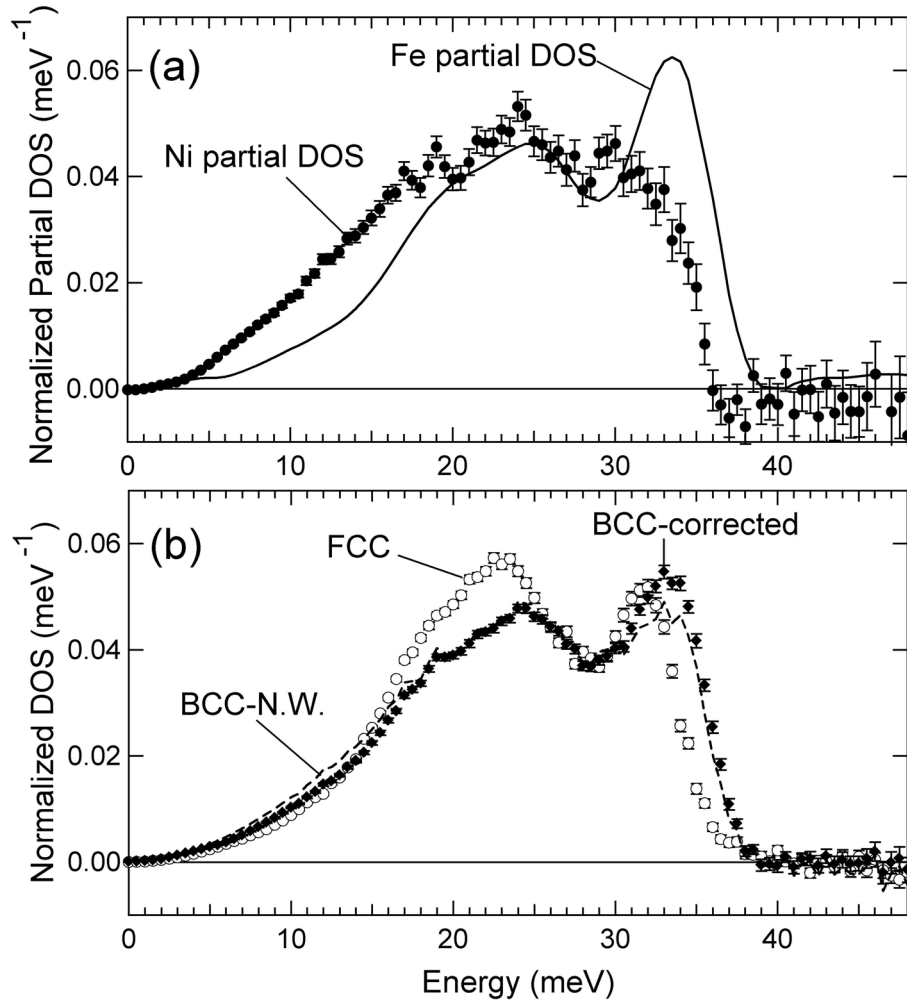


Figure 7.9: a) Partial phonon DOS curves for Fe and Ni in the martensite, at room temperature. Line: Fe-pDOS obtained by Franz *et al.* [155]. Dots: Ni-pDOS determined from Franz's measurement and our martensite total DOS result. b) Room-temperature phonon DOS curves. Dashed line: neutron-weighted DOS for martensite. Diamonds: neutron-weight-corrected DOS for martensite. White circles: neutron-weighted DOS for austenite (the neutron-weight in this case is minor, see text).

Table 7.1: Latent heat and entropy contributions to the  $\gamma \rightarrow \alpha$  and  $\alpha \rightarrow \gamma$  transformations in  $\text{Fe}_{71}\text{Ni}_{29}$ .

	$\Delta Q$ ( $J \text{ mol}^{-1}$ )	$\Delta S_{\text{tot}}$ ( $k_{\text{B}} \text{ atom}^{-1}$ )	$\Delta S_{\text{vib}}$ ( $k_{\text{B}} \text{ atom}^{-1}$ )	$\Delta S_{\text{mag}}$ ( $k_{\text{B}} \text{ atom}^{-1}$ )
$\gamma \rightarrow \alpha$	$-293 \pm 17$	$-0.15 \pm 0.01$	$-0.12 \pm 0.02$	$(-0.03 \pm 0.02)^*$
$\alpha \rightarrow \gamma$	$1800 \pm 150$	$0.32 \pm 0.03$	$(0.12 \pm 0.02)^\dagger$	0.25

## 7.4.2 Entropy

### Calorimetry

Listed in table 7.1 are the latent heat and entropy change in the martensitic phase transformation  $\gamma \rightarrow \alpha$  and the reverse transformation  $\alpha \rightarrow \gamma$  that we obtained by differential scanning calorimetry. Our result for the entropy change in the  $\gamma \rightarrow \alpha$  transformation is in good agreement with the approximate value reported by Goldman and Robertson [154], who obtained  $\Delta S_{\text{tot}}^{\gamma \rightarrow \alpha} = -0.8 \text{ cal mol}^{-1} = -0.1 k_{\text{B}} \text{ atom}^{-1}$  for the total entropy change from differential thermal analysis measurements on Fe - 29%at Ni. The total enthalpy and entropy values we report for the  $\gamma \rightarrow \alpha$  transformation were corrected for the fact that the martensitic transformation is not complete at the lowest temperature of 173 K we could attain with our calorimeter. We estimated from our phase-fraction measurements that there was 15% austenite remaining at this temperature, so our calorimetry results for the  $\gamma \rightarrow \alpha$  transformation were increased by 15% to account for this. On the other hand, the starting material in the  $\alpha \rightarrow \gamma$  DSC measurement was nearly fully martensitic (with perhaps 5% austenite), and our result for the enthalpy change  $\Delta H^{\alpha \rightarrow \gamma} = 1800 \pm 150 \text{ J mol}^{-1}$  is in excellent agreement with the value of  $\Delta H^{\alpha \rightarrow \gamma} = 1800 \text{ J mol}^{-1}$  reported by Porter and Easterling [159].

The values we found for the enthalpy and entropy changes during the reverse  $\alpha \rightarrow \gamma$  transformation are much larger than their respective magnitudes for the  $\gamma \rightarrow \alpha$  transformation. This can be explained by the different magnetic states of the austenite and martensite, as discussed below.

Yamamoto *et al.* report an even larger value for  $\Delta S^{\alpha \rightarrow \gamma}$  [160]. Yamamoto *et al.* studied

the pressure-induced reverse martensitic transformation in Fe<sub>70</sub>Ni<sub>30</sub> by x-ray diffraction and electric resistance measurements. Using Clapeyron's equation, they estimated the entropy change from the change of  $A_S$  and the change in specific volume between ambient pressure and 8 GPa as  $\Delta S^{\alpha \rightarrow \gamma} = 0.509 k_B/\text{atom}$ . Since the authors used only two pressure points at 0 GPa and 8 GPa, they did not get a precise behavior of the phase boundary and the value they obtained is only an approximation for  $\Delta S^{\alpha \rightarrow \gamma}$  at ambient pressure. In particular, another high-pressure study for the dependence of  $M_S$  on pressure in Fe<sub>70.1</sub>Ni<sub>29.9</sub> has shown a highly non-linear behaviour of  $M_S(P)$  between 0 GPa and 1.5 GPa [161]. In this light, we consider that the results of Yamamoto *et al.* overestimate the true value  $\Delta S^{\alpha \rightarrow \gamma}$ . Also, this estimate of  $\Delta S^{\alpha \rightarrow \gamma}$  should take into account the change in magnetic configuration.

### Phonon Entropy

The vibrational entropy  $S_{\text{vib}}(T)$  at temperature  $T$  is given in the quasiharmonic approximation by

$$S_{\text{vib}}(T) = 3k_B \int_0^{E_{\text{max}}} [(n_T(E) + 1)\ln(n_T(E) + 1) - n_T(E)\ln(n_T(E))] \times g_T(E) \, dE \quad (7.5)$$

where  $n_T(E)$  is the Bose-Einstein distribution,  $g_T(E)$  is the DOS and  $E_{\text{max}}$  the phonon energy cutoff. Using the as-measured austenite DOS curve at 300 K and the neutron-weight corrected martensite also at 300 K, we obtained a difference in vibrational entropy between the two measured materials of  $\Delta S_{\text{vib}} = -0.10 \pm 0.02 k_B \text{ atom}^{-1}$ . Using our phase-fraction determination from neutron diffraction patterns, we estimated there was 20% remaining austenite in the martensitic sample, so we obtained a vibrational entropy change in the martensitic transformation of  $\Delta S_{\text{vib}}^{\gamma \rightarrow \alpha} = -0.12 \pm 0.02 k_B \text{ atom}^{-1}$ .

The softening of the martensite DOS between 80 K and 300 K can be related to the classical softening due to the expansion of the lattice. The classical relationship can be evaluated with our in situ neutron-diffraction measurements and published values of elastic constants. From a refinement of the neutron diffraction patterns, we found lattice parameters for the BCC martensite  $a = 2.858 \pm 0.003 \text{ \AA}$  at 80 K and  $a = 2.863 \pm 0.002 \text{ \AA}$  at 295 K, the latter being in good agreement with the reported density measurement of Goldman

and Robertson [153] at room temperature for BCC Fe-29%at Ni of  $\rho = 8.001 \text{ g cm}^{-3}$ , or equivalently  $a = 2.866 \text{ \AA}$ . The average linear thermal expansion coefficient between these two temperatures is  $\alpha_L = 8 \times 10^{-6}$ , in good agreement with the 100 K-300 K portion of the dilatometric measurement of Acet *et al.* [162] on Fe<sub>70</sub>Ni<sub>30</sub>. Using a bulk modulus  $B = 234 \text{ GPa}$  of the martensite reported by Goldman and Robertson [153], we find the classical contribution to the anharmonic entropy due to the expansion of the lattice against the bulk modulus:

$$\Delta S_{\text{anh}}^{\text{expan}}(T_0, T_1) = \int_{T_0}^{T_1} 9Bv\alpha_L^2 dT, \quad (7.6)$$

where  $v$  is the specific volume. Using the values listed above, we obtained  $\Delta S_{\text{anh}}^{\text{expan}} = 0.02 k_{\text{B}} \text{ atom}^{-1}$ .

We now calculate the anharmonic entropy change from the martensite DOS at 80 K and 295 K. In the quasiharmonic approximation, the anharmonic entropy change is obtained from the DOS as

$$\Delta S_{\text{anh}}(T_0, T_1) = S_{\text{vib}}[n_{T_1}(E), g_{T_1}(E)] - S_{\text{vib}}[n_{T_0}(E), g_{T_0}(E)]. \quad (7.7)$$

Because we do not have a neutron-weight-corrected DOS for the martensite at 80K, we use the neutron-weighted DOS curve at both temperatures; since the neutron-weight affects the martensite DOS similarly at both temperatures, we expect the result to be reliable. We find  $\Delta S_{\text{anh}}(80\text{K}, 295\text{K}) = 0.01 \pm 0.01 k_{\text{B}} \text{ atom}^{-1}$ , in good agreement with the classical result. An average Grüneisen parameter  $\bar{\gamma} = vB\alpha_L/k_{\text{B}}$  was evaluated as  $\bar{\gamma} = 1.6$ , from which we obtain  $\Delta\langle\nu\rangle/\langle\nu\rangle|_{80\text{K}}^{295\text{K}} \approx -1\%$ , in good agreement with the observed shift of the cutoff energy and the average change of frequency:  $\langle\nu\rangle_{295\text{K}}^\alpha/\langle\nu\rangle_{80\text{K}}^\alpha = 0.988$ . Hence the martensite is shown to behave quasiharmonically in this range of temperatures, the only source of phonon softening being the classical effect associated with lattice expansion against the bulk modulus.

### Magnetic Entropy

The magnetization of both the  $\alpha$  and  $\gamma$  phase in Fe - 28.7%at Ni was measured by Peschard [163] across both the martensitic and reverse-martensitic transformations. Peschard's re-

sults show that for this composition, the martensite remains ferromagnetic to the temperature of the  $\alpha \rightarrow \gamma$  transformation. The author estimates through graphical interpolation that without the transformation to austenite, the Curie temperature for the BCC phase would be  $T_C \approx 870$  K. From these magnetisation measurements, we calculated the magnetic entropy in the Bragg-Williams approximation (Chaikin and Lubensky [164]),

$$S_{\text{mag}}(m)/k_B = \ln(2) - 1/2[(1+m)\ln(1+m) + (1-m)\ln(1-m)], \quad (7.8)$$

where  $m$  is the ratio of the magnetization to the saturation magnetization of the sample. The magnetic entropy curves thus obtained are shown in figure 7.10. When comparing the magnetization curves of the  $\alpha$  and  $\gamma$  phases, one should keep in mind that the saturation magnetization in the  $\gamma$  is about half of that in the  $\alpha$ , with an average magnetic moment per atom  $\mu^\gamma = 1.25\mu_B$  compared to  $\mu^\alpha = 2.2\mu_B$  (Crangle and Hallam [165]).

The Curie temperatures for the  $\gamma$  and the  $\alpha$  phases are room-temperature and 870 K, respectively. Above these temperatures, the magnetic spins are oriented randomly, and the magnetic entropies of both phases reach their maximum value of  $\ln(2) k_B \text{ atom}^{-1}$ . However, upon heating, the ferromagnetic  $\alpha$  phase transforms to paramagnetic  $\gamma$  at the reverse martensitic transformation temperature  $A_S$  before it becomes paramagnetic. Upon cooling the  $\gamma$  phase from high temperature, it becomes ferromagnetic below 380 K and then transforms martensitically to the ferromagnetic  $\alpha$  phase. Since the Curie temperature for the austenite is close to  $M_S$  in Fe-29%Ni, it is possible that the austenite is not fully saturated magnetically before it transforms to martensite. The small difference of  $0.03 k_B \text{ atom}^{-1}$  between our values of  $\Delta S_{\text{tot}}^{\gamma \rightarrow \alpha}$  measured by DSC (although a slight underestimate, as discussed above) and  $\Delta S_{\text{vib}}^{\gamma \rightarrow \alpha}$  measured by inelastic neutron scattering possibly originates from a non fully saturated state of the ferromagnetic austenite before it transforms to martensite below 240 K.

From the magnetisation curve for heating of the  $\alpha$  and the magnetisation for the  $\alpha$  phase above  $A_S$  reported by Peschard, we estimated the phase fraction of transformed material,  $x_\gamma(T)$ . By integrating the entropy contribution of each differential element of martensite

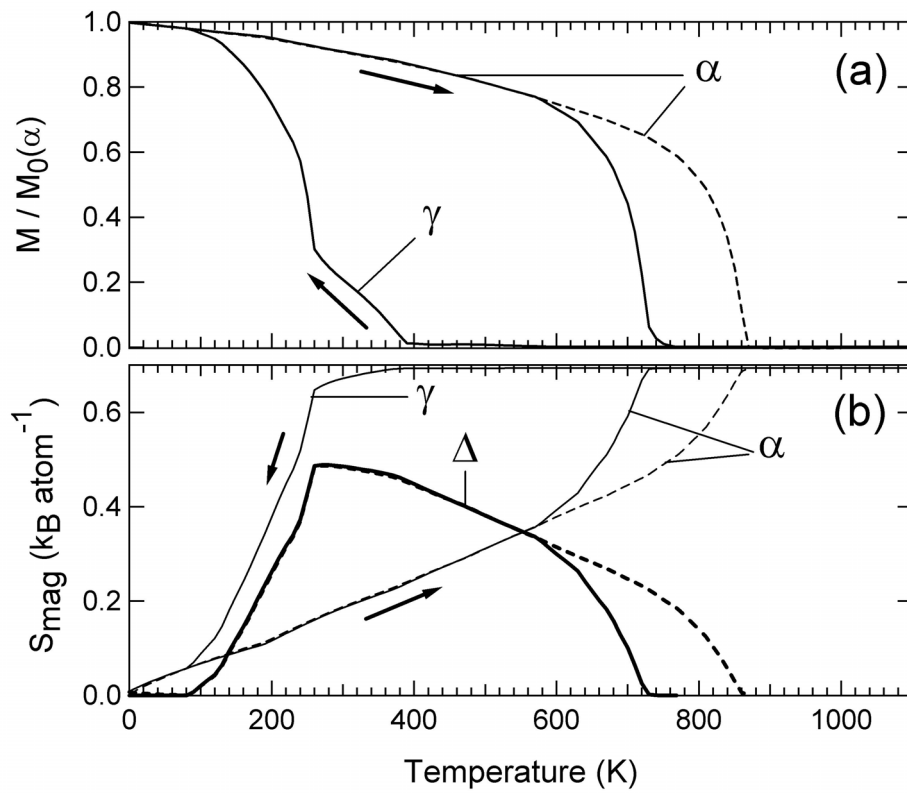


Figure 7.10: a) Magnetisation measurements of Peschard on Fe-28.7%Ni [163]. b) Magnetic entropy curves derived from Peschard's measurements, with the analysis described in the text. The curve labelled  $\Delta$  is the magnetic entropy difference between the austenite ( $\gamma$ ) and the martensite ( $\alpha$ ).

transforming to austenite, we then obtained the magnetic entropy of the transformation

$$\Delta S_{\text{mag}}^{\alpha \rightarrow \gamma} = \int_{A_S}^{A_F} \frac{dx_{\gamma}(T)}{dT} [S_{\text{mag}}(m_{\gamma}(T)) - S_{\text{mag}}(m_{\alpha}(T))] dT, \quad (7.9)$$

where the start and end temperatures for the  $\alpha \rightarrow \gamma$  transformation are  $A_S = 590$  K and  $A_F = 770$  K, respectively. We found  $\Delta S_{\text{mag}}^{\alpha \rightarrow \gamma} = 0.25 k_B \text{ atom}^{-1}$ . This estimate of the magnetic contribution to the increase in entropy at the reverse-martensitic transformation brings our calorimetric measurement  $\Delta S_{\text{total}}^{\alpha \rightarrow \gamma} = 0.32 \pm 0.03 k_B \text{ atom}^{-1}$  in good agreement with our result for the vibrational entropy change at the martensitic and reverse-martensitic transformations,  $\Delta S_{\text{vib}}^{\alpha \rightarrow \gamma} = -\Delta S_{\text{vib}}^{\gamma \rightarrow \alpha} = 0.12 \pm 0.02 k_B \text{ atom}^{-1}$ . Thus it appears that the magnetic contribution to the entropy change at the  $\alpha \rightarrow \gamma$  transformation is twice that due to phonons. The remaining possible contributions to  $\Delta S_{\text{total}}^{\alpha \rightarrow \gamma}$ , such as electronic entropy  $\Delta S_{\text{el}}$ , should be small.

## 7.5 Analysis of Time-of-Flight Coherent Phonon Scattering

So far, we have conducted our analysis of neutron scattering data within the incoherent scattering approximation. Despite the fact that Fe and Ni both present strong coherent neutron scattering cross-sections, we have illustrated the validity of our procedure by reproducing the phonon DOS of FCC Fe-Ni obtained from published interatomic force-constants inferred from triple-axis measurements (see section 7.4). This success can be attributed to the good reciprocal space sampling achieved in our measurement, which allows for a meaningful averaging of the scattering. This incoherent averaging to extract the phonon DOS benefited from the use of polycrystalline samples, which effectively performs a directional average of the phonon dispersions. Our sampling of the scattering function  $S(Q, E)$  also extends to large momentum transfers  $Q$ , and thus encompasses many Brillouin zones in reciprocal space. The phonon DOS is an integral over the phonon dispersions, but the latter contains more information on the lattice dynamics. The coherent nature of the Fe-Ni system allows for a more advanced analysis. Using a lattice-dynamics model, one can calculate the full theoretical  $S_{\text{coh}}^{\text{th}}(Q, E)$  and compare the results directly with the experimental quantity,  $S_{\text{coh}}^{\text{exp}}(Q, E)$ . The incoherent scattering function  $S_{\text{inc}}^{\text{th}}(Q, E)$  can be

obtained similarly from the lattice-dynamics model, and the total inelastic scattering function  $S_{\text{inel}}(Q, E) = S_{\text{coh}}(Q, E) + S_{\text{inc}}(Q, E)$  can thus be calculated. This requires *a priori* knowledge of the lattice dynamics, and in the case of a Born–von Kármán model, one needs the tensorial interatomic force-constants.

The intensity from the inelastic neutron scattering measurements on Pharos were reduced to scattering functions  $S^{\text{exp}}(Q, E)$  for the martensite and austenite phase, both at room temperature. Results are shown in figure 7.11. The diffraction peaks at zero energy transfer are labelled for the FCC and BCC phases. The arches branching out of these diffraction peaks (or reciprocal lattice vectors) are the orientation-averaged phonon dispersions for the polycrystalline samples.

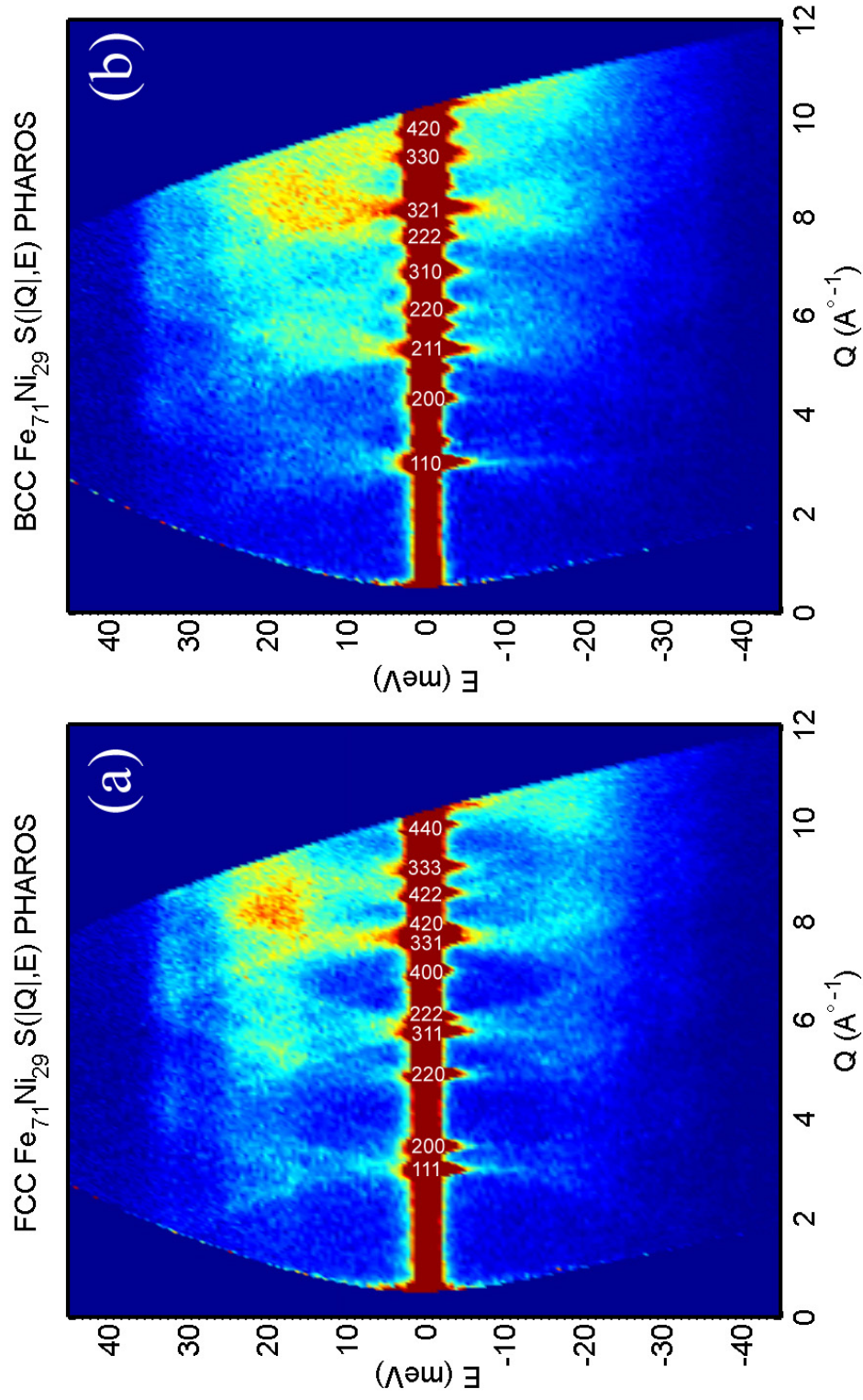


Figure 7.11:  $S^{\text{exp}}(Q, E)$  for  $\text{Fe}_{71}\text{Ni}_{29}$ . (a) FCC phase, (b) BCC phase. Both measurements were carried out at room temperature on the Pharos time-of-flight neutron spectrometer.

### 7.5.1 General Considerations

For coherently scattering nuclei distributed on a Bravais lattice, the scattering function  $S(Q, E)$  is closely related to the phonon dispersions in the crystal [14]. In an inelastic neutron scattering experiment, one measures the double-differential neutron scattering cross-section,  $(d^2\sigma/d\Omega dE)$ , which is directly related to the scattering function,  $S(\mathbf{Q}, E)$ . For a coherent one-phonon creation process in a monatomic crystal, we have

$$\left(\frac{d^2\sigma}{d\Omega dE}\right)_{\text{coh}+1} = \frac{\sigma_{\text{coh}}}{4\pi} \frac{k_f}{k_i} N S_{\text{coh}}(\mathbf{Q}, E), \quad (7.10)$$

where  $E = \hbar\omega$  is the energy transferred from the neutron to the sample,  $\sigma_{\text{coh}}$  is the coherent neutron cross-section for the single species present,  $k_i$  and  $k_f$  are the incident and scattered neutron wave vectors,  $N$  is the number of unit cells in the crystal, and  $\mathbf{Q}$  is the wave vector transferred to the crystal. After an easy correction for the ratio of final and incident wave vectors, one is left with a quantity proportional to  $S_{\text{coh}}(\mathbf{Q}, E)$ . For the case of scattering with the coherent creation of one phonon, the scattering function is given by

$$S_{\text{coh}}(\mathbf{Q}, E) = \frac{(2\pi)^3}{Nv_0} \frac{1}{2M} \exp(-2W) \times \sum_s \sum_{\boldsymbol{\tau}} \frac{(\mathbf{Q} \cdot \mathbf{e}_s)^2}{\omega_s} \langle n_s + 1 \rangle \delta(\omega - \omega_s) \delta(\mathbf{Q} - \mathbf{q} - \boldsymbol{\tau}), \quad (7.11)$$

where  $v_0$  is the unit cell volume;  $M$  is the mass of the atom;  $W$  is the Debye-Waller factor;  $\omega_s$ ,  $\mathbf{e}_s$  and  $n_s$  are the pulsation, polarization vector, and Bose-Einstein thermal occupancy factor for the phonon mode of index  $s$  (which collects branch index  $\sigma$  and wave vector  $\mathbf{q}$ ). The sum over  $\boldsymbol{\tau}$  runs over reciprocal lattice vectors. From Eq. 7.11, we can see that  $S_{\text{coh}}(\mathbf{Q}, E)$  gives us information about the phonon dispersions of the sample  $\omega(\mathbf{q})$ . The scattering function for a given wave vector transfer  $\mathbf{Q}$  and a given energy transfer  $E$  is the sum of contributions from all single phonon modes that can be excited, while preserving conservation of energy and momentum (up to a reciprocal lattice vector). Each phonon mode  $s$  contributes in proportion to how well its polarization vector  $\mathbf{e}_s$  is aligned with the momentum transfer  $\mathbf{Q}$ , giving rise to the polarization factor  $|\mathbf{Q} \cdot \mathbf{e}_s|^2$ . Performing the summation in 7.11 over the first Brillouin zone and applying shifts by reciprocal lattice

vectors  $\boldsymbol{\tau}$  is equivalent to summing over the whole of reciprocal space. We will place ourselves in this “extended zone scheme” and discard  $\boldsymbol{\tau}$  in the rest of this discussion.

When measuring a polycrystalline sample, one obtains only the average of  $S_{\text{coh}}(\mathbf{Q}, E)$  over all orientations of the crystallites relative to the neutron beam. In the absence of preferential orientation for the crystallites in the sample,  $S_{\text{coh}}(\mathbf{Q}, E)$  thus reduces to  $S_{\text{coh}}(Q, E)$ . We can calculate  $S_{\text{coh}}(Q, E)$  from 7.11 using the previously described Born–von Kármán model in the following manner. The possible phonon wave vectors in reciprocal space effectively forming a continuum, we can pick an arbitrary value,  $\mathbf{q}$ , and diagonalize the dynamical matrix at this point. This provides us with phonon eigen–energies at this point,  $\{\omega_{\mathbf{q},\sigma}\}_{\sigma=1,2,3}$ , as well as the polarization vector for each corresponding mode  $\{\mathbf{e}_{\mathbf{q},\sigma}\}_{\sigma=1,2,3}$ . The Dirac delta functions for conservation of momentum and energy in 7.11 then tells us that each of the three modes just calculated can only contribute to  $S_{\text{coh}}(Q, E)$  for  $Q = |\mathbf{q}|$  and  $E \in \{\hbar\omega_{\mathbf{q},\sigma}\}_{\sigma=1,2,3}$ .

We can thus determine the partial contribution of these three modes to  $S_{\text{coh}}(Q, E)$ , by adding  $\langle n_s + 1 \rangle (\mathbf{Q} \cdot \mathbf{e}_s)^2 / \omega_s$  to a histogram of  $S$ . Sweeping reciprocal space with  $\mathbf{q}$ , we thus “build-up” the scattering function  $S_{\text{coh}}(Q, E)$  for any  $Q$ -range. While the range of  $Q$  we calculate might be taken to correspond to our experimental sampling, the range of energy  $E$  is dictated by the lattice dynamics of the system and is not known *a priori*, although it is also limited experimentally. The Debye-Waller factor  $W$  also depends on  $Q$ . For a cubic Bravais crystal, one can show that

$$2W = \frac{1}{3} Q^2 \langle u^2 \rangle, \quad (7.12)$$

where the mean square thermal atomic displacement  $\langle u^2 \rangle$  is related to the phonon DOS  $g(\omega)$  through

$$\langle u^2 \rangle = \frac{3\hbar}{2M} \int_0^{\omega_{\text{max}}} g(\omega) \coth(\beta\hbar\omega/2) / \omega \, d\omega, \quad (7.13)$$

with  $\beta = 1/k_{\text{B}}T$  [14]. Thus, we also need the phonon DOS to obtain  $S(Q, E)$ . A practical approach is to calculate  $S_{\text{coh}}(\mathbf{Q}, E) \exp(2W)$  as we sweep reciprocal space and populate the DOS histogram with the phonon eigen-frequencies determined at each  $\mathbf{q}$ -point. The

Debye-Waller factor is then calculated and factored in to obtain  $S_{\text{coh}}(Q, E)$ . In this way,  $S_{\text{inc}}(Q, E)$  is obtained essentially for free as a by-product. We should mention in passing that this simple procedure does not strictly hold for a non Bravais crystal. In effect, for a unit cell containing more than one atom, the Debye-Waller factor depends on which atom in the basis is considered, as each atom might have a different  $\langle u^2 \rangle$ . The partial differential coherent scattering cross-section is given in this case by

$$\left( \frac{d^2\sigma}{d\Omega dE} \right)_{\text{coh}+1} = \frac{k_f}{k_i} \frac{(2\pi)^3}{2v_0} \sum_s \sum_{\tau} \frac{1}{\omega_s} \left| \sum_{\kappa} \frac{\bar{b}_{\kappa}}{\sqrt{M_{\kappa}}} \exp(-W_{\kappa}) \exp(i\mathbf{Q} \cdot \mathbf{r}_{\kappa}) (\mathbf{Q} \cdot \mathbf{e}_{\kappa s}) \right|^2 \times \langle n_s + 1 \rangle \delta(\omega - \omega_s) \delta(\mathbf{Q} - \mathbf{q} - \boldsymbol{\tau}), \quad (7.14)$$

where  $\kappa$  runs over the atoms in the crystal basis,  $\bar{b}_{\kappa}$  is the average neutron scattering length for the atom  $\kappa$  (average over the isotopes of this species and over the nuclear spin values occupied) and  $\mathbf{r}_{\kappa}$  denotes the atomic positions inside the unit cell [14]. The terms in the sum over  $s = (\mathbf{q}, \sigma)$  in 7.14 then involve a sum over the basis atoms and each basis atom  $\kappa$  involves its own  $W_{\kappa}$ , so that the Debye-Waller factor cannot be factored out. However, in cases where  $W$  is not very dependent on the atom considered, one could use the previous procedure with the approximation  $W_{\kappa} \approx W$ .

### 7.5.2 Calculation of $S(Q, E)$ for FCC and BCC Fe-Ni

We now apply the general considerations of the previous section to the case of the  $\text{Fe}_{71}\text{Ni}_{29}$  solid solution. We use the virtual crystal approximation to treat the alloy as a Bravais lattice. We used the interatomic force-constants for the FCC solid-solution  $\text{Fe}_{70}\text{Ni}_{30}$  determined by Hallman and Brockhouse [156] to calculate  $S_{\text{coh}}(Q, E)$  using the approach described above. Hallman and Brockhouse obtained these force-constants from a fit of a Born-von Kármán model for the FCC alloy in the virtual crystal approximation to the phonon dispersions they measured on a triple-axis spectrometer. To build up  $S_{\text{coh}}(Q, E)$ , we used a random sampling of  $\mathbf{q}$ -points inside a sphere of radius  $Q_{\text{max}} = 10\text{\AA}^{-1}$ , corresponding to the maximum wave vector transfer at the elastic line in our experiments. Since the Born-von Kármán equations for lattice dynamics do not explicitly contain the lattice parameter  $a$  of the crystal, the wave vectors are scaled by  $\frac{2\pi}{a}$  in our calculation. To achieve

a good sampling of  $S_{\text{coh}}(Q, E)$ , we used  $3 \times 10^7$  random  $\mathbf{q}$ -points. The result of our calculation is shown in figure 7.12 (panel a), where it is compared to the experimentally measured scattering  $S_{\text{exp}}(Q, E)$  (panel b). The portion of  $S_{\text{coh}}(Q, E)$  displayed in figure 7.12 (a) is restricted to the region of  $(Q, E)$ -space allowed by the kinematics of scattering in the experimental conditions. The calculated  $S(Q, E)$  in this figure does not include  $S_{\text{inc}}(Q, E)$ , but the latter represents less than 10% of the total scattering in this case. The arches in the  $S_{\text{coh}}(Q, E)$  calculated intensity are the orientation-averaged phonon dispersions from our virtual crystal Born–von Kármán model. The dispersions stem from the points on the elastic line corresponding to reciprocal space lattice vectors. One can observe that the experimental intensity is well reproduced. The positions and slopes of the dispersions are in good agreement, which validates the interatomic force-constants used as input. One should keep in mind that these force-constants were obtained by fitting the phonon dispersions in a limited number of high-symmetry directions, whereas  $S(Q, E)$  samples the whole of reciprocal space.

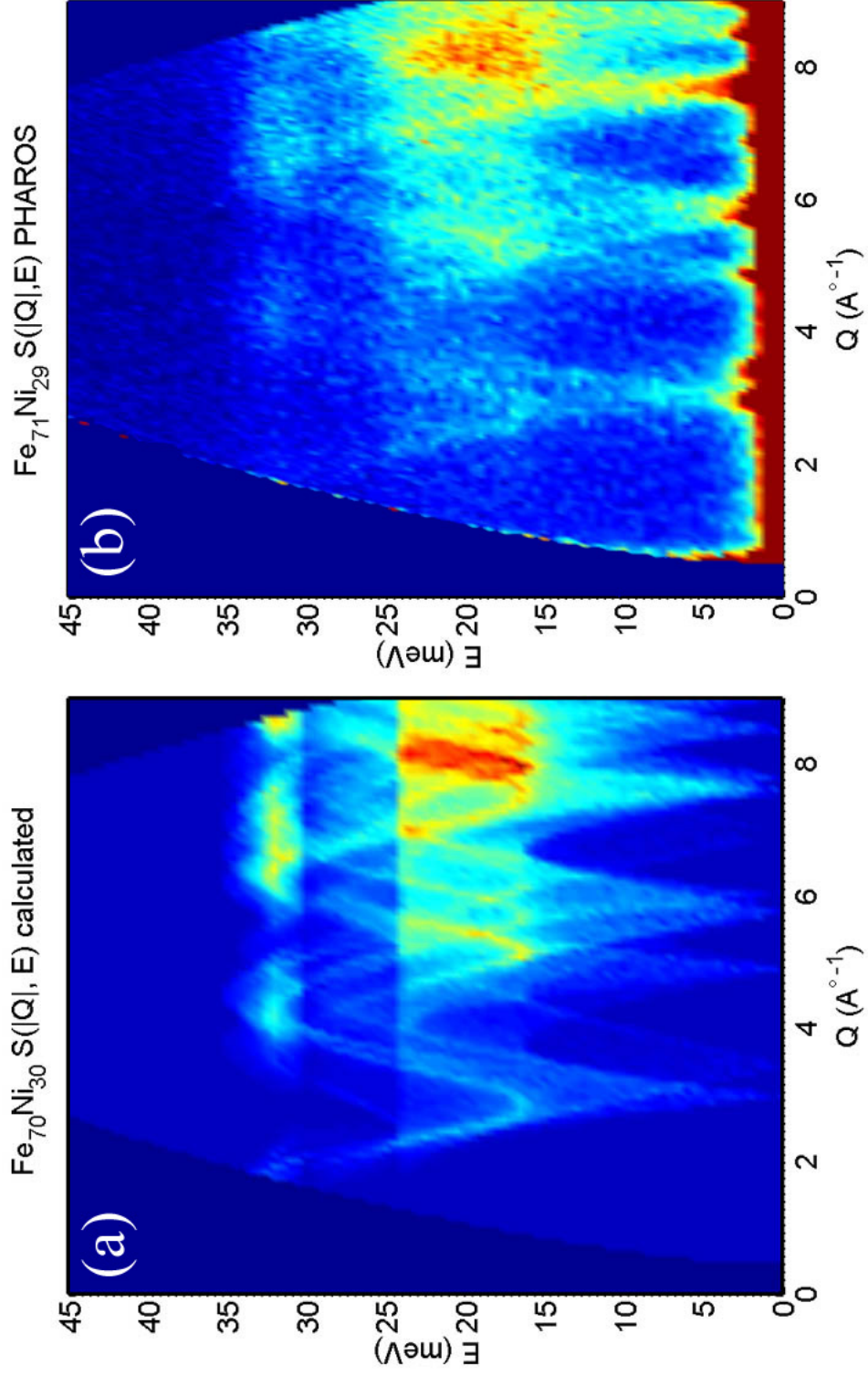


Figure 7.12: a)  $S^{\text{th}}(Q, E)$  for Fe<sub>70</sub>Ni<sub>30</sub> virtual crystal calculated from Born-von Kármán model, as described in text. b)  $S^{\text{exp}}(Q, E)$  for Fe<sub>71</sub>Ni<sub>29</sub> polycrystal measured on the Pharos time-of-flight neutron spectrometer. The color scale is linear; intensities are scaled by an arbitrary factor.

As discussed above, the calculation of  $S_{\text{coh}}(Q, E)$  and  $S_{\text{inc}}(Q, E)$  requires some knowledge of the lattice dynamics of the material. When using a Born–von Kármán description, one needs the interatomic force-constants. However, these can be seen as parameters to be refined by fitting  $S^{\text{th}}(Q, E)$  to  $S^{\text{exp}}(Q, E)$ . The analysis of  $S(Q, E)$  described in this section thus presents a new method to extract information about lattice dynamics from time-of-flight experiments. This method is potentially more powerful than the inversion of the phonon DOS alone, described in chapter 4, since it is based on the phonon dispersions measured over a large swath of reciprocal space, rather than phonon DOS, which is an integral quantity. One can foresee challenging requirements for the proper implementation of such a fitting procedure, such as the accurate accounting of experimental effects associated with the characteristics of the neutron spectrometer, as well as the computational cost of calculating  $S(Q, E)$ . In the case of the Pharos time-of-flight spectrometer, the characteristics of the instrument have been sufficiently well established, through calibrating runs or Monte Carlo simulations, that the resolution function in both  $Q$  and  $E$  is available. At the time the author writes this thesis, however, a full fitting procedure represents a heavy computation, because of the cost of calculating  $S(Q, E)$  from a Born–von Kármán model. Appropriately designed scientific software is needed to tackle this challenge.

## 7.6 Conclusion

Inelastic neutron scattering measurements showed that, although the phonon DOS is overall stiffer in the low-temperature martensite, it also has many modes at low energies. Using the result of Franz *et al.* [155] for the Fe partial DOS in BCC Fe<sub>80</sub>Ni<sub>20</sub>, we extracted the Ni partial DOS, which shows much more intense low-energy modes than its Fe counterpart, as suggested by a previous theoretical study (Meyer and Entel [46]). The phonon entropy change in the martensitic transformation is  $\Delta S_{\text{vib}}^{\gamma \rightarrow \alpha} = -\Delta S_{\text{vib}}^{\alpha \rightarrow \gamma} = -0.12 k_{\text{B}} \text{ atom}^{-1}$ . This value is rather smaller than expected for martensitic transformations (Bogdanoff and Fultz [166]), and this is seen to result from the low energy and presumably large amplitude Ni modes in the martensite. Samples of austenitic  $\gamma$  phase were cooled to induce the martensite transformation, and measurements of phase fraction and phonon DOS were acquired at low temperature and again at room temperature. At any intermediate state of trans-

formation, the phonon DOS for the two-phase sample is the phase-fraction average of the martensite and austenite DOS. There was no observable effect on the DOS from elastic forces at the martensite-austenite interface, for example. The phonon DOS softening of the martensite between 80 K and 300 K is about 1%, consistent with the classical expansion of the lattice against the bulk modulus. From our differential scanning calorimetry measurements, the total entropy changes in the  $\gamma \rightarrow \alpha$  and  $\alpha \rightarrow \gamma$  transformations are, respectively,  $\Delta S_{\text{tot}}^{\gamma \rightarrow \alpha} = -0.15 \pm 0.01 k_{\text{B}} \text{ atom}^{-1}$  and  $\Delta S_{\text{tot}}^{\alpha \rightarrow \gamma} = 0.32 \pm 0.03 k_{\text{B}} \text{ atom}^{-1}$ , in good agreement with previously reported values. Using previous magnetization measurements, we established a magnetic entropy contribution in the  $\alpha \rightarrow \gamma$  transformation of  $\Delta S_{\text{mag}}^{\alpha \rightarrow \gamma} = 0.25 k_{\text{B}} \text{ atom}^{-1}$ , which brings our calorimetry and neutron scattering results in good agreement. This magnetic contribution to the entropy of the  $\alpha \rightarrow \gamma$  transformation is twice as large as the phonon contribution. We performed an analysis of the coherent inelastic scattering  $S_{\text{coh}}(Q, E)$ , based on a Born–von Kármán model for FCC  $\text{Fe}_{71}\text{Ni}_{29}$ . Our calculation of the coherent inelastic scattering function was in very good agreement with the experimental time-of-flight measurement, which validates the interatomic force-constants determined by Hallman and Brockhouse [156] using a triple-axis spectrometer.

## Chapter 8

### Conclusions

#### 8.1 Summary

The experimental investigations conducted in this thesis reemphasize the importance of phonon entropy in binary alloy thermodynamics. In particular, it was shown that a few percent of impurities can have an entropic effect opposite to that expected solely on the basis of configurational degrees of freedom. General considerations as well as more detailed computations in the framework of density functional theory showed that changes in the electronic structure associated with the introduction of impurities play a critical role for the lattice dynamics. Simple considerations of electronegativity and charge transfer may help in predicting general trends for the vibrational entropy of dilute alloys, much in the fashion of the Hume-Rothery rules for alloy formation. Such trends are invaluable to the rationalization of vibrational entropy contributions in binary alloys.

The temperature-dependencies of phonons in pure and alloyed BCC vanadium were investigated with inelastic neutron scattering and calorimetry. It was observed that impurities also affect greatly the vibrational properties of vanadium at elevated temperatures. In particular, the anomalous intrinsic stiffening of the phonons in the pure metal is suppressed by the introduction of late transition metal solutes. This effect was related to known trends in BCC transition metals and electronic structure features, such as the electronic topological transition occurring between V and Cr. The effects of phonon-phonon and electron-phonon couplings on the entropy and heat capacity were estimated. A definite answer as to the origin of the anomalous temperature behavior in pure V has yet to be given, but our as-

assessments show that it could be accessible to careful calorimetric measurements.

The change in phonon entropy and magnetic entropy across a martensitic phase-transition was investigated, through inelastic neutron scattering and calorimetry measurements. The complementarity of the two techniques allowed us to isolate each of the entropy contributions in both the direct and reverse transformations. A significant magnetic entropy contribution to the reverse transformation was deduced, in agreement with previous magnetization measurements. This result emphasizes the need to consider all the microscopic degrees of freedom in accounting for the entropy differences between solid phases.

## 8.2 Future Work

The correlation that was exhibited between charge transfer and vibrational entropy of alloying in the case of V-based solutions prompts further investigations of entropy of alloying in semi-dilute alloys with a few percent of impurities. Effects of impurities on the phonons in the FCC late transition metals are of particular interest. Complementary studies in other BCC metals, such as Nb or Mo would also help to further establish, or invalidate, the uncovered trend. Our charge transfer investigations have established a relationship of the form

$$\Delta S_{\text{vib}} = -c\eta \Delta\chi, \quad (8.1)$$

with  $c$  the solute concentration,  $\Delta\chi$  the difference in electronegativity between solute and host species, and  $\eta$  a constant. Critical evaluation of this relation in other hosts would be very interesting. If this simple linear relationship holds, further examination of the constant  $\eta$  should be performed. Is it universal? How can it be interpreted?

Experimental measurements probing the local structure around the solutes in the case of vanadium would be useful to complement the first-principles simulations presented here. Extended x-ray absorption fine structure, for example, could provide information on the local relaxation and charge state of the solutes and their nearest neighbors.

First-principles calculations of the phonons in dilute vanadium alloys are desirable, in order to make more explicit the relationship between the charge distribution and the changes in the force-constants, and explore their consequence on the lattice dynamics. Alternative

approaches using effective potentials taking into account the salient points of the physics may be an efficient way forward. In particular, such treatments might be helpful to investigate high-temperature phonon thermodynamics.

The simultaneous consideration of high-temperature inelastic neutron scattering experiments, accurate high-temperature measurements of thermophysical properties, and first-principles electronic structure calculations could potentially answer very interesting questions about the high-temperature thermodynamics of transition metals. What is really the nature of anharmonicity? How do phonon-phonon and electron-phonon interactions affect the free energy?

The analysis of inelastic neutron scattering experiments using time-of-flight spectrometers should be developed beyond the practices available today. In particular, the coherent inelastic scattering signal may be informative. The coherent inelastic scattering channel carries useful information about the phonon dispersions, which should be retrieved to obtain a more detailed picture of the lattice dynamics. Such an analysis will require properly designed software for the direct simulation of the measured scattering intensity, and could be interfaced to fitting routines in order to refine lattice-dynamics models.

## Appendix A

### The Electron-Phonon Interaction

This appendix presents a brief introduction to the electron-phonon interaction. The first section introduces the operators that couple the motion of the nuclei to the electronic wave functions, while the second section presents the results of the treatment of these operators as perturbations. For extensive treatments of the subject, the reader is referred to [25, 53].

#### A.1 Coupling Operators

We start from the general hamiltonian for the crystal (Eqs. 2.1, 2.2):

$$\hat{H} = \hat{T}_e + \hat{V}_{e-e} + \hat{T}_n + \hat{V}_{n-n} + \hat{V}_{e-n} , \quad (\text{A.1})$$

where the different terms are defined as in Eq. 2.2. We use a simplified notation for the coordinates of the nuclei and electrons:

$$\begin{aligned} \mathbf{R} &= \{\mathbf{R}_1, \dots, \mathbf{R}_p\} \\ \mathbf{r} &= \{\mathbf{r}_1, \dots, \mathbf{r}_N\} , \end{aligned} \quad (\text{A.2})$$

with  $N = Zp$  and  $Z$  the atomic number of the nuclei (we assume a Bravais crystal for simplicity).

For a given nuclear configuration,  $\mathbf{R}$ , one can in principle determine the many-body

wave function  $\psi_{\mathbf{k}}(\mathbf{r}, \mathbf{R})$ , such that:

$$\hat{H}_e \psi_{\mathbf{k}}(\mathbf{r}, \mathbf{R}) = E_{\mathbf{k}}(\mathbf{R}) \psi_{\mathbf{k}}(\mathbf{r}, \mathbf{R}), \quad (\text{A.3})$$

where  $\hat{H}_e$  is the electronic hamiltonian defined in Eq. 2.4. Since the eigenstates  $\psi_{\mathbf{k}}(\mathbf{r}, \mathbf{R})$  can be determined for any  $\mathbf{R}$ , and form a complete orthonormal state, we can expand the eigenstates of  $\hat{H}$  on this basis:

$$\begin{aligned} \hat{H}\Phi(\mathbf{r}, \mathbf{R}) &= E\Phi(\mathbf{r}, \mathbf{R}) \\ \Phi(\mathbf{r}, \mathbf{R}) &= \sum_{\mathbf{k}} \chi_{\mathbf{k}}(\mathbf{R}) \psi_{\mathbf{k}}(\mathbf{r}, \mathbf{R}). \end{aligned} \quad (\text{A.4})$$

The Shrödinger equation for the nuclei and electron can be re-written:

$$\begin{aligned} \hat{H}\Phi - E\Phi &= 0 \\ &= \hat{H}_e\Phi + [\hat{T}_n + \hat{V}_{n-n}]\Phi - E\Phi \\ &= \sum_{\mathbf{k}} (E_{\mathbf{k}}(\mathbf{R}) - E) \chi_{\mathbf{k}}(\mathbf{R}) \psi_{\mathbf{k}}(\mathbf{r}, \mathbf{R}) \\ &\quad + \sum_{\mathbf{k}} (\hat{T}_n + \hat{V}_{n-n}) \chi_{\mathbf{k}}(\mathbf{R}) \psi_{\mathbf{k}}(\mathbf{r}, \mathbf{R}). \end{aligned} \quad (\text{A.5})$$

Taking the inner product with respect to electronic degrees of freedom in state  $\mathbf{k}'$  (left multiplying by  $\psi_{\mathbf{k}'}(\mathbf{r}, \mathbf{R})$  and integrating over  $\mathbf{r}$ ), we obtain:

$$(E_{\mathbf{k}'}(\mathbf{R}) - E + \hat{V}_{n-n}) \chi_{\mathbf{k}'}(\mathbf{R}) + \sum_{\mathbf{k}} \langle \psi_{\mathbf{k}'}(\mathbf{r}, \mathbf{R}) | \hat{T}_n | \psi_{\mathbf{k}}(\mathbf{r}, \mathbf{R}) \rangle_{\mathbf{r}} \chi_{\mathbf{k}}(\mathbf{R}) = 0. \quad (\text{A.6})$$

Using the definition  $\hat{T}_n = -\sum_I \frac{\hbar^2}{2M} \nabla_{\mathbf{R}_I}^2$ , we can expand the terms in the sum over  $\mathbf{k}$ :

$$\begin{aligned} \langle \psi_{\mathbf{k}'}(\mathbf{r}, \mathbf{R}) | \hat{T}_n | \psi_{\mathbf{k}}(\mathbf{r}, \mathbf{R}) \rangle_{\mathbf{r}} \chi_{\mathbf{k}}(\mathbf{R}) &= -\frac{\hbar^2}{2M} \sum_I \left\{ \langle \psi_{\mathbf{k}'}(\mathbf{r}, \mathbf{R}) | \nabla_{\mathbf{R}_I}^2 \psi_{\mathbf{k}}(\mathbf{r}, \mathbf{R}) \rangle_{\mathbf{r}} \chi_{\mathbf{k}}(\mathbf{R}) \right. \\ &\quad + 2 \langle \psi_{\mathbf{k}'}(\mathbf{r}, \mathbf{R}) | \nabla_{\mathbf{R}_I} \psi_{\mathbf{k}}(\mathbf{r}, \mathbf{R}) \rangle_{\mathbf{r}} \cdot \nabla_{\mathbf{R}_I} \chi_{\mathbf{k}}(\mathbf{R}) \\ &\quad \left. + \langle \psi_{\mathbf{k}'}(\mathbf{r}, \mathbf{R}) | \psi_{\mathbf{k}}(\mathbf{r}, \mathbf{R}) \rangle_{\mathbf{r}} \nabla_{\mathbf{R}_I}^2 \chi_{\mathbf{k}}(\mathbf{R}) \right\}. \end{aligned} \quad (\text{A.7})$$

Since

$$\langle \psi_{\mathbf{k}'}(\mathbf{r}, \mathbf{R}) | \psi_{\mathbf{k}}(\mathbf{r}, \mathbf{R}) \rangle_{\mathbf{r}} = \delta_{\mathbf{k}, \mathbf{k}'} \quad (\text{A.8})$$

for any  $\mathbf{R}$ , we obtain:

$$(E_{\mathbf{k}'}(\mathbf{R}) - E + \hat{V}_{\mathbf{n}-\mathbf{n}} + \hat{T}_{\mathbf{n}}) \chi_{\mathbf{k}'}(\mathbf{R}) + \sum_{\mathbf{k}} (\hat{A}_{\mathbf{k}'\mathbf{k}} + \hat{B}_{\mathbf{k}'\mathbf{k}}) \chi_{\mathbf{k}}(\mathbf{R}) = 0, \quad (\text{A.9})$$

with

$$\begin{aligned} \hat{A}_{\mathbf{k}'\mathbf{k}} &= -\frac{\hbar^2}{M} \sum_I \langle \psi_{\mathbf{k}'}(\mathbf{r}, \mathbf{R}) | \nabla_{\mathbf{R}_I} \psi_{\mathbf{k}}(\mathbf{r}, \mathbf{R}) \rangle_{\mathbf{r}} \cdot \nabla_{\mathbf{R}_I} \\ \hat{B}_{\mathbf{k}'\mathbf{k}} &= -\frac{\hbar^2}{2M} \sum_I \langle \psi_{\mathbf{k}'}(\mathbf{r}, \mathbf{R}) | \nabla_{\mathbf{R}_I}^2 \psi_{\mathbf{k}}(\mathbf{r}, \mathbf{R}) \rangle_{\mathbf{r}}, \end{aligned} \quad (\text{A.10})$$

which are operators coupling the electronic and nuclear degrees of freedom. The Born-Oppenheimer approximation is then equivalent to neglecting the off-diagonal terms  $\hat{A}_{\mathbf{k}'\mathbf{k}}$  and  $\hat{B}_{\mathbf{k}'\mathbf{k}}$ , which results in the eigenvalue problem:

$$(E_{\mathbf{k}'}(\mathbf{R}) - E + \hat{V}_{\mathbf{n}-\mathbf{n}} + \hat{T}_{\mathbf{n}}) \chi_{\mathbf{k}'}(\mathbf{R}) = 0 \quad (\text{A.11})$$

for the nuclear wave functions  $\chi_{\mathbf{k}'}(\mathbf{R})$ . This constitutes an effective Schrödinger equation for the phonons. The electron-phonon interaction occurs through the action of  $\hat{T}_{\mathbf{n}}$  on  $\psi_{\mathbf{k}}(\mathbf{r}, \mathbf{R})$ . In the adiabatic approximation, the movements of the nuclei are sufficiently slow that there is no coupling between  $\psi_{\mathbf{k}}(\mathbf{r}, \mathbf{R})$  and  $\chi_{\mathbf{k}'}(\mathbf{R})$ , so  $\psi_{\mathbf{k}}(\mathbf{r}, \mathbf{R}) \chi_{\mathbf{k}}(\mathbf{R})$  is an eigenstate of  $\hat{H}$ .

## A.2 Perturbative Treatment

### A.2.1 Matrix Elements

First, it is convenient to adopt the notation:

$$\psi_{\mathbf{k}}(\mathbf{r}, \mathbf{R}) \chi_{k,s}(\mathbf{R}) \equiv |k, s\rangle, \quad (\text{A.12})$$

where  $k$  denotes the electronic state and  $s$  the phonon state. With this notation, the uncoupled hamiltonian reads:

$$\hat{H}_{\text{ad}} = \sum_{k,s} \langle k, s | \hat{H} | k, s \rangle | k, s \rangle \langle k, s | , \quad (\text{A.13})$$

and it is diagonal. On the other hand, in the general case:

$$\hat{H} = \sum_{k,k'} \sum_{s,s'} \langle k, s | \hat{H} | k', s' \rangle | k, s \rangle \langle k', s' | . \quad (\text{A.14})$$

One needs to calculate the terms  $\langle k, s | \hat{H} | k', s' \rangle = \langle \psi_k \chi_{k,s} | \hat{H} | \psi_{k'} \chi_{k',s'} \rangle$ . Let  $\hat{C}_{kk'} = \hat{A}_{kk'} + \hat{B}_{kk'}$ . The matrix element we want to calculate is related to  $\hat{C}_{kk'}$  through:

$$\langle \psi_k | \hat{H} | \psi_{k'} \chi_{k',s'} \rangle = \hat{C}_{kk'} \chi_{k',s'} , \quad (\text{A.15})$$

so

$$\langle k, s | \hat{H} | k', s' \rangle = \langle \chi_{k,s} | \hat{C}_{kk'} | \chi_{k',s'} \rangle . \quad (\text{A.16})$$

The evaluation of the matrix elements of  $\hat{C}_{kk'}$  requires to calculate the gradients of the electronic wave functions with respect to nuclear displacements. A small nuclear displacement gives a small change in the external potential for the electrons,  $\delta V$ , and in first-order perturbation theory

$$|\psi_k\rangle = |\psi_k^0\rangle + \sum_{k' \neq k} \frac{\langle \psi_{k'}^0 | \delta V | \psi_k^0 \rangle}{E_k^0 - E_{k'}^0} |\psi_{k'}^0\rangle , \quad (\text{A.17})$$

where we used a zero symbolic superscript to denote the quantities for the unperturbed case. The change in external potential we are considering can be written in the form:

$$\delta V = \sum_I \mathbf{W}_I^0 \cdot \mathbf{u}_I , \quad (\text{A.18})$$

in first order in  $\mathbf{u}_I = \mathbf{R}_I - \mathbf{R}_I^0$ , the displacement of nucleus  $I$ , and  $\mathbf{W}_I^0$  the gradient of the electron-ion potential with respect to the coordinate of nucleus  $I$ , around the equilibrium

position:

$$\mathbf{W}_I^0 = \nabla_{\mathbf{R}_I} \hat{V}_{e-n} | \mathbf{R}_I^0 \rangle . \quad (\text{A.19})$$

Inserting (A.19) into (A.17) yields:

$$|\psi_k\rangle = |\psi_k^0\rangle + \sum_I \sum_{k' \neq k} |\psi_{k'}^0\rangle \frac{\langle \psi_{k'}^0 | \mathbf{W}_I^0 | \psi_k^0 \rangle}{E_k^0 - E_{k'}^0} \cdot \mathbf{u}_I , \quad (\text{A.20})$$

In first order in  $\mathbf{u}_I$ , the gradient in the electronic wave function is thus:

$$\nabla_{\mathbf{R}_I} |\psi_k\rangle = \sum_{k' \neq k} |\psi_{k'}^0\rangle \frac{\langle \psi_{k'}^0 | \mathbf{W}_I^0 | \psi_k^0 \rangle}{E_k^0 - E_{k'}^0} . \quad (\text{A.21})$$

We obtain the expression for  $\hat{A}_{kk'}$  in first order in  $\mathbf{u}_I$  by substituting the gradient by its expression in Eq. A.10:

$$\begin{aligned} \hat{A}_{kk'} &\simeq -\frac{\hbar^2}{M} \sum_I \sum_{k'' \neq k'} \langle \psi_k^0 | \psi_{k''}^0 \rangle \frac{\langle \psi_{k''}^0 | \mathbf{W}_I^0 | \psi_{k'}^0 \rangle}{E_{k'}^0 - E_{k''}^0} \cdot \nabla_{\mathbf{R}_I} \\ &= -\frac{\hbar^2}{M} \sum_I \frac{\langle \psi_k^0 | \mathbf{W}_I^0 | \psi_{k'}^0 \rangle}{E_{k'}^0 - E_k^0} \cdot \nabla_{\mathbf{R}_I} . \end{aligned} \quad (\text{A.22})$$

On the other hand,  $\hat{B}_{kk'}$  is zero in lowest order in  $\mathbf{u}_I$ , since it involves  $\nabla_{\mathbf{R}_I}^2 |\psi_k\rangle$ . The matrix elements (A.16) for the total hamiltonian are thus:

$$\langle k, s | \hat{H} | k', s' \rangle = -\frac{\hbar^2}{M} \sum_I \frac{\langle \psi_k^0 | \mathbf{W}_I^0 | \psi_{k'}^0 \rangle}{E_{k'}^0 - E_k^0} \cdot \langle \chi_{k,s} | \nabla_{\mathbf{R}_I} | \chi_{k',s'} \rangle . \quad (\text{A.23})$$

This expression is referred to as Bloch's relation. Using the fact that the phonon wave functions satisfy the nuclear Schrödinger equation (A.11), one obtains in first order in displacement:

$$-\frac{\hbar^2}{M} \langle \chi_{k,s} | \nabla_{\mathbf{R}_I} | \chi_{k',s'} \rangle = (E_{ks} - E_{k's'} + E_{k'}^0 - E_k^0) \langle \chi_{k,s} | \mathbf{u}_I | \chi_{k',s'} \rangle , \quad (\text{A.24})$$

and the matrix elements of the total hamiltonian become:

$$\langle k, s | \hat{H} | k', s' \rangle = \left( 1 - \frac{E_{k's'} - E_{ks}}{E_{k'}^0 - E_k^0} \right) \sum_I \frac{\langle \psi_k^0 | \mathbf{W}_I^0 | \psi_{k'}^0 \rangle}{E_{k'}^0 - E_k^0} \cdot \langle \chi_{k,s} | \mathbf{u}_I | \chi_{k',s'} \rangle. \quad (\text{A.25})$$

### A.2.2 Coupling Functions

A simple approximation for the change in external potential  $\delta V$  perceived by the electrons (Eq. A.18) consists in considering that the potential associated with an ion is rigidly displaced with the position of its nucleus. This constitutes the ‘‘rigid-ion approximation’’. In this approximation:

$$\mathbf{W}_I^0 = -\nabla_{\mathbf{r}} V(\mathbf{r} - \mathbf{R}_I^0). \quad (\text{A.26})$$

Using the expression for the displacement operator for the solution  $s = (\mathbf{q}, j)$  of the phonon eigenvalue problem (Eq. 3.10), one can rewrite the matrix element A.25 for the case of phonon absorption as [53]:

$$\langle k, s | \hat{H} | k', s' \rangle = \sum_I \frac{1}{N} g(\mathbf{k}\mathbf{k}'; s) e^{(i\mathbf{k}\cdot\mathbf{R}_I^0)} e^{(i(\mathbf{k}-\mathbf{k}')\cdot\mathbf{R}_I^0)} (n(\mathbf{q}, j))^{1/2}, \quad (\text{A.27})$$

where we introduced the coupling function:

$$g(\mathbf{k}\mathbf{k}'; s) = -\left( \frac{\hbar}{2MN\omega_s} \right)^{1/2} \mathbf{e}(\mathbf{q}, j) \tilde{I}(\mathbf{k}, \mathbf{k}'), \quad (\text{A.28})$$

with  $\mathbf{e}(\mathbf{q}, j)$  the phonon polarization and

$$\tilde{I}(\mathbf{k}, \mathbf{k}') = \langle \psi_{k'}^0 | \nabla_{\mathbf{r}} V(\mathbf{r} - \mathbf{R}_I^0) | \psi_k^0 \rangle. \quad (\text{A.29})$$

Another important quantity is the matrix element  $I(\mathbf{k}, \mathbf{k}')$  and its average over the Fermi surface (see [53]):

$$\begin{aligned} I(\mathbf{k}, \mathbf{k}') &= \langle \psi_{k'}^0 | \mathbf{u}_I \cdot \nabla_{\mathbf{r}} V(\mathbf{r} - \mathbf{R}_I^0) | \psi_k^0 \rangle \\ \langle I(\mathbf{k}, \mathbf{k}') \rangle &= \sum_{\mathbf{k}, \mathbf{k}' \in S_F} I(\mathbf{k}, \mathbf{k}') / \sum_{\mathbf{k}, \mathbf{k}' \in S_F}, \end{aligned} \quad (\text{A.30})$$

which enters the expression for  $\lambda$  in McMillan's theory (Eq. 5.5). Also, the direction-averaged Eliashberg coupling function  $\alpha^2 F(\omega)$  is defined as (see [53]):

$$\alpha^2 F(\omega) = N(E_F) \sum_s \int \frac{d\Omega_k}{4\pi} \int \frac{d\Omega'_k}{4\pi} |g(\mathbf{k}\mathbf{k}'; s)|^2 \delta(\hbar\omega - \hbar\omega_s), \quad (\text{A.31})$$

which gives access to the electron-phonon interaction strength through:

$$\lambda = 2 \int_0^{\omega_{\max}} \frac{\alpha^2 F(\omega)}{\omega} d\omega. \quad (\text{A.32})$$

## Appendix B

### Implementations of DFT

#### B.1 Approximations for Exchange and Correlation

As discussed in chapter 2, the strength of the Hohenberg-Kohn-Sham approach lies both in the effective independent-particle formulation, and the separation of long-ranged and well-known terms from the more difficult exchange-correlation terms in the hamiltonian. In this approach, one seeks to numerically solve the Kohn-Sham hamiltonian:

$$\hat{H}_{\text{KS}} = \hat{T}_{\text{ni}} + \hat{V}_{\text{H}} + \hat{V}_{\text{xc}} + \hat{V}_{\text{ext}} , \quad (\text{B.1})$$

where an expression for the exchange-correlation potential  $\hat{V}_{\text{xc}}$  has to be specified. Since an actual expression for  $\hat{V}_{\text{xc}}$  (or a way to compute it exactly) is not yet known, approximations are necessary.

One of the first approximations devised for this purpose is the local density approximation (LDA), which is still widely being used. The LDA builds upon our knowledge of the exchange energy and correlation energy for the homogeneous electron gas. Namely, the expression for the exchange energy  $E_{\text{x}}(\rho)$ , as function of the homogeneous electron density  $\rho(\mathbf{r}) = \rho$ , is known in that case, and the correlation energy  $E_{\text{c}}(\rho)$  for the homogeneous electron gas has been calculated and tabulated, so it is also known [15]. The LDA provides a simple extension to the case of a non-uniform electronic density, as encountered in a solid, by considering that the exchange-correlation energy for this more complex density is the

sum over small volumes in which the electronic density is approximately constant, so that:

$$E_{\text{xc}}(\rho) = \int \rho(\mathbf{r}) \epsilon_{\text{xc}}(\rho(\mathbf{r})) d^3r, \quad (\text{B.2})$$

where  $\epsilon_{\text{xc}}(\rho(\mathbf{r}))$  is the exchange-correlation energy for the homogeneous gas of density  $\rho(\mathbf{r})$  in the small volume  $d^3r$  around  $\mathbf{r}$ . It can be perceived that this approximation should work well in principle for systems in which the electronic density varies little over distances corresponding to the range of the exchange and interaction energies. If, on the other hand, the density varies significantly over this range, then we cannot divide the system into small volumes of constant density and still capture the exchange and correlation terms by using the homogeneous electron gas model. In the latter case, one has to consider the gradients in the electronic density and their effects on exchange and correlation. Numerous so-called generalized gradient approximations (GGA) have been devised to incorporate the effects of non-homogeneous electron densities [15]. In practice, the LDA works well for systems with slowly varying densities, such as nearly free electron metals, but the GGAs tend to perform better for systems with stronger gradients. One of the successes of GGA methods over the more primitive LDA is to better predict the cohesive energy of solids, in general.

## B.2 Solving the Kohn-Sham Equations

Once a functional is provided for the exchange-correlation term, the effective hamiltonian is defined, leading to the Kohn-Sham equations:

$$\hat{H}_{\text{KS}}\phi_i = \epsilon_i\phi_i. \quad (\text{B.3})$$

We seek to determine the Kohn-Sham wave functions  $\phi_i$  and their associated energies  $\epsilon_i$ , keeping in mind that the hamiltonian depends on the wave functions through the total density. We can decompose the wave functions in a basis of our choice, which we denote  $\{\varphi_r\}$ :

$$\phi_i = \sum_r c_r^i \varphi_r, \quad (\text{B.4})$$

where in practice the sum is truncated (finite basis set). The hamiltonian operator can be expressed in this basis set as well and we are left with a matrix diagonalization problem. The actual implementation requires to pick a basis set that makes this problem as easy to solve as possible. That is, we want to be able to calculate the terms efficiently and use as few basis vectors as possible to reduce the size of the hamiltonian matrix. The trade-off is that the basis set should be general enough that any system will be accurately and efficiently treated.

### B.2.1 Pseudopotentials and Plane Waves

One popular approach, as implemented in the computer package VASP [33, 100], is to use a plane wave basis set. In the case of a crystalline material, this approach can be motivated by considering Bloch's theorem [49]. Bloch's theorem tells us that, for a hamiltonian with periodic translation symmetry, the eigenstates correspond to wave functions satisfying:

$$\begin{aligned}\phi_i(\mathbf{r}) &= \psi_{n,\mathbf{k}}(\mathbf{r}) \\ &= \exp(i\mathbf{k} \cdot \mathbf{r})u_{n,\mathbf{k}}(\mathbf{r}),\end{aligned}\tag{B.5}$$

with a  $u_{n,\mathbf{k}}(\mathbf{r})$  a function having the periodicity of the lattice. Since  $u_{n,\mathbf{k}}(\mathbf{r})$  is periodic, it can be written as a Fourier series:

$$u_{n,\mathbf{k}}(\mathbf{r}) = \sum_{\mathbf{G}} c_{\mathbf{G}}^{n,\mathbf{k}} \exp(i\mathbf{G} \cdot \mathbf{r}),\tag{B.6}$$

where the vectors  $\{\mathbf{G}\}$  are the reciprocal lattice vectors. So the wave functions we seek are written as

$$\psi_{n,\mathbf{k}}(\mathbf{r}) = \sum_{\mathbf{G}} c_{\mathbf{G}}^{n,\mathbf{k}} \exp(i(\mathbf{G} + \mathbf{k}) \cdot \mathbf{r}).\tag{B.7}$$

The basis set is then  $\{\exp(i(\mathbf{G} + \mathbf{k}) \cdot \mathbf{r})\} = \{|\mathbf{G} + \mathbf{k}\rangle\}$ , and it depends on the wavevector  $\mathbf{k}$ . This means that the problem must be solved at a series of  $\mathbf{k}$ -points independently, for example on a grid in the irreducible portion of the Brillouin zone.

The number of plane waves (or reciprocal lattice vectors  $\mathbf{G}$ ) that are included has to

be kept finite, and it is customary to include the  $\mathbf{G}$ -vectors inside a sphere of radius  $\mathbf{G}_{\max}$ , corresponding to a cutoff energy  $E_{\text{cut}} = \hbar^2 \mathbf{G}_{\max}^2 / 2m_e$ . In practice, the number of plane waves that have to be included to faithfully represent the wave functions can be quite large. Wave functions tend to oscillate rapidly around the nuclei and their complexity in the core region greatly increases the number of plane waves required to describe them. A way around this difficulty consists in discarding the part of the wave functions close to the atomic nuclei, since it is not involved in the bonding properties, and it will be very similar to that in a free atom. One way to achieve this is to modify the atomic potential  $V_{\text{ext}}$  so that the wave functions do not oscillate and vary smoothly inside some core radius. Such a modified potential is called a pseudopotential. This pseudopotential and plane waves approach has been quite successful, and it is implemented in numerous DFT computer programs, such as VASP, and Abinit [33, 100, 43]. Nowadays, it is superseded by the so-called projector-augmented wave method (PAW), which keeps the core part of the wave functions as a frozen atomic configuration, but still treats the more distant part with plane waves [101, 102].

### B.2.2 Augmented Plane Waves

Recognizing that plane waves are well-suited to describe the electronic wave functions in a periodic solid, but that the wave functions are very atomic-like close to the nucleus, a hybrid description can be conceived. Close to the nucleus, the wave functions can be decomposed on a basis of atomic orbitals, and in between nuclei, they can be expanded onto plane waves. This “best of both worlds” approach leads to the following basis functions

$$\begin{aligned} \varphi_{\mathbf{G}}^{\mathbf{k}}(\mathbf{r}, E) &= \Delta_I(\mathbf{r}) \frac{1}{\sqrt{V}} \exp(i(\mathbf{G} + \mathbf{k}) \cdot \mathbf{r}) \\ &+ \sum_{\alpha} \sum_{l,m} \Delta_{\alpha}(\mathbf{r}) A_{l,m}^{\alpha, \mathbf{G}+\mathbf{k}} u_l^{\alpha}(\mathbf{r} - \mathbf{r}_{\alpha}, E) Y_l^m(\mathbf{r} - \mathbf{r}_{\alpha}), \end{aligned} \quad (\text{B.8})$$

where  $\Delta_I(\mathbf{r})$  is equal to one if  $\mathbf{r}$  lies in the interstitial region and zero otherwise, and  $\Delta_{\alpha}(\mathbf{r})$  is equal to one if  $\mathbf{r}$  is inside a “muffin-tin” sphere of radius  $R_{\alpha}$  around nucleus  $\alpha$ , and zero otherwise. The geometry is illustrated in figure B.1. In Eq. B.8, the  $Y_l^m$  are the spherical harmonics, and  $u_l^{\alpha}(\mathbf{r} - \mathbf{r}_{\alpha}, E)$  is the radial part of the solution to the Schrödinger equation for a coulombic potential centered at  $\mathbf{r}_{\alpha}$ , corresponding to orbital angular momentum  $l$  and

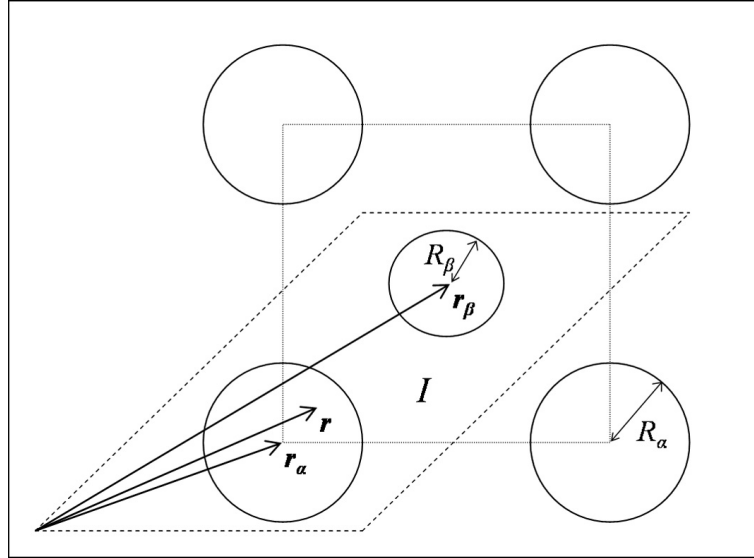


Figure B.1: Spatial decomposition in APW approach.

energy  $E$ . The solutions to the coulombic potential are subjected to boundary conditions on the muffin-tin sphere, which leads to solutions at any energy  $E$ , besides the discrete energy levels of a free atom. The requirement that the basis wave function be continuous on the surface of the muffin-tin sphere  $\alpha$  fixes the coefficients  $A_{l,m}^{\alpha, \mathbf{G}+\mathbf{k}}$  for that nucleus, once the energy  $E$  is set.

Although the APW basis set and its derivatives (LAPW, APW+lo, etc) is more complicated than the plane wave basis set discussed above, its advantage is that it describes the wave functions in the core region as well as in the interstitial volume. This allows one to compute the hyperfine magnetic field at the nucleus, for instance. Such an implementation of DFT is found in the computer software Wien2k [16, 98, 99].

## Appendix C

### VASP and Wien2k Input Files

#### C.1 VASP files

This section presents typical VASP input files for computations on the  $2 \times 2 \times 2$  V-Ti supercell.

##### C.1.1 INCAR file

general:

```
SYSTEM = V15Ti - rlx
# to start from scratch:
# ISTART = 0 ; ICHARG=2
# To use wavecar and chgcar files:
  ISTART = 1 ; ICHARG = 1
  ENCUT = 275
# To take care of Pulay stress:
# ENCUT = 360
  ISMEAR = 1 ; SIGMA = 0.2
  LORBIT=11
# Relax only ion positions:
# IBRION = 2 ; ISIF = 1 ; NSW = 15
# Relax all:
# IBRION = 2 ; ISIF = 3 ; NSW = 15
```

```
EDIFF = 1e-5 # or smaller
# EDIFFG = -0.001
# use real space projection operators for large cells:
LREAL = .FALSE.
PREC = Accurate
ALGO = Normal
#parallelization options
LPLANE = .TRUE. # recommended for Linux clusters
NPAR = 10 # number of nodes
LSCALU = .FALSE.
NSIM = 4
# Wigner-Seitz radii (to compute integrated atomic charge, moment)
# RWIGS = 1.4843 1.4843
```

### C.1.2 POSCAR file

V15Ti - relaxed

```
6.029260
1.0 0.0 0.0
0.0 1.0 0.0
0.0 0.0 1.0
```

1 15

Direct

```
0.500000 0.500000 0.500000
0.245909 0.245909 0.245900
0.754092 0.754092 0.754092
0.754092 0.245909 0.245909
0.245909 0.754092 0.754092
0.754092 0.754092 0.245909
0.245909 0.245909 0.754092
0.245909 0.754092 0.245909
```

```

0.754092    0.245909    0.754092
0.500000    0.500000    0.000000
0.000000    0.500000    0.500000
0.500000    0.000000    0.500000
0.500000    0.000000    0.000000
0.000000    0.500000    0.000000
0.000000    0.000000    0.500000
0.000000    0.000000    0.000000

```

### C.1.3 KPOINTS file

K-Points

0

Monkhorst Pack

16 16 16

0 0 0

### C.1.4 POTCAR file

```
>> grep TITEL POTCAR
```

```
TITEL = PAW_GGA Ti_sv 07Sep2000
```

```
TITEL = PAW_GGA V_sv 14Sep2000
```

```
>> grep ENMAX POTCAR
```

```
ENMAX = 274.616; ENMIN = 205.962 eV
```

```
ENMAX = 263.695; ENMIN = 197.772 eV
```

## C.2 Wien2k files

This section presents typical Wien2k input files for computations on the  $2 \times 2 \times 2$  V-Ti supercell.

## C.2.1 case.struct file

V15Ti supercell

```

P                               5221_Pm-3m

      RELA

11.388126 11.388126 11.388126 90.000000 90.000000 90.000000
ATOM  1: X=0.50000000 Y=0.50000000 Z=0.50000000
      MULT= 1          ISPLIT= 2
Ti      NPT= 781  R0=.000100000 RMT=  2.20000  Z: 22.00000
LOCAL ROT MATRIX:  1.0000000 0.0000000 0.0000000
                   0.0000000 1.0000000 0.0000000
                   0.0000000 0.0000000 1.0000000
ATOM  -2: X=0.24579932 Y=0.24579932 Z=0.24579932
      MULT= 8          ISPLIT= 4
      -2: X=0.75420068 Y=0.75420068 Z=0.75420068
      -2: X=0.75420068 Y=0.24579932 Z=0.24579932
      -2: X=0.24579932 Y=0.75420068 Z=0.75420068
      -2: X=0.75420068 Y=0.75420068 Z=0.24579932
      -2: X=0.24579932 Y=0.24579932 Z=0.75420068
      -2: X=0.24579932 Y=0.75420068 Z=0.24579932
      -2: X=0.75420068 Y=0.24579932 Z=0.75420068
V 1NN      NPT= 781  R0=.000100000 RMT=  2.20000  Z: 23.00000
LOCAL ROT MATRIX:  0.4082483-0.7071068 0.5773503
                   0.4082483 0.7071068 0.5773503
                   -0.8164966 0.0000000 0.5773503
ATOM  -3: X=0.50000000 Y=0.50000000 Z=0.00000000
      MULT= 3          ISPLIT=-2
      -3: X=0.00000000 Y=0.50000000 Z=0.50000000
      -3: X=0.50000000 Y=0.00000000 Z=0.50000000
V 2NN      NPT= 781  R0=.000100000 RMT=  2.20000  Z: 23.00000
LOCAL ROT MATRIX:  1.0000000 0.0000000 0.0000000

```

```

0.0000000 1.0000000 0.0000000
0.0000000 0.0000000 1.0000000
ATOM -4: X=0.50000000 Y=0.00000000 Z=0.00000000
      MULT= 3          ISPLIT=-2
-4: X=0.00000000 Y=0.50000000 Z=0.00000000
-4: X=0.00000000 Y=0.00000000 Z=0.50000000
V 3NN      NPT= 781  RO=.000100000 RMT= 2.20000 Z: 23.00000
LOCAL ROT MATRIX: 0.0000000 0.0000000 1.0000000
                   0.0000000 1.0000000 0.0000000
                   -1.0000000 0.0000000 0.0000000
ATOM 5: X=0.00000000 Y=0.00000000 Z=0.00000000
      MULT= 1          ISPLIT= 2
V 5NN      NPT= 781  RO=.000100000 RMT= 2.20000 Z: 23.00000
LOCAL ROT MATRIX: 1.0000000 0.0000000 0.0000000
                   0.0000000 1.0000000 0.0000000
                   0.0000000 0.0000000 1.0000000

```

### C.2.2 case.inst file

```

Ti
Ar 2 5
3, 2,2.0 P
3, 2,0.0 P
4,-1,1.0 P
4,-1,1.0 P
V 1NN
Ar 2 5
3, 2,2.0 P
3, 2,1.0 P
4,-1,1.0 P
4,-1,1.0 P

```

V 2NN

Ar 2 5

3, 2,2.0 P

3, 2,1.0 P

4,-1,1.0 P

4,-1,1.0 P

V 3NN

Ar 2 5

3, 2,2.0 P

3, 2,1.0 P

4,-1,1.0 P

4,-1,1.0 P

V 5NN

Ar 2 5

3, 2,2.0 P

3, 2,1.0 P

4,-1,1.0 P

4,-1,1.0 P

\*\*\*\* End of Input

\*\*\*\* End of Input

### C.2.3 case.in1 file

WFFIL (WFPRI, SUPWF)

7.00 10 4 (R-MT\*K-MAX; MAX L IN WF, V-NMT

0.30 5 0 (GLOBAL E-PARAMETER WITH n OTHER CHOICES, global APW/LAPW)

0 0.30 0.000 CONT 1

0 -4.35 0.005 STOP 1

1 -2.58 0.010 CONT 1

1 0.30 0.000 CONT 1

2 0.30 0.010 CONT 1

```

0.30  5  0      (GLOBAL E-PARAMETER WITH n OTHER CHOICES, global APW/LAPW)
0  0.30      0.000 CONT 1
0  -4.89      0.005 STOP 1
1  0.30      0.000 CONT 1
1  -2.94      0.005 STOP 1
2  0.30      0.010 CONT 1

0.30  5  0      (GLOBAL E-PARAMETER WITH n OTHER CHOICES, global APW/LAPW)
0  0.30      0.000 CONT 1
0  -4.89      0.005 STOP 1
1  0.30      0.000 CONT 1
1  -2.94      0.005 STOP 1
2  0.30      0.010 CONT 1

0.30  5  0      (GLOBAL E-PARAMETER WITH n OTHER CHOICES, global APW/LAPW)
0  0.30      0.000 CONT 1
0  -4.89      0.005 STOP 1
1  0.30      0.000 CONT 1
1  -2.94      0.005 STOP 1
2  0.30      0.010 CONT 1

0.30  5  0      (GLOBAL E-PARAMETER WITH n OTHER CHOICES, global APW/LAPW)
0  0.30      0.000 CONT 1
0  -4.89      0.005 STOP 1
1  0.30      0.000 CONT 1
1  -2.94      0.005 STOP 1
2  0.30      0.010 CONT 1

K-VECTORS FROM UNIT:4  -7.0      1.5      emin/emax window

```

#### C.2.4 case.in2 file

```

FOR          (FOR,FOR,QTL,EFG,FERMI)
-6.0        207.0 0.50 0.05          EMIN, NE, ESEPERMIN, ESEPERO
TETRA      0.000          (GAUSS,ROOT,TEMP,TETRA,ALL      eval)

```

```
0 0 4 0 4 4 6 0 6 4 8 0 8 4 8 8
0 0 1 0 2 0 3 0 3 3 4 0 4 3 5 0 5 3 6 0 6 3 6 6 \\
7 0 7 3 7 6 8 0 8 3 8 6
0 0 2 0 4 0 4 4 6 0 6 4 8 0 8 4 8 8
0 0 2 0 4 0 4 4 6 0 6 4 8 0 8 4 8 8
0 0 4 0 4 4 6 0 6 4 8 0 8 4 8 8
```

14. GMAX

FILE FILE/NOFILE write recprlist

### C.2.5 case.inm file

BROYD 0.0 YES (BROYD/PRATT, extra charge (+1 for additional e), norm)

0.10 FACTOR

## Appendix D

### Calculation of BCC Elastic Moduli from Interatomic Force-Constants

This appendix presents the details of our calculation of the elastic moduli for the BCC lattice from interatomic force-constants, resulting in the relations of Eq. 4.3.

Much of this discussion follows the derivation for a FCC lattice given in Brüesch [23], section 3.2, and our notation is similar to the notation used in this reference.

#### D.1 General Considerations

We consider a crystal, which is subjected to a periodic wave-like deformation of long wavelength. We introduce a continuous displacement field  $\mathbf{u}(\mathbf{x})$  such that:

$$\mathbf{u}(\mathbf{x} = \mathbf{x}(l\kappa)) = \mathbf{u}(l\kappa) . \quad (\text{D.1})$$

In the following, we restrict the discussion to the case of a Bravais crystal, for simplicity. The displacement field is assumed to vary slowly from cell to cell, and it can be expanded in the form [23]:

$$u_\beta(l) = u_\beta(0) + \sum_\gamma \left( \frac{\partial u_\beta}{\partial x_\gamma} \right)_0 r_\gamma(l) + \frac{1}{2} \sum_{\gamma\delta} \left( \frac{\partial^2 u_\beta}{\partial x_\gamma \partial x_\delta} \right)_0 r_\gamma(l)r_\delta(l) + \dots . \quad (\text{D.2})$$

The equation of motion for the atom in the origin unit cell is

$$M\ddot{u}_\alpha(l) = - \sum_{l\beta} \Phi_{\alpha\beta}(0;l)u_\beta(l) , \quad (\text{D.3})$$

and inserting (D.2) in (D.3), one obtains:

$$\rho\ddot{u}_\alpha(l) = \sum_{\beta\gamma\delta} \tilde{C}_{\alpha\beta,\gamma\delta} \left( \frac{\partial^2 u_\beta}{\partial x_\gamma \partial x_\delta} \right)_0 , \quad (\text{D.4})$$

with

$$\tilde{C}_{\alpha\beta,\gamma\delta} = -\frac{1}{2\Omega} \sum_l \Phi_{\alpha\beta}(0;l)x_\gamma(l)x_\delta(l) , \quad (\text{D.5})$$

with  $\Omega$  the unit cell volume. These quantities can be shown to verify the following relations [23]:

$$\tilde{C}_{\alpha\beta,\gamma\delta} = \tilde{C}_{\beta\alpha,\gamma\delta} = \tilde{C}_{\alpha\beta,\delta\gamma} \quad (\text{D.6})$$

$$\tilde{C}_{\alpha\beta,\gamma\delta} = \tilde{C}_{\gamma\delta,\alpha\beta} \quad (\text{D.7})$$

The macroscopic elastic constants  $C_{\alpha\beta,\gamma\delta}$  relate the stress tensor  $\boldsymbol{\sigma}$  to the strain tensor  $\boldsymbol{\epsilon}$

$$\sigma_{\alpha\beta} = \sum_{\gamma\delta} C_{\alpha\beta,\gamma\delta} \epsilon_{\gamma\delta} , \quad (\text{D.8})$$

and can be related to the quantities  $\tilde{C}_{\alpha\beta,\gamma\delta}$  through [23]:

$$C_{\alpha\gamma,\beta\delta} = \tilde{C}_{\alpha\beta,\gamma\delta} + \tilde{C}_{\gamma\beta,\alpha\delta} - \tilde{C}_{\gamma\alpha,\delta\beta} , \quad (\text{D.9})$$

thus providing the connection to the interatomic force-constants.

The Voigt contraction can be introduced to simplify the notation:

$$\begin{aligned} 11 &\rightarrow 1 & 23, 32 &\rightarrow 4 \\ 22 &\rightarrow 2 & 31, 13 &\rightarrow 5 \\ 33 &\rightarrow 3 & 12, 21 &\rightarrow 6 . \end{aligned} \quad (\text{D.10})$$

For a cubic crystal, the following relations limit the number of independent elastic constants:

$$\begin{aligned} c_{11} &= c_{22} = c_{33} \\ c_{44} &= c_{55} = c_{66} \quad , \\ c_{12} &= c_{13} = c_{23} = c_{31} = c_{32} \end{aligned}$$

and similarly

$$\begin{aligned} C_{11,11} &= C_{22,22} = C_{33,33} \\ C_{23,23} &= C_{31,31} = C_{12,12} \quad . \\ C_{11,22} &= C_{11,33} = C_{22,33} = C_{33,11} = C_{33,22} = C_{22,11} \end{aligned}$$

Crystal symmetries constrain the force-constant tensor to verify certain relations, which can be used to minimize the number of independent entries of the tensor. If we consider an operation  $g$  of the symmetry group of the crystal, represented by the matrix  $S$ :

$$\Phi(gl\ g\kappa; gl'\ g\kappa') = S\Phi(l\kappa; l'\kappa')S^T \quad (\text{D.11})$$

For a Bravais crystal, we can use the simplified notation

$$\Phi_{\alpha\beta}(l\kappa; l'\kappa') = \Phi_{\alpha\beta}(\mathbf{L}) \quad , \quad (\text{D.12})$$

with  $\mathbf{L}$  the bond vector, such that  $\mathbf{L} = \mathbf{x}(l'\kappa') - \mathbf{x}(l\kappa)$ . With this notation:

$$\Phi(g\mathbf{L}) = S\Phi(\mathbf{L})S^T \quad . \quad (\text{D.13})$$

## D.2 BCC Lattice

We present here a detailed evaluation of the general equations of the previous section for the case of a BCC lattice. In the case of a BCC lattice, each atom has eight 1NN bonds:

$$\vec{L} \in \{\pm d(1, 1, 1), \pm d(-1, 1, 1), \pm d(1, -1, 1), \pm d(1, 1, -1)\} \quad , \quad (\text{D.14})$$

with  $d = a_0/2$ , where we write  $a_0$  for the lattice constant. The lattice is invariant under a rotation of  $2\pi/3$  along  $[111]$ , which corresponds to the transformation matrix

$$S_{C_3[111]} = \begin{pmatrix} 0 & 0 & 1 \\ 1 & 0 & 0 \\ 0 & 1 & 0 \end{pmatrix}$$

in the  $(\hat{e}_x, \hat{e}_y, \hat{e}_z)$  basis (one can verify that  $S^3 = I$ ). If we write  $\Phi$ , for  $\vec{L} = d(1, 1, 1)$ , as

$$\Phi = \begin{pmatrix} a & b & c \\ d & e & f \\ g & h & k \end{pmatrix},$$

the relation (D.13) then yields

$$\Phi = \begin{pmatrix} a & b & c \\ c & a & b \\ b & c & a \end{pmatrix}.$$

Similarly, the crystal is invariant in a reflection with respect to the plane  $x = y$ ,

$$S_{\sigma_{xy}} = \begin{pmatrix} 0 & 1 & 0 \\ 1 & 0 & 0 \\ 0 & 0 & 1 \end{pmatrix},$$

and the application of (D.13) to  $\Phi$  further constrains the form of the force-constant matrix:

$$\Phi^{(1)} \equiv \Phi(\pm d(1, 1, 1)) = \begin{pmatrix} a & b & b \\ b & a & b \\ b & b & a \end{pmatrix}.$$

Similarly, we would obtain:

$$\begin{aligned}\Phi^{(2)} \equiv \Phi(\pm d(-1, 1, 1)) &= \begin{pmatrix} a & -b & -b \\ -b & a & b \\ -b & b & a \end{pmatrix}, & \Phi^{(3)} \equiv \Phi(\pm d(1, -1, 1)) &= \begin{pmatrix} a & -b & b \\ -b & a & -b \\ b & -b & a \end{pmatrix}, \\ \Phi^{(4)} \equiv \Phi(\pm d(1, 1, -1)) &= \begin{pmatrix} a & b & -b \\ b & a & -b \\ -b & -b & a \end{pmatrix}.\end{aligned}$$

We can already calculate (D.5) up to the 1NN shell:

$$\tilde{C}_{\alpha\beta,\gamma\delta} = -\frac{1}{2\Omega} \left\{ \underbrace{\sum_{l \in 1\text{NN}} \Phi_{\alpha\beta}(0; l) x_\gamma(l) x_\delta(l)}_{\Sigma^{1\text{NN}}} + \underbrace{\sum_{l \in 2\text{NN}} \dots}_{\Sigma^{2\text{NN}}} + \underbrace{\sum_{l \in 3\text{NN}} \dots}_{\Sigma^{3\text{NN}}} \right\}, \quad (\text{D.15})$$

with

$$\Sigma_{\alpha\beta,\gamma\delta}^{1\text{NN}} = \Phi^{(1)}[\gamma\delta + (-\gamma)(-\delta)] + \Phi^{(2)} \dots \quad (\text{D.16})$$

## D.3 Calculation up to 1NN shell

### D.3.1 $c_{11}$ elastic constant

More explicitly, for the  $c_{11}$  elastic constant:

$$c_{11} = C_{11,11} = \tilde{C}_{11,11} + \tilde{C}_{11,11} - \tilde{C}_{11,11} = \tilde{C}_{11,11}, \quad (\text{D.17})$$

so, for the 1NN shell only:

$$c_{11} = \tilde{C}_{11,11} = \frac{-1}{2\Omega} \Sigma_{11,11}^{1\text{NN}}, \quad (\text{D.18})$$

and

$$\begin{aligned}\Sigma_{11,11}^{1\text{NN}} &= \underbrace{\Phi_{11}^{(1)} \times d \times d}_{\vec{L}=d(1,1,1)} + \underbrace{\Phi_{11}^{(1)} \times (-d) \times (-d)}_{\vec{L}=-d(1,1,1)} + 2\Phi_{11}^{(2)} d^2 + 2\Phi_{11}^{(3)} d^2 + 2\Phi_{11}^{(4)} d^2 \\ &= 2d^2(a + a + a + a)\end{aligned}$$

$$= 8ad^2 . \quad (\text{D.19})$$

Thus, we finally obtain

$$c_{11} = -\frac{2}{a_0}a = \frac{2}{a_0}\text{C1XX} , \quad (\text{D.20})$$

where the last equality refers to the notation often encountered in the literature for force-constant tensors.

### D.3.2 $c_{12}$ elastic constant

For the  $c_{12}$  elastic constant, we obtain:

$$c_{12} = 2\tilde{C}_{44} - \tilde{C}_{12} = 2\tilde{C}_{23,23} - \tilde{C}_{11,22} . \quad (\text{D.21})$$

The first term is

$$\tilde{C}_{23,23} = -\frac{1}{2\Omega}\Sigma_{23,23}^{\text{1NN}} . \quad (\text{D.22})$$

where

$$\begin{aligned} \Sigma_{23,23}^{\text{1NN}} &= 2 \underbrace{\Phi_{23}^{(1)}}_{=b} d^2 + 2 \underbrace{\Phi_{23}^{(2)}}_{=b} d^2 + 2 \underbrace{\Phi_{23}^{(3)}}_{=-b} (-d^2) + 2 \underbrace{\Phi_{23}^{(4)}}_{=-b} (-d^2) \\ &= 8bd^2 . \end{aligned} \quad (\text{D.23})$$

For the last term:

$$\begin{aligned} \Sigma_{11,22}^{\text{1NN}} &= 2ad^2 + 2ad^2 + 2ad^2 + 2ad^2 \\ &= 8ad^2 . \end{aligned} \quad (\text{D.24})$$

So the  $c_{12}$  elastic constant, including only 1NN bonds, is given by:

$$c_{12} = -\frac{8d^2}{2\Omega}(2a - b) = -\frac{2}{a_0}(2a - b) = \frac{2}{a_0}(2\text{C1XX} - \text{C1XY}) . \quad (\text{D.25})$$

### D.3.3 $c_{44}$ elastic constant

For the  $c_{44}$  elastic constant, we have:

$$c_{44} = C_{23,23} = \tilde{C}_{23,23} + \tilde{C}_{32,23} - \underbrace{\tilde{C}_{32,32}}_{=\tilde{C}_{32,23}} . \quad (\text{D.26})$$

We can re-use previous calculations, since:

$$c_{44} = \tilde{C}_{23,23} = \tilde{C}_{23} = \tilde{C}_{12} = \tilde{C}_{11,22} , \quad (\text{D.27})$$

so, the result is

$$c_{44} = -\frac{8ad^2}{2\Omega} = \frac{2}{a_0} \text{C1XX} . \quad (\text{D.28})$$

We can evaluate these relations with values of interatomic force-constant tensors reported in the literature, which are typically obtained through a fit to measured phonon dispersions. For example, in the case of vanadium, the value reported by Colella and Bateman [79] are  $\text{C1XX} = 10.9 \text{ N/M}$  and  $\text{C1XY} = 7.24 \text{ N/M}$ , which, using a lattice parameter value of  $a_0 = 3.03 \text{ \AA}$ , yield

$$\begin{aligned} c_{11}^{1\text{NN}} &= c_{44}^{1\text{NN}} = 72 \text{ GPa} \\ c_{12}^{1\text{NN}} &= 96 \text{ GPa} . \end{aligned} \quad (\text{D.29})$$

These results are not in very good agreement with the measured values reported in [167]:

$$\begin{aligned} c_{11} &= 228 \text{ GPa} \\ c_{12} &= 119 \text{ GPa} \\ c_{44} &= 42.6 \text{ GPa} , \end{aligned} \quad (\text{D.30})$$

which indicates that the truncation of interatomic force-constants at the 1NN shell is not a good approximation for V. On the other hand, for Ni with 1NN bonds only, we obtain (the

expressions for the elastic constants in the case of a FCC lattice are given in [23]):

$$\begin{aligned}
c_{11}^{1\text{NN}} &= \frac{4}{a_0} C1\text{XX} = 197 \text{ GPa} \\
c_{12}^{1\text{NN}} &= \frac{2}{a_0} (2C1\text{XY} - C1\text{XX} - C1\text{ZZ}) = 121 \text{ GPa} \\
c_{44}^{1\text{NN}} &= \frac{2}{a_0} (C1\text{XX} + C1\text{ZZ}) = 96 \text{ GPa} ,
\end{aligned} \tag{D.31}$$

where the interatomic force-constants are taken from [82], and we use  $a_0 = 3.42 \text{ \AA}$ . These calculated values are in fair agreement with the measured values reported in the Landolt-Börnstein:

$$\begin{aligned}
c_{11} &= 247 \text{ GPa} \\
c_{12} &= 153 \text{ GPa} \\
c_{44} &= 122 \text{ GPa} ,
\end{aligned} \tag{D.32}$$

## D.4 Calculation up to 2NN shell

For the 2NN shell, the bond vector is given by

$$\vec{L} \in \{\pm a_0(1, 0, 0), \pm a_0(0, 1, 0), \pm a_0(0, 0, 1)\} . \tag{D.33}$$

Using the symmetry operations  $C_{2x}$ ,  $\sigma_{xy}$ ,  $C_{4x}$  and  $I$ , the force-constant matrices can be reduced to

$$\begin{aligned}
\Phi(\pm a_0(1, 0, 0)) &= \begin{pmatrix} a' & 0 & 0 \\ 0 & b' & 0 \\ 0 & 0 & b' \end{pmatrix} , & \Phi(\pm a_0(0, 1, 0)) &= \begin{pmatrix} b' & 0 & 0 \\ 0 & a' & 0 \\ 0 & 0 & b' \end{pmatrix} , \\
\Phi(\pm a_0(0, 0, 1)) &= \begin{pmatrix} b' & 0 & 0 \\ 0 & b' & 0 \\ 0 & 0 & a' \end{pmatrix} ,
\end{aligned}$$

and following the same procedure as in the previous section, we find:

$$c_{11}^{2\text{NN}} = -\frac{2}{a_0}a' = \frac{2}{a_0}C2\text{XX} . \quad (\text{D.34})$$

For  $c_{12}$ , we find:

$$c_{12}^{2\text{NN}} = 2\tilde{C}_{44} - \tilde{C}_{12} = 2\tilde{C}_{23,23} - \tilde{C}_{11,22} = 0 + \frac{2}{a_0}b' = -\frac{2}{a_0}C2\text{YY} , \quad (\text{D.35})$$

and for  $C_{44}$ :

$$c_{44}^{2\text{NN}} = \tilde{C}_{11,22} = -\frac{2}{a_0}b' = \frac{2}{a_0}C2\text{YY} . \quad (\text{D.36})$$

## D.5 Sum up to 3NN shell

For the 3NN shell,

$$\vec{L} \in \{\pm a_0(1, 1, 0), \pm a_0(1, 0, 1), \pm a_0(0, 1, 1), \pm a_0(-1, 1, 0), \pm a_0(-1, 0, 1), \pm a_0(0, -1, 1)\} . \quad (\text{D.37})$$

We have in this case:

$$c_{11}^{3\text{NN}} = \tilde{C}_{11,11} = -\frac{1}{a_0^3}\{2b''a_0^2 + 2b''a_0^2 + 0 + 2b''a_0^2 + 2b''a_0^2 + 0\} , \quad (\text{D.38})$$

$$c_{11}^{3\text{NN}} = -\frac{8}{a_0}b'' = \frac{8}{a_0}C3\text{XX} . \quad (\text{D.39})$$

Following the same calculations as for 1NN and 2NN shells, we obtain:

$$c_{12}^{3\text{NN}} = \frac{4}{a_0}(2C3\text{XY} - C3\text{XX} - C3\text{ZZ}) , \quad (\text{D.40})$$

$$c_{44}^{3\text{NN}} = \frac{4}{a_0}(C3\text{XX} + C3\text{ZZ}) . \quad (\text{D.41})$$

Finally, summing the contributions of shells up to 3NN, we obtain the result of Eq. 4.3:

$$\begin{aligned} c_{11}^{\leq 3\text{NN}} &= \frac{2}{a}(C1\text{XX} + C2\text{XX} + 4C3\text{XX}) \\ c_{12}^{\leq 3\text{NN}} &= \frac{2}{a}(2C1\text{XX} - C1\text{XY} - C2\text{YY} + 2(2C3\text{XY} - C3\text{XX} - C3\text{ZZ})) \end{aligned}$$

$$c_{44}^{\leq 3\text{NN}} = \frac{2}{a}(C1\text{XX} + C2\text{YY} + 2(C3\text{XX} + C3\text{ZZ})) \quad (\text{D.42})$$

The evaluation of these expressions in the case of BCC vanadium, with the interatomic force-constants reported by Colella and Batterman [79], gives:

$$\begin{aligned} c_{11}^{\leq 3\text{NN}} &= 194 \text{ GPa} \\ c_{12}^{\leq 3\text{NN}} &= 150 \text{ GPa} \\ c_{44}^{\leq 3\text{NN}} &= 35 \text{ GPa} , \end{aligned} \quad (\text{D.43})$$

which is in fairly good agreement with (D.30). The agreement should become better if one were to include contributions of more distant shells.

## Appendix E

### Mannheim Impurity Model and Application to V-X Alloys

The lattice-dynamics of crystals with dilute impurities has been investigated by Mannheim using Green's function techniques [168]. The derivation conducted by Mannheim relied on the following approximation: the interatomic force-constants are described by a single longitudinal stiffness, and the introduction of the impurity only perturbs the 1NN bonds around the impurity. Within this model, Mannheim has derived an analytical expression for the impurity partial phonon DOS.

We present in this appendix a Mathematica notebook for calculating the impurity partial DOS, given the DOS of the pure host, the mass ratio of the impurity and host atoms, and the ratio of impurity-host and host-host force-constants. The equations are implemented in the form in which they are presented in the article of Seto *et al.* [169].

We first start by loading the DOS histogram for the pure host:

```
Get["NumericalMath`CauchyPrincipalValue`"]
CauchyPrincipalValue[1/(x + x^2), {x, -1/2, {0}, 1}]
-0.693147
vpure = ReadList["Vdos.dat", Number]
ListPlot[vpure]

vdos = Interpolation[data, InterpolationOrder -> 2]
Plot[vdos[x], {x, 0, 40}]
```

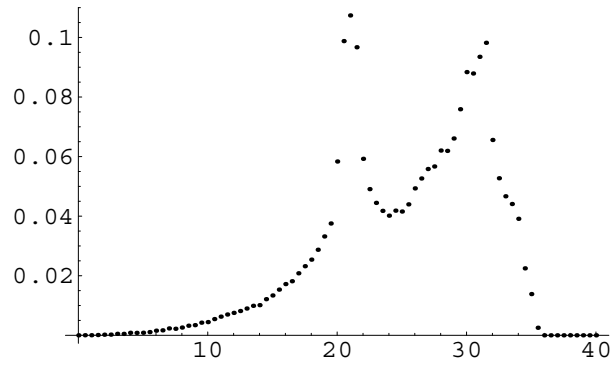


Figure E.1: Pure host phonon DOS histogram in the case of V.

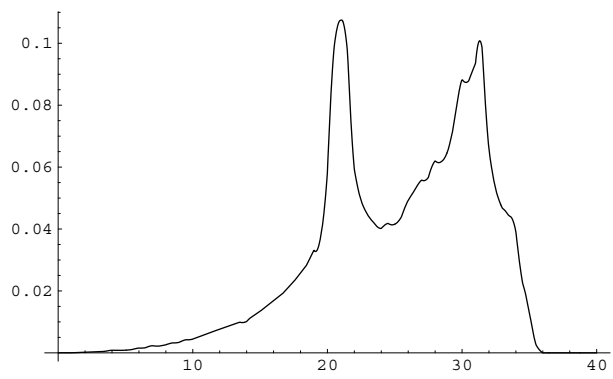


Figure E.2: Interpolated phonon DOS for pure host.

We convert the DOS from meV to angular frequency ( $2\pi \times 10^{12} \text{s}^{-1}$ ):

```
G[w_] := vdos[w/1.5193]/1.5193
Plot[G[w], {w, 0, 60}]

and define the impurity partial DOS  $G'(\omega)$ :

cutoff = 55.0
S[w_] := CauchyPrincipalValue[y^2*((y^2-w^2))^-1]*G[y], {y,0,{w},cutoff},
      MinRecursion -> 7, MaxRecursion -> 20]
mu[n_] := NIntegrate[w^n*G[w], {w,0,cutoff}, MinRecursion -> 7,
      MaxRecursion -> 20]
rho[w_] := Mratio - 1 + w^2 *(1.0 - Kratio)/mu[2]
T[w_] := w^4 * NIntegrate[(y^2 - w^2)^(-2)*G[y], {y,0,cutoff}]
Gp[w_] := Mratio*G[w]/( (1 + rho[w]*S[w])^2 + (N[Pi]/2*w*G[w]*rho[w])^2 )
```

Now, we define the mass and force-constant ratios. Here, we try for a Pt-V force-constant twice as large as the V-V force-constant:

```
Mratio = 50.94 / 195.08
Kratio = 1/2.0
```

and we evaluate the impurity partial DOS at a list of frequencies:

```
freq = Range[55]/1.
values = Table[Evaluate[Gp[w]], {w, 55}]
ListPlot[Transpose[{freq/1.5193, values*1.5193}], PlotRange -> {0, 0.2},
  PlotJoined -> True, PlotStyle -> Hue[.6]]
```

The partial DOS for Pt impurities in V obtained from the Mannheim model using a force-constant ratio of 2.0 is shown in figure E.4. The Mannheim model reproduces the resonance mode behavior that was obtained from our Born–von Kármán lattice-dynamics inversion in chapter 4. The position of the resonance mode around 12 meV and the associated estimate of the 1NN bond stiffening are in good agreement with the strong 1NN stiffening deduced from Born–von Kármán calculations. The shape of the partial phonon DOS, in

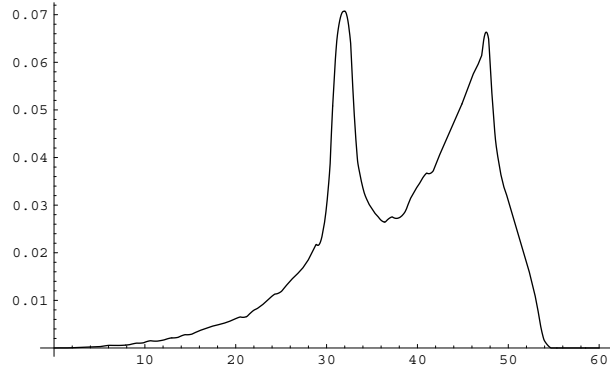


Figure E.3: Interpolated phonon DOS for pure host  $G(\omega)$ , in angular frequency units.

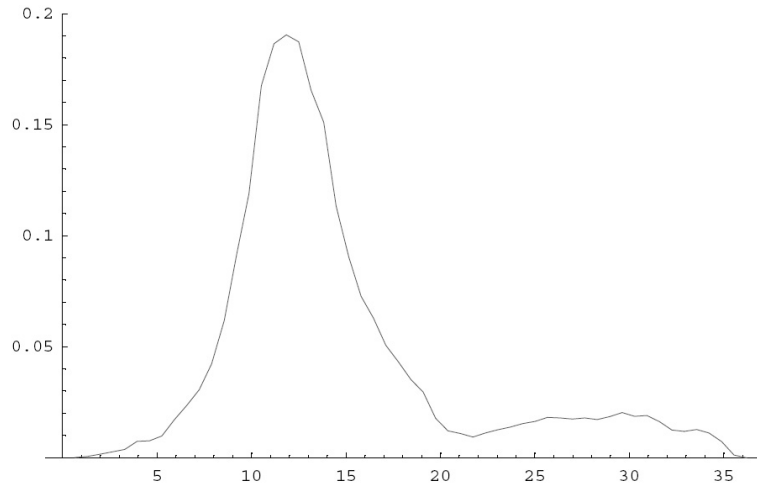


Figure E.4: Impurity partial phonon DOS for Pt in V in Mannheim model, assuming Pt-V force-constant twice as large as V-V force-constant. Energy axis is in meV.

particular, is in surprisingly good agreement with the result from our Born–von Kármán model, considering that the Mannheim model only uses one free parameter. The change in force-constant derived from the Mannheim model, in order to reproduce the Born–von Kármán Pt partial DOS, is smaller than that obtained from the Born–von Kármán inversion procedure itself. However, the approximations used in the Mannheim model are very stringent and in particular the model does not account for the difference in the behavior of the longitudinal and transverse force-constants.

## Bibliography

- [1] Kaufman, L. and Bernstein, H. *Computer calculation of phase diagrams with special reference to refractory metals*. Academic Press, New York, NY, (1970).
- [2] Kikuchi, R. *Phys. Rev.* **81**, 988 (1951).
- [3] Ducastelle, F. *Order and phase stability in alloys*. Elsevier, New York, (1991).
- [4] de Fontaine, D. *Cluster approach to order-disorder transformations in alloys*. Solid State Physics. Academic Press, New York, NY, (1994).
- [5] Anthony, L., Okamoto, J., and Fultz, B. *Phys. Rev. Lett.* **70**, 1128 (1993).
- [6] Fultz, B., Anthony, L., Nagel, L., Nicklow, R., and Spooner, S. *Phys. Rev. B* **52**, 3315 (1995).
- [7] Ozolins, V., Wolverton, C., and Zunger, A. *Phys. Rev. B* **57**, 6427 (1998).
- [8] van de Walle, A. and Ceder, G. *Revs. Mod. Phys.* **74**, 11–45 (2002).
- [9] Delaire, O., Swan-Wood, T., and Fultz, B. *Phys. Rev. Lett.* **93**, 185704 (2004).
- [10] Ozoliņš, V. and Asta, M. *Phys. Rev. Lett.* **86**, 448 (2001).
- [11] Ozoliņš, V., Sadigh, B., and Asta, M. *J. Phys.-Condens. Mat.* **17**, 2197 (2005).
- [12] Placzek, G. and Hove, L. V. *Phys. Rev.* **93**, 1207 (1954).
- [13] Lovesey, S. *Theory of neutron scattering from condensed matter*. Clarendon Press, Oxford, (1984).

- [14] Squires, G. *Introduction to the theory of thermal neutron scattering*. Cambridge Univ. Press, Cambridge, (1978).
- [15] Martins, R. *Electronic structure, basic theory and practical methods*. Cambridge Univ. Press, Cambridge, (2004).
- [16] Cottenier, S. *Density functional theory and the family of (L)APW methods: a step-by-step introduction*. Instituut voor Kern- en Stralingsfysica, K.U. Leuven, Belgium, (2002).
- [17] Hohenberg, P. and Kohn, W. *Phys. Rev. B* **136**, 864 (1964).
- [18] Kohn, W. and Sham, L. J. *Phys. Rev. A* **140**, 1133 (1965).
- [19] Gonze, X. and Vigneron, J.-P. *Phys. Rev. B* **39**, 13120 (1989).
- [20] Born, M. and Huang, K. *Dynamical theory of crystal lattices*. Clarendon Press, Oxford, (1988).
- [21] Maradudin, A., Montroll, E., Weiss, G., and Ipatova, I. *Theory of lattice dynamics in the harmonic approximation*. Academic Press, New York, second edition, (1971).
- [22] Venkataraman, G., Feldkamp, L., and Sahni, V. *Dynamics of perfect crystals*. MIT Press, Cambridge MA, (1975).
- [23] Brüesch, P. *Phonons: theory and experiments. I, Lattice dynamics and models of interatomic forces*. Springer-Verlag, Berlin, (1982).
- [24] Cohen-Tannoudji, C., Diu, B., and Laloë, F. *Quantum Mechanics*. Wiley, New York, (1977).
- [25] J.M. Ziman. *Electrons and phonons*. Oxford Univ. Press, Oxford, (1960).
- [26] Fu, C.-L., Ho, K.-M., Harmon, B., and Liu, S. *Phys. Rev. B* **28**, 2957 (1983).
- [27] Ye, Y.-Y., Chen, Y., Ho, K.-M., Harmon, B., and Lindgård, P.-A. *Phys. Rev. Lett.* **58**, 1769 (1987).
- [28] Ho, K.-M., Fu, C., and Harmon, B. *Phys. Rev. B* **29**, 1575 (1984).

- [29] Feynman, R. *Phys. Rev.* **56**, 340 (1939).
- [30] Parlinski, K. *Phonon Manual, ver. 4.24*. Institute of Nuclear Physics, Cracow, Poland, 2005. <http://wolf.ifj.edu.pl/phonon>.
- [31] Frank, W., Elsässer, C., and Fähnle, M. *Phys. Rev. Lett.* **74**, 1791 (1995).
- [32] Kresse, G., Furthmüller, J., and Hafner, J. *Europhys. Lett.* **32**, 729 (1995).
- [33] G. Kresse and J. Furthmüller. *Comput. Mat. Sci.* **6**, 15–50 (1996).
- [34] Alfé, D. *Phon*, A program to calculate phonons using the small displacement method. University College London, 1998. <http://chianti.geol.ucl.ac.uk/dario/>.
- [35] Cowley, E. *Can. J. Phys.* **52**, 1714 (1974).
- [36] Shaw, W. and Muhlestein, L. *Phys. Rev. B* **4**, 969 (1971).
- [37] Minkiewicz, V., Shirane, G., and Nathans, R. *Phys. Rev.* **162**, 528 (1967).
- [38] Baroni, S., Gianozzi, P., and Testa, A. *Phys. Rev. Lett.* **58**, 1861 (1987).
- [39] Baroni, S., Gianozzi, P., and Testa, A. *Phys. Rev. Lett.* **59**, 2662 (1987).
- [40] Gonze, X., Allan, D., and Teter, M. *Phys. Rev. Lett.* **68**, 3603 (1992).
- [41] Savrasov, S. *Phys. Rev. Lett.* **69**, 2819 (1992).
- [42] de Gironcoli, S. *Phys. Rev. B* **51**, 6773 (1995).
- [43] Gonze, X., Beuken, J.-M., Caracas, R., Detraux, F., Fuchs, M., Rignanese, G.-M., Sindic, L., Verstraete, M., Zerah, G., Jollet, F., Torrent, M., Roy, A., Mikami, M., Ghosez, P., Raty, J.-Y., and Allan, D. *Computational Materials Science* **25**, 478 (2002).
- [44] Baroni, S., Corso, A. D., de Gironcoli, S., Giannozzi, P., Cavazzoni, C., Ballabio, G., Scandolo, S., Chiarotti, G., Focher, P., Pasquarello, A., Laasonen, K., Trave, A., Car, R., Marzari, N., and Kokalj, A. <http://www.pwscf.org/>.
- [45] Willaime, F. and Massobrio, C. *Phys. Rev. Lett.* **63**, 2244 (1989).

- [46] Meyer, R. and Entel, P. *Phys. Rev. B* **57**, 5140 (1998).
- [47] Kirchoff, F., Mehl, M. J., Papanicolaou, N. I., Papaconstantopoulos, D. A., and Kahn, F. S. *Phys. Rev. B* **63**, 195101 (2001).
- [48] Car, R. and Parrinello, M. *Phys. Rev. Lett.* **55**, 2471 (1985).
- [49] Ashcroft, N. and Mermin, N. *Solid State Physics*. Saunders College, Philadelphia, (1976).
- [50] G. Grimvall. *Thermophysical properties of materials, enlarged and revised edition*. North Holland, Amsterdam, (1999).
- [51] D.C. Wallace. *Thermodynamics of crystals*. Dover, Mineola, NY, (1999).
- [52] D.C. Wallace. *Statistical physics of crystals and liquids. A guide to highly accurate equations of state*. World Scientific, Singapore, (2002).
- [53] G. Grimvall. *The electron-phonon interaction in metals*. North-Holland, Amsterdam, (1981).
- [54] Barron, T. *Proc. Int. Conf. Lattice Dynamics*, 247. Pergamon Press, Oxford (1963).
- [55] Hui, J. and Allen, P. *J. Phys. C: Solid State Phys.* **8**, 2923 (1975).
- [56] Eriksson, O., Wills, J., and Wallace, D. *Phys. Rev. B* **46**, 5221 (1992).
- [57] Hove, L. V. *Phys. Rev.* **95**, 249 (1954).
- [58] Bogdanoff, P., Fultz, B., and Rosenkranz, S. *Phys. Rev. B* **60**, 3976 (1999).
- [59] Katahara, K., Manghnani, M., and Fisher, E. *J. Phys. F: Metal Phys.* **9**, 773 (1979).
- [60] Katahara, K., Nimalendran, M., Manghnani, M., and Fisher, E. *J. Phys. F: Metal Phys.* **9**, 2167 (1979).
- [61] J.T. Lenkkeri and E.E. Lähteenkorva. *J. Phys. F: Metal Phys.* **8**, 1643 (1978).
- [62] Lenkkeri, J. *J. Phys. F: Metal Phys.* **10**, 611 (1980).

- [63] Ohta, Y. and Shimizu, M. *J. Phys. F: Metal Phys.* **13**, 761 (1983).
- [64] Walker, E. *Solid State Commun.* **28**, 587 (1978).
- [65] Ashkenazi, J., Dacorogna, M., Peter, M., Talmor, Y., and Walker, E. *Phys. Rev. B* **18**, 4120 (1978).
- [66] Bujard, P., Sanjines, R., Walker, E., J.Ashkenazi, and Peter, M. *J. Phys. F: Metal Phys.* **11**, 775 (1981).
- [67] Bujard, P. and Walker, E. *Solid State Commun.* **43**, 65 (1982).
- [68] Mozer, B., Otnes, K., and Thaper, C. *Phys. Rev.* **152**, 535 (1966).
- [69] Syrykh, G., Zemlyanov, G., Chernoplekov, N., and Koltygin, V. *Sov. Phys. JETP* **46**, 162 (1977).
- [70] Syrykh, G., Zhernov, A., Zemlyanov, M., Mironov, S., Chernoplekov, N., and Shitikov, Y. *Sov. Phys. JETP* **43**, 183 (1976).
- [71] Syrykh, G., Zhernov, A., Zemlyanov, M., Chernoplekov, N., and Solovev, G. *Phys. Stat. Sol. B* **79**, 105 (1977).
- [72] Syrykh, G., Zhernov, A., Zhemlyanov, M., Chernoplekov, N., and Shitikov, Y. *Sov. Phys. Solid State* **26**, 1890 (1984).
- [73] Daümer, W., Kettschau, A., Khan, H., Lüders, K., Raub, C., H.Rieseemeier, and Roth, G. *Phys. Stat. Sol. B* **112**, K67 (1982).
- [74] Teatum, E., K.A. Gschneidner, J., and Waber, J. Technical Report No. LA-4003, Los Alamos National Laboratory, (1968).
- [75] Sears, V. *Neutron News* **3**, 26 (1992).
- [76] Sears, V., Svensson, E., and Powell, B. *Can. J. Phys.* **73**, 726 (1995).
- [77] Bogdanoff, P., Fultz, B., Robertson, J., and Crow, L. *Phys. Rev. B* **65**, 014303 (2001).

- [78] Press, W., Teukolsky, S., Vetterling, W., and Flannery, B. *Numerical Recipes in C, The art of scientific computing*. Cambridge University Press, Cambridge, second edition, (1994).
- [79] Colella, R. and Batterman, B. *Phys. Rev. B* **1**, 3913 (1970).
- [80] Rose, J., Smith, J., Guinea, F., and Ferrante, J. *Phys. Rev. B* **29**, 2963 (1984).
- [81] Dederichs, P. and Zeller, R. *Point defects in metals. II, Dynamical properties*, volume 87 of *Springer Tracts in Modern Physics*. Springer-Verlag, Berlin (1980).
- [82] de Wit, G. and Brockhouse, B. *J. Appl. Phys.* **39**, 451 (1968).
- [83] Muller, A. and Brockhouse, B. *Can. J. Phys.* **49**, 704 (1971).
- [84] Dutton, D., Brockhouse, B., and Muller, A. *Can. J. Phys.* **50**, 1207 (1972).
- [85] Maglić, K. *Int. J. Thermophys.* **24**, 489 (2002).
- [86] Touloukian, Y., Kirby, R., Taylor, R., and Desai, P. *Thermophysical properties of matter, vol 12*. IFI/Plenum, New York, (1975).
- [87] Petry, W. *Phase Transitions* **31**, 119 (1991).
- [88] Petry, W. *Journal de Physique IV* **C2**, 15 (1995).
- [89] Petry, W., Trampenau, J., and Herzig, C. *Phys. Rev. B* **48**, 881 (1993).
- [90] Güthoff, F., Petry, W., Stassis, C., Heiming, A., Hennion, B., Herzig, C., and Trampenau, J. *Phys. Rev. B* **47**, 2563 (1993).
- [91] Petry, W., Heiming, A., Trampenau, J., Alba, M., Herzig, C., Schober, H., and Vogl, G. *Phys. Rev. B* **43**, 10933 (1991).
- [92] Heiming, A., Petry, W., Trampenau, J., Alba, M., Herzig, C., Schober, H., and Vogl, G. *Phys. Rev. B* **43**, 10948 (1991).
- [93] Trampenau, J., Heiming, A., Petry, W., Alba, M., Herzig, C., Miekeley, W., and Schober, H. *Phys. Rev. B* **43**, 10963 (1991).

- [94] Price, D., Singwi, K., and Tosi, M. *Phys. Rev. B* **2**, 2983 (1970).
- [95] Higuera, B., Brotzen, F., Smith, H., and Wakabayashi, N. *Phys. Rev. B* **31**, 730 (1985).
- [96] Powell, B., Martel, P., and Woods, A. *Can. J. Phys.* **55**, 1601 (1977).
- [97] Pettifor, D. *Bonding and structure of molecules and solids*. Oxford University Press, Oxford, (1996).
- [98] Blaha, P., Schwarz, K., and Sorantin, P. *Comput. Phys. Commun.* **59**, 399 (1990).
- [99] Blaha, P., Schwarz, K., Madsen, G., Kvasnicka, D., and Luitz, J. *WIEN2k, An augmented plane wave + local orbitals program for calculating crystal properties*. Karlheinz Schwarz, Techn. Universitat Wien, Austria, (2001).
- [100] G. Kresse and J. Furthmüller. *Phys. Rev. B* **54**, 11169 (1996).
- [101] P.E. Blöchl. *Phys. Rev. B* **50**, 17953 (1994).
- [102] Kresse, G. and Joubert, J. *Phys. Rev. B* **59**, 1758 (1999).
- [103] Perdew, J., Burke, K., and Ernzerhof, M. *Phys. Rev. Lett.* **77**, 3865 (1996).
- [104] Monckhorst, H. and Pack, J. *Phys. Rev. B* **13**, 5188 (1976).
- [105] Murnaghan, F. *Proceedings of the National Academy of Sciences* **30**, 244 (1944).
- [106] Singh, J., Singh, P., Rattan, S., and Prakash, S. *Phys. Rev. B* **49**, 932 (1994).
- [107] Wills, J. and Harrison, W. *Phys. Rev. B* **28**, 4363 (1983).
- [108] Kanzaki, H. *J. Phys. Chem. Solids* **2**, 24 (1957).
- [109] Singh, P., Prakash, S., and Singh, J. *Phys. Rev. B* **49**, 12259 (1994).
- [110] Friedel, J. *Adv. Phys.* **3**, 446 (1954).
- [111] Sutton, A. *Electronic structure of materials*. Oxford University Press, Oxford, (1993).

- [112] Bruno, E., Ginatempo, B., Giuliano, E., Ruban, A., and Vekilov, Y. *Phys. Rep.* **249**, 353 (1994).
- [113] Vaks, V. and Trefilov, A. *J. Phys. F: Metal Phys.* **18**, 213 (1988).
- [114] Vaks, V. and Trefilov, A. *J. Phys.-Condens. Mat.* **3**, 1389 (1991).
- [115] Kokalj, A. *Comp. Mater. Sci.* **28**, 155 (2003). Code available from <http://www.xcrysden.org/>.
- [116] Buckel, W. and Kleiner, R. *Superconductivity, fundamentals and applications. Second edition*. Wiley-VCH, Weinheim, (2004).
- [117] McMillan, W. *Phys. Rev.* **167**, 331 (1968).
- [118] Allen, P. and Dynes, R. *Phys. Rev. B* **12**, 905 (1975).
- [119] Kuentzler, R. and Khan, H. *Physics Letters* **113A**, 89 (1985).
- [120] Isino, M., Akutsu, K., and Muto, Y. *J. Phys. Soc. Japan* **54**, 289 (1985).
- [121] Kuentzler, R. and Khan, H. *Solid State Commun.* **59**, 299 (1986).
- [122] Koch, C., Kernohan, R., and Sekula, S. *J. Appl. Phys.* **38**, 4359 (1967).
- [123] Turchi, P., Waterstrat, R., Kuentzler, R., Drchal, V., and Kudrnovský, J. *J. Phys.: Condens. Matter* **16**, 5615 (2004).
- [124] Kuentzler, R. *Solid State Commun.* **63**, 671 (1987).
- [125] Bader, R. *Atoms in molecules: a quantum theory*. Oxford University Press, New York, (1990).
- [126] de Proft, F., van Alsenoy, C., Peeters, A., Langenaeker, W., and Geerlings, P. *J. Comput. Chem.* **23**, 1198 (2002).
- [127] Harrison, W. *Electronic structure and the properties of solids. The physics of the chemical bond*. Dover, New York, (1989).
- [128] Ghosez, P., Michenaud, J.-P., and Gonze, X. *Phys. Rev. B* **58**, 6224 (1998).

- [129] Henkelman, G., Arnaldsson, A., and Jónsson, H. *Comput. Mater. Sci.* **in press** (2005).
- [130] R.E. Watson and L.H. Bennett. *Phys. Rev. B* **15**, 5136 (1977).
- [131] Watson, R. and Bennett, L. *Phys. Rev. B* **18**, 6439 (1978).
- [132] Powell, B., Martel, P., and Woods, A. *Phys. Rev.* **171**, 727 (1968).
- [133] Pynn, R., Stirling, W., Ishikawa, M., and Walker, E. *Solid State Commun.* **32**, 767 (1979).
- [134] Varma, C. and Weber, W. *Phys. Rev. Lett.* **39**, 1094 (1977).
- [135] Savrasov, S. and Savrasov, D. *Phys. Rev. B* **54**, 16487 (1996).
- [136] Suzuki, N. and Otani, M. *J. Phys.: Condens. Matter* **14**, 10869 (2002).
- [137] Ho, K.-M., Fu, C., and Harmon, B. *Phys. Rev. B* **28**, 6687 (1983).
- [138] Chen, Y., Fu, C.-L., Ho, K.-M., and Harmon, B. *Phys. Rev. B* **31**, 6775 (1985).
- [139] Ye, Y., Ho, K. M., Chen, Y., and Harmon, B. N. *J. Phys.-Condens. Mat.* **3**, 9629 (1991).
- [140] Grimvall, G., Thiessen, M., and Guillermet, A. *Phys. Rev. B* **36**, 7816 (1987).
- [141] Guillermet, A. and Grimvall, G. *Phys. Rev. B* **44**, 4332 (1991).
- [142] Trampenau, J., Petry, W., and Herzig, C. *Phys. Rev. B* **47**, 3132 (1993).
- [143] Güthoff, F., Hennion, B., Herzig, C., Petry, W., Schober, H., and Trampenau, J. *J. Phys.-Condens. Mat.* **6**, 6211 (1994).
- [144] Allen, P. and Hui, J. *Z. Physik B* **37**, 33 (1980).
- [145] Bock, N., Coffey, D., and Wallace, D. *Phys. Rev. B* **72**, 155120 (2005).
- [146] Bock, N., Coffey, D., and Wallace, D. *arXiv:cond-mat/0509305* (2005).
- [147] White, G. *Physica B* **149**, 255 (1988).

- [148] McDonald, R. and Shukla, R. *Phys. Rev. B* **32**, 4961 (1985).
- [149] Owen, W. *Mat. Sci. Eng. A* **127**, 197 (1990).
- [150] Cochran, W. *Adv. Phys.* **9**, 387 (1960).
- [151] Kaufman, L. and Cohen, M. *Transactions AIME* **206**, 1393 (1956).
- [152] Fultz, B. T. and Howe, J. M. *Transmission electron microscopy and diffractometry of materials. Second edition.* Springer-Verlag, Berlin, (2002).
- [153] Goldman, A. and Robertson, W. *Acta Metall.* **12**, 1265 (1964).
- [154] Goldman, A. and Robertson, W. *Acta Metall.* **13**, 391 (1965).
- [155] Franz, H., Asthalter, T., Dommach, M., Ehnes, A., Messel, K., and Sergueev, I. *Hyperfine Interact.* **141/142**, 131 (2002).
- [156] Hallman, E. and Brockhouse, B. *Can. J. Phys.* **47**, 1117 (1969).
- [157] G. Oomi and Nobuo Mōri. *J. Phys. Soc. Jpn.* **50**, 2917 (1981).
- [158] Herper, H., Hoffmann, E., Entel, P., and Weber, W. *J. Phys IV - C8* **5**, 293 (1995).
- [159] Porter, D. and Easterling, K. *Phase transformations in metals and alloys. Second edition.* Chapman & Hall, London, (1992).
- [160] Yamamoto, K., Asano, M., Endo, S., and Oomi, G. *Mat. Trans. JIM* **32**, 305 (1991).
- [161] Kakeshita, T., Shimizu, K., Akahama, Y., Endo, S., and Fujita, F. *T. Jpn. I. Met.* **29**, 109 (1987).
- [162] Acet, M., Schneider, T., and Wasserman, E. F. *J. Phys IV - C8* **5**, 105 (1995).
- [163] Peschard, M. *Rev. Metall.* **22**, 581 (1925).
- [164] Chaikin, P. and Lubensky, T. *Principles of condensed matter physics.* Cambridge University Press, Cambridge, (1995).
- [165] Crangle, J. and Hallam, G. C. *Proc. Roy. Soc.(London), ser. A* **272**, 119 (1963).

- [166] Bogdanoff, P. and Fultz, B. *Philos. Mag. B* **81**, 299 (2001).
- [167] Bolef, D. *J. Appl. Phys.* **32**, 100 (1961).
- [168] Mannheim, P. *Phys. Rev.* **165**, 1011 (1968).
- [169] Seto, M., Kobayashi, Y., Kitao, S., Haruki, R., Mitsui, T., Yoda, Y., Nasu, S., and Kikuta, S. *Phys. Rev. B* **61**, 11420 (2000).